Investigation of Renormalization Group Methods for the Numerical Simulation of Isotropic Turbulence

Alistair John Young

A thesis submitted in fulfilment of the requirements

for the degree of Doctor of Philosophy

to the

University of Edinburgh

1999

Abstract

Numerical simulations are becoming increasingly important and useful tools in the study of turbulent flows. Direct numerical simulation (DNS) is a method of computation in which all the important scales of motion are fully-resolved. However, flows with the sort of complexity and turbulent intensity that one might find in the laboratory, or in nature, lie well beyond our current computational reach.

The problem lies with the large number of degrees of freedom. In large eddy simulations (LES) this number is reduced by simulating only the large scales of motion, while the effects of the small scales are modelled in some way.

In Fourier space the problem becomes one of eliminating high-wavenumber modes, in some statistical sense, in order to bring the reduced number of degrees of freedom within the capacity of current (or even future) computers. In this thesis, two methods by which such a reduction in the number of modes may be obtained are explored.

A conventional approach to the problem is to model the effects of the absent modes by way of an increased viscosity. A number of theoretical ways of obtaining such an *eddy-viscosity* have been proposed. In this work, we look first at the closely-related renormalization group (RG) theories of McComb [W.D. McComb and A.G. Watt, Phys. Rev. A **46**, 4797 (1992)] and Yang [T.-J. Yang, PhD thesis, University of Edinburgh (1998)]. In these theories, a *conditional average* is introduced, allowing the high-wavenumber modes to be averaged out, whilst the

low-wavenumber modes remain unaffected. The theory of Yang also introduces a model field which is used to aid in the evaluation of the conditional averages. This averaging technique is applied iteratively, in order to eliminate a series of a narrow bands until a fixed point is reached.

Utilising the results from a DNS, the underlying feasibility of using these theories to obtain an eddy-viscosity is assessed in a number of ways. Firstly, we make a study of the properties of the nonlinear term in the Navier-Stokes equation. This term has been partitioned in the same manner as in the RG theories and the results obtained are discussed in both general and RG contexts. Secondly, we give an averaging method which may be regarded as a *computable* approximation to the conditional average. Results are given and the degree to which this technique actually models the conditional average is considered. Finally, a brief examination of Yang's model field — and its use in the evaluation of the conditional average — is made. The results of these studies suggest that there may be problems with the way in which the RG eddy-viscosity is obtained. However, we note that the majority of our tests have necessarily been limited to relatively low Reynolds number cases.

For the second wavenumber mode reduction technique, we introduce an *ad hoc* method of compensating for absent modes. Here, the energy spectrum is examined at each computational time step and the characteristic energy pile-up, indicative of an under-resolved system, is located. An extrapolation technique is then employed to correct the problem. It is seen that this method gives reasonable results for a large range of Reynolds numbers. Furthermore, *a posteriori* analysis allows us to generate equivalent eddy-viscosities for comparison with standard spectral LES techniques. It is seen that these equivalent eddy-viscosities show an excellent match for wavenumbers approaching the cutoff, but that they are flawed at low-k. The reason for this is explained, and possible methods for improving the technique are outlined.

Acknowledgements

I would like to thank my supervisor, David McComb, for his guidance and support throughout this work.

I would also like to thank all the members of the turbulence group for stimulating discussions and helpful advice, particularly Gary Fullerton and Craig Johnston, but not forgetting Adrian Hunter and Anthony Quinn.

This research project was funded by EPSRC, and their support is gratefully acknowledged.

High performance computing facilities were provided by the Edinburgh Parallel Computing Centre. Particular thanks go to David Henty and Mario Antonioletti.

To Chris Brown, Alex Rennie and Paul Spencer: thanks for all the good times.

Finally, I would like to thank my parents for their support, both financial and moral. This thesis is dedicated to them.

Table of Contents

List of Figures

List of Tables

Nomenclature

Latin symbols

$D_{\alpha\beta}$	projection operator
E	total energy
$E(k)$	energy spectrum
$\mathcal{E}(\mathcal{K})$	logarithmic energy spectrum: $\ln E(k)$
f_α	forcing term
j_α, k_α, l_α	wavevectors
j, k, l	wavenumbers
k_d	Kolmogorov wavenumber
$\mathcal{K}$	logarithmic wavenumber: $\ln k$
L	integral length scale
L_{box}	size of computational box
$M_{\alpha\beta\gamma}$	symmetric momentum transfer operator
$Q_{\alpha\beta}$	velocity correlation function
Q	isotropic velocity correlation function
p	pressure field
R	correlation
R_L	integral scale Reynolds number
R_λ	Taylor microscale Reynolds number
r_α	real space difference vector
S	longitudinal velocity derivative skewness
$T(k)$	energy transfer spectrum
t	time
u_α	velocity field
u	r.m.s. velocity
x_α	real space vector

Greek symbols

α	Kolmogorov constant
ε	energy dissipation rate
ε_w	energy input rate
η	Kolmogorov length scale
Θ	phase difference
$\theta^-(k)$, $\theta^+(k)$	spectral sharp cutoff filters
λ	Taylor microscale
ν, ν_0	kinematic viscosity
ξ	biased subensemble constraint
$\delta\nu(k)$	eddy-viscosity
$\Pi(k)$	energy transport power spectrum
ρ	fluid density
τ_E	eddy turnover time
Φ_α	difference between two velocity fields
ϕ_α	the integrated nonlinear term
ψ_α	the nonlinear term
ω_α	vorticity field

Decorations

$\langle X \rangle$	ensemble average
$\langle X \rangle_s$	shell average
$\langle X \rangle_c$	conditional average
$\langle X \rangle_\tau$	partial time average
X^*	complex conjugate
X^-, X^+	filtered variables
X_{--}	filtering within the nonlinear term
$X_{(--)}$	complement: $X - X_{--}$
$X_{\{-,-,-\}}$	filtering of triadic interaction

Abbreviations

DNS	direct numerical simulation
EDQNM	eddy-damped quasi-normal Markovian approximation
(F)FT	(fast) Fourier transform
LES	large eddy simulation
OpLES	operational large eddy simulation
RG	renormalization group

Chapter 1

Introduction

The governing equations for fluid turbulence, resulting from work carried out by luminaries such as d'Alembert, Euler, Navier, Cauchy, Poisson, Saint-Venant and Stokes [1], have been known for over 150 years. It may seem incredible that after so long, the problem still fascinates so many people working in the fields of physics, applied mathematics and engineering. Indeed, it as often said that turbulence is the "unsolved problem of classical physics" [2]. Sir Horace Lamb put it rather more colourfully — he is quoted as saying, "I am an old man now, and when I die and go to Heaven there are two matters on which I hope enlightenment. One is quantum electrodynamics and the other is turbulence of fluids. About the former, I am really rather optimistic" [3].

The pioneering studies of Osborne Reynolds in 1883 [4] were responsible for a new perspective on turbulence. Working with what is still a standard experimental set up, Reynolds investigated fluid flow through circular pipes and demonstrated that, for a given fluid and pipe, the transition from laminar to turbulent flow would occur at some critical speed.

In order to characterize the flow, Reynolds introduced a dimensionless parameter,

$$R = \frac{Ud}{\nu}, \tag{1.1}$$

which we now know as the Reynolds number. Here ν is the kinematic viscosity of

the fluid — defined as the ratio of the dynamic viscosity to the fluid density — while U and d are representative velocity and length scales respectively. Reynolds chose to use the bulk mean velocity of the flow and the diameter of the pipe for which he found that the minimum value of R for which the flow in a pipe could be laminar was around 2000.

Reynolds' impressive range of work included introducing the world to the so-called closure problem. This is encountered when one attempts to form an equation for a low-order moment such as the mean energy. Such an equation is always found to contain a higher-order moment, so that a hierarchy of equations is generated which, at any level, contains one more unknown than there are equations. In order to close the hierarchy, some sort of additional assumptions are required, and this feature has driven much of the research in turbulence that has followed. The mathematics underlying the fundamental approach to turbulence theory will be explored in greater detail in Chapter 2.

Over the past three decades, the rapid increase in the performance and availability of computer systems has meant that computers have become increasingly important tools in turbulence research. The single biggest problem facing experimental researchers in this (or any) field is the difficulty in making accurate measurements on the system under study. Computer simulations allow for measurements, that would otherwise be impossible, to be taken with ease and allow for very tight control over initial and/or boundary conditions. Additionally, by working directly with the unaveraged equations and computing moments at a later stage, the closure problem is neatly sidestepped. In Chapter 3, the basics of direct numerical simulation are explained, this is then followed in Chapters 4 and 5 by an account of the development and testing of a DNS code on the parallel Cray T3D, administered by the Edinburgh Parallel Computing Centre (EPCC).

Of course, the field of numerical simulation has its own set of drawbacks — most importantly the limitations finite computers must necessarily place on the size

and complexity of the systems they are able to model. As will be explained in the following chapters, the system we consider is as simple as we can make it, whilst still ensuring that it has interesting properties: our flow has periodic boundary conditions in all three coordinate directions and is, in addition, statistically both homogeneous (invariant under translation of axes) and isotropic (invariant under rotation of axes). This concept was first introduced by Taylor [5]. Even with all these simplifications — and even with 32Gb of memory available to us — we still find ourselves limited to relatively low-Reynolds number flows. These difficulties are compounded for researchers who wish to study high-Reynolds number flows, or flows taking place within complex geometries.

One possible solution to this problem is what are known as *large eddy simulations* (LES), covered in Chapter 6. For most engineering applications, it is the large scale motions of the flow which are of interest and, accordingly, in a LES it is only these scales which are explicitly simulated, with the net effect of the small-scale (or subgrid) modes being modelled in some way. The challenge for LES, then, is to find suitable models for the subgrid effects and Chapter 6 describes two *a priori* methods of testing such models.

In this thesis, on the subject of mode elimination, we firstly concern ourselves with two closely related theories — the two-field theory of McComb and Watt [6, 7, 8], and a derivative of that theory centred on the introduction of a model field due to McComb and Yang [9]. These theories are outlined in Chapter 7. We have performed a series of *a priori* tests on these theories by exploring some of the underpinning ideas (the results of *a posteriori* tests are expected soon [10, 11]). The results of these tests are presented in Chapters 8, 9 and 10, with a discussion of their applicability to the two-field theory given in Chapter 12.

Finally, in Chapter 11, we introduce an apparently very different approach to the problem of compensating for the missing modes. Here an *ad hoc* method is outlined, implemented and tested, and a simple way in which it may be related

Chapter 2

Turbulence Theory

The aim of this chapter is to give, in some detail, the basic definitions and derivations that will be used later, in both computational and theoretical work.

We begin with the real space equations of fluid motion which we then transform into Fourier space, making a number of simplifications along the way. There then follows a discussion of some of the more important statistical properties of turbulence.

2.1 The equations of motion of a fluid

The Navier-Stokes equations, which describe the motion of an incompressible, Newtonian fluid, are given by,

$$\frac{\partial u_\alpha(\mathbf{x},t)}{\partial t} + u_\beta(\mathbf{x},t)\frac{\partial u_\alpha(\mathbf{x},t)}{\partial x_\beta} = -\frac{1}{\rho}\frac{\partial p(\mathbf{x},t)}{\partial x_\alpha} + \nu\frac{\partial^2 u_\alpha(\mathbf{x},t)}{\partial x_\beta \partial x_\beta}, \tag{2.1}$$

$$\frac{\partial u_\beta(\mathbf{x},t)}{\partial x_\beta} = 0, \tag{2.2}$$

where $\mathbf{u}(\mathbf{x},t)$ is the velocity field, $p(\mathbf{x},t)$ is the pressure field, ρ is the density of the fluid and ν is the kinematic viscosity. Here and throughout this thesis we employ the Einstein summation convention so that repeated indices are summed. Equation (2.1) expresses conservation of momentum of the fluid and will often

be referred to simply as the momentum equation. Equation (2.2) expresses conservation of mass and will often be referred to as the *continuity equation.*

2.2 Fourier representation

Consider turbulence in a cubic box of side L_{box} with periodic boundary conditions. The velocity and pressure fields, $u_\alpha(\mathbf{x},t)$ and $p(\mathbf{x},t)$, can be expanded in terms of Fourier series,

$$u_\alpha(\mathbf{x},t) = \sum_{\mathbf{k}} u_\alpha(\mathbf{k},t)e^{i\mathbf{k}\cdot\mathbf{x}}, \tag{2.3}$$

$$p(\mathbf{x},t) = \sum_{\mathbf{k}} p(\mathbf{k},t)e^{i\mathbf{k}\cdot\mathbf{x}}, \tag{2.4}$$

where the wavevectors, $\mathbf{k}$, are given by,

$$k_\alpha = \frac{2\pi}{L_{box}} n_\alpha \tag{2.5}$$

for integer n_α.

We can now apply these to our equations of motion, recalling the general properties of the Fourier transform (FT) that,

$$\frac{\partial}{\partial x_\alpha} A(\mathbf{x}) \xrightarrow{FT} ik_\alpha A(\mathbf{k}), \tag{2.6}$$

$$A(\mathbf{x})B(\mathbf{x}) \xrightarrow{FT} \sum_{\mathbf{j}+\mathbf{l}=\mathbf{k}} A(\mathbf{j})B(\mathbf{l}). \tag{2.7}$$

We begin with the continuity equation (2.2) which becomes,

$$k_\alpha u_\alpha(\mathbf{k},t) = 0, \tag{2.8}$$

asserting that $\mathbf{u}(\mathbf{k},t)$ is orthogonal to $\mathbf{k}$.

Noting that, due to equation (2.2),

$$u_\beta(\mathbf{x},t)\frac{\partial u_\alpha(\mathbf{x},t)}{\partial x_\beta} = \frac{\partial}{\partial x_\beta}\left[u_\alpha(\mathbf{x},t)u_\beta(\mathbf{x},t)\right], \tag{2.9}$$

we can also transform the conservation of momentum equation, (2.1), to give

$$\frac{\partial u_\alpha(\mathbf{k},t)}{\partial t} + ik_\beta \sum_{\mathbf{j}+\mathbf{l}=\mathbf{k}} u_\alpha(\mathbf{j},t)u_\beta(\mathbf{l},t) = -\frac{ik_\alpha}{\rho}p(\mathbf{k},t) - \nu k^2 u_\alpha(\mathbf{k},t), \tag{2.10}$$

where $k^2 = k_\alpha k_\alpha = |\mathbf{k}|^2$.

Next we eliminate the pressure field, $p(\mathbf{k},t)$, by first rewriting equation (2.10) for u_β (so that $\alpha \to \beta$ and $\beta \to \gamma$), multiplying through by k_γ and using the continuity equation, (2.8), to give,

$$-\frac{i}{\rho}p(\mathbf{k},t) = \frac{ik_\beta k_\gamma}{k^2} \sum_{\mathbf{j}+\mathbf{l}=\mathbf{k}} u_\beta(\mathbf{j},t)u_\gamma(\mathbf{l},t). \tag{2.11}$$

This may be substituted back into equation (2.10) giving, with some rearrangement,

$$\left(\frac{\partial}{\partial t} + \nu k^2\right) u_\alpha(\mathbf{k},t) = ik_\alpha \frac{k_\beta k_\gamma}{k^2} \sum_{\mathbf{j}+\mathbf{l}=\mathbf{k}} u_\beta(\mathbf{j},t)u_\gamma(\mathbf{l},t) - ik_\beta \sum_{\mathbf{j}+\mathbf{l}=\mathbf{k}} u_\alpha(\mathbf{j},t)u_\beta(\mathbf{l},t). \tag{2.12}$$

Next we relabel the dummy index in the second term on the RHS ($\beta \to \gamma$) and introduce the Kronecker delta function in order to give both sums on the RHS the same form,

$$\left(\frac{\partial}{\partial t} + \nu k^2\right) u_\alpha(\mathbf{k},t) = ik_\alpha \frac{k_\beta k_\gamma}{k^2} \sum_{\mathbf{j}+\mathbf{l}=\mathbf{k}} u_\beta(\mathbf{j},t)u_\gamma(\mathbf{l},t) - ik_\gamma \delta_{\alpha\beta} \sum_{\mathbf{j}+\mathbf{l}=\mathbf{k}} u_\beta(\mathbf{j},t)u_\gamma(\mathbf{l},t). \tag{2.13}$$

Introducing,

$$D_{\alpha\beta}(\mathbf{k}) = \delta_{\alpha\beta} - \frac{k_\alpha k_\beta}{k^2}, \tag{2.14}$$

equation (2.13) may be written as,

$$\left(\frac{\partial}{\partial t} + \nu k^2\right) u_\alpha(\mathbf{k},t) = -ik_\gamma D_{\alpha\beta}(\mathbf{k}) \sum_{\mathbf{j}+\mathbf{l}=\mathbf{k}} u_\beta(\mathbf{j},t)u_\gamma(\mathbf{l},t). \tag{2.15}$$

The term on the RHS contains the dummy indices, β and γ, and the dummy variables, $\mathbf{j}$ and $\mathbf{l}$. This means that we are free to exchange them ($\beta \leftrightarrow \gamma$ and $\mathbf{j} \leftrightarrow \mathbf{l}$), so that,

$$k_\gamma D_{\alpha\beta}(\mathbf{k}) \sum_{\mathbf{j}+\mathbf{l}=\mathbf{k}} u_\beta(\mathbf{j},t)u_\gamma(\mathbf{l},t) = k_\beta D_{\alpha\gamma}(\mathbf{k}) \sum_{\mathbf{j}+\mathbf{l}=\mathbf{k}} u_\beta(\mathbf{j},t)u_\gamma(\mathbf{l},t). \tag{2.16}$$

With this in mind, we can define the symmetric operator,

$$M_{\alpha\beta\gamma}(\mathbf{k}) = \frac{1}{2i}\left[k_\beta D_{\alpha\gamma}(\mathbf{k}) + k_\gamma D_{\alpha\beta}(\mathbf{k})\right], \tag{2.17}$$

giving us a final form for the Navier-Stokes equation of,

$$\left(\frac{\partial}{\partial t} + \nu k^2\right) u_\alpha(\mathbf{k},t) = M_{\alpha\beta\gamma}(\mathbf{k}) \sum_{\mathbf{j}} u_\beta(\mathbf{j},t) u_\gamma(\mathbf{k}-\mathbf{j},t), \tag{2.18}$$

where we have rewritten the sum in a more explicit form.

2.3 Velocity field moments

Working in real space, we are able to define the two-point, two-time velocity field moment by,

$$Q_{\alpha\beta}(\mathbf{x},\mathbf{x}';t,t') = \langle u_\alpha(\mathbf{x},t) u_\beta(\mathbf{x}',t')\rangle, \tag{2.19}$$

and at this point we introduce our first simplification: (spatial) homogeneity.

By specifying that the system we are considering is homogeneous, we are restricting our attention to velocity fields for which the mean properties do not vary under spatial translation. So, introducing,

$$\mathbf{r} = \mathbf{x} - \mathbf{x}', \tag{2.20}$$

we can write,

$$\begin{aligned} Q_{\alpha\beta}(\mathbf{x},\mathbf{x}';t,t') &= \langle u_\alpha(\mathbf{x},t) u_\beta(\mathbf{x}',t')\rangle \\ &= \langle u_\alpha(\mathbf{x}'+\mathbf{r},t) u_\beta(\mathbf{x}',t')\rangle \\ &= \langle u_\alpha(\mathbf{r},t) u_\beta(\mathbf{0},t')\rangle \\ &= Q_{\alpha\beta}(\mathbf{r};t,t') \text{ say.} \end{aligned} \tag{2.21}$$

Now, moving back into Fourier space, we wish to know what the two-point moment looks like. We begin by writing down the expression for the Fourier coefficients in equation (2.3),

$$u_\alpha(\mathbf{k},t) = \left(\frac{1}{L_{box}}\right)^3 \int \mathrm{d}^3x \; u_\alpha(\mathbf{x},t) e^{-i\mathbf{k}\cdot\mathbf{x}}, \tag{2.22}$$

where the integral with respect to $\mathbf{x}$ is over the volume, L_{box}^3, of the box. Next we can write down an expression for the moment of two Fourier modes,

$$\begin{aligned}
\langle u_\alpha(\mathbf{k},t)u_\beta(\mathbf{k}',t')\rangle &= \left(\frac{1}{L_{box}}\right)^6 \int\int \mathrm{d}^3x\ \mathrm{d}^3x' \langle u_\alpha(\mathbf{x},t)u_\beta(\mathbf{x}',t')\rangle\, e^{-i(\mathbf{k}\cdot\mathbf{x}+\mathbf{k}'\cdot\mathbf{x}')} \\
&= \left(\frac{1}{L_{box}}\right)^6 \int\int \mathrm{d}^3x\ \mathrm{d}^3r \langle u_\alpha(\mathbf{x},t)u_\beta(\mathbf{x}-\mathbf{r},t')\rangle\, e^{-i(\mathbf{k}\cdot\mathbf{x}+\mathbf{k}'\cdot\mathbf{x}-\mathbf{k}'\cdot\mathbf{r})} \\
&= \left(\frac{1}{L_{box}}\right)^6 \int\int \mathrm{d}^3x\ \mathrm{d}^3r \langle u_\alpha(\mathbf{0},t)u_\beta(-\mathbf{r},t')\rangle\, e^{-i(\mathbf{k}\cdot\mathbf{x}+\mathbf{k}'\cdot\mathbf{x}-\mathbf{k}'\cdot\mathbf{r})} \\
&= \left(\frac{1}{L_{box}}\right)^6 \int \mathrm{d}^3r\ Q_{\alpha\beta}(\mathbf{r};t,t')e^{i\mathbf{k}'\cdot\mathbf{r}} \int \mathrm{d}^3x\ e^{-i(\mathbf{k}+\mathbf{k}')\cdot\mathbf{x}}, \qquad (2.23)
\end{aligned}$$

where $\mathbf{r}$ is defined in equation (2.20) and we have used homogeneity in the last two steps.

Noting that[1],

$$\left(\frac{1}{L_{box}}\right)^3 \int \mathrm{d}^3x\ e^{-i(\mathbf{k}+\mathbf{k}')\cdot\mathbf{x}} = \delta_{\mathbf{k}+\mathbf{k}',0} \qquad (2.24)$$

we may write equation (2.23) as,

$$\langle u_\alpha(\mathbf{k},t)u_\beta(\mathbf{k}',t')\rangle = \delta_{\mathbf{k}+\mathbf{k}',0}\left(\frac{1}{L_{box}}\right)^3 \int \mathrm{d}^3r\ Q_{\alpha\beta}(\mathbf{r};t,t')e^{i\mathbf{k}'\cdot\mathbf{r}}. \qquad (2.25)$$

The presence of the delta function immediately tells us that the correlation between modes $\mathbf{k}$ and $\mathbf{k}'$ is non-zero if and only if $\mathbf{k}' = -\mathbf{k}$. Specializing to this case, we can write,

$$\langle u_\alpha(\mathbf{k},t)u_\beta(-\mathbf{k},t')\rangle = \left(\frac{1}{L_{box}}\right)^3 \int \mathrm{d}^3r\ Q_{\alpha\beta}(\mathbf{r};t,t')e^{-i\mathbf{k}\cdot\mathbf{r}}, \qquad (2.26)$$

and hence,

$$Q_{\alpha\beta}(\mathbf{r};t,t') = \sum_{\mathbf{k}} \langle u_\alpha(\mathbf{k},t)u_\beta(-\mathbf{k},t')\rangle\, e^{i\mathbf{k}\cdot\mathbf{r}}. \qquad (2.27)$$

These equations imply that the Fourier transform of $Q_{\alpha\beta}(\mathbf{r};t,t')$ is given by the (discrete) function,

$$Q_{\alpha\beta;\mathbf{k}}(t,t') = \langle u_\alpha(\mathbf{k},t)u_\beta(-\mathbf{k},t')\rangle\,. \qquad (2.28)$$

[1]For details see, for example, appendix D of reference [2]

At this point, we prepare to take the limit $L_{box} \to \infty$. The first step is to connect the discrete spectral tensor to the continuous version by writing [12],

$$\begin{aligned} Q_{\alpha\beta}(\mathbf{k};t,t') &= \left(\frac{L_{box}}{2\pi}\right)^3 Q_{\alpha\beta;\mathbf{k}}(t,t') \\ &= \left(\frac{L_{box}}{2\pi}\right)^3 \langle u_\alpha(\mathbf{k},t) u_\beta(-\mathbf{k},t')\rangle \,. \end{aligned} \tag{2.29}$$

In addition to allowing us, shortly, to take the infinite system limit, this connection is also of vital importance for numerical simulations. In such situations, we cannot take the infinite system limit, but equation (2.29) allows us to connect numerical results to those predicted by theory.

The Fourier integral transform pair now obtained when $L_{box} \to \infty$ is then,

$$Q_{\alpha\beta}(\mathbf{r};t,t') = \int \mathrm{d}^3k \; Q_{\alpha\beta}(\mathbf{k};t,t') e^{i\mathbf{k}\cdot\mathbf{r}}, \tag{2.30}$$

$$Q_{\alpha\beta}(\mathbf{k};t,t') = \left(\frac{1}{2\pi}\right)^3 \int \mathrm{d}^3r \; Q_{\alpha\beta}(\mathbf{r};t,t') e^{-i\mathbf{k}\cdot\mathbf{r}}, \tag{2.31}$$

and equation (2.29) becomes,

$$Q_{\alpha\beta}(\mathbf{k};t,t') = \langle u_\alpha(\mathbf{k},t) u_\beta(-\mathbf{k},t')\rangle \,. \tag{2.32}$$

2.4 Isotropic turbulence

In the previous section, we introduced the simplification of homogeneity to our system. In this section we simplify things further by introducing *isotropy* — statistical invariance under rotation of axes.

Robertson [13], whose work in this area is summarized by Batchelor [14], showed that any isotropic second order tensor — and, in particular, the correlation tensor, $Q_{\alpha\beta}(\mathbf{k};t,t')$, can be written as

$$Q_{\alpha\beta}(\mathbf{k};t,t') = Q(k;t,t')\delta_{\alpha\beta} + A(k;t,t')k_\alpha k_\beta, \tag{2.33}$$

where $A(k;t,t')$ and $Q(k;t,t')$ are even functions of $|\mathbf{k}| = k$.

From the definition of $Q_{\alpha\beta}(\mathbf{k};t,t')$ in equation (2.29), and invoking continuity we may write,

$$k_\beta Q_{\alpha\beta}(\mathbf{k};t,t') = 0 = Q(k;t,t')k_\alpha + A(k;t,t')k^2 k_\alpha. \tag{2.34}$$

Since this must hold for all k_α, we may infer that

$$Q(k;t,t') = -k^2 A(k;t,t'), \tag{2.35}$$

giving rise to,

$$\begin{aligned} Q_{\alpha\beta}(\mathbf{k};t,t') &= Q(k;t,t')\delta_{\alpha\beta} - Q(k;t,t')\frac{k_\alpha k_\beta}{k^2} \\ &= D_{\alpha\beta}(\mathbf{k})Q(k;t,t'), \end{aligned} \tag{2.36}$$

where $D_{\alpha\beta}(\mathbf{k})$ is given by equation (2.14).

Equation (2.32) can then be used to give,

$$\langle u_\alpha(\mathbf{k},t)u_\beta(-\mathbf{k},t')\rangle = D_{\alpha\beta}(\mathbf{k})Q(k;t,t'), \tag{2.37}$$

which, noting that $D_{\alpha\alpha}(\mathbf{k}) = 2$, gives us,

$$\frac{1}{2}\langle u_\alpha(\mathbf{k},t)u_\alpha(-\mathbf{k},t')\rangle = Q(k;t,t'). \tag{2.38}$$

For the case of single time correlations we will write,

$$Q(k;t,t) = Q(k,t) = \frac{1}{2}\langle u_\alpha(\mathbf{k},t)u_\alpha(-\mathbf{k},t)\rangle = \frac{1}{2}Q_{\alpha\alpha}(\mathbf{k};t,t). \tag{2.39}$$

2.5 The energy spectrum

In real space, the total energy, E, per unit mass of incompressible fluid is given by,

$$\begin{aligned} E(t) &= \tfrac{1}{2}\langle u_\alpha(\mathbf{x},t)u_\alpha(\mathbf{x},t)\rangle \\ &= \tfrac{1}{2}Q_{\alpha\alpha}(\mathbf{r}=\mathbf{0};t,t) \\ &= \tfrac{1}{2}\int \mathrm{d}^3k\; Q_{\alpha\alpha}(\mathbf{k};t,t) \end{aligned} \tag{2.40}$$

where the last step follows from equation (2.30). Using isotropy to write $Q_{\alpha\alpha}(\mathbf{k};t,t) = 2Q(k,t)$ we obtain,

$$\begin{aligned} E(t) &= \int \mathrm{d}^3k\ Q(k,t) \\ &= \int \mathrm{d}k\ 4\pi k^2 Q(k,t) \\ &= \int \mathrm{d}k\ E(k,t), \end{aligned} \tag{2.41}$$

where,

$$E(k,t) = 4\pi k^2 Q(k,t). \tag{2.42}$$

The term, $E(k,t)$, is the energy spectrum of the system, and the way it is related to the underlying velocity field depends upon whether the system is continuous or discrete. For the continuous case, we invoke equation (2.38), giving,

$$E(k,t) = 2\pi k^2 \left\langle u_\alpha(\mathbf{k},t) u_\alpha(-\mathbf{k},t') \right\rangle. \tag{2.43}$$

For the discrete case — important for numerical simulations — we use equations (2.29) and (2.36) to give,

$$E(k,t) = L_{box}^3 \frac{k^2}{4\pi^2} \left\langle u_\alpha(\mathbf{k},t) u_\alpha(-\mathbf{k},t') \right\rangle. \tag{2.44}$$

2.6 The energy balance equation

Starting with the Navier-Stokes equation in Fourier-space given by equation (2.18), we take the infinite system limit, multiply through by $u_\alpha(-\mathbf{k},t)$, and average to give,

$$\begin{aligned} &\left\langle u_\alpha(-\mathbf{k},t) \left(\frac{\partial}{\partial t} + \nu k^2 \right) u_\alpha(\mathbf{k},t) \right\rangle \\ &\quad = M_{\alpha\beta\gamma}(\mathbf{k}) \int \mathrm{d}^3j\ \left\langle u_\alpha(-\mathbf{k},t) u_\beta(\mathbf{j},t) u_\gamma(\mathbf{k}-\mathbf{j},t) \right\rangle. \end{aligned} \tag{2.45}$$

We next take the complex conjugate of this equation to give,

$$\begin{aligned} &\left\langle u_\alpha(\mathbf{k},t) \left(\frac{\partial}{\partial t} + \nu k^2 \right) u_\alpha(-\mathbf{k},t) \right\rangle \\ &\quad = \left\{ M_{\alpha\beta\gamma}(\mathbf{k}) \int \mathrm{d}^3j\ \left\langle u_\alpha(-\mathbf{k},t) u_\beta(\mathbf{j},t) u_\gamma(\mathbf{k}-\mathbf{j},t) \right\rangle \right\}^*. \end{aligned} \tag{2.46}$$

Through isotropy, we note that the LHS of equations (2.45) and (2.46) are equal, and hence must both be real. The same must obviously apply to the RHS and so adding the two equations together gives us,

$$\left(\frac{\partial}{\partial t} + 2\nu k^2\right) \langle u_\alpha(\mathbf{k},t) u_\alpha(-\mathbf{k},t)\rangle$$
$$= \; 2M_{\alpha\beta\gamma}(\mathbf{k}) \int \mathrm{d}^3 j \; \langle u_\alpha(-\mathbf{k},t) u_\beta(\mathbf{j},t) u_\gamma(\mathbf{k}-\mathbf{j},t)\rangle \,. \tag{2.47}$$

Now, in analogy with equation (2.32) we introduce,

$$Q_{\alpha\beta\gamma}(\mathbf{k},\mathbf{j};t,t',t'') = \langle u_\alpha(\mathbf{k},t) u_\beta(\mathbf{j},t') u_\gamma(-\mathbf{k}-\mathbf{j},t'')\rangle \,, \tag{2.48}$$

so that equation (2.47) may be written as,

$$\left(\frac{\partial}{\partial t} + 2\nu k^2\right) 2Q(k;t,t) = 2M_{\alpha\beta\gamma}(\mathbf{k}) \int \mathrm{d}^3 j \; Q_{\alpha\beta\gamma}(-\mathbf{k},\mathbf{j};t,t,t), \tag{2.49}$$

where we have used equation (2.38) on the LHS. Finally, multiplying through by $2\pi k^2$ gives,

$$\left(\frac{\partial}{\partial t} + 2\nu k^2\right) E(k,t) = T(k,t), \tag{2.50}$$

where,

$$T(k,t) = 4\pi k^2 M_{\alpha\beta\gamma}(\mathbf{k}) \int \mathrm{d}^3 j \; Q_{\alpha\beta\gamma}(-\mathbf{k},\mathbf{j};t,t,t). \tag{2.51}$$

It may not be immediately obvious that the RHS of equation (2.51) is dependent only on $k = |\mathbf{k}|$, but this must follow from equation (2.49).

Equation (2.50) is the energy balance equation, and $T(k,t)$ is known as the energy transfer spectrum — the reason for this name will become clear shortly.

We can obtain an equation for the evolution of the total energy by integrating through equation (2.50) with respect to k,

$$\frac{\mathrm{d}E(t)}{\mathrm{d}t} + \int_0^\infty 2\nu k^2 E(k,t)\mathrm{d}k = \int_0^\infty T(k,t)\mathrm{d}k. \tag{2.52}$$

We now deal separately with the term on the right-hand side, by first expanding out the integral to give,

$$\int_0^\infty T(k,t)\mathrm{d}k \;=\; \int_0^\infty \mathrm{d}k \; 4\pi k^2 M_{\alpha\beta\gamma}(\mathbf{k}) \int \mathrm{d}^3 j \; Q_{\alpha\beta\gamma}(-\mathbf{k},\mathbf{j};t,t,t)$$
$$= \int \mathrm{d}^3 k \int \mathrm{d}^3 j \; M_{\alpha\beta\gamma}(\mathbf{k}) Q_{\alpha\beta\gamma}(-\mathbf{k},\mathbf{j};t,t,t). \tag{2.53}$$

This equation is given in terms of the symmetric operator, $M_{\alpha\beta\gamma}(\mathbf{k})$. For the following analysis it is more convenient to use the non-symmetric form of the Navier-Stokes equation (2.15) so that we may write,

$$\int_0^\infty T(k,t)\mathrm{d}k = \int \mathrm{d}^3k \int \mathrm{d}^3j \; [-ik_\gamma D_{\alpha\beta}(\mathbf{k})]\, Q_{\alpha\beta\gamma}(-\mathbf{k},\mathbf{j};t,t,t). \tag{2.54}$$

We then note that,

$$\begin{aligned} D_{\alpha\beta}(\mathbf{k})Q_{\alpha\beta\gamma}(-\mathbf{k},\mathbf{j};t,t,t) &= \left(\delta_{\alpha\beta} - \frac{k_\alpha k_\beta}{|\mathbf{k}|^2}\right)\langle u_\alpha(-\mathbf{k},t)u_\beta(\mathbf{j},t)u_\gamma(\mathbf{k}-\mathbf{j},t)\rangle \\ &= \langle u_\beta(-\mathbf{k},t)u_\beta(\mathbf{j},t)u_\gamma(\mathbf{k}-\mathbf{j},t)\rangle \\ &\quad - \langle k_\alpha u_\alpha(-\mathbf{k},t)k_\beta u_\beta(\mathbf{j},t)u_\gamma(\mathbf{k}-\mathbf{j},t)\rangle / |\mathbf{k}|^2 \\ &= Q_{\beta\beta\gamma}(-\mathbf{k},\mathbf{j};t,t,t), \end{aligned} \tag{2.55}$$

where the last step follows from continuity ($k_\alpha u_\alpha(-\mathbf{k},t) = 0$). From equation (2.54) we then have,

$$\int_0^\infty T(k,t)\mathrm{d}k = -\int \mathrm{d}^3k \int \mathrm{d}^3j \; ik_\gamma Q_{\beta\beta\gamma}(-\mathbf{k},\mathbf{j};t,t,t). \tag{2.56}$$

Now, because $\mathbf{k}$ and $\mathbf{j}$ are dummy variables, we are permitted to interchange them. In addition, we are integrating over all space with respect to these variables and so we may then flip their signs, $\mathbf{k} \leftrightarrow -\mathbf{k}$ and $\mathbf{j} \leftrightarrow -\mathbf{j}$. This gives us,

$$\begin{aligned} \int_0^\infty T(k,t)\mathrm{d}k &= -\int \mathrm{d}^3k \int \mathrm{d}^3j \; [ij_\gamma Q_{\beta\beta\gamma}(-\mathbf{j},\mathbf{k};t,t,t)] \\ &= \int \mathrm{d}^3k \int \mathrm{d}^3j \; [ij_\gamma Q_{\beta\beta\gamma}(\mathbf{j},-\mathbf{k};t,t,t)] \\ &= \int \mathrm{d}^3k \int \mathrm{d}^3j \; [ij_\gamma Q_{\beta\beta\gamma}(-\mathbf{k},\mathbf{j};t,t,t)], \end{aligned} \tag{2.57}$$

where the last step relies on the repeated β index. Now, using continuity, we may write,

$$(k_\gamma - j_\gamma)u_\gamma(\mathbf{k}-\mathbf{j}) = 0, \tag{2.58}$$

so that,

$$k_\gamma u_\gamma(\mathbf{k}-\mathbf{j}) = j_\gamma u_\gamma(\mathbf{k}-\mathbf{j}), \tag{2.59}$$

and hence we may replace the j_γ on the RHS of equation (2.57) with k_γ, giving,

$$\int_0^\infty T(k,t)\mathrm{d}k = \int \mathrm{d}^3k \int \mathrm{d}^3j \; [ik_\gamma Q_{\beta\beta\gamma}(-\mathbf{k},\mathbf{j};t,t,t)], \tag{2.60}$$

Adding this to equation (2.56) and dividing by two then gives us the final result,

$$\int_0^\infty T(k,t)\mathrm{d}k = 0. \tag{2.61}$$

This implies that $T(k,t)$ does not contribute to the overall energy balance. Its purpose is to move energy between modes and hence its description as the *energy transfer spectrum.*

With this in mind, the integrated energy balance equation, (2.52), becomes simply,

$$\frac{\mathrm{d}E(t)}{\mathrm{d}t} + \varepsilon(t) = 0, \tag{2.62}$$

where the dissipation rate, $\varepsilon(t)$ is given by,

$$\varepsilon(t) = \int_0^\infty 2\nu k^2 E(k,t)\mathrm{d}k. \tag{2.63}$$

2.7 Forced turbulence

The equation of motion, (2.18), and energy balance equations, (2.50) and (2.62), seen so far describe the evolution of turbulence undergoing free decay. In order to describe a flow where the level of turbulence is sustained, it is common practice to include a forcing term in the Navier-Stokes equation,

$$\left(\frac{\partial}{\partial t} + \nu k^2\right) u_\alpha(\mathbf{k},t) = M_{\alpha\beta\gamma}(\mathbf{k}) \sum_{\mathbf{j}} u_\beta(\mathbf{j},t) u_\gamma(\mathbf{k}-\mathbf{j},t) + f_\alpha(\mathbf{k},t), \tag{2.64}$$

where $f_\alpha(\mathbf{k},t)$ must be isotropic, homogeneous and satisfy continuity,

$$k_\alpha f_\alpha(\mathbf{k},t) = 0. \tag{2.65}$$

The energy balance equation, (2.50), in this case becomes,

$$\left(\frac{\partial}{\partial t} + 2\nu k^2\right) E(k,t) = T(k,t) + \varepsilon_w(k,t), \tag{2.66}$$

where the energy input term is given by,

$$\varepsilon_w(k) = 4\pi k^2 \left\langle u_\alpha(-\mathbf{k}) f_\alpha(\mathbf{k}) \right\rangle. \tag{2.67}$$

Integrating with respect to k then gives,

$$\frac{\mathrm{d}E(t)}{\mathrm{d}t} + \varepsilon(t) = \varepsilon_w(t). \tag{2.68}$$

Assuming that the forcing term provides a reasonably steady energy input rate, its presence will describe (statistically) stationary turbulence. The turbulence adjusts itself until the dissipation rate matches the energy input rate, $\varepsilon = \varepsilon_w$, and stationarity is achieved.

The question of forcing will be revisited in Chapters 3 and 4.

2.8 The inertial range & Kolmogorov's spectrum

Turbulence involves motion on a large number of length scales. We now consider the range of scales involved. The largest possible eddy will be limited by the size of the system and so, referring back to equation (2.5), the smallest possible wavenumber, k_{min}, is given by,

$$k_{min} = 2\pi / L_{box}. \tag{2.69}$$

The smallest possible size of eddy will be determined by viscous dissipation. The only relevant physical parameters available are the viscosity and the dissipation rate and hence the Kolmogorov length scale, η, is defined through dimensional arguments to be,

$$\eta = (\nu^3/\varepsilon)^{1/4}. \tag{2.70}$$

Inverting this gives us Kolmogorov's dissipation wavenumber, k_d, an approximate measure of the maximum possible wavenumber,

$$k_d = 1/\eta = (\varepsilon/\nu^3)^{1/4}. \tag{2.71}$$

In 1941, Kolmogorov made two hypotheses which allow us to write down a theoretical form for the energy spectrum [15, 16]. Firstly we argue that for sufficiently

high wavenumbers, the only two relevant physical parameters are the viscosity and the dissipation rate. Following a dimensional argument, we may then write the energy spectrum as,

$$E(k) = \nu^{5/4}\varepsilon^{1/4} f(k/k_d) \tag{2.72}$$

where f is an unknown function.

Kolmogorov's second hypothesis was that, in the limit of infinite Reynolds number, the form of the energy spectrum should become independent of the viscosity. This gives a form of the unknown function, f, of,

$$f(k/k_d) = \alpha(k/k_d)^{-5/3} = \alpha\nu^{-5/4}\varepsilon^{5/12}k^{-5/3}, \tag{2.73}$$

where α is the *Kolmogorov constant*. Substituting this back into equation (2.72) gives,

$$E(k) = \alpha\varepsilon^{2/3}k^{-5/3} \tag{2.74}$$

in the infinite Reynolds number limit.

For large, but finite, Reynolds numbers it is possible to obtain a similar, if restricted conclusion. It has long been known experimentally that the energy in a turbulent system is determined by the largest scales, while the dissipation is determined by the smallest scales [17]. The *inertial range* of scales, $k_{min} \ll k \ll k_d$, acts as a link between energy input at the large scales and energy output (dissipation) at the small scales. As in the infinite Reynolds number limit, we expect that wavenumbers in the inertial range are independent of the viscosity. We now postulate a slightly more complicated form for f given by,

$$f(k/k_d) = \alpha(k/k_d)^{-5/3}F(k/k_d), \tag{2.75}$$

with $F(0) = 1$. Substituting this into equation (2.72) gives us,

$$E(k) = \alpha\varepsilon^{2/3}k^{-5/3}F(k/k_d) \tag{2.76}$$

for $k \gg k_{min}$. In the inertial range, this form for the energy spectrum tends asymptotically towards that given in equation (2.74).

2.9 Energy transport

The transport power, $\Pi(k,t)$, was introduced by Kraichnan [18] and is defined by,

$$\Pi(k,t) = \int_k^\infty T(k',t)\mathrm{d}k' = -\int_0^k T(k',t)\mathrm{d}k', \tag{2.77}$$

where the last step follows from equation (2.61). This gives the rate at which energy is transferred from modes with $k' < k$ to those with $k' > k$.

Now we consider a mode, k, lying within an inertial range so that it is independent of the viscosity. If we assume that the turbulence is stationary (so that $\mathrm{d}E(k,t)/\mathrm{d}t = 0$) and that the forcing is confined to modes $k' < k$, then we can integrate the energy balance equation (2.66) from k to infinity to give,

$$\Pi(k,t) = \varepsilon(t). \tag{2.78}$$

Equation (2.78) gives us a very handy means of testing for the presence of an inertial range. This is a far more reliable method than simply looking for $k^{-5/3}$ behaviour in the energy spectrum.

2.10 Velocity, length and time scales

We end this chapter by defining some important quantities, calculable from a turbulent velocity field. These will be frequently referred to throughout the rest of this thesis.

A generic Reynolds number was introduced in Chapter 1. In addition to the kinematic viscosity, computation of a Reynolds number requires both a velocity scale and a length scale. For the first of these, we introduce the r.m.s. velocity, $u(t)$, given by,

$$u(t) = \sqrt{\frac{2}{3}E(t)}. \tag{2.79}$$

We then introduce two length scales [2] — the integral length scale (usually taken to be representative of the large scales), $L(t)$, and the Taylor microscale, $\lambda(t)$ (taken to be intermediate between the energy input and dissipation scales [19]). These are defined as,

$$L(t) = \left[\frac{3\pi}{4}\int_0^\infty k^{-1}E(k,t)\mathrm{d}k\right]/E(t), \tag{2.80}$$

$$\lambda(t) = \left[5E(t)/\int_0^\infty k^2E(k,t)\mathrm{d}k\right]^{1/2}. \tag{2.81}$$

With these definitions in mind, we are now able to define the integral and microscale Reynolds numbers as,

$$R_L(t) = \frac{L(t)u(t)}{\nu}, \tag{2.82}$$

$$R_\lambda(t) = \frac{\lambda(t)u(t)}{\nu}. \tag{2.83}$$

Finally, we define the *eddy turnover time*, a measure of the typical time for a structure of size $\sim L(t)$ to undergo significant distortion due to the relative motion of its components [20]. This is given by,

$$\tau_E(t) = \frac{L(t)}{u(t)}. \tag{2.84}$$

Chapter 3

Direct Numerical Simulation of Turbulence

In 1969, Orszag introduced the idea of simulating the Navier-Stokes equations directly on a computer [21]. At that time, the scope of such simulations was severely limited by the power of the computers available. Indeed, the IBM Model 360-95 computer used by Orszag, with approximately 16Mb of memory and a clock speed of approximately 1MHz, meant that he was restricted to a Reynolds number of $R_\lambda \approx 20$. Computer technology has made great progress over the past three decades, but despite now having access to machines with over a thousand times the memory and processing power, we are only just starting to approach Reynolds numbers that are genuinely comparable with interesting laboratory flows. This is due to the immense computational complexity of the problem — the number of points needed along each grid axis in a simulation goes like $Re^{3/4}$ and hence memory requirements for a three-dimensional system go like $Re^{9/4}$ [2]. However, while the computation is undoubtedly complicated, the idea underpinning direct numerical simulation (DNS) is very simple — namely that we consider a fully-resolved picture of turbulence by computing the evolution of a velocity field at all significant length scales using the Navier-Stokes equations.

3.1 Navier-Stokes Equation Revisited

In Chapter 2 we derived a form for the Navier-Stokes equation in Fourier space, given by equation (2.18). Our first step in this chapter is to rederive this equation, in a form more suited to numerical simulation.

We return to equation (2.1) which, for convenience of manipulation, we rewrite in vector notation,

$$\frac{\partial \mathbf{u}(\mathbf{x},t)}{\partial t} + [\mathbf{u}(\mathbf{x},t)\cdot\nabla]\,\mathbf{u}(\mathbf{x},t) = -\frac{1}{\rho}\nabla p(\mathbf{x},t) + \nu\nabla^2\mathbf{u}(\mathbf{x},t). \tag{3.1}$$

Employing a standard identity [22], we may write,

$$(\mathbf{u}(\mathbf{x},t)\cdot\nabla)\,\mathbf{u}(\mathbf{x},t) = (\nabla\times\mathbf{u}(\mathbf{x},t))\times\mathbf{u}(\mathbf{x},t) + \tfrac{1}{2}\nabla u^2(\mathbf{x},t), \tag{3.2}$$

where,

$$u^2(\mathbf{x},t) = \mathbf{u}(\mathbf{x},t)\cdot\mathbf{u}(\mathbf{x},t) = |\mathbf{u}(\mathbf{x},t)|^2. \tag{3.3}$$

The *vorticity* is given by the curl of $\mathbf{u}(\mathbf{x},t)$:

$$\omega(\mathbf{x},t) = \nabla\times\mathbf{u}(\mathbf{x},t), \tag{3.4}$$

so that we may write,

$$(\mathbf{u}(\mathbf{x},t)\cdot\nabla)\,\mathbf{u}(\mathbf{x},t) = \omega(\mathbf{x},t)\times\mathbf{u}(\mathbf{x},t) + \tfrac{1}{2}\nabla u^2(\mathbf{x},t). \tag{3.5}$$

Substituting this into equation (3.1) and rearranging gives,

$$\left(\frac{\partial}{\partial t} - \nu\nabla^2\right)\mathbf{u}(\mathbf{x},t) = \mathbf{W}(\mathbf{x},t) - \nabla\left(\frac{1}{\rho}p(\mathbf{x},t) + \tfrac{1}{2}u^2(\mathbf{x},t)\right), \tag{3.6}$$

where,

$$\mathbf{W}(\mathbf{x},t) = \mathbf{u}(\mathbf{x},t)\times\omega(\mathbf{x},t). \tag{3.7}$$

Next we transform into Fourier space, using $\mathcal{F}$ to represent the transforms of those terms that we do not wish to deal with explicitly:

$$\left(\frac{\partial}{\partial t} + \nu k^2\right)\mathbf{u}(\mathbf{k},t) = \mathbf{W}(\mathbf{k},t) - i\mathbf{k}\mathcal{F}\left(\frac{1}{\rho}p(\mathbf{x},t) + \tfrac{1}{2}u^2(\mathbf{x},t)\right). \tag{3.8}$$

Now, as in Chapter 2, we take the scalar product of each term with $\mathbf{k}$ and use the continuity equation, (2.8), to give,

$$i\mathcal{F}\left(\frac{1}{\rho}p(\mathbf{x},t)+\tfrac{1}{2}u^2(\mathbf{x},t)\right)=\frac{1}{k^2}\mathbf{k}\cdot\mathbf{W}(\mathbf{k},t). \tag{3.9}$$

Substituting this back into equation (3.8) gives,

$$\left(\frac{\partial}{\partial t}+\nu k^2\right)\mathbf{u}(\mathbf{k},t)=\mathbf{W}(\mathbf{k},t)-\frac{\mathbf{k}}{k^2}\mathbf{k}\cdot\mathbf{W}(\mathbf{k},t). \tag{3.10}$$

Finally, we return to index notation so that:

$$\begin{aligned}\left(\frac{\partial}{\partial t}+\nu k^2\right)u_\alpha(\mathbf{k},t) &= W_\alpha(\mathbf{k},t)-\frac{k_\alpha}{k^2}k_\beta W_\beta(\mathbf{k},t)\\ &= \delta_{\alpha\beta}W_\beta(\mathbf{k},t)-\frac{k_\alpha k_\beta}{k^2}W_\beta(\mathbf{k},t)\\ &= \left(\delta_{\alpha\beta}-\frac{k_\alpha k_\beta}{k^2}\right)W_\beta(\mathbf{k},t),\end{aligned} \tag{3.11}$$

or, referring to equation (2.14) for the definition of $D_{\alpha\beta}(\mathbf{k})$,

$$\left(\frac{\partial}{\partial t}+\nu k^2\right)u_\alpha(\mathbf{k},t)=D_{\alpha\beta}(\mathbf{k})W_\beta(\mathbf{k},t). \tag{3.12}$$

At this point it is worth noting that we have not given an explicit form for $W_\beta(\mathbf{k},t)$[1] — it is represented simply as the Fourier transform of $W_\beta(\mathbf{x},t)$. However, this is not a problem and, as will be seen later in Section 3.5, actually reflects the computational algorithm used.

3.2 The Basics of DNS

Our starting point is the Navier-Stokes equation in the form we have just derived,

$$\left(\frac{\partial}{\partial t}+\nu k^2\right)u_\alpha(\mathbf{k},t)=D_{\alpha\beta}(\mathbf{k})W_\beta(\mathbf{k},t)+f_\alpha(\mathbf{k},t), \tag{3.13}$$

where $f_\alpha(\mathbf{k},t)$ is a forcing term which may be used to sustain the turbulence — if it is set to zero then the equation represents freely decaying turbulence.

[1] Although a form may be obtained by comparison with equation (2.15).

Repeating equation (2.5) for the wavevectors,

$$k_\alpha = \frac{2\pi n_\alpha}{L_{box}} \quad \text{with} \quad n_\alpha = 0, \pm 1, \pm 2, \ldots, \tag{3.14}$$

we see that provided L_{box} is finite, wavenumber space is discrete, but infinite in extent. If we assume that the system will then be simulated on an $N \times N \times N$ grid, this restricts n_α in equation (3.14) to

$$n_\alpha = 0, \pm 1, \pm 2, \ldots, \pm(N/2 - 1), -N/2, \tag{3.15}$$

where the decision to include $-N/2$ rather than $+N/2$ is an arbitrary one. This now gives us a cutoff wavenumber,

$$k_{max} = \frac{\pi N}{L_{box}}, \tag{3.16}$$

which means that wavenumber space has been reduced to a discrete, *finite* system. The cutoff corresponds to a choice of *resolution* in physical space with,

$$x_\alpha = \frac{m}{N} L_{box} \quad \text{with} \quad m = 0, 1, 2, ..., N - 1. \tag{3.17}$$

The choice of k_{max} must be made so that the most significant modes in the system are retained. The Kolmogorov dissipation wavenumber, given by equation (2.71), is usually used as the basis for such a decision, with the criterion that $k_{max}/k_d > 1$ for adequate resolution of the small scales (see, for example, [23]).

The precise choice, however, will depend on exactly what is being investigated. Moin and Mahesh [24], for example, state that "spectral DNS shows very good agreement with experiments even though the Kolmogorov lengthscale is not resolved." They then go on to say, "It appears that the relevant requirement to obtain reliable first and second order statistics is that the resolution be fine enough to accurately capture most of the dissipation. The smallest lengthscale that must be accurately resolved depends on the energy spectrum, and is typically greater than the Kolmogorov lengthscale." However, these comments seem to apply primarily to engineering flows — for example, Moin and Mahesh refer

to a paper by Moser and Moin [25] in which it is noted that most of the dissipation in a curved channel occurs at scales fifteen or more times greater than the Kolmogorov length scale. For our homogeneous, isotropic case, things are likely to be somewhat different. Indeed, Eswaran and Pope [26] note that, in such cases, quantities which are dominated by the extreme high-wavenumber end of the energy spectrum (including the dissipation rate) "may have more stringent requirements."

As the computing resources available continue to increase, the current trend is to use these extra resources in order to obtain larger values of k_{max}/k_d ($k_{max}/k_d > 1.5$) — see, for example, references [27] and [28]. There is, however, always a trade-off between resolution and the Reynolds number that may be obtained.

Once a suitable choice of k_{max} has been made, the DNS algorithm is then, essentially,

1. Set up some initial field.
2. Make any required measurements on the field.
3. Compute the nonlinear term, $D_{\alpha\beta}(\mathbf{k})W_\beta(\mathbf{k},t)$.
4. Use (a time-discretized form of) the Navier-Stokes equation to evolve the velocity field to the next time step.
5. Repeat from step 2.

Each of these steps will now be considered in turn.

3.3 Initial Field Generation

The task here is to generate an initial velocity field, $u_\alpha(\mathbf{k},0)$ which satisfies the following conditions:

1. Its Fourier transform should be real, and so $u_\alpha(\mathbf{k},0) = u_\alpha(-\mathbf{k},0)^*$.

2. It should have a zero mean, and should be statistically homogeneous and isotropic.

3. It must satisfy the continuity equation, $k_\alpha u_\alpha(\mathbf{k},0) = 0$.

4. It should have some chosen energy spectrum, $E(k)$.

A means of achieving this was given by Orszag [21] for a system with $L_{box} = 1$. It is trivial, however, to extend the algorithm to a general box size and this is outlined below.

The first step is to select two zero-mean, Gaussian, real vector fields, $\mathbf{r}(\mathbf{k})$ and $\mathbf{s}(\mathbf{k})$. These should satisfy,

1. $\langle r_\alpha(\mathbf{k}) r_\beta(\mathbf{k}')\rangle = \langle s_\alpha(\mathbf{k}) s_\beta(\mathbf{k}')\rangle = 0 \quad (\mathbf{k} \neq \mathbf{k}')$
   (each wavevector is independent of every other wavevector)

2. $\langle r_\alpha(\mathbf{k}) r_\beta(\mathbf{k})\rangle = \langle s_\alpha(\mathbf{k}) s_\beta(\mathbf{k})\rangle = \delta_{\alpha\beta} v(k)$ where $v(k) = \pi^2 E(k)/2L_{box}^3 k^2$
   (each component is independent and chosen with a variance of $v(k)$)

3. $\langle r_\alpha(\mathbf{k}) s_\beta(\mathbf{k}')\rangle = 0$
   ($\mathbf{r}(\mathbf{k})$ and $\mathbf{s}(\mathbf{k})$ are independent)

The initial velocity field is then chosen to be,

$$u_\alpha(\mathbf{k},0) = D_{\alpha\beta}(\mathbf{k})\left[r_\beta(\mathbf{k}) + r_\beta(-\mathbf{k}) + is_\beta(\mathbf{k}) - is_\beta(-\mathbf{k})\right]. \tag{3.18}$$

Immediately we see that the first two properties required of our velocity field are satisfied, namely that $u_\alpha(\mathbf{k},0) = u_\alpha(-\mathbf{k},0)^*$ and $\langle u_\alpha(\mathbf{k},0)\rangle = 0$.

We now check the continuity equation and see that,

$$k_\alpha u_\alpha(\mathbf{k},0) \;=\; k_\alpha D_{\alpha\beta}(\mathbf{k})\left[\cdots\right]$$

$$\begin{aligned} &= k_\alpha \left(\delta_{\alpha\beta}(\mathbf{k} - k_\alpha k_\beta/k^2\right) [\cdots] \\ &= \left(k_\beta - k_\alpha k_\alpha k_\beta/k^2\right) [\cdots] \\ &= 0, \end{aligned} \tag{3.19}$$

as required.

Finally we check that we have the correct energy spectrum. $u_\alpha(\mathbf{k},0)$ and $u_\beta(\mathbf{k},0)$ are given by,

$$u_\alpha(\mathbf{k},0) = D_{\alpha\rho}(\mathbf{k})\left[r_\rho(\mathbf{k}) + r_\rho(-\mathbf{k}) + is_\rho(\mathbf{k}) - is_\rho(-\mathbf{k})\right] \tag{3.20}$$

$$u_\beta(\mathbf{k},0) = D_{\beta\sigma}(\mathbf{k})\left[r_\sigma(\mathbf{k}) + r_\sigma(-\mathbf{k}) + is_\sigma(\mathbf{k}) - is_\sigma(-\mathbf{k})\right] \tag{3.21}$$

so that,

$$\begin{aligned} \langle u_\alpha(\mathbf{k},0)u_\beta(-\mathbf{k},0)\rangle &= D_{\alpha\rho}(\mathbf{k})D_{\beta\sigma}(-\mathbf{k}) \\ &\times \Big\langle [r_\rho(\mathbf{k}) + r_\rho(-\mathbf{k}) + is_\rho(\mathbf{k}) - is_\rho(-\mathbf{k})] \\ &\times [r_\sigma(-\mathbf{k}) + r_\sigma(\mathbf{k}) + is_\sigma(-\mathbf{k}) - is_\sigma(\mathbf{k})]\Big\rangle \\ &= D_{\alpha\rho}(\mathbf{k})D_{\beta\sigma}(-\mathbf{k}) \\ &\times \Big\{ \langle r_\rho(\mathbf{k})r_\sigma(\mathbf{k})\rangle + \langle r_\rho(-\mathbf{k})r_\sigma(-\mathbf{k})\rangle \\ &+ \langle s_\rho(\mathbf{k})s_\sigma(\mathbf{k})\rangle + \langle s_\rho(-\mathbf{k})s_\sigma(-\mathbf{k})\rangle \Big\} \\ &= 4D_{\alpha\rho}(\mathbf{k})D_{\beta\sigma}(-\mathbf{k})\delta_{\sigma\rho}v(k) \\ &= 4D_{\alpha\rho}(\mathbf{k})D_{\beta\rho}(-\mathbf{k})v(k). \end{aligned} \tag{3.22}$$

Now we may write,

$$\begin{aligned} D_{\alpha\rho}(\mathbf{k})D_{\beta\rho}(-\mathbf{k}) &= D_{\alpha\rho}(\mathbf{k})D_{\beta\rho}(\mathbf{k}) \\ &= \left(\delta_{\alpha\rho} - k_\alpha k_\rho/k^2\right)\left(\delta_{\beta\rho} - k_\beta k_\rho/k^2\right) \\ &= \delta_{\alpha\beta} - k_\alpha k_\beta/k^2 - k_\alpha k_\beta/k^2 + k_\alpha k_\beta k_\rho k_\rho/k^4 \\ &= D_{\alpha\beta}(\mathbf{k}) \end{aligned} \tag{3.23}$$

so that we now have,

$$\langle u_\alpha(\mathbf{k},0)u_\beta(-\mathbf{k},0)\rangle = 4D_{\alpha\beta}(\mathbf{k})v(k). \tag{3.24}$$

Finally, we set $\alpha = \beta$, sum using $D_{\alpha\alpha}(\mathbf{k}) = 2$ and rearrange to give,

$$L_{box}^3 \frac{k^2}{4\pi^2} \langle u_\alpha(\mathbf{k}, 0) u_\alpha(-\mathbf{k}, 0) \rangle = E(k) \tag{3.25}$$

which, recalling that we are working with a discrete system, is the the required form for the energy spectrum as given by equation (2.44).

3.4 Computing velocity field statistics

Isotropy allows us to obtain statistics from a single velocity field by replacing the ensemble average with a *shell* average. Here, quantities are averaged over spherical shells in wavenumber space centred on a given wavenumber, k_n, and having a shell thickness given by Δk. The shell averaged energy spectrum, for example, can then be defined by

$$E(k_n, t) = L_{box}^3 \frac{k_n^2}{2\pi^2} \frac{1}{P} \sum_{k_n - \frac{1}{2}\Delta k \leq |\mathbf{k}| < k_n + \frac{1}{2}\Delta k} \tfrac{1}{2} \mathbf{u}(\mathbf{k}, t) \cdot \mathbf{u}(-\mathbf{k}, t) \tag{3.26}$$

where P is the number of points in the shell. In the literature, such a shell average is often given simply as,

$$E(k_n, t) = \frac{1}{\Delta k} \sum_{k_n - \frac{1}{2}\Delta k \leq |\mathbf{k}| < k_n + \frac{1}{2}\Delta k} \tfrac{1}{2} \mathbf{u}(\mathbf{k}, t) \cdot \mathbf{u}(-\mathbf{k}, t). \tag{3.27}$$

In fact, the difference between these two calculations is rather small, particularly at higher values of k_n, however, equation (3.26) is the more accurate. This is a view shared by Eswaran and Pope [26] who compute their shell-average in the way given by equation (3.27) but then multiply by "the ratio of the expected value of the number of nodes in each wavenumber band to the actual number therein". The "expected number of nodes" will be given by,

$$P_E = 4\pi n^2 \Delta n, \tag{3.28}$$

where n is the integer label of the grid point corresponding to k_n and Δn is the shell width in terms of grid spacing. Recalling that $k_n = 2\pi n / L_{box}$ and hence

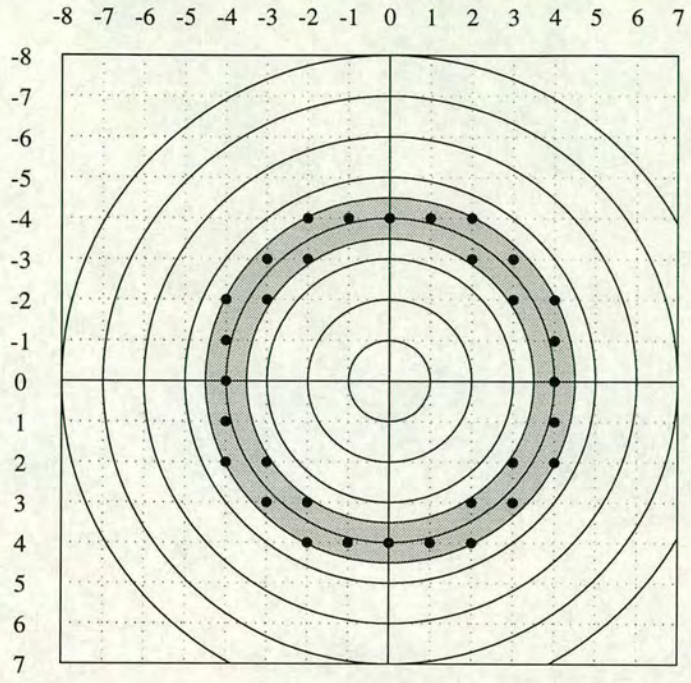

Figure 3.1: Schematic illustration of a slice through a shell average on a 16^3 grid. The shaded region represents shell 4 with $\Delta k = 1$ so that $3.5 \leq |\mathbf{k}| < 4.5$. The dots represent those points included in the average.

$\Delta k = 2\pi\Delta n / L_{box}$, this may then be rewritten in terms of k to give,

$$P_E = L_{box}^3 \frac{k_n^2}{2\pi^2} \Delta k. \tag{3.29}$$

It is then clear that multiplying equation (3.27) through by P_E/P takes us back to equation (3.26).

In either case, the scope of the sum remains the same and this is illustrated in Figure 3.1.

3.5 Computing the nonlinear term

The complicated part of the nonlinear term, in the form of the Navier-Stokes equation we are considering here, is given in equation (3.13) by $\mathbf{W}(\mathbf{k}, t)$ which is

the Fourier transform of

$$\mathbf{W}(\mathbf{x},t) = \mathbf{u}(\mathbf{x},t) \times \omega(\mathbf{x},t) \tag{3.30}$$

or, in index notation,

$$W_\alpha(\mathbf{x},t) = \varepsilon_{\alpha\beta\gamma} u_\beta(\mathbf{x},t)\omega_\gamma(\mathbf{x},t) \tag{3.31}$$

where $\varepsilon_{\alpha\beta\gamma}$ is the permutation (or Levi-Civita) tensor [29]. Invoking the convolution theorem we may then write,

$$W_\alpha(\mathbf{k},t) = \varepsilon_{\alpha\beta\gamma} \sum_{\mathbf{j}} u_\beta(\mathbf{j},t)\omega_\gamma(\mathbf{k}-\mathbf{j},t). \tag{3.32}$$

This, given a velocity field in Fourier space, is what must be calculated. However, to compute this sum directly is a task which is so time-consuming that, for all practical purposes, it is beyond even today's most powerful computers. This problem was noted by Orszag who introduced a simple method by which this problem may be overcome [21]. Essentially, a number of fast Fourier transforms (FFTs) are employed to shift the problem between Fourier and real space according to which is easier for a given calculation. The algorithm is outlined below.

Fourier ($\mathbf{k}$) Space		Real ($\mathbf{x}$) Space
$\mathbf{u}(\mathbf{k},t)$	$\xrightarrow{FFT}$	$\mathbf{u}(\mathbf{x},t)$
$\omega(\mathbf{k},t) = i\mathbf{k} \times \mathbf{u}(\mathbf{k},t)$	$\xrightarrow{FFT}$	$\omega(\mathbf{x},t)$
$\mathbf{W}(\mathbf{k},t)$	$\xleftarrow{FFT}$	$\mathbf{W}(\mathbf{x},t) = \mathbf{u}(\mathbf{x},t) \times \omega(\mathbf{x},t)$

This is a straightforward and very efficient means of calculating $\mathbf{W}(\mathbf{k},t)$. There is, however, a subtle but important point which arises due to the fact that we have truncated our system — namely the existence of *aliasing errors.*

3.6 Aliasing errors

In order to illustrate the problem, we will work with a one-dimensional analogue of the convolution sum in equation (3.32). Namely,

$$W(k) = \sum_{\substack{j+l=k \\ |j|,|l|\leq k_{max}}} u(j)\omega(l), \tag{3.33}$$

where the sum has been further restricted by insisting that both $|j|$ and $|l| = |k-j|$ are less than the cutoff wavenumber, k_{max}. We now suppose that we have both $u(x)$ and $\omega(x)$ where,

$$u(x) = \sum_{|k|\leq k_{max}} u(k)e^{ikx} \tag{3.34}$$

$$\omega(x) = \sum_{|k|\leq k_{max}} \omega(k)e^{ikx}. \tag{3.35}$$

If we then form the product, we can write

$$W(x) = u(x)\omega(x) \tag{3.36}$$

$$= \left(\sum_{|k|\leq k_{max}} u(k)e^{ikx}\right)\left(\sum_{|k|\leq k_{max}} \omega(k)e^{ikx}\right) \tag{3.37}$$

$$= \sum_{|j|\leq k_{max}} \sum_{|l|\leq k_{max}} u(j)\omega(l)e^{i(j+l)x}. \tag{3.38}$$

Now we carry out the inverse transform to give,

$$\hat{W}(k) = \frac{1}{N}\sum_x W(x)e^{-ikx} \tag{3.39}$$

$$= \frac{1}{N}\sum_x \sum_{|j|\leq k_{max}} \sum_{|l|\leq k_{max}} u(j)\omega(l)e^{i(j+l-k)x} \tag{3.40}$$

$$= \sum_{|j|,|l|\leq k_{max}} u(j)\omega(l)\frac{1}{N}\sum_x e^{i(j+l-k)x}. \tag{3.41}$$

We now use the one dimensional analogues of equations (3.14) and (3.17), which give the discrete values of k and x respectively, to rewrite the second sum,

$$\sum_x e^{i(j+l-k)x} = \sum_{m_x=0}^{N-1} e^{i\frac{2\pi}{N}(n_j+n_l-n_k)m_x}, \tag{3.42}$$

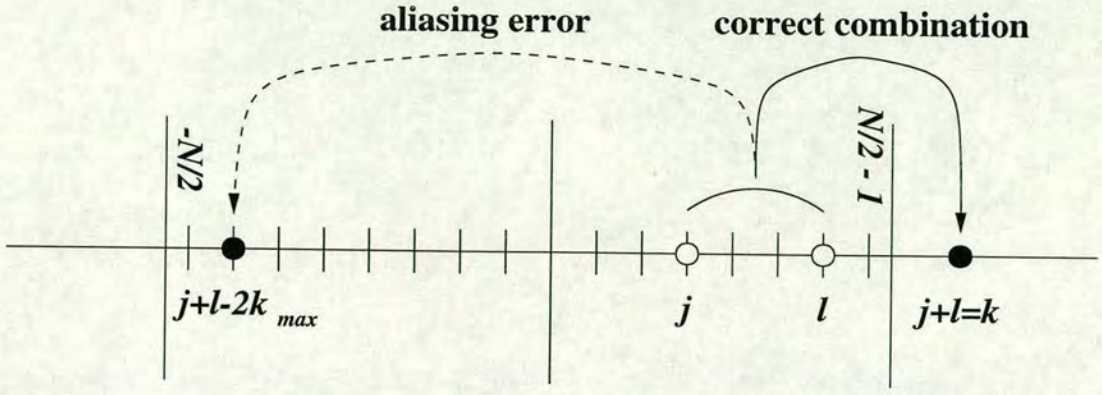

Figure 3.2: Illustration of the aliasing error problem. Two wavenumbers, j and l should only couple to give $j + l = k$. However, aliasing errors mean that they also contribute to $j + l - 2k_{max}$.

where m_x, n_j, n_l and n_k are integers. Then, we may write [30],

$$\sum_{m_x=0}^{N-1} e^{i\frac{2\pi}{N}(n_j+n_l-n_k)m_x} = \begin{cases} N \text{ if } n_j + n_l \equiv n_k \ (\mathrm{mod} N) \\ 0 \text{ otherwise} \end{cases}, \tag{3.43}$$

and hence equation (3.41) becomes

$$\hat{W}(k) = \sum_{\substack{j+l=k \\ |j|,|l| \leq k_{max}}} u(j)\omega(l) + \sum_{\substack{j+l=k\pm 2k_{max} \\ |j|,|l| \leq k_{max}}} u(j)\omega(l) \tag{3.44}$$

which is *almost*, but not quite, equation (3.33) which we were hoping for. The error term is due to the inability of the inverse transform to distinguish between k and its *aliases*, $k + 2k_{max}$ and $k - 2k_{max}$. This problem is illustrated in Figure 3.2.

3.7 Anti-aliasing

For some simulations, the aliasing errors are simply ignored and — in most cases — this is not too bad an approximation. For each pair of wavenumbers which contribute to the aliasing errors, at least one will be in the outer region of wavenumber space, $|k| > k_{max}/2$, where the magnitude of the velocity field is typically relatively small and so the product of the wavenumber pair is also expected to be small.

However, the task of removing these aliasing errors has been tackled by a number of authors, most notably Patterson and Orszag [31] and Orszag [30] although Rogallo [32] also provides a good review. Some of the more common methods are outlined below.

3.7.1 Spectral truncation

It is possible to remove aliasing errors by truncating, or zeroing, selected parts of the velocity field. Imagine we truncate the velocity field for all wavenumbers beyond k_T, where $k_T < k_{max}$. Then, whenever a j, l pair arises which satisfies,

$$j + l = k \pm 2k_{max}, \tag{3.45}$$

we require at least one of the following to be true:

$$|j| \geq k_T \tag{3.46}$$

$$|l| \geq k_T \tag{3.47}$$

$$|k| \geq k_T. \tag{3.48}$$

The first two of these conditions would ensure that the product in the convolution sum will be zero, while the third condition would ensure that k is outside of our region of interest and hence aliasing errors would be irrelevant. The problem, then, is to choose k_T so that this is always the case.

We begin by making some general observations:

$$|j|, |l|, |k| \leq k_{max} \tag{3.49}$$

which implies that,

$$|j + l| \leq 2k_{max}. \tag{3.50}$$

Case A. Suppose that $k > 0$, then inequality (3.50) means that the only possible aliasing combination is,

$$j + l = k - 2k_{max}. \tag{3.51}$$

Since $k - 2k_{max} \leq -k_{max}$, we must have $j, l \leq 0$, and we can write,

$$-|j| - |l| = |k| - 2k_{max}. \tag{3.52}$$

Case B. Suppose that $k < 0$. In this case the only possible aliasing combination is,

$$j + l = k + 2k_{max}, \tag{3.53}$$

and we can deduce that $j, l \geq 0$. This gives,

$$|j| + |l| = -|k| + 2k_{max}. \tag{3.54}$$

Case C. Suppose that $k = 0$. The first aliasing combination is,

$$j + l = -2k_{max}, \tag{3.55}$$

which implies that $j = l = -k_{max}$ and we can write,

$$-|j| - |l| = |k| - 2k_{max}. \tag{3.56}$$

The second aliasing combination is,

$$j + l = 2k_{max}, \tag{3.57}$$

giving, $j = l = k_{max}$ so that,

$$|j| + |l| = -|k| + 2k_{max}. \tag{3.58}$$

Note that equations (3.52), (3.54), (3.56) and (3.58) are, in fact, identical and may be rewritten as,

$$|j| + |l| = 2k_{max} - |k|. \tag{3.59}$$

As we have stated, for any aliasing combination, we require that one of $|j|$, $|l|$ or $|k|$ lies beyond k_T. That is,

$$\max(|j|, |l|, |k|) \geq k_T. \tag{3.60}$$

From equation (3.59) it can be seen that the *minimum* value of $\max(|j|, |l|, |k|)$ will occur when $|j| = |l| = |k|$, giving

$$3|k| = 2k_{max}, \tag{3.61}$$

so that we may write,

$$k_T \leq \frac{2k_{max}}{3}, \tag{3.62}$$

giving the optimal (i.e. least wasteful) choice of cutoff as,

$$k_T = \frac{2k_{max}}{3}. \tag{3.63}$$

Here, the size of the Fourier transform is fixed by k_{max} and so the maximum 'active' wavenumber, k_T, is chosen to ensure alias-free results. If it is the maximum wavenumber which must be fixed, then the size of the Fourier transform must be increased in a manner converse to that discussed above. Implementation of this 'padding' technique (known as the '3/2' method) can be problematic, since Fast Fourier Transform routines perform best on data sets whose size is a power of 2.

Truncation is a fast and easy to implement way by which the aliasing errors may be removed. The downside, however, is obvious — we are throwing away points in our computational domain.

In practice, simulations are often carried out with a choice of $k_T > (2/3)k_{max}$ as *any* truncation will remove *some* of the aliasing errors. For example, Patterson and Orszag [31] showed that a choice of,

$$k_T = (2\sqrt{2}/3)k_{max}, \tag{3.64}$$

will eliminate errors due to aliasing in two or more directions and this choice is often made. Orszag [30] later introduced a scheme with the same result, whereby truncation took place outside of an 18-sided polyhedron. Although this technique requires a less severe truncation, Orszag notes that the spherical truncation implied by equation (3.64) seems more natural for the simulation of isotropic turbulence.

3.7.2 Grid shifting

Like the truncation methods described above, grid shifting can allow us to perform both *full* and *partial* dealiasing, based on the same idea. Again, we will work in one dimension in order to keep things as simple as possible.

Suppose that the velocity field, $u(k)$, is phase shifted as follows,

$$\tilde{u}(k) = e^{ik\Delta}u(k) \tag{3.65}$$

which in turn implies that the vorticity, $\omega(k)$, is similarly shifted,

$$\tilde{\omega}(k) = e^{ik\Delta}\omega(k). \tag{3.66}$$

Equation (3.44) then gives us,

$$\begin{aligned}\tilde{W}(k) &= \sum_{\substack{j+l=k \\ |j|,|l|\leq k_{max}}} e^{i(j+l)\Delta}u(j)\omega(l) + \sum_{\substack{j+l=k\pm 2k_{max} \\ |j|,|l|\leq k_{max}}} e^{i(j+l)\Delta}u(j)\omega(l) \\ &= e^{ik\Delta}\sum_{\substack{j+l=k \\ |j|,|l|\leq k_{max}}} u(j)\omega(l) + e^{i(k\pm 2k_{max})\Delta}\sum_{\substack{j+l=k\pm 2k_{max} \\ |j|,|l|\leq k_{max}}} u(j)\omega(l),\end{aligned} \tag{3.67}$$

which we can then phase shift back to give,

$$e^{-ik\Delta}\tilde{W}(k) = \sum_{\substack{j+l=k \\ |j|,|l|\leq k_{max}}} u(j)\omega(l) + e^{\pm i2k_{max}\Delta}\sum_{\substack{j+l=k\pm 2k_{max} \\ |j|,|l|\leq k_{max}}} u(j)\omega(l), \tag{3.68}$$

which we will rewrite as,

$$\tilde{W}_\Delta(k) = \sum_{\substack{j+l=k \\ |j|,|l|\leq k_{max}}} u(j)\omega(l) + e^{\pm i2k_{max}\Delta}\sum_{\substack{j+l=k\pm 2k_{max} \\ |j|,|l|\leq k_{max}}} u(j)\omega(l), \tag{3.69}$$

Comparing the RHS of equation (3.69) with the RHS of equation (3.44) we immediately see that this shifting operation has *only affected the aliasing errors* and that $\hat{W}(k) = \tilde{W}_0(k)$.

If we now select $2k_{max}\Delta = \pi$, i.e. $\Delta = L/2N$ then equation (3.69) becomes,

$$\tilde{W}_{L/2N}(k) = \sum_{\substack{j+l=k \\ |j|,|l|\leq k_{max}}} u(j)\omega(l) - \sum_{\substack{j+l=k\pm 2k_{max} \\ |j|,|l|\leq k_{max}}} u(j)\omega(l), \tag{3.70}$$

and we see immediately that the fully dealiased nonlinear term, $W(k)$, is given by,

$$W(k) = \tfrac{1}{2}\left(\tilde{W}_0(k) + \tilde{W}_{L/2N}(k)\right). \tag{3.71}$$

The advantage of this method is that a *complete*, fully-dealiased field is obtained — unlike the truncation method where we must sacrifice some of our data. There are two disadvantages. Firstly, in this one-dimensional case, the nonlinear term must be evaluated *twice* — and in the full three-dimensional case, this increases to $2^3 = 8$ evaluations. This gives rise to a large time overhead. Secondly, additional storage space is required in order to hold the shifted field.

As with the truncation method, and as mentioned earlier in this section, we can follow Rogallo [32] and adapt the grid shifting method to provide us with *partial* dealiasing. Here, the phase shifting is performed as the time-integration proceeds so that the aliasing error at one step will be *nearly* cancelled at the next. In this case each pair of shifts is chosen randomly, and the shifts in each direction are uncorrelated with one another. If the integration scheme used itself requires more than one evaluation of the nonlinear term (such as the Runge-Kutta method described a little later) then the two shifts will take place during the same time step.

3.8 Evolving the velocity field

We have already stated, in equation (3.13), the equation which governs the behaviour of the simulated velocity field. There are many standard techniques which may be used to numerically integrate such an equation, but in this section we look specifically at how this is dealt with in the code developed here.

We begin by inverting the differential operator through the use of an integrating

factor to give,

$$e^{\nu_0 k^2 t} u_\alpha(\mathbf{k}, t) = \int_{-\infty}^{t} ds\; e^{\nu_0 k^2 s} \left[D_{\alpha\beta}(\mathbf{k}) W_\beta(\mathbf{k}, s) + f_\alpha(\mathbf{k}, s) \right]. \tag{3.72}$$

We then discretize time by introducing a time step, δt, so that

$$t_n = n\delta t, \tag{3.73}$$

and then rewrite equation (3.72) as,

$$\begin{aligned} e^{\nu_0 k^2 t_{n+1}} u_\alpha(\mathbf{k}, t_{n+1}) &= e^{\nu_0 k^2 t_n} u_\alpha(\mathbf{k}, t_n) \\ &+ \int_{t_n}^{t_{n+1}} ds\; e^{\nu_0 k^2 s} \left[D_{\alpha\beta}(\mathbf{k}) W_\beta(\mathbf{k}, s) + f_\alpha(\mathbf{k}, s) \right]. \end{aligned} \tag{3.74}$$

This is still only partially discretized due to the integral on the right hand side. At this point we invoke *Heun's method* [33] which is a second order Runge-Kutta method, to give us a two-step predictor-corrector algorithm. The predictor is given by,

$$\begin{aligned} u_\alpha^P(\mathbf{k}, t_{n+1}) &= e^{-\nu_0 k^2 \delta t} u_\alpha(\mathbf{k}, t_n) \\ &+ \delta t e^{-\nu_0 k^2 \delta t} \left[D_{\alpha\beta}(\mathbf{k}) W_\beta(\mathbf{k}, t_n) + f_\alpha(\mathbf{k}, t_n) \right], \end{aligned} \tag{3.75}$$

with the corrector given by,

$$\begin{aligned} u_\alpha(\mathbf{k}, t_{n+1}) &= e^{-\nu_0 k^2 \delta t} u_\alpha(\mathbf{k}, t_n) \\ &+ \tfrac{1}{2} \delta t D_{\alpha\beta}(\mathbf{k}) \left[e^{-\nu_0 k^2 \delta t} W_\beta(\mathbf{k}, t_n) + W_\beta^P(\mathbf{k}, t_{n+1}) \right] \\ &+ \tfrac{1}{2} \delta t \left[e^{-\nu_0 k^2 \delta t} f_\alpha(\mathbf{k}, t_n) + f_\alpha^P(\mathbf{k}, t_{n+1}) \right] \end{aligned} \tag{3.76}$$

Together, equations (3.75) and (3.76) are used to generate the velocity field at time t_{n+1}, given the velocity field at time t_n.

3.9 Summary

We end this chapter with a summary of each step of the DNS.

1. Set up some initial field.

   This is done randomly, but in such a way as to give some prescribed energy spectrum.

2. Make any required measurements on the field.

   Shell-averaging allows us to obtain statistical quantities ordinarily requiring the use of ensemble averages.

3. Compute the nonlinear term.

   The convolution is computed by Fourier transforming to and from real space. A number of techniques are available to remove or reduce the aliasing errors that this method of evaluation introduces.

4. Evolve the velocity field to the next time step.

   Some numerical integration scheme, in our case a second order Runge-Kutta method, is used.

5. Repeat from step 2.

Chapter 4

Simulating Turbulence on the Cray T3D

The basics of direct numerical simulation were described in Chapter 3. In this chapter, issues specific to the implementation of DNS on the Cray T3D parallel computer are discussed.

In the final section, we then briefly outline which of the various techniques discussed in Chapter 3 have been used for our DNS runs.

4.1 The Cray T3D at Edinburgh

The Cray T3D at Edinburgh, administered by the Edinburgh Parallel Computing Centre (EPCC), is a parallel supercomputer consisting of 512 DEC Alpha processors, each running at 150MHz and having 64Mb of local memory. This gives the whole machine a total memory of 32Gb and a potential maximum speed of 75GHz.

The T3D is a *Virtual Shared Memory machine* which means, essentially, that each processor can directly access not only its local block of memory, but also the memory of any other processor. This offers the possibility of very fast interprocessor communications — although this will often be at the expense of

N	Memory	T3D Processors
64	64Mb	1
128	512Mb	8
256	4Gb	64
512	32Gb	512
1024	256Gb	4096

Table 4.1: Memory and processor requirements for various sizes of simulation.

code portability. To address this issue, the T3D also supports a number of parallel computing standards including High Performance Fortran (for *data parallel* coding, where the compiler does most of the parallelization) and the Message Passing Interface or MPI (for *message passing* coding, where the parallelization is explicit). The MPI standard was chosen to implement the parallel DNS for its added flexibility.

4.2 Memory issues

A single Alpha processor provides sufficient memory for a simulation to be carried out on a 64^3 grid, but memory requirements go like N^3 (where N is the grid size, as measured by the number of grid points along each of the axes), and so it is not long before we reach the limits of even a machine as powerful as the T3D. Table 4.2 lists the requirements for simulations at a number of different grid sizes and it is obvious that the largest possible simulation would take place on a 512^3 grid. In practice, restrictions of time rather than space, have meant that the greatest resolution achieved in this work is 256^3.

4.3 Domain decomposition

The velocity field, $u(\mathbf{k})$, is distributed equally across all of the available processors. The Fast Fourier Transform (FFT) routines used require that the distribution along x-axis is *degenerate* — i.e. present in its entirety on all processors. It is

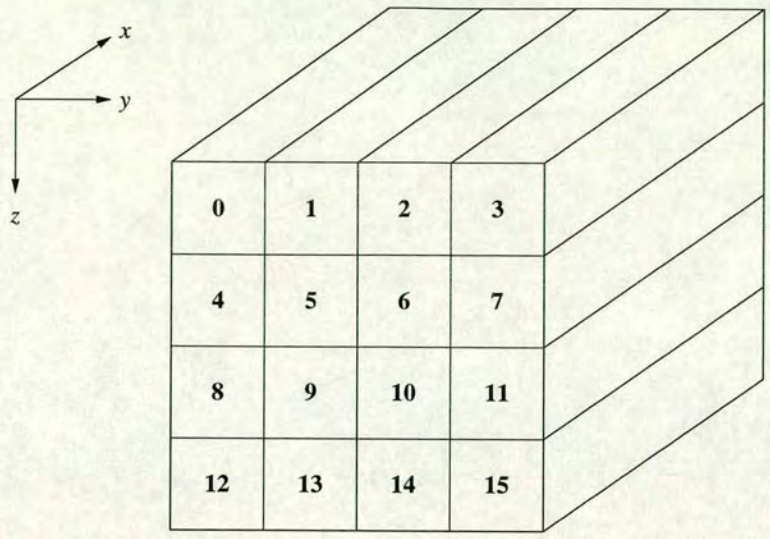

Figure 4.1: Example decomposition of the velocity field across 16 processors.

thus only the y- and z-axes that are decomposed, and this is illustrated in Figure 4.1. Experimentation with different processor topologies revealed that the exact distribution of processors across each of the axes had a negligible effect on the speed of the computation.

4.4 Parallel implementation of DNS algorithms

4.4.1 Initial field generation

Because $u_\alpha(\mathbf{x})$ must be real, the velocity field in Fourier space must satisfy $u_\alpha(\mathbf{k}) = u_\alpha(-\mathbf{k})^*$. It is this non-local condition which complicates the process of initial field generation on a parallel architecture.

The algorithm, based upon that given in section 3.3, is as follows:

1. Each processor generates a local section of $r_\alpha(\mathbf{k})$ and $s_\alpha(\mathbf{k})$.

2. A series of interprocessor sends and receives are used so that each processor builds two new fields, $r'_\alpha(\mathbf{k}) = r_\alpha(-\mathbf{k})$ and $s'_\alpha(\mathbf{k}) = s_\alpha(-\mathbf{k})$.

3. Equation (3.18) is used to generate the local section of the velocity field.

4.4.2 Computing statistics

As discussed in Section 3.4, statistics are obtained by use of a shell-averaging technique which involves summing over volumes of Fourier-space.

In the parallel environment, each processor carries out partial sums over its local section of Fourier-space. A global sum is then performed and a single processor, nominated to be the *master*, completes the computation.

4.4.3 Integration

At first glance, the Navier-Stokes equation,

$$\left(\frac{\partial}{\partial t} + \nu k^2\right) u_\alpha(\mathbf{k}, t) = M_{\alpha\beta\gamma}(\mathbf{k}) \sum_{\mathbf{j}} u_\beta(\mathbf{j}, t) u_\gamma(\mathbf{k} - \mathbf{j}, t) \tag{4.1}$$

does not appear to lend itself immediately to parallelization. The nonlinear term, on the right hand side, is extremely nonlocal, involving, as it does, a sum over all of wavenumber space. Fortunately, the spectral methods, outlined in section 3.5, offer us a way around the problem.

Here, the use of Fourier transforms reduces the nonlocal sum in wavenumber space to a local product in real space which is easy to calculate. The only remaining problem is the computation of the FFTs themselves — however, highly-optimized parallel FFT routines are available amongst the software libraries provided by Cray. The use of these routines means that, to all intents and purposes, the non-locality of the Navier-Stokes equation is all but hidden from the programmer.

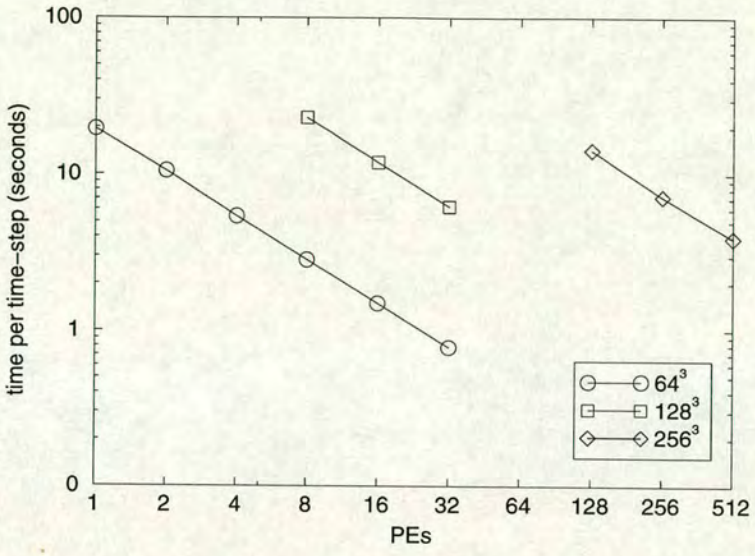

Figure 4.2: Clock-time required per time-step for 64^3, 128^3 and 256^3 grids on varying numbers of processors.

4.5 Timing

4.5.1 Integration

A number of timing runs have been carried out in order to ascertain the scaling behaviour of the code as the number of processors on which it is running increases. The major part of the time the code is running for is accounted for by the time-integration of the velocity field. Although other tasks, such as shell-averaging or the input and output of velocity fields can take a significant amount of time, these are only performed periodically. For this reason, we concentrate here on the integration step.

In Figure 4.2 we have plotted the amount of clock-time required to carry out a single integration step. Each line represents a different grid size and shows how the problem scales as the number of processors increases. As can be seen, the problem scales extremely well — if the number of processors is doubled then the time required is approximately halved.

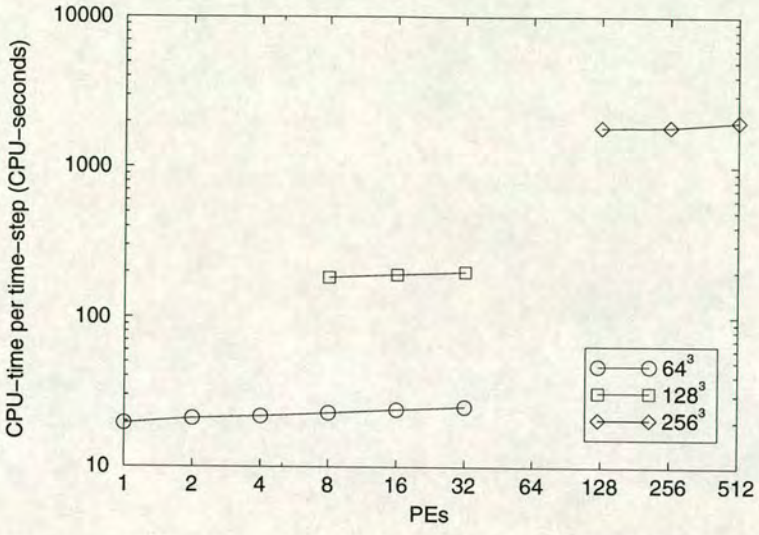

Figure 4.3: CPU-time required per time-step for 64^3, 128^3 and 256^3 grids on varying numbers of processors.

Figure 4.3 shows the amount of *CPU-time*, defined as clock-time multiplied by the number of processors, required to carry out an integration step. This shows more clearly the deviation from "perfect" scaling, with the amount of CPU-time slowly rising as the number of processors increases.

Finally, in Figure 4.4 we have plotted the average CPU-time requirements against grid size. An FFT requires time of order $N^3 \log N$, and this is also plotted — scaled so that the two lines coincide at $N = 64$. This demonstrates quite clearly the fact that the FFTs are the most significant part of the integration process.

4.5.2 Other Numerical Tasks

As noted earlier, while the time-integration is the most important part of the code by virtue of it being performed at every time-step, there are other tasks which are performed less frequently. The timing and scaling behaviour of these operations are detailed here.

In Figure 4.5 we have first plotted the CPU-time required to generate the initial velocity field. Obviously this is a step which will only be performed once for any

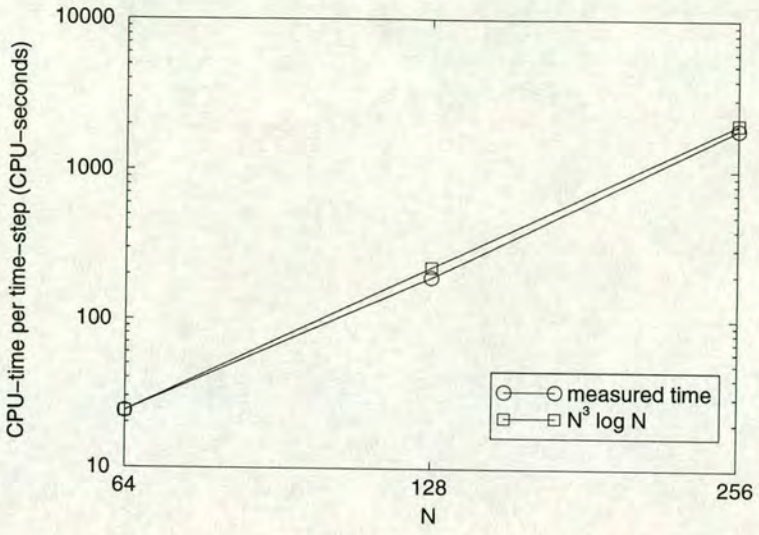

Figure 4.4: Average CPU-time required per time-step for 64^3, 128^3 and 256^3 grids compared with a plot of $N^3 log N$, the order of an FFT.

given simulation run, but the scaling data is given here for completeness. As can be seen, the procedure scales well with increasing processor number.

Plotted in the same figure are the CPU-time requirements for the shell-average where we see that CPU-time actually *increases* as we add processors to the problem. The reason for this is simple — at the end of the shell average routine there is an essentially serial section of code during which the master processor completes the averages and then writes out the results. The speed of this task will, of course, be unaffected by the number of processors available and during this period the remaining processors will be standing idle.

Finally we turn to the read and write field operations. For large N, in particular, this involves the movement of large quantities of data to and from hard disk and the speed of the disk gives rise to something of a bottleneck.

In Figure 4.6 we have plotted the clock-time required for read and write operations against the number of processors. We see that the time required is, very approximately, independent of the number of processors — in fact there is a steady *increase* in the clock-time as we add processors. This reflects the fact that

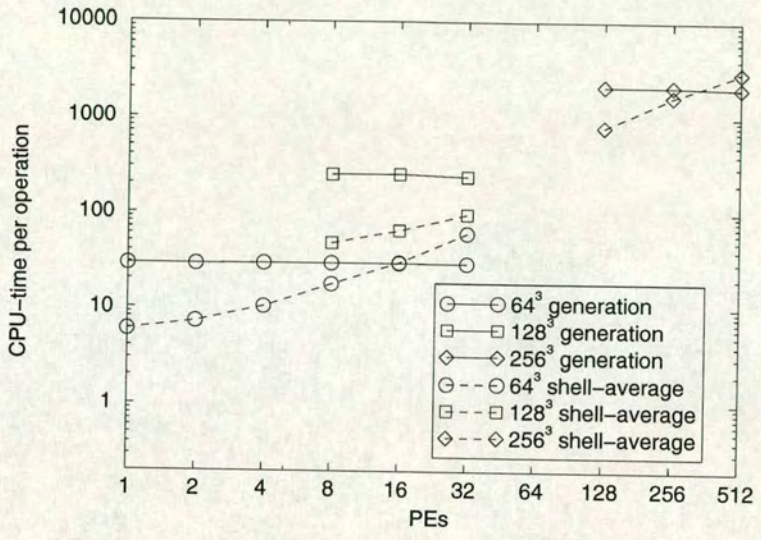

Figure 4.5: CPU-time required to generate the initial velocity field and to carry out shell-averaging on 64^3, 128^3 and 256^3 grids on varying numbers of processors.

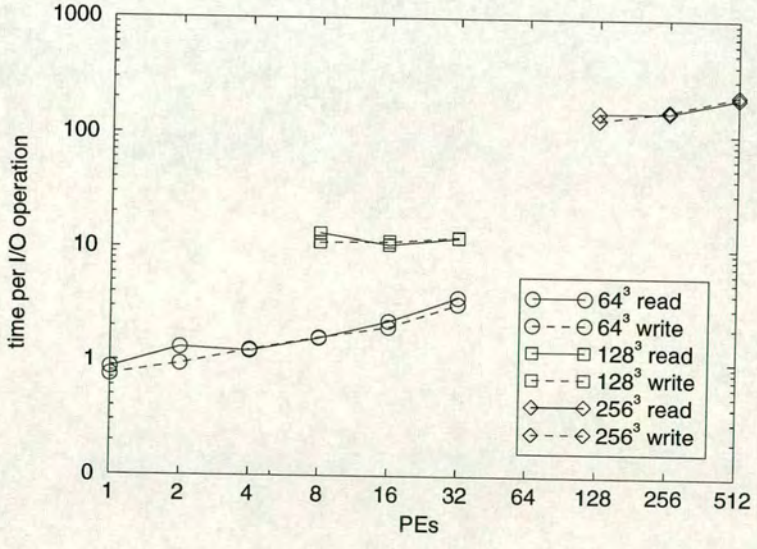

Figure 4.6: Clock-time required to carry out velocity field I/O operations for 64^3, 128^3 and 256^3 grids on varying numbers of processors.

the speed at which this task may be performed is limited by the speed of the disk.

4.6 Description of our DNS

A number of simulations have been carried out in order to support the work presented in this thesis. At the centre of the work has been a 256^3 simulation, which has been allowed to evolve for a period of approximately 25 eddy turnover times and which attained a Taylor Reynolds number of $R_\lambda = 190$. In addition to this, a number of lower-resolution runs have been performed in order to probe specific points. The important features of all of these runs are given below.

For all of our simulations, the initial velocity fields have been set up in precisely the way described in Section 3.3 — except for the case of the Taylor-Green vortex problem discussed in Chapter 5 where a specific velocity field is set up in real space.

All of the results presented have been taken from simulations of stationary turbulence, with the forcing term in the Navier-Stokes equation given by,

$$f_\alpha(\mathbf{k},t) = \begin{cases} \varepsilon_w u_\alpha(\mathbf{k},t)/(2E_f(t)) & \text{if } 0 < k < k_f \\ 0 & \text{otherwise} \end{cases}, \tag{4.2}$$

where ε_w is a constant energy input rate, k_f is the maximum forced wavenumber and $E_f(t)$ is the energy contained within the band of forced modes,

$$E_f(t) = \int_0^{k_f} E(k,t)\mathrm{d}k. \tag{4.3}$$

For all of our simulations we have set $k_f = 1.5$ which, with $L_{box} = 2\pi$, means that we are only applying the forcing to the first shell of wavenumbers. The value of ε_w varies from one simulation to the next. For the 256^3 simulation we have chosen $\varepsilon_w = 0.149$ and $\nu = 0.001$ (in arbitrary units) giving $k_d \approx 110$. These parameters match those used by Machiels [34].

Random-shifting has always been employed as a means of partially dealiasing the convolution sum, although in the case of the smaller simulations this has been augmented by additionally truncating the velocity field at $(2\sqrt{2}/3)k_{max}$.

Chapter 5

Code Validation

In this chapter, we detail a number of tests which were carried out in order to validate the DNS code. By comparing the output of the code with the results of other authors we are able to test whether or not the simulation is performing in the expected manner.

5.1 The Taylor-Green vortex

The Taylor-Green vortex is named for Taylor and Green [35] who were the first to study the problem of a system developing from initial conditions of the form,

$$u_x(\mathbf{x}, 0) = A \cos ax \sin by \sin cz \tag{5.1}$$

$$u_y(\mathbf{x}, 0) = B \sin ax \cos by \sin cz \tag{5.2}$$

$$u_z(\mathbf{x}, 0) = C \sin ax \sin by \sin cz, \tag{5.3}$$

eventually specializing to the case where $a = b = c$, $A = -B$ and $C = 0$. When Brachet, Meiron, Orszag, Nickel, Morf and Frisch [36] came to look at the problem, they specialized further to $a = b = c = A = -B = 1$ with $C = 0$ so that the initial conditions became,

$$u_x(\mathbf{x}, 0) = \sin x \cos y \cos z \tag{5.4}$$

$$u_y(\mathbf{x}, 0) = -\cos x \sin y \cos z \tag{5.5}$$

$$u_z(\mathbf{x}, 0) \;=\; 0. \tag{5.6}$$

Note that Brachet *et al* also applied a shift of origin, giving rise to the exchange of the sin and cos functions.

As an exercise in code validation, one of the Taylor-Green vortex experiments performed by Brachet *et al* has been repeated and the results compared with those presented in reference [36].

5.1.1 Simulation details

The initial conditions were those given in equations (5.4)–(5.6) and, furthermore, we consider an *inviscid* system — that is, $\nu = 0$.

The simulation was carried out on a 128^3 grid (Brachet *et al* performed simulations at resolutions ranging from 32^3 to 256^3) and full anti-aliasing was achieved by truncating the velocity field in wavenumber space at $k = 42$ (see Section 3.7.1). The simulation was allowed to run for 2,000 time-steps which, with a time-step of $\delta t = 0.002$, corresponds to $t_{\max} = 4$ (Brachet *et al* provided results for $t = 0 \ldots 3.5$).

5.1.2 Results

The Taylor-Green vortex represents a highly symmetric flow. In particular, no fluid crosses any of the planes given by x, y or $z = n\pi$ for any integer n. This means that although we are simulating a system of size $L_{box} = 2\pi$ we often need only concern ourself with the *impermeable box* defined by $0 \leq x, y, z \leq \pi$. The contents of this impermeable box is illustrated in Figure 5.1, showing streamlines in an instantaneous velocity field.

We take advantage of this simplification in our first set of results where we present some visualizations of the flow. Figures 5.2–5.5 show the evolution of the x- and

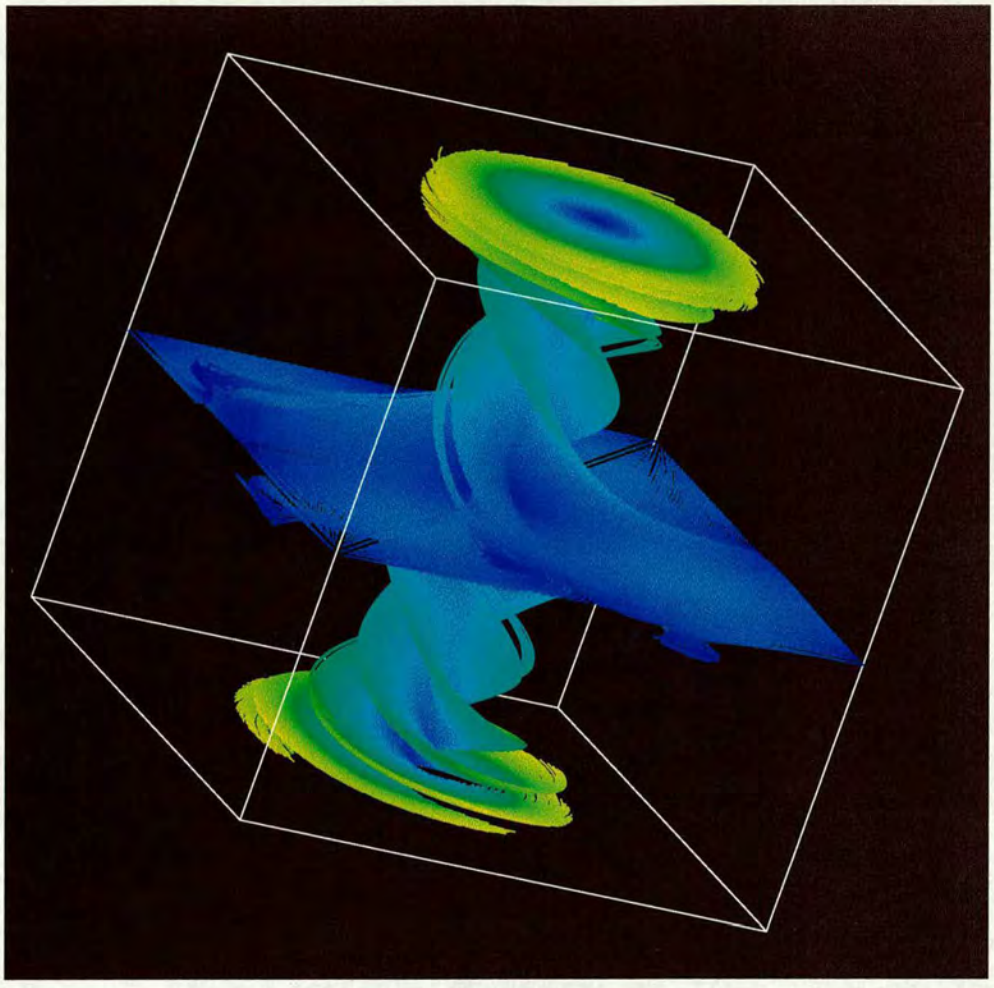

Figure 5.1: A visualisation of a Taylor-Green Vortex, obtained by plotting streamlines in an instantaneous velocity field.

y-components of the velocity field in the $z = 0$ plane at times $t = 0, 1, 2, 3$. Then, in Figures 5.6–5.9, isovorticity contours have been plotted in the same plane, and for the same times.

It is possible to carry out a qualitative comparison of these plots with those given in Figure 1 of reference [36]. Doing so, it is seen that there is good agreement. In Figure 5.8 the contour lines appear more ragged than those shown in the corresponding plot of reference [36] — this is most likely due to resolution effects (most of the results of Brachet *et al* were taken from their highest resolution of 256^3).

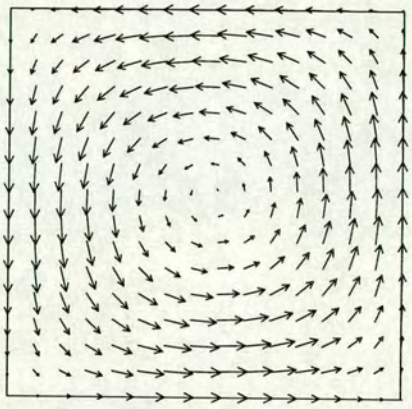

Figure 5.2: Velocity field in the $z = 0$ plane at time $t = 0$.

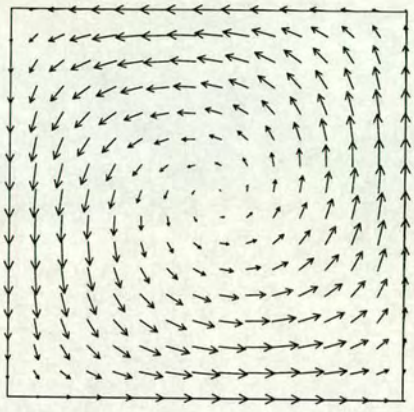

Figure 5.3: Velocity field in the $z = 0$ plane at time $t = 1$.

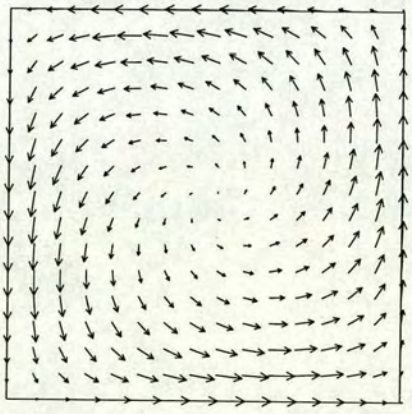

Figure 5.4: Velocity field in the $z = 0$ plane at time $t = 2$.

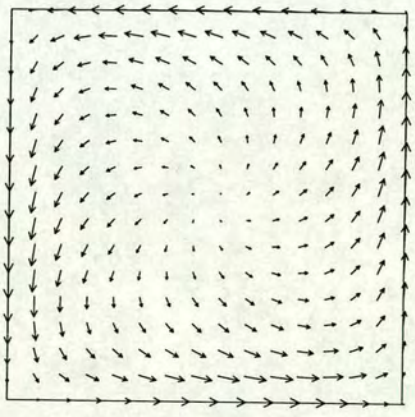

Figure 5.5: Velocity field in the $z = 0$ plane at time $t = 3$.

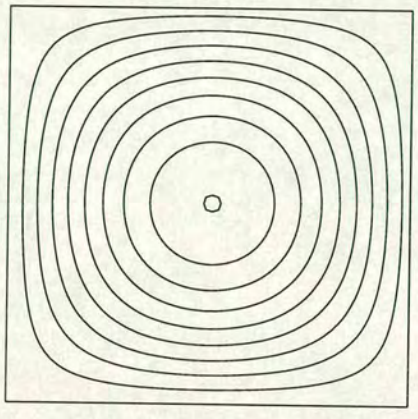

Figure 5.6: Isovorticity contours in the $z = 0$ plane at time $t = 0$.

Figure 5.7: Isovorticity contours in the $z = 0$ plane at time $t = 1$.

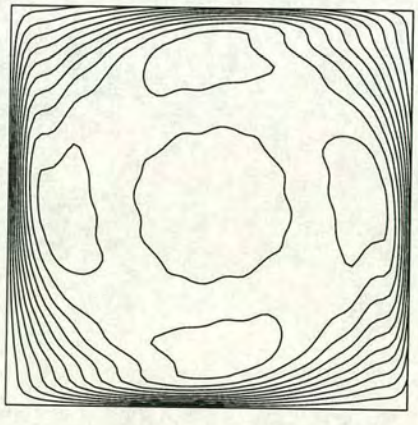

Figure 5.8: Isovorticity contours in the $z = 0$ plane at time $t = 2$.

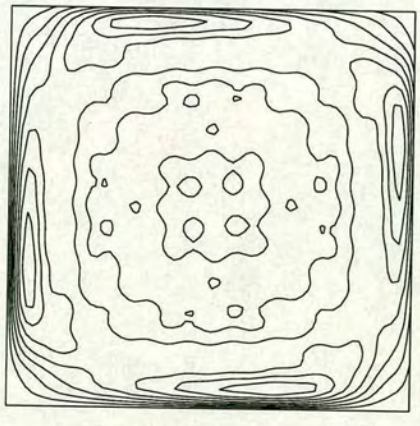

Figure 5.9: Isovorticity contours in the $z = 0$ plane at time $t = 3$.

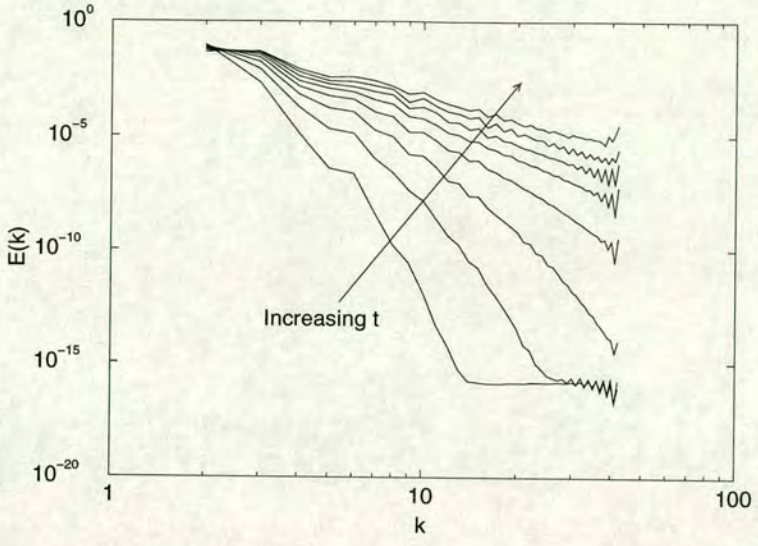

Figure 5.10: The evolution of the energy spectrum of a Taylor-Green vortex for $t = 0.5 \ldots 3.5$ in steps of 0.5.

To provide a more quantitative comparison, we turn to the evolution of the energy spectrum. Brachet *et al* noted that, "for later times, an unusual difference between the values of even and odd k develops." This oscillatory behaviour can also be seen in our data, plotted in Figure 5.10. This problem was circumvented by Brachet *et al* by increasing the scope of the shell average from the standard $\Delta k = 1$ to $\Delta k = 2$ (see Section 3.4). We follow suit, and the subsequent energy spectra presented in this section correspond to this "fattened" shell average.

Brachet *et al* assumed that the energy spectrum at a given time, t, took the form

$$E(k,t) = A(t)k^{-n(t)}e^{-2\delta(t)k} \tag{5.7}$$

where a least-squares fit of $\log E(k,t)$ was used to determine $A(t)$, $n(t)$ and $\delta(t)$. They provide values for $n(t)$ and $\delta(t)$ in reference [36], but not for $A(t)$. Therefore, in order to compare the spectra, we have set $n(t)$ and $\delta(t)$ equal to the values given in reference [36] and then performed a fit for the remaining parameter, $A(t)$.

When fitting the parameters, Brachet *et al* considered those points with $10 \leq k \leq 36$ except at time $t = 0.5$, when the range $4 \leq k \leq 22$ was employed. We have used the same ranges except at $t = 0.5$ and $t = 1.0$ where the flat tails of our

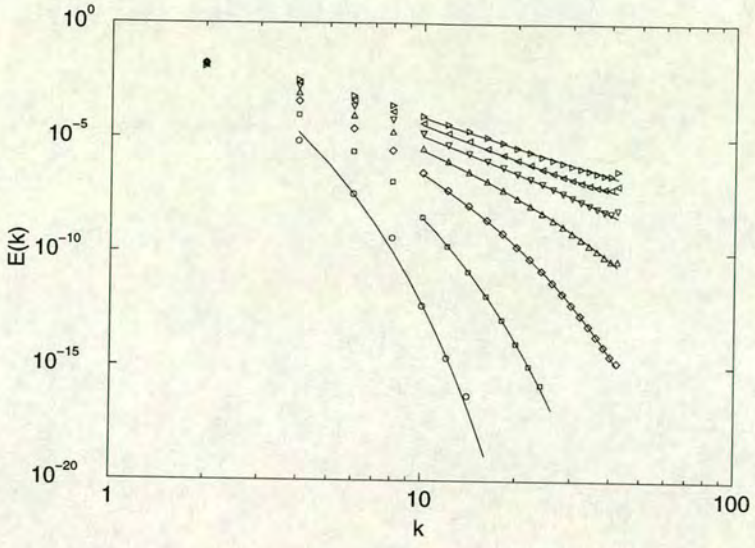

Figure 5.11: The evolution of the energy spectrum (averaged with shell-width $\Delta k = 2$) of a Taylor-Green vortex for $t = 0.5 \ldots 3.5$ in steps of 0.5. The symbols represent our DNS data, while the solid lines indicate the curve fitted according to Brachet *et al.*

t	$A(t)$	$n(t)$	$\delta(t)$
0.5	46.092	4.31	1.107
1.0	2.824	5.02	0.453
1.5	0.874	4.86	0.192
2.0	0.418	4.48	0.080
2.5	0.889	4.71	0.020
3.0	10.056	5.63	−0.022
3.5	2.188	4.51	−0.007

Table 5.1: Parameters in the fit of $E(k,t) = A(t)k^{-n(t)}e^{-2\delta(t)k}$ to the energy spectra obtained from the simulation of the Taylor-Green vortex.

spectra meant that we had to restrict the ranges to $4 \leq k \leq 12$ and $10 \leq k \leq 24$ respectively. Table 5.1 gives the values of $A(t)$, $n(t)$ and $\delta(t)$ used for the fits.

Figure 5.11 shows our DNS data and the corresponding curves fitted according to Brachet *et al.* We note that although we have had to fix one remaining parameter, this prefactor $A(t)$ cannot affect the *shape* of the curves and so we conclude that our results are in excellent agreement with those of Brachet *et al.*

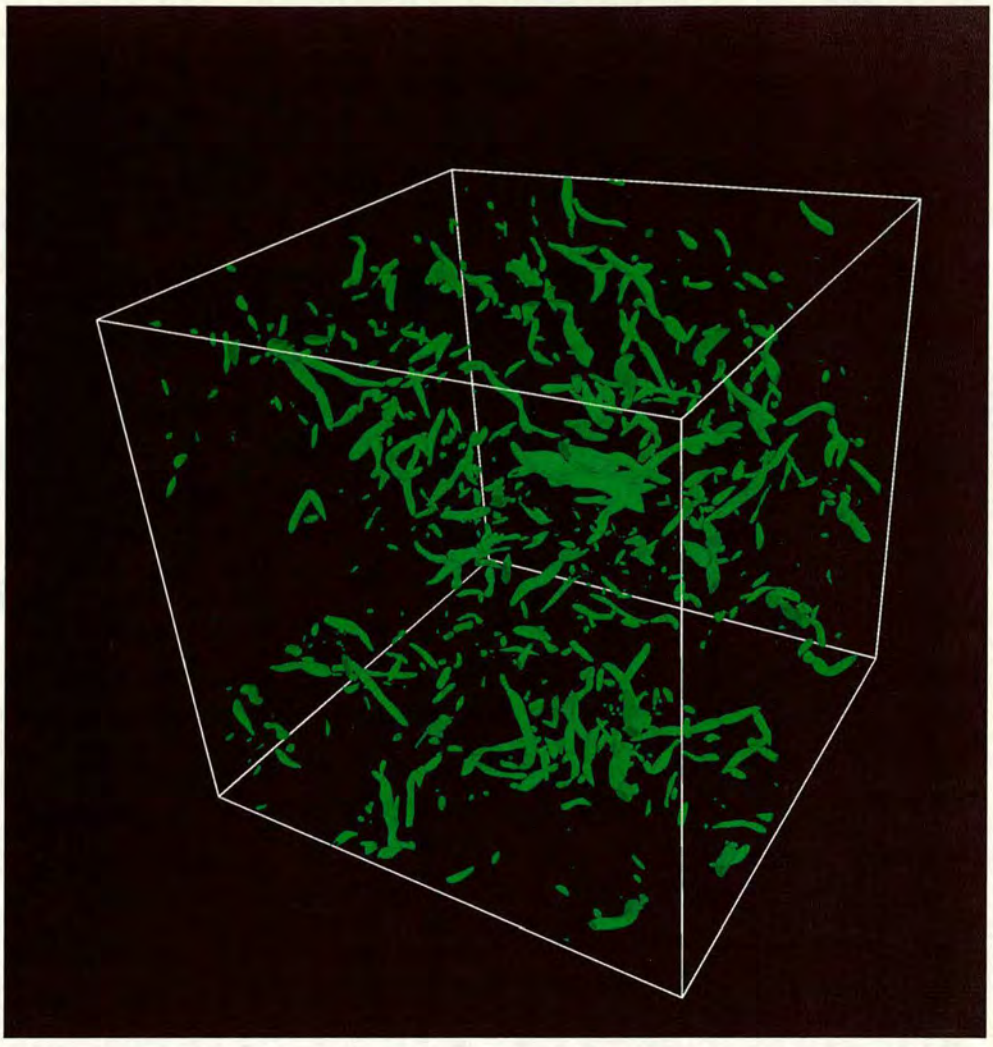

Figure 5.12: Surfaces of isovorticity for $|\omega|$ equal to 50% of the maximum.

5.2 Flow visualization of forced turbulence

In this section we have taken an evolved velocity field from our 256^3 simulation run and, in Figure 5.12, have plotted surfaces of constant vorticity. This is a standard way of illuminating the vortex structure contained within such a field and while it may not be the most accurate method of vortex identification [37], it is by far the simplest and is more than adequate for our needs. The figure clearly shows that the vorticity has organized itself into thin, elongated tubes which is in agreement with the work of many authors [38, 39, 40]. This is in contrast to

a random initial field which shows little in the way of coherent structures. We may conclude, therefore, that our simulations develop structure in the anticipated way.

5.3 Computing key turbulence parameters

In this section, we look at how values (including error bounds) have been obtained for some of the most important turbulence parameters — the longitudinal velocity derivative skewness, S, the Kolmogorov constant, α, and the non-dimensional dissipation rate, $D = \varepsilon L/u^3$. In the next section, we shall then see how well these compare with values obtained by other authors.

Given a single velocity field, we have seen that it is possible to obtain values for all of these quantities through the use of shell averaging. However, these values will fluctuate with time and so we will use time-averaging to provide a single mean value and also to compute an estimate of the error.

Our 256^3 simulation, from which the majority of results presented in this work are taken, computes various (shell-averaged) quantities every 25 time-steps, corresponding to an interval of 0.015 eddy turnover times. Once the initial period of transition had passed (approximately 10 evolved eddy turnover times), the simulation was then run on for a further 15 eddy turnover times and the averaging is performed over this interval. For example, the time-averaged value for the total energy is given by,

$$\overline{E} = \frac{1}{N_T} \sum_{t_i} E(t_i), \tag{5.8}$$

where N_T is the number of time-steps considered in the sum.

An estimate of the error is taken to be twice the standard deviation, σ, where, for example,

$$\sigma_E^2 = \overline{E^2} - \overline{E}^2. \tag{5.9}$$

We now look at each of the three quantities mentioned above in turn.

5.3.1 Longitudinal velocity derivative skewness

The longitudinal velocity derivative skewness (often referred to simply as the skewness) is defined by,

$$S(t) = -\frac{\left\langle (\partial u_1(\mathbf{x},t)/\partial x_1)^3 \right\rangle}{\left\langle (\partial u_1(\mathbf{x},t)/\partial x_1)^2 \right\rangle^{3/2}}, \tag{5.10}$$

and is sometimes regarded as being amongst the most sensitive of turbulence parameters [2].

Within the DNS code, the differentials are first computed in Fourier space as $k_1 u_1$ before being transformed into real space. Then homogeneity is used to compute the averages as space averages.

Time-averaging is performed, as described above, to give a value for the skewness of,

$$S = 0.497 \pm 0.072. \tag{5.11}$$

5.3.2 The Kolmogorov constant

The Kolmogorov constant, α, appears in the famous equation for the energy spectrum in the inertial range (see Section 2.8),

$$E(k) = \alpha \varepsilon^{2/3} k^{-5/3}. \tag{5.12}$$

Its value (and, indeed, whether it is a true constant) has been the subject of debate for decades.

In a recent paper, Yeung and Zhou [41] revisited the results of a number of previous authors, and pointed out that in many cases the location of the inertial range in numerical simulations had been misidentified, leading to overestimates for the constant, α.

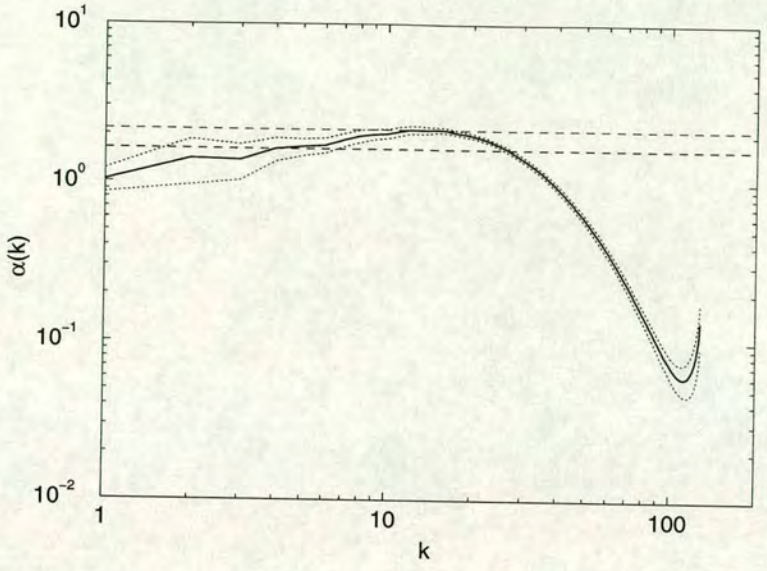

Figure 5.13: The compensated energy spectrum, $\alpha(k) = \varepsilon^{-2/3}k^{5/3}E(k)$ with error bounds. The horizontal dashed lines indicate the plateaus at $\alpha = 2.14$ and $\alpha = 1.624$.

They pointed out that in such simulations it is usual to observe two regions in the energy spectrum which apparently exhibit Kolmogorov ($k^{-5/3}$) scaling, occuring in wavenumber regions given approximately by $0.02 \leq k/k_d \leq 0.05$ and $0.1 \leq k/k_d \leq 0.2$

In Figure 5.13, we have plotted the *compensated* energy spectrum obtained by rearranging equation (5.12) for the Kolmogorov spectrum,

$$\alpha(k) = \varepsilon^{-2/3}k^{5/3}E(k). \tag{5.13}$$

The time-averaging used to obtain the mean value and the error estimates was performed over this entire expression. That is,

$$\overline{\alpha(k)} = \overline{\varepsilon^{-2/3}k^{5/3}E(k)} \neq (\overline{\varepsilon})^{-2/3}\, k^{5/3}\overline{E(k)}. \tag{5.14}$$

The two plateaus noted by Yeung and Zhou are indicated by horizontal dashed lines and it is the first of these which they claim represents inertial range behaviour. Their argument focuses on the dissipation spectrum, $D(k) = 2\nu k^2 E(k)$, demonstrating that the second region of apparent Kolmogorov scaling coincides

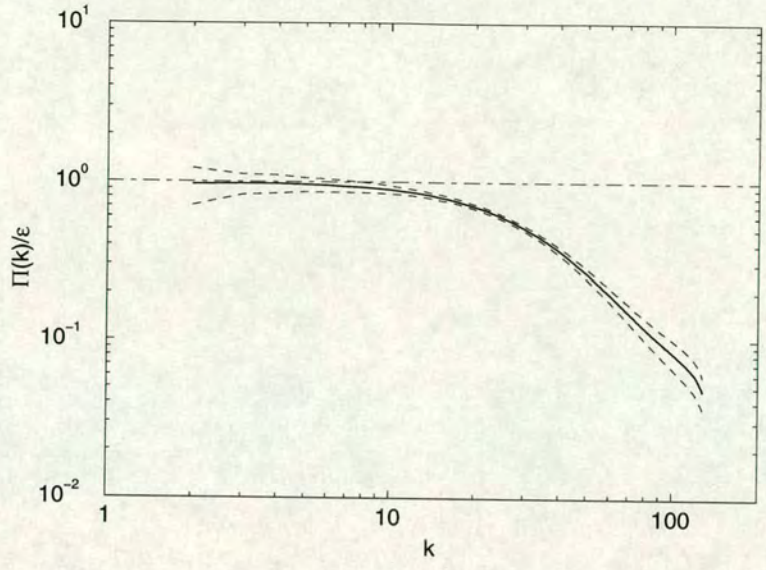

Figure 5.14: The scaled transport power, $\Pi(k)/\varepsilon$, with error bounds. Inertial range behaviour should give $\Pi(k)/\varepsilon = 1$.

with the peak of this spectrum and hence cannot represent inertial range behaviour. This is also true for our data, where the peak of the dissipation spectrum occurs at $k_p \approx 15$.

A simple test for inertial range behaviour involves the transport power, defined in Section 2.9 and representing rate at which energy is transferred from modes $k' < k$ to modes $k' > k$. In the inertial range, this must satisfy,

$$\Pi(k,t) = \varepsilon(t). \tag{5.15}$$

In Figure 5.14, we have plotted $\Pi(k)/\varepsilon$ which, if inertial range behaviour is present, should equal unity by equation (5.15). As can be seen, with errors taken into account one could argue for an inertial range in the region $2 \leq k \leq 8$ — corresponding to the first plateau in Figure 5.13 and in agreement with Yeung and Zhou. In fact, for the purpose of obtaining the Kolmogorov constant we take the point with the maximum transport power, $k = 4$, and use the data presented in Figure 5.13 to obtain a value of,

$$\alpha = 1.624 \pm 0.122. \tag{5.16}$$

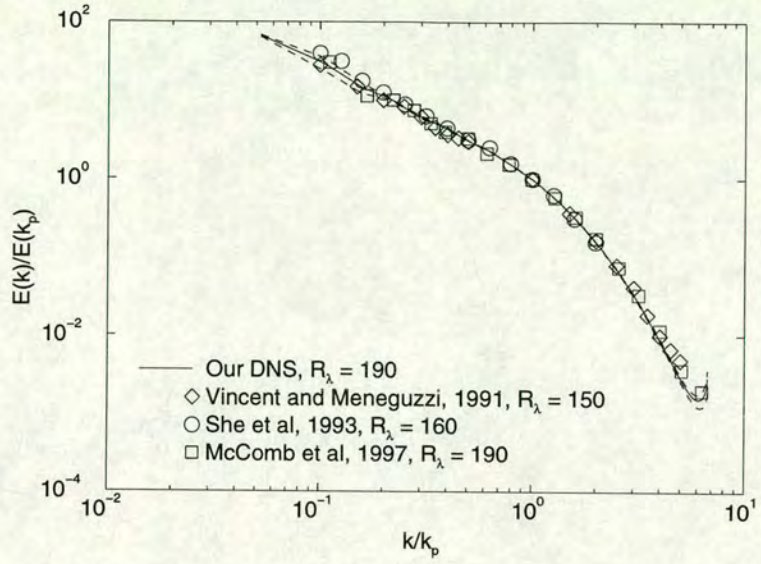

Figure 5.15: Comparison of scaled energy spectra taken from our current DNS (plotted with error bounds) and from three independent simulations [38, 43, 44].

5.3.3 Non-dimensional dissipation rate

It has long been thought that, for the case of high Reynolds number flows, the mean energy dissipation rate, ε, should be independent of the viscosity, ν. It is then expected, from dimensional arguments, that,

$$D = \varepsilon \frac{L}{u^3}, \tag{5.17}$$

should approach a constant of order unity as Reynolds number increases [42]. As such, it provides a useful quantity for comparison with the work of other authors. From our DNS we obtain a value of,

$$D = 0.407 \pm 0.043. \tag{5.18}$$

5.4 Comparison with other simulations

We begin this section by comparing the energy spectrum obtained from our 256^3 DNS run, with those obtained in other, independent simulations due to Vincent and Meneguzzi in 1991 [38], She, Chen, Doolen, Kraichnan and Orszag in 1993

Simulation	N	R_λ	S	α	$\varepsilon L/u^3$
Our DNS	256	190.741 ± 13.195	0.497 ± 0.072	1.624 ± 0.122	0.407 ± 0.043
[34, 44][a]	256	190.606	0.51	1.722 ± 0.188	0.465
[42][b]		∞			0.44 ± 0.055
[41][c]	384	180		1.62	0.41
[27][d]	256	151	0.498	1.68 ± 0.15	0.428
[45][e]	512	168.1	0.525	~ 2	0.69
[38][f]	256	150	0.5	2.0	

[a]Machiels, 1997
[b]Sreenivasan, 1998
[c]Yeung and Zhou, 1997
[d]Wang *et al*, 1996
[e]Jiménez *et al*, 1993
[f]Vincent and Meneguzzi, 1991

Table 5.2: Comparison of several key turbulence parameters between our simulation results and those of other authors.

[43] and McComb, Yang, Young and Machiels in 1997 [44] (simulation work in this last case carried out by Machiels). The spectra attributed to Vincent and Meneguzzi and She *et al* have been obtained by reading them off from printed figures. Results are given in Figure 5.15. The scaling used is that suggested by She *et al* who found that spectra at various Reynolds numbers collapse when scaled on the wavenumber, k_p, corresponding to the peak of the dissipation spectrum and on the spectrum level at k_p. The graph shows a good collapse of all four data sets.

In the remainder of this section we will take the three quantities described in the previous section and compare them each in turn with those given by other authors. In this way we are able to further validate the code.

The results for each of these parameters, along with grid size, N, and microscale Reynolds number, R_λ, are given in Table 5.2. Where possible, bounds of uncertainty are given.

This data is presented again in a somewhat more easy to digest form in Figure 5.16, allowing for simple comparisons between the various results.

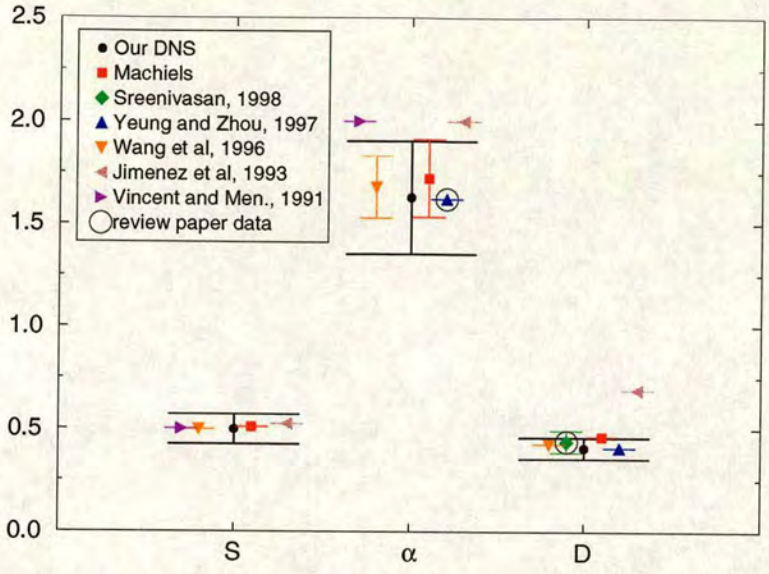

Figure 5.16: Values for the skewness, S, the Kolmogorov constant, α and the non-dimensional dissipation rate, D from our simulation, compared with values given by other authors. The ringed data points correspond to papers which have themselves taken data from other authors in an attempt to give a consensus result.

5.4.1 Longitudinal velocity derivative skewness

Kolmogorov's 1941 theory leads to a relationship between the Kolmogorov constant and the skewness given by [15, 46],

$$\alpha = \left(\frac{16}{15S}\right)^{2/3}, \tag{5.19}$$

which is consistent with the values for both S and α obtained from our simulation. Stolovitzky, Sreenivasan and Juneja [46] gave an expression taking into account intermittency[1] relating the skewness to the microscale Reynolds number,

$$S(t) = 0.27 R_\lambda(t)^{0.1}. \tag{5.20}$$

This implies that there is a Reynolds number dependence. However, for the range of Reynolds numbers present in the results from which we have drawn values for the skewness ($R_\lambda \approx 150$–200), this still gives a fairly tight theoretical bound on the skewness: 0.44–0.46.

[1] Kolmogorov's 1941 theory assumes self-similarity of the random velocity field in the inertial range of scales. Deviations from this self-similarity are known as intermittency effects. A good discussion of this subject is given by Frisch [20].

Indeed, as Figure 5.16 demonstrates, all the values used are in good agreement with one another, and lie well within our error bars. We note, however, that the theoretical value of the skewness given by equation (5.20) appears to slightly underestimate that seen in the simulations.

5.4.2 Kolmogorov constant

As can be seen in Figure 5.16, the values for the Kolmogorov constant taken from various papers are in good agreement — with two exceptions which will be dealt with shortly. In particular, the value provided by Yeung and Zhou [41] matches our value closely and was the result of a survey of a large amount of independent data. It should be noted that the value and errors attributed to Machiels have been generated by the current author from a single energy spectrum and, as such, should not be taken to represent the opinion of Machiels.

Of the two anomalous values, the one due to Jiménez *et al* [45] is only given as approximate and that due to Vincent and Meneguzzi [38] can probably be attributed to the misidentification of the inertial range, as discussed in Section 5.3.2.

5.4.3 Non-dimensional dissipation rate

In a recent paper, Sreenivasan [42] collected together data from a number of authors in an attempt to provide a consensus on the value of $D = \varepsilon L/u^3$. By plotting the values of D against microscale Reynolds number, R_λ, Sreenivasan found what appeared to be two asymptotic values for D — one at around 0.7 (which included the result due to Jiménez *et al* [45], lying outside our error bounds in Figure 5.16) and one at around 0.44. This dual behaviour was put down to the effects of the forcing scheme or the large-scale structure of the flow.

For the purpose of comparison with our simulation, we have used the lower value

as it gives better agreement. Taking the data given in the paper, it is possible to get a rough error estimate (again taken as twice the standard deviation) giving a value according to Sreenivasan of 0.44 ± 0.055.

As Figure 5.16 clearly shows, there is once again good agreement between our simulation results and the results of others.

5.5 Isotropy

As our aim is to simulate isotropic turbulence, it is worth testing to ensure that the resultant velocity field actually has this property.

A means of testing for isotropy was given by Curry, Herring, Loncaric and Orszag [47], which we have modified slightly.

We begin by defining two mutually orthogonal unit vectors, each also perpendicular to the wavevector, $\mathbf{k}$,

$$\mathbf{e}_1(\mathbf{k}) = \frac{\mathbf{k} \times \hat{\mathbf{z}}(\mathbf{k})}{|\mathbf{k} \times \hat{\mathbf{z}}(\mathbf{k})|}, \tag{5.21}$$

$$\mathbf{e}_2(\mathbf{k}) = \frac{\mathbf{k} \times \mathbf{e}_1(\mathbf{k})}{|\mathbf{k} \times \mathbf{e}_1(\mathbf{k})|}, \tag{5.22}$$

where $\hat{\mathbf{z}}(\mathbf{k})$ is a randomly oriented unit vector (subject to the constraint that it should be non-parallel to $\mathbf{k}$).

We then compute the average energy along each of these components,

$$\Psi_1(k,t) = \left\langle |\mathbf{e}_1(\mathbf{k}) \cdot \mathbf{u}(\mathbf{k})|^2 \right\rangle, \tag{5.23}$$

$$\Psi_2(k,t) = \left\langle |\mathbf{e}_2(\mathbf{k}) \cdot \mathbf{u}(\mathbf{k})|^2 \right\rangle. \tag{5.24}$$

For isotropic turbulence we would expect to find that $\Psi_1(k,t) = \Psi_2(k,t)$ and so a measure of isotropy is given by,

$$I(k,t)^2 = \Psi_1(k,t)/\Psi_2(k,t). \tag{5.25}$$

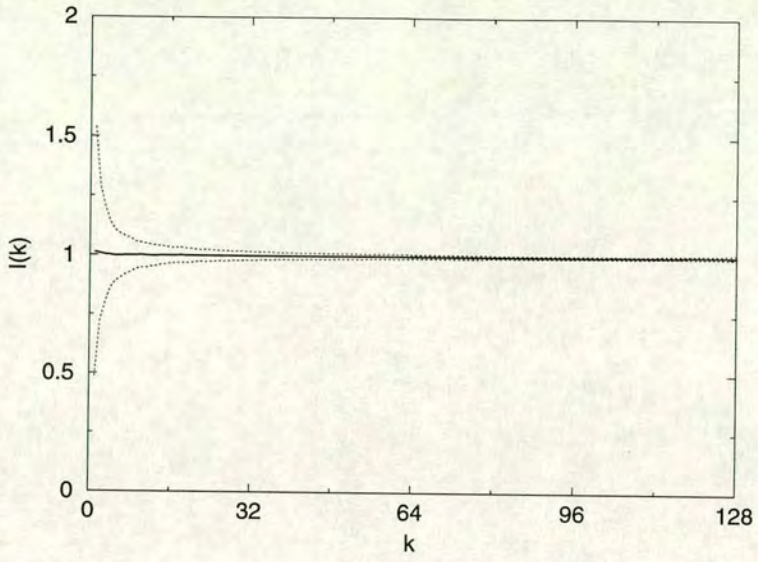

Figure 5.17: A measure of the isotropy in our numerical simulations.

This has been averaged in the way outlined in Section 5.3 and the result is plotted in Figure 5.17. As hoped, the mean value is approximately unity for all values of k, although the error bounds highlight the increased variation at low-k, which will be due to the low resolution of these shells.

An overall value for isotropy has also been computed, by performing sums over all of Fourier-space, rather than in individual shells. This also gives a satisfactory value of 1.002 ± 0.214 allowing us to conclude that the simulation does not display significant deviations from isotropy.

The code for the isotropy calculation was provided by Gary Fullerton [48].

5.6 Conclusions

We have investigated the validity of our DNS code in four ways.

Firstly, we have performed a simulation of the evolution of the Taylor-Green vortex, which is a standard test problem. We were able to show that our results were in good agreement with those given by Brachet *et al* [36].

Secondly, we have plotted isosurfaces of $|\omega|$ in order to visualize vortex structure. These have shown qualitative agreement with results of other authors.

Thirdly, we have compared our energy spectrum and the values for a number of key turbulence parameters with those of other authors. With a few easily explained exceptions we have seen excellent agreement. Our error bars encompass the values of other authors and — where available — the error bars of other authors encompass our results.

Finally, we have successfully demonstrated that the system exhibits isotropic properties.

It seems safe to conclude, therefore, that our simulation code is behaving in the expected manner and that we may have confidence in the results it produces.

Chapter 6

Spectral Large Eddy Simulation of Homogeneous Isotropic Turbulence

As has been discussed, large eddy simulation (LES) is one technique which has been used to tackle the large computational cost of DNS. For many engineering applications, it is only the large scale motions of the fluid that are of interest and so, in a LES, only these scales are explicitly simulated with the effects of the small scales being modelled in some way.

In this chapter we give a brief introduction to the technique, concentrating on the LES of homogeneous isotropic turbulence in spectral space. We shall then discuss one standard model and see some ways in which it may be tested.

6.1 LES formalism

A good review of LES techniques has been given, for example, by Lesieur and Métais [49]. We shall just give an outline of the general concept of LES here.

Consider a real-space simulation taking place on a grid with mesh spacing given by Δx. The *subgrid scales* are those scales of motion with wavelength less than this. To give a more formal definition, we introduce a filtering function, G, of

width Δx which filters out the subgrid scales so that the *filtered* velocity field is defined by,

$$\begin{aligned} \bar{u}_\alpha(\mathbf{x},t) &= \int \mathrm{d}^3y\; u_\alpha(\mathbf{y},t)G(\mathbf{x}-\mathbf{y}) \\ &= \int \mathrm{d}^3y\; u_\alpha(\mathbf{x}-\mathbf{y})G(\mathbf{y}). \end{aligned} \tag{6.1}$$

The subgrid scale velocity field, u'_α is then defined as the departure of the actual velocity field from this filtered field,

$$u_\alpha(\mathbf{x},t) = \bar{u}_\alpha(\mathbf{x},t) + u'_\alpha(\mathbf{x},t). \tag{6.2}$$

It may be shown, using integration by parts [50], that the filtering operation defined in equation (6.1) commutes with both spatial and temporal derivatives. This means that the filtered field still satisfies the continuity equation,

$$\frac{\partial \bar{u}_\alpha(\mathbf{x},t)}{\partial x_\alpha} = 0. \tag{6.3}$$

We may also apply the filter to the momentum conservation equation, (2.1), to give,

$$\frac{\partial \bar{u}_\alpha(\mathbf{x},t)}{\partial t} + \frac{\partial \overline{u_\alpha(\mathbf{x},t)u_\beta(\mathbf{x},t)}}{\partial x_\beta} = -\frac{1}{\rho}\frac{\partial \bar{p}(\mathbf{x},t)}{\partial x_\alpha} + \nu\frac{\partial^2 \bar{u}_\alpha(\mathbf{x},t)}{\partial x_\beta \partial x_\beta}. \tag{6.4}$$

Introducing the *subgrid scale tensor*,

$$T_{\alpha\beta}(\mathbf{x},t) = \bar{u}_\alpha(\mathbf{x},t)\bar{u}_\beta(\mathbf{x},t) - \overline{u_\alpha(\mathbf{x},t)u_\beta(\mathbf{x},t)}, \tag{6.5}$$

the filtered momentum equation may be rewritten as,

$$\frac{\partial \bar{u}_\alpha(\mathbf{x},t)}{\partial t} + \frac{\partial \bar{u}_\alpha(\mathbf{x},t)\bar{u}_\beta(\mathbf{x},t)}{\partial x_\beta} = -\frac{1}{\rho}\frac{\partial \bar{p}(\mathbf{x},t)}{\partial x_\alpha} + \nu\frac{\partial^2 \bar{u}_\alpha(\mathbf{x},t)}{\partial x_\beta \partial x_\beta} + \frac{\partial T_{\alpha\beta}(\mathbf{x},t)}{\partial x_\beta}. \tag{6.6}$$

As can be seen, this is simply the momentum conservation equation for $\bar{u}_\alpha(\mathbf{x},t)$, with the addition of an extra term on the right hand side. The subgrid scale tensor represents the effects of the subgrid scales and it is this which must be modelled in a LES.

Recalling our definition of the fluctuating component of the velocity field, the subgrid scale tensor may be expressed as the sum of the *Leonard tensor*,

$$L_{\alpha\beta} = \bar{u}_\alpha\bar{u}_\beta - \overline{\bar{u}_\alpha\bar{u}_\beta}, \tag{6.7}$$

the *Reynolds tensor*,

$$R_{\alpha\beta} = -\overline{u'_\alpha u'_\beta}, \tag{6.8}$$

and the *cross tensor*,

$$C_{\alpha\beta} = -\left(\overline{\bar{u}_\alpha u'_\beta} + \overline{u'_\alpha \bar{u}_\beta}\right), \tag{6.9}$$

where we have suppressed the time and space coordinates for clarity. The Leonard tensor is an explicit term which may be computed in terms of the filtered field, but the other terms are unknown. Some authors advocate the separate modelling of each of these terms [51] (claiming that it can give rise to increased accuracy, but noting that there is also an increase in the computational cost) while others believe that it is preferable to model the subgrid scale tensor as a whole [49]. For this brief discussion we shall follow the latter route.

Most subgrid scale models make an eddy-viscosity assumption, whereby the subgrid scale tensor is related to the strain rate of the filtered velocity field, $\bar{S}_{\alpha\beta}$, by,

$$T_{\alpha\beta} - \frac{1}{3}T_{\gamma\gamma}\delta_{\alpha\beta} = 2\delta\nu\bar{S}_{\alpha\beta} = \delta\nu\left(\frac{\partial\bar{u}_\alpha}{\partial x_\beta} + \frac{\partial\bar{u}_\beta}{\partial x_\alpha}\right), \tag{6.10}$$

where we note that the trace has been removed and where $\delta\nu$ is the eddy-viscosity which is generally assumed to be a scalar quantity (Boussinesq's assumption [52, 53]). In the momentum equation, (6.6), $T_{\alpha\beta}$ appears within a derivative and so we may invoke continuity to write,

$$\begin{aligned}\frac{\partial T_{\alpha\beta}}{\partial x_\beta} &= \delta\nu\frac{\partial}{\partial x_\beta}\left(\frac{\partial\bar{u}_\alpha}{\partial x_\beta} + \frac{\partial\bar{u}_\beta}{\partial x_\alpha}\right) + \frac{1}{3}\delta_{\alpha\beta}\frac{\partial T_{\gamma\gamma}}{\partial x_\beta} \\ &= \delta\nu\frac{\partial^2\bar{u}_\alpha}{\partial x_\beta\partial x_\beta} + \frac{1}{3}\frac{\partial T_{\gamma\gamma}}{\partial x_\alpha}.\end{aligned} \tag{6.11}$$

If we then substitute this into equation (6.6) we obtain,

$$\frac{\partial\bar{u}_\alpha(\mathbf{x},t)}{\partial t} + \frac{\partial\bar{u}_\alpha(\mathbf{x},t)\bar{u}_\beta(\mathbf{x},t)}{\partial x_\beta} = -\frac{1}{\rho}\frac{\partial\bar{P}(\mathbf{x},t)}{\partial x_\alpha} + (\nu+\delta\nu)\frac{\partial^2\bar{u}_\alpha(\mathbf{x},t)}{\partial x_\beta\partial x_\beta}, \tag{6.12}$$

where the trace of of the subgrid scale tensor has been absorbed into a modified pressure given by,

$$\bar{P} = \bar{p} - \frac{1}{3}\rho T_{\gamma\gamma}. \tag{6.13}$$

At this point, the LES problem has been reduced to one of modelling the eddy-viscosity, $\delta\nu$.

6.1.1 Smagorinsky's model

One model which has had much success is that due to Smagorinsky [54] in which the eddy-viscosity is given by,

$$\delta\nu = (C_S \delta x)^2 \, |\bar{S}|, \tag{6.14}$$

where C_S is a constant of the model and,

$$|\bar{S}|^2 = 2\bar{S}_{\alpha\beta}\bar{S}_{\alpha\beta}. \tag{6.15}$$

An approximate value for the constant, C_S, may be obtained by assuming that the cutoff wavenumber in Fourier space corresponding to the filter width, $k_c \approx \pi/\Delta x$, lies within a $k^{-5/3}$ range — i.e. $E(k) = \alpha\varepsilon^{2/3}k^{-5/3}$. It is then possible to adjust C_S so that the subgrid dissipation rate is equal to ε [55]. This then gives,

$$C_S \approx \frac{1}{\pi}\left(\frac{3\alpha}{2}\right)^{3/4}. \tag{6.16}$$

This model, and indeed this brief discussion of large eddy simulation in real space, is only given for the sake of completeness. They will not be discussed further.

6.2 Spectral LES

6.2.1 The spectral cutoff filter

In Fourier space, we are presented with an appealingly simple picture. The filtering operation is defined in terms of some cutoff wavenumber, $k_c \approx \pi/\Delta x$ with the "large scales" given by those wavenumbers $k < k_c$, and the "small scales" give by those wavenumbers $k > k_c$. Mathematically, we introduce the function

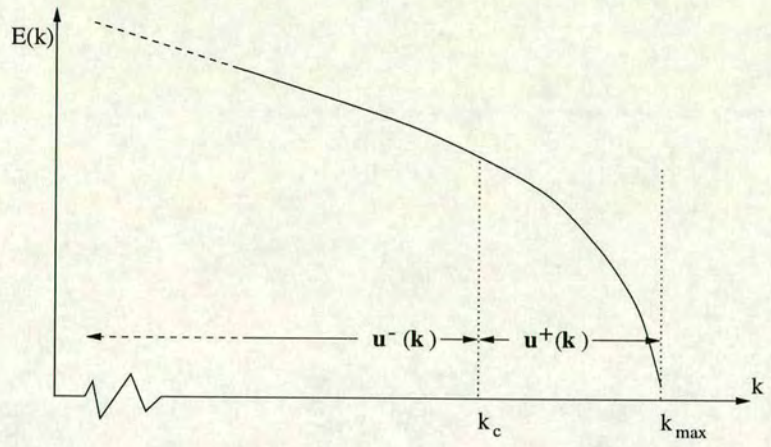

Figure 6.1: A schematic illustration of a spectral LES, showing the division of Fourier space into grid scale ($k < k_c$) and subgrid scale ($k > k_c$) components for a cutoff wavenumber, k_c.

$\theta^-(k)$ to denote this filtering procedure, defined by,

$$\theta^-(k) = \begin{cases} 1 & \text{if } k \leq k_c \\ 0 & \text{if } k > k_c \end{cases}, \tag{6.17}$$

and its complement,

$$\theta^+(k) = 1 - \theta^-(k) = \begin{cases} 0 & \text{if } k \leq k_c \\ 1 & \text{if } k > k_c \end{cases}. \tag{6.18}$$

We can then define the grid and subgrid scale velocity fields respectively by,

$$u_\alpha^-(\mathbf{k}) = \theta^-(k) u_\alpha(\mathbf{k}), \tag{6.19}$$

$$u_\alpha^+(\mathbf{k}) = \theta^+(k) u_\alpha(\mathbf{k}), \tag{6.20}$$

which also implies that,

$$u_\alpha(\mathbf{k}) = u_\alpha^-(\mathbf{k}) + u_\alpha^+(\mathbf{k}). \tag{6.21}$$

In the context of the previous section, we could make the definitions $u^- \equiv \bar{u}$ and $u^+ \equiv u'$ if so desired.

This wavenumber division is illustrated in Figure 6.1.

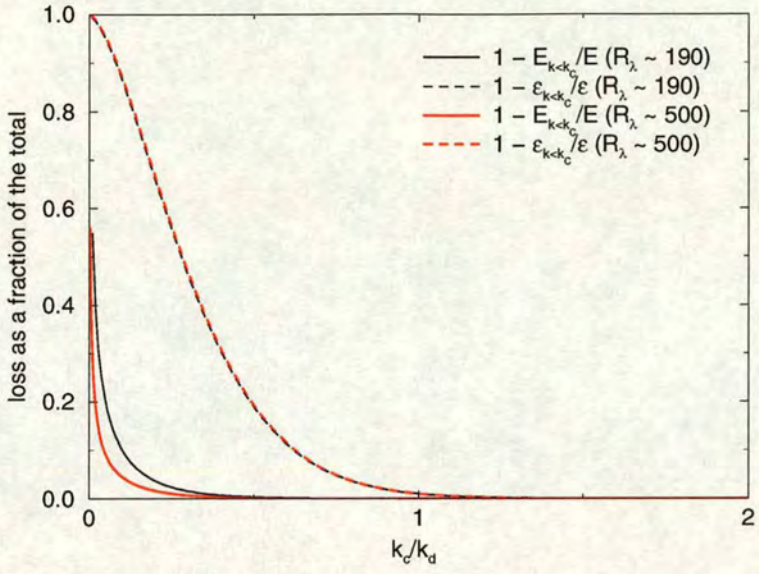

Figure 6.2: A schematic illustration showing the amount of energy and energy dissipation lost as a result of spectral truncation.

6.2.2 Effects of spectral truncation

Considering a fully-resolved velocity field, the immediate effects of eliminating those wavenumber modes with $k > k_c$ are the loss of the energy in the eliminated modes and a reduction in the total dissipation rate. This latter quantity is of interest since, for a statistically stationary state, the energy dissipation rate in the subgrid modes must be equal to the rate at which energy is transferred from the grid to subgrid scales.

Figure 6.2 shows how much of the energy and dissipation is lost for a range of cutoff wavenumbers, $0 < k_c/k_d \leq 2$. The data in this graph was computed using Qian's model spectrum (see Section 6.3.2 for details) with parameters giving Reynolds numbers of $R_\lambda = 190$ and $R_\lambda = 500$.

As expected, this graph shows that the effects on the dissipation are far more severe than those on the total energy — for $k_c/k_d \approx 0.5$, for example, we see that while virtually no energy has been lost, somewhere in the region of 20% of the dissipation has been removed. We also note that while increasing the Reynolds

number reduces the energy loss corresponding to any given choice of k_c/k_d, it has almost no effect on the loss of dissipation.

6.2.3 Notation

At this point, it is worth taking some time to introduce the shorthand notation that will be used throughout much of the rest of this thesis. Firstly, we shall use ψ to represent the nonlinear term in the Navier-Stokes equations so that we may write,

$$\psi_\alpha(\mathbf{k},t) = M_{\alpha\beta\gamma}(\mathbf{k}) \sum_{\mathbf{j}} u_\beta(\mathbf{j},t) u_\gamma(\mathbf{k}-\mathbf{j},t). \tag{6.22}$$

We have already seen the use of superscript '$-$' and '$+$' to denote variables which have been filtered by θ^- and θ^+ respectively so that, for example,

$$\begin{aligned} \psi^-_\alpha(\mathbf{k},t) &= \theta^-(k) M_{\alpha\beta\gamma}(\mathbf{k}) \sum_{\mathbf{j}} u_\beta(\mathbf{j},t) u_\gamma(\mathbf{k}-\mathbf{j},t) \\ &= M^-_{\alpha\beta\gamma}(\mathbf{k}) \sum_{\mathbf{j}} u_\beta(\mathbf{j},t) u_\gamma(\mathbf{k}-\mathbf{j},t). \end{aligned} \tag{6.23}$$

We now also introduce *subscript* notation to indicate filtering on the variables within the nonlinear term. For example,

$$\psi^-_{\alpha++}(\mathbf{k},t) = M^-_{\alpha\beta\gamma}(\mathbf{k}) \sum_{\mathbf{j}} u^+_\beta(\mathbf{j},t) u^+_\gamma(\mathbf{k}-\mathbf{j},t), \tag{6.24}$$

and note that, by definition, we include both permutations within the cross term, i.e.,

$$\begin{aligned} \psi^-_{\alpha-+}(\mathbf{k},t) &= M^-_{\alpha\beta\gamma}(\mathbf{k}) \sum_{\mathbf{j}} \left(u^-_\beta(\mathbf{j},t) u^+_\gamma(\mathbf{k}-\mathbf{j},t) + u^+_\beta(\mathbf{j},t) u^-_\gamma(\mathbf{k}-\mathbf{j},t) \right) \\ &= 2M^-_{\alpha\beta\gamma}(\mathbf{k}) \sum_{\mathbf{j}} u^-_\beta(\mathbf{j},t) u^+_\gamma(\mathbf{k}-\mathbf{j},t). \end{aligned} \tag{6.25}$$

Justification for this second step may be provided as follows:

$$\begin{aligned} M^-_{\alpha\beta\gamma}(\mathbf{k}) \sum_{\mathbf{j}} u^+_\beta(\mathbf{j},t) u^-_\gamma(\mathbf{k}-\mathbf{j},t) &= M^-_{\alpha\beta\gamma}(\mathbf{k}) \sum_{\mathbf{j}+\mathbf{l}=\mathbf{k}} u^+_\beta(\mathbf{j},t) u^-_\gamma(\mathbf{l},t) \\ &= M^-_{\alpha\gamma\beta}(\mathbf{k}) \sum_{\mathbf{j}+\mathbf{l}=\mathbf{k}} u^-_\beta(\mathbf{j},t) u^+_\gamma(\mathbf{l},t) \\ &= M^-_{\alpha\beta\gamma}(\mathbf{k}) \sum_{\mathbf{j}} u^-_\beta(\mathbf{j},t) u^+_\gamma(\mathbf{k}-\mathbf{j},t), \end{aligned} \tag{6.26}$$

where the penultimate step is simply the interchange of the dummy variables, $\beta \leftrightarrow \gamma$ and $\mathbf{j} \leftrightarrow \mathbf{l}$, and where the final step is due to the symmetry of $M^-_{\alpha\beta\gamma}(\mathbf{k})$ in the last two indices.

Finally, for this section, we will introduce the use of parentheses to indicate terms which have been excluded. For example,

$$\begin{aligned}\psi^-_{\alpha(--)}(\mathbf{k},t) &= \psi^-_\alpha(\mathbf{k},t) - \psi^-_{\alpha--}(\mathbf{k},t) \\ &= \psi^-_{\alpha-+}(\mathbf{k},t) + \psi^-_{\alpha++}(\mathbf{k},t) \\ &= M^-_{\alpha\beta\gamma}(\mathbf{k}) \sum_{\mathbf{j}} \Big(2u^-_\beta(\mathbf{j},t) u^+_\gamma(\mathbf{k}-\mathbf{j},t) \\ &\qquad + u^+_\beta(\mathbf{j},t) u^+_\gamma(\mathbf{k}-\mathbf{j},t) \Big). \end{aligned} \tag{6.27}$$

6.2.4 The filtered Navier-Stokes equation

We now apply the filter, θ^-, to the momentum equation in Fourier space, given by (2.18), and then substitute equation (6.21) into the right hand side in order to expand the nonlinear term. Using the notation given in the previous section, we may then write,

$$\left(\frac{\partial}{\partial t} + \nu k^2 \right) u^-_\alpha(\mathbf{k},t) = \psi^-_{\alpha--}(\mathbf{k},t) + \psi^-_{\alpha(--)}(\mathbf{k},t). \tag{6.28}$$

As was the case in the real space formulation, we have thus decomposed the momentum equation into explicit and subgrid contributions, given by ψ^-_{--} and $\psi^-_{(--)}$ respectively. The goal of a spectral LES is to find a model for $\psi_{(--)}$.

Once again, we make an eddy-viscosity assumption — this time proposing that there is a linear relationship between the subgrid terms and the filtered velocity,

$$\psi^-_{\alpha(--)}(\mathbf{k},t) = -\delta\nu(k,t) k^2 u^-_\alpha(\mathbf{k},t), \tag{6.29}$$

where the eddy-viscosity, $\delta\nu(k,t)$, is a scalar quantity, with a dependency on wavenumber. Substituting this into equation 6.28 then gives,

$$\left(\frac{\partial}{\partial t} + [\nu + \delta\nu(k,t)] k^2 \right) u^-_\alpha(\mathbf{k},t) = \psi^-_{\alpha--}(\mathbf{k},t). \tag{6.30}$$

6.2.5 A theoretical form for the eddy-viscosity

In Section 2.6 we derived the energy balance equation, given by equation (2.50). Filtering this, and then using equation (6.21) to expand the transfer term, $T(k)$, we may write,

$$\left(\frac{\partial}{\partial t} + 2\nu k^2\right) E^-(k,t) = T^-_{--}(k,t) + T^-_{(--)}(k,t), \tag{6.31}$$

where, from equation (2.51), the transfer terms are given by,

$$T^-_{--}(k,t) = 4\pi k^2 \left\langle u^-_\alpha(\mathbf{k},t)\psi^-_{\alpha--}(\mathbf{k},t)\right\rangle, \tag{6.32}$$

$$T^-_{(--)}(k,t) = 4\pi k^2 \left\langle u^-_\alpha(\mathbf{k},t)\psi^-_{\alpha(--)}(\mathbf{k},t)\right\rangle. \tag{6.33}$$

We may also derive an energy balance equation corresponding to equation (6.30), which can be written as,

$$\left(\frac{\partial}{\partial t} + 2\nu k^2 + 2\delta\nu(k,t)k^2\right) E^-(k,t) = T^-_{--}(k,t). \tag{6.34}$$

A comparison of these two equations can then be used to give an expression for the eddy-viscosity [56], namely,

$$\delta\nu(k) = -\frac{T^-_{(--)}(k,t)}{2k^2E^-(k,t)}. \tag{6.35}$$

Of course, as it stands, equation (6.35) is not actually of any use when performing a LES — the $T^-_{(--)}$ term is an unknown. In order to provide a useful result, closure theories have often been employed in the evaluation of this term. Kraichnan originally used the Test Field Model (TFM) [56] while Chollet and Lesieur [57] applied the Eddy-Damped Quasi-Normal Markovian (EDQNM) theory to obtain a very similar result,

$$\delta\nu(k,t) = \frac{1}{15}\int_{k_c}^{\infty} \theta_{kjj}\left[5E(j) + j\frac{\partial E}{\partial p}\right] \mathrm{d}p, \tag{6.36}$$

where θ_{kjl} is the EDQNM relaxation time for triple correlations. Assuming that k_c lies within an extended range of $k^{-5/3}$ behaviour, Chollet and Lesieur expressed

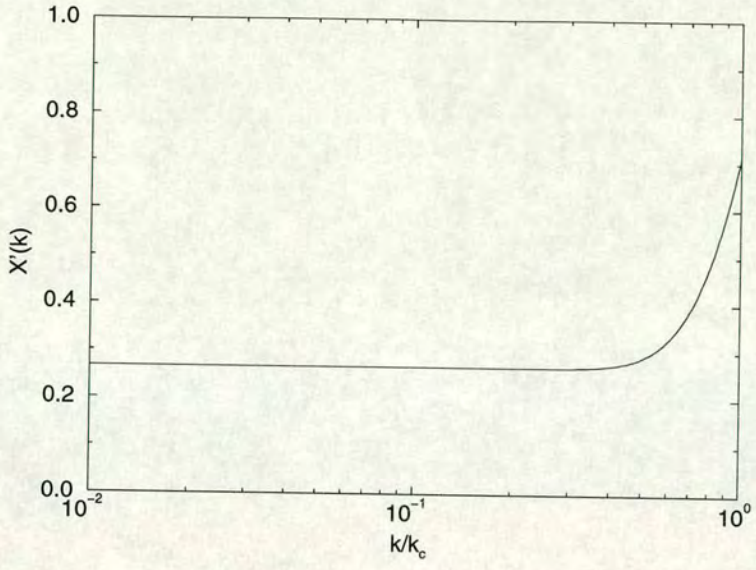

Figure 6.3: The shape of a spectral eddy-viscosity, $X'(k)$, predicted by the EDQNM closure theory.

the eddy-viscosity as,

$$\delta\nu(k,t) = 0.441\alpha^{-3/2}X(k)\left[\frac{E(k_c,t)}{k_c}\right]^{1/2}, \tag{6.37}$$

where $X(k) = 1$ for approximately $k \leq 0.3k_c$ and where it was later stated [58] that,

$$X'(k) = 0.441\alpha^{-3/2}X(k) \approx 0.267 + 9.21e^{-3.03(k_c/k)}, \tag{6.38}$$

may be used as an approximation if we assume that k_c lies within an extended inertial range. The plateau value of 0.267 is obtained by assuming a Kolmogorov constant of $\alpha = 1.4$.

The function, $X'(k)$, is plotted in Figure 6.3 where the basic shape of a spectral eddy-viscosity obtained via the EDQNM closure theory may be seen. It exhibits a plateau up to $k/k_c \approx 0.3$ at which point it rises sharply.

6.3 Spectral LES comparisons

In this section we give two methods by which we may obtain spectral eddy-viscosities for comparison with models such as that obtained from EDQNM, as outlined in the previous section, and discuss the results we obtain.

6.3.1 Computation from DNS data

In equation (6.35), we wrote down an expression for the eddy-viscosity, which we repeat here,

$$\delta\nu(k,t) = -\frac{T^-_{(--)}(k,t)}{2k^2E^-(k,t)}. \tag{6.39}$$

We noted that, when performing a LES, this expression is of no use, since $T^-_{(--)}$ is an unknown quantity. However, as first done by Domaradzki, Metcalfe, Rogallo and Riley [59], we may calculate this term directly through the use of a fully-resolved DNS database. An artificial cutoff wavenumber, $k_c < k_{max}$, is introduced and it then becomes possible to compute the "subgrid" contributions to the nonlinear term directly.

This is done by first zeroing the u^+ modes and then computing the nonlinear term in the usual way (see Section 3.5). By setting $u^+ = 0$, we have ensured that the '$-+$' and '$++$' terms will also be zero and hence this procedure gives us ψ_{--}. We then compute the full nonlinear term, ψ, and generate $\psi_{(--)} = \psi - \psi_{--}$ from which we may calculate $T^-_{(--)}$ and hence the eddy-viscosity, $\delta\nu(k)$.

We have computed such an eddy-viscosity using data taken from our 256^3 DNS ($R_\lambda \approx 190$). The results for a number of cutoff wavenumbers, k_c, are plotted in Figure 6.4. As a general point, we see that the eddy-viscosities increase with decreasing k_c, but for low-k it appears that we may split them into two different cases. For $k_c \leq 24$ the eddy-viscosities exhibit a significant positive plateau at low-k, while for $k_c \geq 32$ the plateau value is approximately zero and even becomes slightly negative. For $k_c \geq 40$, this change of sign occurs at $k/k_c = 0.5$

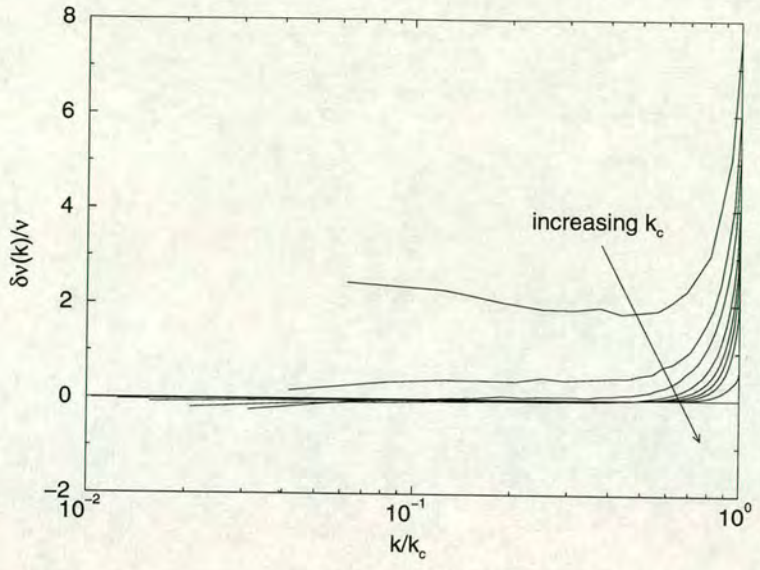

Figure 6.4: Eddy-viscosities computed from DNS data, scaled on the molecular viscosity, for k_c = 16,24,32,48,64,80,96,112.

and this is also seen, if not always commented on, in the data of other authors [60, 61]. This negativity is obviously in disagreement with the theoretical result given earlier and this disparity is almost certainly due to the assumption of an extended inertial range made in the derivation of equation (6.38) [59]. At this rather low Reynolds number we are only just beginning to see inertial range behaviour and even then only at the lowest-wavenumbers. Indeed, the computed eddy-viscosities that most resemble the theoretical prediction are those for which k_c is closest to our inertial range.

The theoretical form given by equation (6.38) also predicts that the eddy-viscosities should scale on $[E(k_c)/k_c]^{1/2}$. However, as may be seen in Figure 6.5, this scaling does not appear to apply in our case. Again, this may be attributed to the low Reynolds number we are considering. Miyauchi *et al* [61] considered DNS data taken from a simulation with $R_\lambda = 37.2$ and suggested an alternative scaling of $[E(k_c)/k_c]^{1/2}\,[k_c/k_d]^2$. This gave a reasonable collapse of their data and we have performed the same scaling on our data, shown in Figure 6.6. If one neglects certain values of k_c (as appears to have been done by Miyauchi *et al*), this does

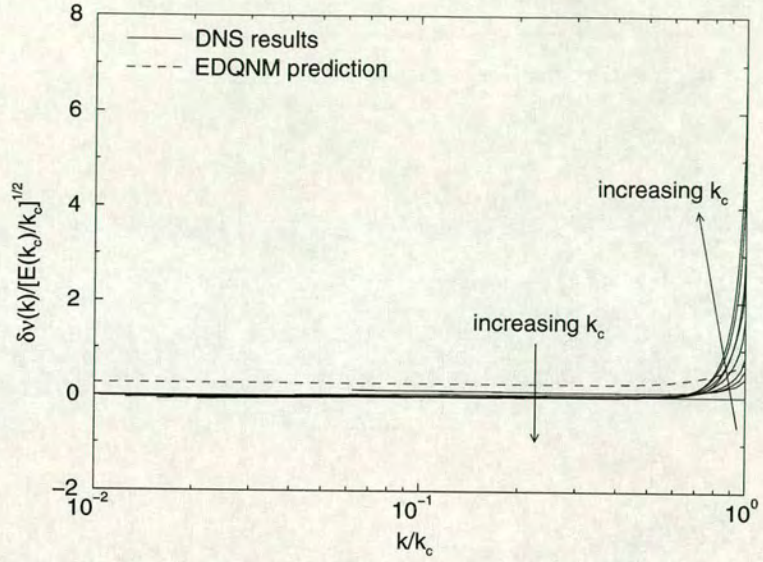

Figure 6.5: Eddy-viscosities computed from DNS data, compared with the EDQNM prediction, scaled on $[E(k_c)/k_c]^{1/2}$. $k_c = 16,24,32,48,64,80,96,112$.

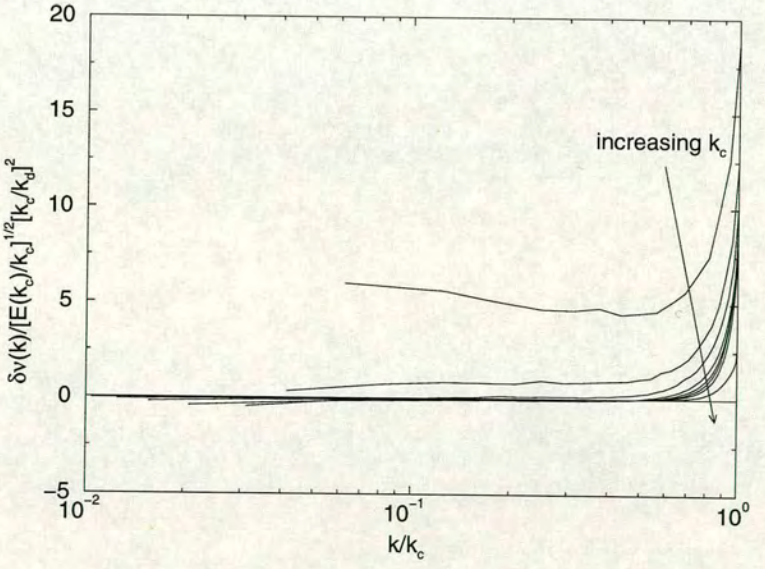

Figure 6.6: Eddy-viscosities computed from DNS data, scaled on $[E(k_c)/k_c]^{1/2}\,[k_c/k_d]^2$. $k_c = 16,24,32,48,64,80,96,112$.

appear to give a better collapse of the data for $40 \leq k_c \leq 96$.

The Reynolds number limitation is the biggest problem with this method of obtaining eddy-viscosities. The sort of Reynolds numbers at which LES is applied are simply not attainable. In an attempt to get around this, several authors, including Lesieur and Rogallo [12], have used LES velocity fields rather than DNS velocity fields as the basis for this computation.

The familiar plateau-cusp picture still emerges from such calculations however, on this technique, Lesieur and Rogallo commented that their calculations "are not fully self-consistent in the sense stressed by a referee, that is, the eddy viscosity computed across $k_c/2$ differs from the one used in the large-eddy simulation with a cutoff at k_c" — their scaled plateau was at a value of ~ 0.15 in contrast to the EDQNM value of 0.267 [12]. However, in a later paper, Métais and Lesieur [60] pointed out that such an eddy-viscosity, obtained by way of a LES, must be corrected in order to account for the additional energy transfers across the actual LES cutoff. With the artificial cutoff denoted by k_c', it may be stated that,

$$\begin{aligned} \text{energy transfer into } k_c' < k < k_c \;\; &= \;\; \text{energy transfer into } k > k_c' \\ &- \;\; \text{energy transfer into } k > k_c. \end{aligned} \tag{6.40}$$

Using equations (6.37) and (6.38) this then gives us that, for some $k \ll k_c'$,

$$P' \left[\frac{E(k_c')}{k_c'}\right]^{1/2} = P \left[\frac{E(k_c')}{k_c'}\right]^{1/2} - P \left[\frac{E(k_c)}{k_c}\right]^{1/2}, \tag{6.41}$$

where P and P' are the actual eddy-viscosity plateau and that computed from the LES data respectively. Rearranging, this becomes,

$$P = \frac{P'}{1 - \left(\frac{E(k_c)k_c'}{E(k_c')k_c}\right)^{1/2}}, \tag{6.42}$$

and if we then further assume that both k_c and k_c' lie within a $k^{-5/3}$ range this then gives,

$$P = \frac{P'}{1 - (k_c'/k_c)^{1/2}}. \tag{6.43}$$

So, for the case of Métais and Lesieur with $k_c' = k_c/2$, this gives,

$$P = 1.66P' = 1.66 \times 0.15 = 0.25, \tag{6.44}$$

in reasonable agreement with the EDQNM prediction of 0.267.

In the next section we give an alternative method by which simulations may be used to obtain high-Reynolds number eddy-viscosities.

6.3.2 Computation from a fixed-spectrum LES

In order to obtain high-Reynolds number eddy-viscosities by way of a simulation, it seems apparent that we need to put something "extra" in. For the LES technique discussed in the previous section, this "extra" is, itself, an eddy-viscosity. Here, we put forward the idea of using a prescribed energy spectrum instead.

We carry out a simulation including only those modes with $k < k_c$. Numerical integration is carried out in the usual way — however, after each such step, we modify the velocity field so that it conforms to some choice of model energy spectrum. Diagrammatically, the procedure is then,

$$E(k,t_n) \overset{\text{integrate}}{\longrightarrow} E'(k,t_{n+1}) \overset{\text{conform to model spectrum}}{\longrightarrow} E(k,t_{n+1}).$$

Since this will give rise to a constant energy spectrum, we shall refer to this technique as a *fixed-spectrum LES*.

When the model spectrum is applied to the velocity field, this will obviously give rise to a change in the energy, and the rate of this change may be approximated by,

$$\left.\frac{\mathrm{d}E(k,t)}{\mathrm{d}t}\right|_{t=t_n}^{\text{(due to application of model spectrum)}} \approx \frac{E(k,t_{n+1}) - E'(k,t_{n+1})}{\delta t}. \tag{6.45}$$

From equation (6.34) it is straightforward to obtain an expression for the rate of change of energy due to an eddy-viscosity,

$$\left.\frac{\mathrm{d}E(k,t)}{\mathrm{d}t}\right|_{t=t_n}^{\text{(due to eddy-viscosity)}} = -2\delta\nu(k,t_n)k^2E(k,t_n). \tag{6.46}$$

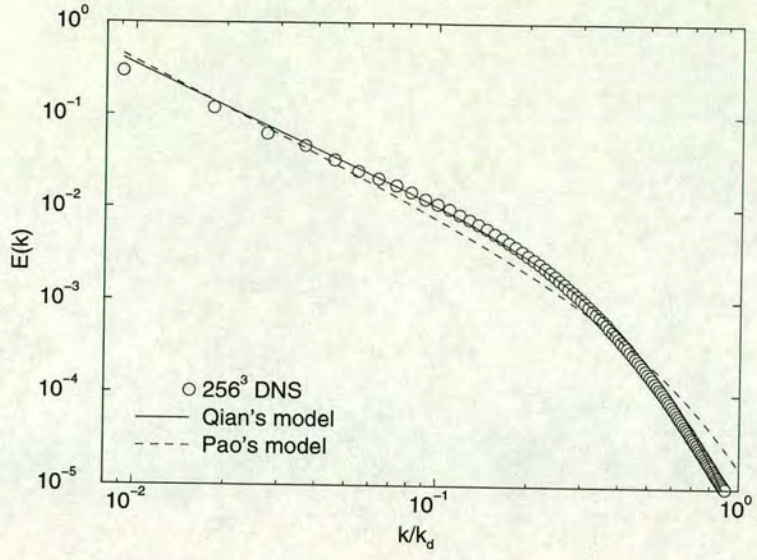

Figure 6.7: The model energy spectra of Qian and Pao compared with that obtained from a 256^3 DNS.

We may then identify the two with each other to give,

$$2\delta\nu(k,t_n)k^2E(k,t_n) \equiv \frac{E'(k,t_{n+1}) - E(k,t_{n+1})}{\delta t}, \tag{6.47}$$

or, rearranging,

$$\delta\nu(k,t_n) \equiv \frac{E'(k,t_{n+1}) - E(k,t_{n+1})}{2k^2\delta t E(k,t_n)}. \tag{6.48}$$

The choice of model spectrum used is obviously an important one, and we must have confidence that it gives a reasonable prediction for $E(k)$ in the simulated region ($k < k_c$). For very high Reynolds numbers one might simply choose a Kolmogorov spectrum, $E(k) = \alpha\varepsilon^{2/3}k^{-5/3}$, or the frequently used model derived by Pao [62]. We have instead chosen the model given by Qian [63] on the basis that it agrees better with our (relatively low Reynolds number) DNS results and that it appears to give a better fit to experimental data at high-k (although this latter point is of no direct importance in this case). Qian's model spectrum takes the form,

$$E(k) = 1.19\varepsilon^{2/3}k^{-5/3}\left(1 + 5.3\,(k/k_d)^{2/3}\right)\exp\left(-5.4\,(k/k_d)^{4/3}\right), \tag{6.49}$$

and is plotted in Figure 6.7. This figure shows how well this model fits our DNS

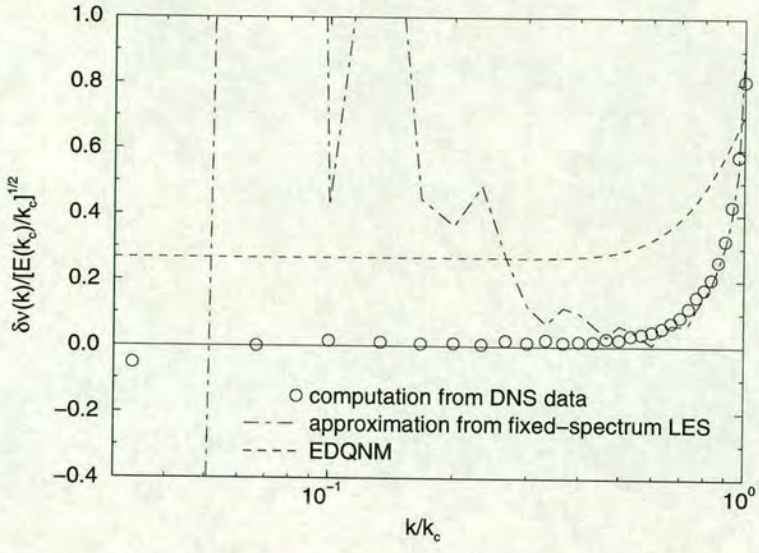

Figure 6.8: The eddy-viscosity obtained by performing a fixed-spectrum LES using the parameters of our 256^3 DNS. This is compared with the prediction made from DNS data and the value obtained by the EDQNM closure.

data — particularly when compared with the Pao's model.

We have performed a fixed-spectrum LES using Qian's model spectrum with $k_c = 30$ and with all other input parameters identical to those used in our 256^3 simulation. The resulting (time-averaged) eddy-viscosity is plotted in Figure 6.8, where it has been scaled on $[E(k_c)/k_c]^{1/2}$ obtained from Qian's model. At high-k, we see excellent agreement between the fixed-spectrum LES result and that obtained empirically from the DNS data. At low-k, the fixed-spectrum LES eddy-viscosity exhibits wild behaviour which may possibly be attributed to a problem with the model spectrum in this region. An alternative cause might be the 'unnatural' constancy of the energy in the system over time, resulting from the application of Qian's spectrum after each integration step — with our forcing we expect to see some fluctuations. However, these problems only appear to manifest themselves in what would be the plateau region and, consequently, we believe that the fixed-spectrum LES technique will still allow us to make good comparisons at higher Reynolds numbers. In future, for the sake of clarity, we shall simply not plot the low-k values.

Run	N	ν	ε_w	k_c/k_d	k_c	k_d	R_λ
I	64	1×10^{-3}	0.149	0.27	30	110	190
II	64	4×10^{-4}	0.150	0.14	30	220	280
III	128	2×10^{-4}	0.274	0.14	60	430	430
IV	64	6×10^{-5}	0.150	0.033	30	913	680
V	64	8×10^{-6}	0.150	0.0072	30	4137	1773
VI	64	1×10^{-6}	0.150	0.0015	30	19680	4871

Table 6.1: Details of fixed-spectrum LES runs performed.

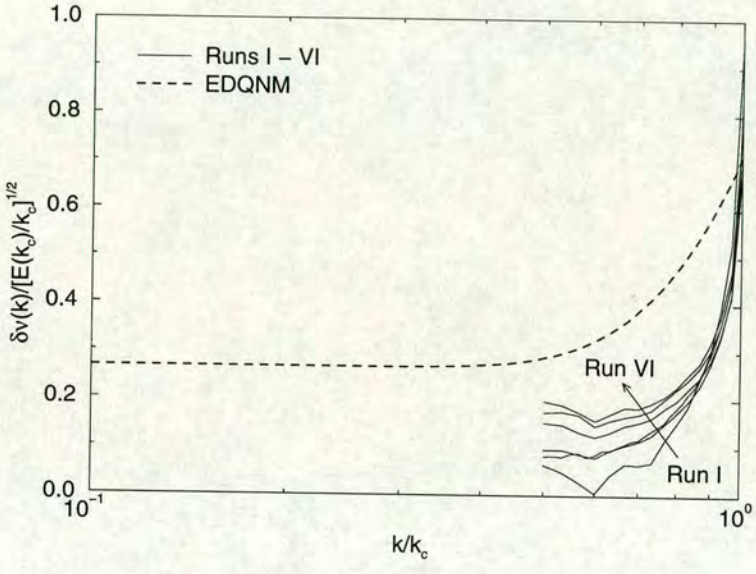

Figure 6.9: Eddy-viscosities obtained using the fixed-spectrum LES technique for a variety of input parameters. These are scaled on $[E(k_c)/k_c]^{1/2}$ and compared with the EDQNM prediction.

We have performed a total of six fixed-spectrum LES runs, detailed in Table 6.1. The values for the Reynolds numbers, R_λ, have been estimated using Qian's model spectrum. The parameters of Run I correspond to our 256^3 simulation and we have already seen the eddy-viscosity obtained via the fixed-spectrum LES method. However, it is plotted again, in Figure 6.9, along with results from the other runs, all scaled on $[E(k_c)/k_c]^{1/2}$.

It is difficult to make any general statements based on only six results. However, the trend seems to be for the (scaled) plateau value to increase with decreasing k_c/k_d. It is very interesting to note that the two runs with identical k_c/k_d (II and III) agree extremely well, in spite of their differing Reynolds numbers. This

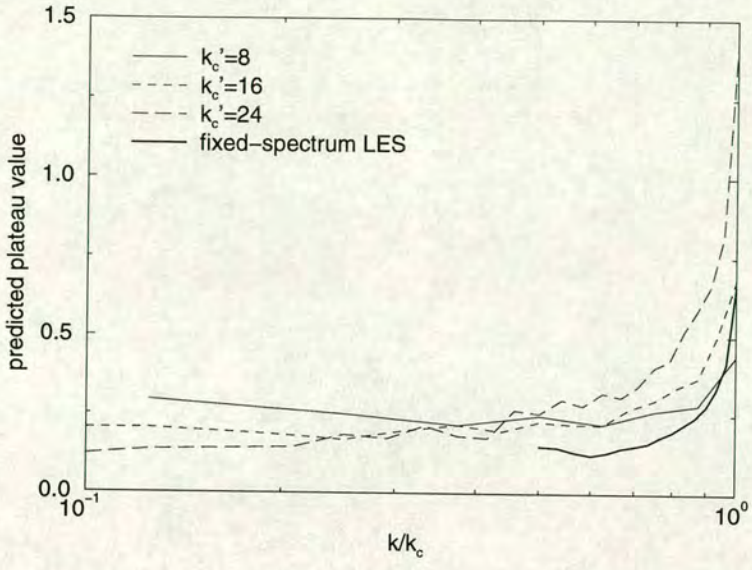

Figure 6.10: Eddy-viscosity plateaus obtained by further partitioning of the LES data from run IV, scaled according to equation (6.41), compared with the fixed-spectrum LES prediction.

suggests that the viscosities may collapse better if the scaling were to involve k_c/k_d in some way. However, it was found that the scaling proposed by Miyauchi *et al* [61] discussed earlier (where the viscosities are scaled on $(k_c/k_d)^2$) did not give a good collapse of the data, and we were unable to find a suitable alternative.

6.3.3 Artificial cutoffs in fixed-spectrum LES data

To complete this work, we have also used the artificial cutoff method outlined in the previous section to obtain values for the scaled eddy-viscosity plateau from fixed-spectrum LES velocity fields taken from runs IV, V and VI. With $k_c = 30$, we chose three values for the artificial cutoff, $k_c' = 8, 16, 24$, and used equation (6.41) to obtain scaled plateau values. These results are shown in Figures 6.10–6.12 and we note that, in these graphs, the values near the cusp are meaningless.

For run IV, the fixed-spectrum LES predicts a scaled plateau value of ~ 0.13 while the rescaled data obtained from the LES velocity field suggests a value of ~ 0.22. We suspect that this disparity is due to the failure of our eddy-viscosities

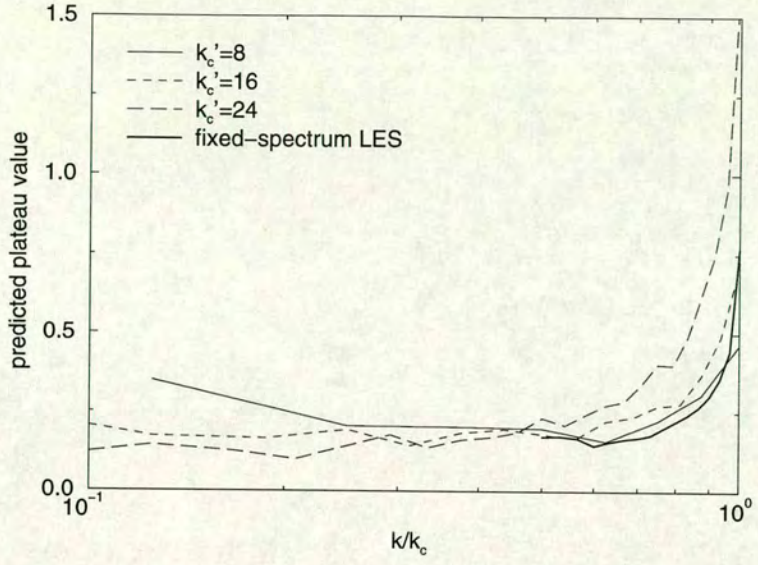

Figure 6.11: Eddy-viscosity plateaus obtained by further partitioning of the LES data from run V, scaled according to equation (6.41), compared with the fixed-spectrum LES prediction.

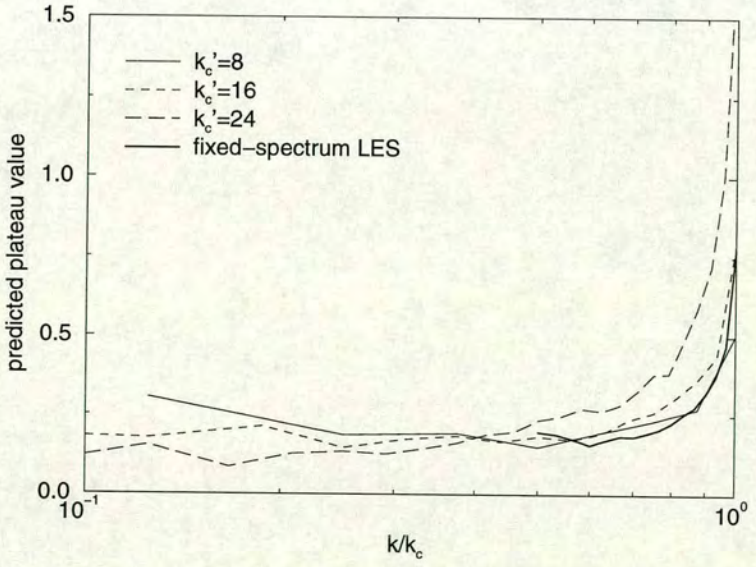

Figure 6.12: Eddy-viscosity plateaus obtained by further partitioning of the LES data from run VI, scaled according to equation (6.41), compared with the fixed-spectrum LES prediction.

to scale on $[E(k_c)/k_c]^{1/2}$, hence invalidating equation (6.41).

For the higher Reynolds number cases explored through runs V and VI, however, there is reasonable agreement between the fixed-spectrum LES predictions and the results obtained from the artificial cutoff method, giving plateau values of ~ 0.16 and ~ 0.18 respectively. This provides us with a useful internal consistency check.

6.4 Conclusions

As noted earlier, Métais and Lesieur [60] used the results from a LES to provide support for the plateau value predicted by EDQNM. For the range of Reynolds numbers considered here ($190 \leq R_\lambda \leq 4871$), our plateau values do not agree with the EDQNM prediction and, indeed, do not scale on $[E(k_c)/k_c]^{1/2}$ (except, perhaps, for our two highest Reynolds number cases). It is worth commenting on these differences.

Firstly, it would appear that as k_c/k_d is decreased, the scaled plateau value begins to approach the EDQNM prediction and it may be that, at Reynolds numbers *significantly* in excess of those considered here, the EDQNM plateau will be reached. In fact, runs V and VI were devised to test this hypothesis, but they still fall short. The simulation used in the work of Lesieur *et al* is detailed in [64], although it is not clear at what sort of Reynolds number it was performed. Secondly, there is also an important distinction from our case in that their simulation was of decaying turbulence, giving rise to a different evolved energy spectrum to the one considered here, and it is quite possible that this gives rise to the disagreement in our results. Thirdly we note that in later work [65] the EDQNM eddy-viscosity was modified to take into account spectra which behave in a manner other than $k^{-5/3}$ at the cutoff. It was found that modifying the eddy-viscosity dynamically, by measuring the gradient of the spectrum at $k = k_c$ as the system evolved, better

results were obtained.

Irrespective of the value of the scaled plateau value, it does appear that (for forced simulations of the type we are considering, at least) the EDQNM cusp is insufficiently sharp and that the plateau should extend to $k/k_c \approx 0.6$ rather than $k/k_c \approx 0.3$ as in the EDQNM case.

We should note, of course, that the validity of our results depend on the accuracy of Qian's model. By introducing artificial cutoffs into the LES data, we have seen that (for high Reynolds number cases) our results appear to be internally consistent. For the purposes of further comparison, we also computed an eddy-viscosity for the parameters of run V by performing a fixed-spectrum LES with a simple Kolmogorov spectrum, $E(k) = \alpha\varepsilon^{2/3}k^{-5/3}$ (where a value of $\alpha = 1.62$ was used, corresponding to the value obtained from our DNS data, and discussed in Section 5.3). The resulting scaled eddy-viscosity plateau was found to be larger than that given by Qian's model, but only by approximately 5%. Furthermore, the eddy-viscosity plateaus obtained by repartitioning the LES data differed by only approximately 1%. It would seem, therefore, that although our fixed-spectrum LES results behave poorly at low-k, they allow us to estimate plateau values and give a good indication of how actual eddy-viscosities should behave as $k \to k_c$.

Chapter 7

Renormalization Group Theory

In Chapter 6, we discussed the concept of a large eddy simulation (LES), in which only the large scales of motion are explicitly simulated. The effect of the small scales are modelled in some way, often through an increment to the viscosity.

In recent years, renormalization group (RG) methods [66] have been studied with a view to providing a systematic reduction of modes, culminating in such a viscosity increment. This technique was first applied to a turbulence-related problem by Rose [67], who considered scalar diffusion within a turbulent flow. At around the same time, Forster, Nelson and Stephen [68, 69] were studying stirred hydrodynamics. This is a problem which is distinct from turbulence, but there are certain similarities, and it may be argued that their work was later extended to the full turbulence problem by Yakhot and Orszag [70, 71]. In this chapter, we shall concentrate on the RG theories of McComb *et al* [6, 7, 8] and a derivative of that theory given by Yang [9].

7.1 Two-field theory

The two-field theory of incompressible-fluid turbulence is given in a series of papers by McComb *et al* [6, 7, 8]. Here we shall give a summary of the important results, and an outline of the method used to obtain them. For full details, the

reader is referred to the papers just cited.

7.1.1 Filtering the velocity field

The essentials of the Fourier-space decomposition have already been given in Sections 6.2.1, 6.2.3 and 6.2.4. For clarity, and to highlight a few minor notation changes, this is repeated here.

We consider a turbulent velocity field, $\mathbf{u}(\mathbf{k}, t)$, defined on the interval $0 \leq k \leq k_0$, where k_0 is defined through the dissipation integral,

$$\varepsilon = \int_0^\infty 2\nu_0 k^2 E(k) \mathrm{d}k \approx \int_0^{k_0} 2\nu_0 k^2 E(k) \mathrm{d}k, \tag{7.1}$$

and where $\nu_0 \equiv \nu$ is the molecular viscosity.

This velocity field represents a system with our usual simplifications of isotropy and homogeneity, and is also statistically stationary in time (i.e. total energy remains constant).

The velocity field is then filtered at a wavenumber, $k = k_1$, using a sharp spectral filter, so that,

$$u_\alpha(\mathbf{k}, t) = \begin{cases} u_\alpha^-(\mathbf{k}, t) & \text{for } 0 \leq k \leq k_1 \\ u_\alpha^+(\mathbf{k}, t) & \text{for } k_1 < k \leq k_0 \end{cases} . \tag{7.2}$$

The partitioning wavenumber, k_1, is defined by,

$$k_1 = (1 - \eta) k_0 = h k_0, \tag{7.3}$$

where the bandwidth parameter, η, satisfies the condition $0 \leq \eta \leq 1$.

The basic idea of RG is quite simple. The aim is to average out, in some sense, the effects of the high-k shell of modes ($k_1 \leq k \leq k_0$), upon the low-k modes. This will result in an increment to the viscosity. Once this has been achieved, the basic variables are rescaled so that the Navier-Stokes equation for $0 \leq k \leq k_1$ looks like the original equation on $0 \leq k \leq k_0$ and the process is repeated, until a fixed point is found.

7.1.2 The conditional average

In order to facilitate the averaging out of the high-k modes, a *conditional average* is introduced. From the full ensemble of turbulent velocity fields, a subensemble is selected so that, in principle, the low-k modes of each member are equal to some reference field, $\mathbf{u}^-(\mathbf{k},t)$. A conditional average, denoted $\langle\cdots\rangle_c$, is then performed over this subensemble and, it is hoped, the high-k modes will be averaged out in some sense, while the low-k modes are unaffected.

However, because the Navier-Stokes equation describes a deterministic process, to prescribe $\mathbf{u}^-$ is to prescribe $\mathbf{u}^+$. To get around this problem, the constraint applied to the low-k modes is weakened somewhat by introducing a degree of uncertainty into the criterion for the conditional average. Now, rather than insisting that the low-k modes of the members of the subensemble are equal to the reference field, they are allowed to differ by a small amount, $\mathbf{\Phi}^-(\mathbf{k},t)$, where

$$\max|\mathbf{\Phi}^-(\mathbf{k},t)| \leq \xi, \tag{7.4}$$

for some bounding value, ξ [7].

By appealing to ideas of chaos, it then seems reasonable to suggest that as k increases beyond k_1, the size of this uncertainty will grow so that the restriction upon the high-k modes is relaxed.

We can now lay out the defining properties of the conditional average as follows,

$$\left\langle u_\alpha^-(\mathbf{k},t)\right\rangle_c = u_\alpha^-(\mathbf{k},t), \tag{7.5}$$

$$\left\langle u_\alpha^-(\mathbf{k},t)u_\beta^-(\mathbf{k}',t)\right\rangle_c = u_\alpha^-(\mathbf{k},t)u_\beta^-(\mathbf{k}',t), \tag{7.6}$$

and so on, for all products of the low-wavenumber modes.

In order to satisfy equation (7.5), $\Phi_\alpha^-(\mathbf{k},t)$ must be chosen so that,

$$\left\langle \Phi_\alpha^-(\mathbf{k},t)\right\rangle_c = 0. \tag{7.7}$$

However, equation (7.6) can only be satisfied as an approximation and requires $\Phi^-_\alpha(\mathbf{k},t)$ to be small, in the sense that,

$$\left\langle \Phi^-_\alpha(\mathbf{k},t)\Phi^-_\beta(\mathbf{k}',t)\right\rangle_c \approx 0, \tag{7.8}$$

so that equation (7.6) should be rewritten as,

$$\left\langle u^-_\alpha(\mathbf{k},t)u^-_\beta(\mathbf{k}',t)\right\rangle_c = u^-_\alpha(\mathbf{k},t)u^-_\beta(\mathbf{k}',t) + \mathrm{O}\left(\left\langle \Phi^-\Phi^-\right\rangle_c\right). \tag{7.9}$$

7.1.3 Application to the Navier-Stokes equation

Using the conditional average, it is possible to generate equations for both the low- and high-k modes. Details are given by McComb and Watt [8], but we just state the results here,

$$\begin{aligned}\left[\frac{\partial}{\partial t}+\nu_0 k^2\right]u^-_\alpha(\mathbf{k},t) &= M^-_{\alpha\beta\gamma}(\mathbf{k})\int \mathrm{d}^3j\Big\{u^-_\beta(\mathbf{j},t)u^-_\gamma(\mathbf{k}-\mathbf{j},t)\\ &+ 2u^-_\beta(\mathbf{j},t)\left\langle u^+_\gamma(\mathbf{k}-\mathbf{j},t)\right\rangle_c + 2\left\langle \Phi^-_\beta(\mathbf{j},t)u^+_\gamma(\mathbf{k}-\mathbf{j},t)\right\rangle_c\\ &+ \left\langle u^+_\beta(\mathbf{j},t)u^+_\gamma(\mathbf{k}-\mathbf{j},t)\right\rangle_c + \mathrm{O}\left(\left\langle \Phi^-\Phi^-\right\rangle_c\right)\Big\}, \qquad (7.10)\\ \left[\frac{\partial}{\partial t}+\nu_0 k^2\right]u^+_\alpha(\mathbf{k},t) &= M^+_{\alpha\beta\gamma}(\mathbf{k})\int \mathrm{d}^3j\Big\{2u^-_\beta(\mathbf{j},t)u^+_\gamma(\mathbf{k}-\mathbf{j},t)\\ &+ u^+_\beta(\mathbf{j},t)u^+_\gamma(\mathbf{k}-\mathbf{j},t)\Big\} + H_\alpha(\mathbf{k},t), \qquad (7.11)\end{aligned}$$

where the exact form of $H_\alpha(\mathbf{k},t)$ is given in [8] where it is also shown that its later contribution is negligible.

7.1.4 Eliminating the first shell

Our objective is to use the high-k mode equation (7.11) to close the low-k mode equation (7.10). In order to do this, we will find that we need to relate the conditional averages to full ensemble averages. It is at this point that we introduce the second field from which this theory takes its name by writing down the *exact* decomposition,

$$u^+_\alpha(\mathbf{k},t) = v^+_\alpha(\mathbf{k},t) + \Delta^+_\alpha(\mathbf{k},t), \tag{7.12}$$

where $\mathbf{v}^+$ is any other realization taken from the full ensemble and hence $\boldsymbol{\Delta}^+$ may be regarded as the phase difference between the two realizations. We then apply the conditional average to equation (7.12) to give,

$$\left\langle u_\alpha^+(\mathbf{k},t)\right\rangle_c = \left\langle v_\alpha^+(\mathbf{k},t)\right\rangle + \left\langle \Delta_\alpha^+(\mathbf{k},t)\right\rangle_c , \tag{7.13}$$

where the step, $\langle v_\alpha^+(\mathbf{k},t)\rangle_c = \langle v_\alpha^+(\mathbf{k},t)\rangle$, is given extensive justification in [7] but amounts to an assumption that the set of $\mathbf{v}^+$ fields form a *representative* subensemble (i.e. a subensemble with the same statistics as the full ensemble).

We have already noted that as k increases beyond k_1, we expect the uncertainty in the subensemble to grow. Accordingly, if the bandwidth parameter, η, is not too small, we may expect that $\mathbf{u}^+(\mathbf{k}_0,t)$ is independent of $\mathbf{u}^+(\mathbf{k}_1,t)$ so that we may write,

$$\left\langle \mathbf{u}^+(\mathbf{k}_0,t)\right\rangle_c = \left\langle \mathbf{u}^+(\mathbf{k}_0,t)\right\rangle = \left\langle \mathbf{v}^+(\mathbf{k}_0,t)\right\rangle . \tag{7.14}$$

In order to provide a relationship between $\mathbf{u}^+$ and $\mathbf{v}^+$, we now take $\mathbf{v}^+$ to be a first-order truncation of the Taylor-series expansion of $\mathbf{u}^+$ about $\mathbf{k}=\mathbf{k}_0$,

$$v_\alpha^+(\mathbf{k},t) = u_\alpha^+(\mathbf{k},t) + (\mathbf{k}-\mathbf{k}_0)\cdot\nabla_k\, u_\alpha^+(\mathbf{k},t)\Big|_{k=k_0} , \tag{7.15}$$

so that we may write,

$$u_\alpha^+(\mathbf{k},t) = v_\alpha^+(\mathbf{k},t) + \mathrm{O}(\eta^2). \tag{7.16}$$

The conclusion that terms of order η^2 have been neglected is due to the fact that the maximum value of $|\mathbf{k}-\mathbf{k}_0|$ is ηk_0. A comparison of equations (7.12) and (7.16) then gives,

$$\left\langle \boldsymbol{\Delta}^+(\mathbf{k},t)\right\rangle_c = \mathrm{O}(\eta^2). \tag{7.17}$$

It is apparent that this sequence of steps has imposed both upper and lower bounds on η. Firstly, η must be large enough so that we may assume that $\mathbf{u}^+(\mathbf{k}_0,t)$ is independent of $\mathbf{u}^+(\mathbf{k}_1,t)$ but, secondly, it must be small enough so that terms of order η^2 may be neglected.

Application of this relationship to the low-k equation (7.10) gives,

$$\left[\frac{\partial}{\partial t}+\nu_0 k^2\right] u_\alpha^-(\mathbf{k},t) = M^-_{\alpha\beta\gamma}(\mathbf{k})\int \mathrm{d}^3 j \Big\{ u_\beta^-(\mathbf{j},t)u_\gamma^-(\mathbf{k}-\mathbf{j},t) + \left\langle u_\beta^+(\mathbf{j},t)u_\gamma^+(\mathbf{k}-\mathbf{j},t)\right\rangle_c + \mathrm{O}\left(\left\langle \mathbf{\Delta}^+\right\rangle_c, \left\langle \Phi^-\Phi^-\right\rangle_c, \left\langle \Phi^-\Delta^+\right\rangle_c\right)\Big\}, \tag{7.18}$$

where the neglected terms are assumed to be $\mathrm{O}(\eta^2)$. Equation (7.11) is then used to obtain an expression for the term involving $\mathbf{u}^+$ modes [8],

$$\begin{aligned} & M^-_{\alpha\beta\gamma}(\mathbf{k})\int \mathrm{d}^3 j \left\langle u_\beta^+(\mathbf{j},t)u_\gamma^+(\mathbf{k}-\mathbf{j},t)\right\rangle_c \\ &= 2M^-_{\alpha\beta\gamma}(\mathbf{k})\int \mathrm{d}^3 j \int_{-\infty}^{t} \mathrm{d}t' \exp\left[-(\nu_0 j^2+\nu_0|\mathbf{k}-\mathbf{j}|^2)(t-t')\right] M^+_{\beta\delta\epsilon}(\mathbf{j}) \\ &\times \int \mathrm{d}^3 p \Big\{ 2u_\delta^-(\mathbf{p},t')\left\langle v_\epsilon^+(\mathbf{j}-\mathbf{p},t')v_\gamma^+(\mathbf{k}-\mathbf{j},t')\right\rangle \\ &+ \left\langle u_\delta^+(\mathbf{p},t')u_\epsilon^+(\mathbf{j}-\mathbf{p},t')u_\gamma^+(\mathbf{k}-\mathbf{j},t')\right\rangle_c \Big\} + \mathrm{O}(\eta^2). \end{aligned} \tag{7.19}$$

Next we assume, on the grounds that the u^- will generally be larger in magnitude than the u^+, that the $u^+u^+u^+$ term may be neglected in comparison to the $u^-u^+u^+$ term to give,

$$\begin{aligned} & M^-_{\alpha\beta\gamma}(\mathbf{k})\int \mathrm{d}^3 j \left\langle u_\beta^+(\mathbf{j},t)u_\gamma^+(\mathbf{k}-\mathbf{j},t)\right\rangle_c \\ &= 4M^-_{\alpha\beta\gamma}(\mathbf{k})\int \mathrm{d}^3 j \int_{-\infty}^{t} \mathrm{d}t' \exp\left[-\omega_2(j,l)(t-t')\right] M^+_{\beta\delta\epsilon}(\mathbf{j}) \\ &\times \int \mathrm{d}^3 p\; 2u_\delta^-(\mathbf{p},t')\left\langle v_\epsilon^+(\mathbf{j}-\mathbf{p},t')v_\gamma^+(\mathbf{k}-\mathbf{j},t')\right\rangle, \end{aligned} \tag{7.20}$$

where $\omega_2(j,l)=\nu_0(j^2+l^2)$ and $l=|\mathbf{k}-\mathbf{j}|$.

Now, because $\mathbf{v}^+$ is a statistically stationary, homogeneous and isotropic field, we may write,

$$\left\langle v_\epsilon^+(\mathbf{j}-\mathbf{p},t')v_\gamma^+(\mathbf{k}-\mathbf{j},t')\right\rangle = Q_v^+(|\mathbf{k}-\mathbf{j}|)D_{\epsilon\gamma}(\mathbf{k}-\mathbf{j})\delta(\mathbf{k}-\mathbf{p}), \tag{7.21}$$

in analogy with equation (2.37). Substituting this into equation (7.20) then gives,

$$\begin{aligned} & M^-_{\alpha\beta\gamma}(\mathbf{k})\int \mathrm{d}^3 j \left\langle u_\beta^+(\mathbf{j},t)u_\gamma^+(\mathbf{k}-\mathbf{j},t)\right\rangle_c \\ &= 4M^-_{\alpha\beta\gamma}(\mathbf{k})\int \mathrm{d}^3 j M^+_{\beta\delta\epsilon}(\mathbf{j})D_{\epsilon\gamma}(\mathbf{k}-\mathbf{j})Q_v^+(|\mathbf{k}-\mathbf{j}|) \\ &\times \int_0^\infty \mathrm{d}\tau\; \exp\left[-\omega_2(j,l)\tau\right] u_\delta^-(\mathbf{k},t-\tau). \end{aligned} \tag{7.22}$$

The next assumption made is that the $\mathbf{u}^-$ modes are slowly varying on the time scales of the $\mathbf{u}^+$ modes. This allows us to represent $\mathbf{u}^-(\mathbf{k}, t-\tau)$ as a Taylor series in τ, about $\tau = 0$, truncated at zero order, i.e.,

$$\begin{aligned}\int_0^\infty \mathrm{d}\tau\ \exp\left[-\omega_2(j,l)\tau\right] u_\delta^-(\mathbf{k}, t-\tau) &= \int_0^\infty \mathrm{d}\tau\ \exp\left[-\omega_2(j,l)\tau\right]\left[u_\delta^-(\mathbf{k},t) + \mathrm{O}(\tau)\right] \\ &\approx u_\delta^-(\mathbf{k},t)\int_0^\infty \mathrm{d}\tau\ \exp\left[-\omega_2(j,l)\tau\right]. \quad (7.23)\end{aligned}$$

The integral with respect to τ is simple to solve, and the result is then substituted into equation (7.22) to give,

$$\begin{aligned}& M_{\alpha\beta\gamma}^-(\mathbf{k})\int \mathrm{d}^3 j \left\langle u_\beta^+(\mathbf{j},t) u_\gamma^+(\mathbf{k}-\mathbf{j},t)\right\rangle_c \\ &= 4M_{\alpha\beta\gamma}^-(\mathbf{k})\int \mathrm{d}^3 j \frac{1}{\nu_0 j^2 + \nu_0|\mathbf{k}-\mathbf{j}|^2} M_{\beta\delta\epsilon}^+(\mathbf{j}) \\ &\times\ D_{\epsilon\gamma}(\mathbf{k}-\mathbf{j}) Q_v^+(|\mathbf{k}-\mathbf{j}|) u_\delta^-(\mathbf{k},t). \quad (7.24)\end{aligned}$$

7.1.5 The viscosity increment

The most important feature of the result given in equation (7.24) is that it is linear in $\mathbf{u}^-$ and hence may be interpreted as a viscosity increment, so that the low-k equation becomes,

$$\left[\frac{\partial}{\partial t} + \nu_0 k^2 + \delta\nu_0(k)k^2\right] u_\alpha^-(\mathbf{k},t) = M_{\alpha\beta\gamma}^-(\mathbf{k})\int \mathrm{d}^3 j\ u_\beta^-(\mathbf{j},t) u_\gamma^-(\mathbf{k}-\mathbf{j},t). \quad (7.25)$$

The viscosity increment is given by [8, 72],

$$\delta\nu_0(k) = \frac{1}{k^2}\int \mathrm{d}^3 j \frac{L(\mathbf{k},\mathbf{j}) Q_v^+(|\mathbf{k}-\mathbf{j})}{\nu_0 j^2 + \nu_0|\mathbf{k}-\mathbf{j}|^2}, \quad (7.26)$$

with,

$$0 \le k \le k_1;\ k_1 < j, |\mathbf{k}-\mathbf{j}| \le k_0, \quad (7.27)$$

and where,

$$L(\mathbf{k},\mathbf{j}) = -2M_{\rho\beta\gamma}(\mathbf{k}) M_{\beta\rho\delta}(\mathbf{j}) D_{\delta\gamma}(\mathbf{k}-\mathbf{j}). \quad (7.28)$$

In the same way that the $\mathbf{v}^+$ field was defined in terms of a Taylor-series expansion, so too is Q_v^+. The expression for the viscosity increment then becomes,

$$\delta\nu_0(k) = \frac{1}{k^2}\int \mathrm{d}^3 j \frac{L(\mathbf{k},\mathbf{j})\left\{Q(l)|_{l=k_0} + (l-k_0)\frac{\partial Q(l)}{\partial l}\Big|_{l=k_0}\right\}}{\nu_0 j^2 + \nu_0|\mathbf{k}-\mathbf{j}|^2}. \quad (7.29)$$

Accordingly, the total effective viscosity is given by,

$$\nu_1(k) = \nu_0 + \delta\nu_0(k). \tag{7.30}$$

7.1.6 The iterative process

Once the first shell of modes has been eliminated, it is a relatively simple matter to repeat the process to eliminate subsequent shells. This is carried out as follows:

1. Set $\mathbf{u}^- \equiv \mathbf{u}$ in the equation for the explicit modes. This gives a Navier-Stokes equation with viscosity, $\nu_1(k)$, defined on the interval $0 \leq k \leq k_1$.

2. Perform another decomposition, this time at $k = k_2 = hk_1$. This gives $\mathbf{u}^-$ on $0 \leq k \leq k_2$ and $\mathbf{u}^+$ on $k_2 \leq k \leq k_1$.

3. Repeat the elimination process to eliminate modes in the band $k_2 \leq k \leq k_1$.

The nth shell is defined in terms of its cutoff wavenumber,

$$k_n = h^n k_0, \tag{7.31}$$

and the total effective viscosity is,

$$\nu_{n+1}(k) = \nu_n(k) + \delta\nu_n(k), \tag{7.32}$$

where the viscosity increment is,

$$\delta\nu_n(k) = \frac{1}{k^2}\int \mathrm{d}^3 j \frac{L(\mathbf{k},\mathbf{j})\left\{ Q(l)|_{l=k_n} + (l-k_n)\frac{\partial Q(l)}{\partial l}\Big|_{l=k_n}\right\}}{\nu_n(j)j^2 + \nu_n(|\mathbf{k}-\mathbf{j}|)|\mathbf{k}-\mathbf{j}|^2}. \tag{7.33}$$

7.1.7 Scaling and the fixed point

In practice, the iterative calculation is performed in terms of a scaled total effective viscosity, ν_n^*, which is related to the unscaled effective viscosity by,

$$\nu_n(k) = \alpha^{1/2}\varepsilon^{1/3}k_n^{-4/3}\nu_n^*(k/k_n). \tag{7.34}$$

The iterative procedure is repeated until a fixed point is reached — this is taken to be the point at which,

$$\nu^*_{n+1}(k/k_{n+1}) = \nu^*_n(k/k_n) \equiv \nu^*_N(k/k_N), \text{ say,} \tag{7.35}$$

and where, for the purposes of a large eddy simulation, one might identify $k_c \equiv k_N$ and $\delta\nu(k) \equiv \delta\nu_N(k)$. This scaled effective viscosity is found to be independent of the choice of ν^*_0. In principle, one would hope that it would be independent of the bandwidth, but this does not turn out to be the case. The problem of choosing a value of η is touched upon in Section 7.3.

7.2 Perturbative two-field theory

The perturbative two-field theory of Yang [9] is described as a "systematic re-derivation of the results of the two-field theory." As such, it naturally gives rise to the same result for the eddy-viscosity and we shall not give a full derivation here. Instead, we outline the central difference between this theory and that given earlier.

7.2.1 The model field

The perturbative two-field theory introduces a model field which aims to be defined in such a way that the conditional average of the high-k modes can be evaluated exactly.

In order to do this, it is proposed that a field, $\mathbf{v}$, is chosen so that its low-k modes are given by some member of the turbulent ensemble (distinct from $\mathbf{u}$). The high-k modes are defined by way of a new dynamical equation,

$$\begin{aligned}\left[\frac{\partial}{\partial t} + \nu_0 k^2\right] v^+_\alpha(\mathbf{k},t) \\ = \; M^+_{\alpha\beta\gamma}(\mathbf{k}) \int \mathrm{d}^3 j \; v^-_\beta(\mathbf{j},t) v^-_\gamma(\mathbf{k}-\mathbf{j},t) + v^+_\beta(\mathbf{j},t) v^+_\gamma(\mathbf{k}-\mathbf{j},t),\end{aligned} \tag{7.36}$$

which is just the Navier-Stokes equation for the high-k modes, in the absence of the cross term $(v^- v^+)$.

Two important assumptions are then made. Firstly it is hoped that the omitted term will not play a major role in the transfer of energy. To justify this, the idea of turbulent energy transfer as a local (in wavenumber) cascade is called upon.

Secondly, it is assumed that the absence of the cross term will remove the coupling between the $\mathbf{v}^-$ and $\mathbf{v}^+$ fields so that although $\mathbf{v}^-$ is fixed, the $\mathbf{v}^+$ field is completely unconstrained.

The proposed properties of the $\mathbf{v}$ field under the conditional average are then given as,

$$\left\langle \mathbf{v}^- \right\rangle_c = \mathbf{v}^-, \tag{7.37}$$

$$\left\langle \mathbf{v}^- \mathbf{v}^- \right\rangle_c = \mathbf{v}^- \mathbf{v}^-, \tag{7.38}$$

since the low-k modes of $\mathbf{v}$ are held constant, and,

$$\left\langle \mathbf{v}^+ \right\rangle_c = \left\langle \mathbf{v}^+ \right\rangle = 0, \tag{7.39}$$

$$\left\langle \mathbf{v}^+ \mathbf{v}^+ \right\rangle_c = \left\langle \mathbf{v}^+ \mathbf{v}^+ \right\rangle, \tag{7.40}$$

due to the lack of coupling between the high- and low-k modes.

In the analysis which then follows, the $\mathbf{v}^+$ field is used as a zero-order model for $\mathbf{u}^+$ which allows for the necessary connection between the conditional and ensemble averages to be made. As stated at the start of this section, this analysis will not be pursued here and the interested reader is directed to [9].

7.3 The Kolmogorov constant

The total effective viscosity, computed using either of the methods outlined in the previous sections, may be used to obtain a value for the Kolmogorov constant,

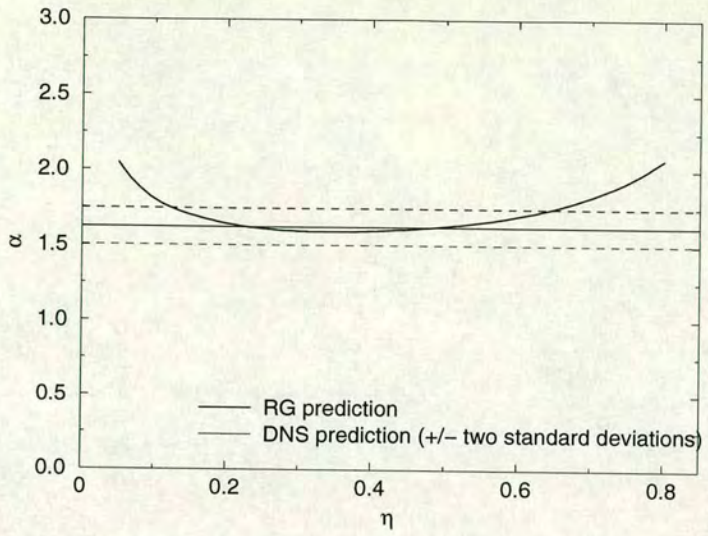

Figure 7.1: The Kolmogorov constant obtained from RG calculations, as a function of the bandwidth parameter, η. Also plotted is the value obtained from our 256^3 DNS, with error bounds.

α, as described in [8]. The results of such a calculation are given in Figure 7.1, where α is plotted as a function of the bandwidth parameter, η.

As was noted in Section 7.1.4, the bandwidth parameter must be small enough so that terms in η^2 may be neglected, yet large enough so that the $\mathbf{u}^+$ field experiences sufficient freedom. These bounds may be quantified by comparing the value for α obtained from the RG with that obtained empirically from our 256^3 DNS. It may be seen that there is good agreement for $0.25 \leq \eta \leq 0.45$ for which $\alpha = 1.60 \pm 0.01$ and this is generally taken to be the valid range of η.

This analytic evaluation of the Kolmogorov constant is arguably the two field theory's greatest triumph.

Chapter 8

Partitioning the Nonlinear Term

Following the introduction of a cutoff wavenumber as the first step in formulating a spectral LES, the nonlinear term may be divided into three partitions. This chapter presents a study of the relative importance of each of these partitions and we shall also see how the results may be tied in with more general studies into the validity of the eddy-viscosity concept and of interscale dynamics.

8.1 The partitions of the nonlinear term

In Section 6.2.3 we introduced some shorthand notation to ease the discussion of the partitions of the nonlinear term in the Navier-Stokes equation. This notation will be extended and used extensively throughout this chapter. Recall that ψ is used to denote the nonlinear term and that subscript symbols (ψ_{--},ψ_{-+},ψ_{++}) indicate filtering on the variables within the nonlinear term. This idea is illustrated schematically in Figure 8.1.

This chapter begins with a discussion of the *integrated partitions* which we shall denote by $\phi(\mathbf{k})$. We shall define these by first considering the forced Navier-Stokes equation,

$$\left[\frac{\partial}{\partial t} + \nu k^2\right] u_\alpha(\mathbf{k},t) = \psi_{\alpha--}(\mathbf{k},t) + \psi_{\alpha-+}(\mathbf{k},t) + \psi_{\alpha++}(\mathbf{k},t) + f_\alpha(\mathbf{k},t). \quad (8.1)$$

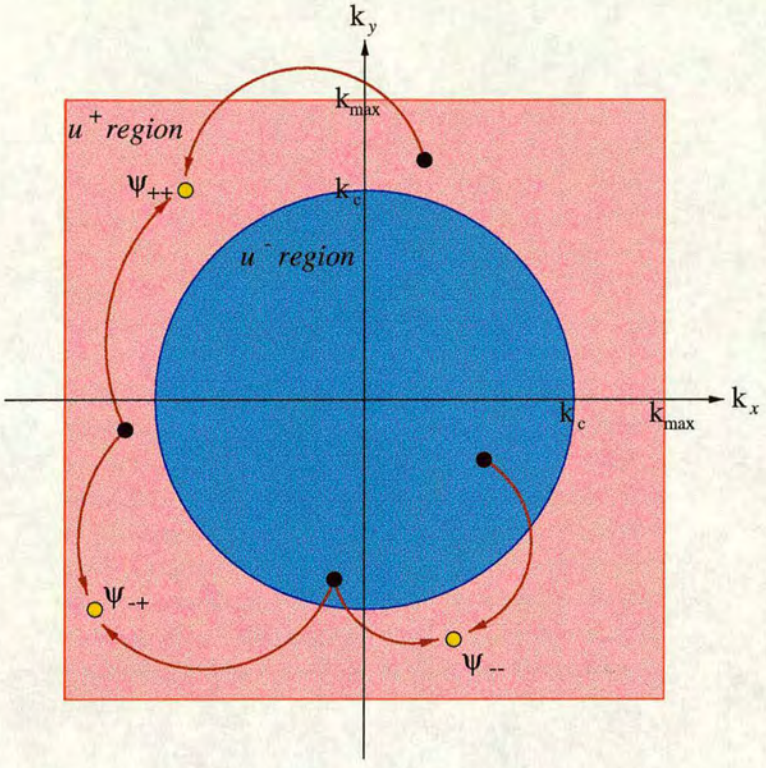

Figure 8.1: Illustration of the different regions present in a velocity field, looking at a slice through the origin. The red square represents the whole computational domain, while the inner blue circle represents the partitioning wavenumber. The yellow dots demonstrate contributions to each of the partitions of the nonlinear term.

The operator on the LHS may then be inverted using an integrating factor to obtain,

$$\begin{aligned} u_\alpha(\mathbf{k},t) &= \int_{-\infty}^{t} \mathrm{d}t' e^{-\nu k^2 (t-t')} \Big\{ \psi_{\alpha--}(\mathbf{k},t') + \psi_{\alpha-+}(\mathbf{k},t') + \psi_{\alpha++}(\mathbf{k},t') + f_\alpha(\mathbf{k},t') \Big\} \\ &= \phi_{\alpha--}(\mathbf{k},t) + \phi_{\alpha-+}(\mathbf{k},t) + \phi_{\alpha++}(\mathbf{k},t) + \mathcal{F}_\alpha(\mathbf{k},t), \text{ say.} \end{aligned} \tag{8.2}$$

Furthermore, we define,

$$\phi_\alpha(\mathbf{k},t) = \phi_{\alpha--}(\mathbf{k},t) + \phi_{\alpha-+}(\mathbf{k},t) + \phi_{\alpha++}(\mathbf{k},t). \tag{8.3}$$

Direct numerical simulation has been used as a tool to explore the properties of both the instantaneous (ψ) and integrated (ϕ) fields.

8.2 Computing the ψ- and ϕ-fields

In Section 3.5, it was explained how the total nonlinear term, ψ, is computed with the aid of several FFTs. As noted in Section 6.3.1, it is straightforward to adapt this procedure to calculate the partitions of the nonlinear term. First, ψ is computed in the usual way. Then the u^+ and u^- fields are zeroed in turn and the procedure is repeated to give ψ_{--} and ψ_{++} respectively. The final partition, ψ_{-+}, is calculated simply by subtracting ψ_{--} and ψ_{++} from the total nonlinear term.

There is however, one extra subtlety in the computation of the ψ-fields, due to the presence of aliasing errors. In the DNS code, partial anti-aliasing is achieved by performing a random shift at each time step (Section 3.7.2). For these calculations, in the absence of time-integration, we achieve partial dealiasing by truncating the velocity field in Fourier space for $k > (2\sqrt{2}/3)k_{max}$ (Section 3.7.1).

Each of the ψ-fields can be calculated from a single velocity field at any given instant in time. The ϕ-fields, on the other hand, are defined in terms of time integrals and consequently must be evolved alongside the velocity field. These integrals have been computed using a simple and inexpensive trapezoidal method [33], but the calculation of the integrands (i.e. the partitions of ψ) at *every* time step leads to a code that is roughly three times as computationally expensive as a standard DNS.

Further problems arise out of the necessity to choose suitable initial ϕ-fields with which to begin the computation. The choice has been made to begin by zeroing each of the ϕ-fields for all values of $\mathbf{k}$, in the expectation that after a sufficient number of time steps the initial conditions will have been forgotten. To this end, the modified DNS code has been run until the four ϕ-fields have reached a statistically stationary state, and we assume that this indicates convergence to their true values.

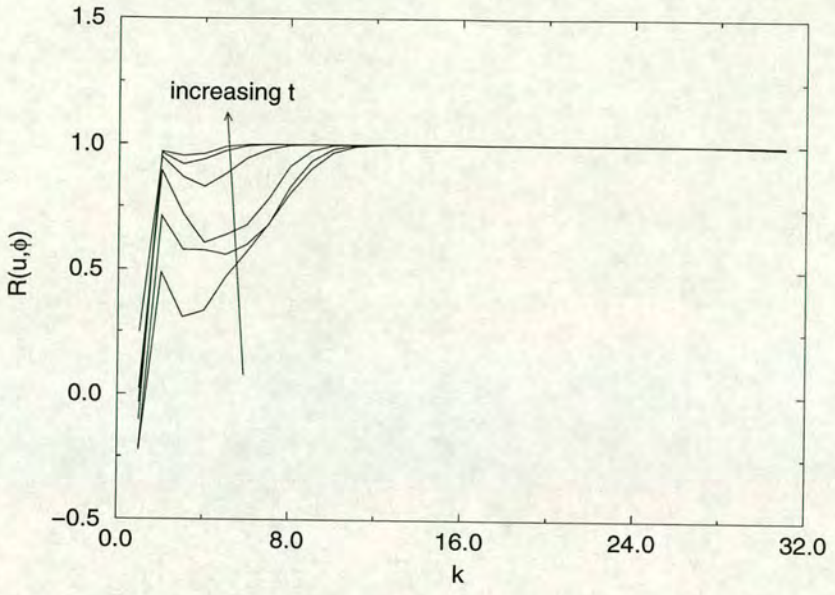

Figure 8.2: Correlation between u and the evolving ϕ computed on a 64^3 grid, with the initial ϕ-fields zeroed. Times shown are $t/\tau_E = 0.5,\ 1.0,\ 2.0,\ 4.0,\ 6.0,\ 8.0$ where τ_E is the evolved eddy turnover time. Forcing is applied for $k \leq 1.5$ and hence we do not expect the two fields to be correlated in the first shell.

Further evidence may be provided by noting the fact that our forcing is limited to the low wavenumber region, $k < k_f$, so that we have from equation (8.2),

$$u = \phi \text{ for } k_f < k < k_{max}. \tag{8.4}$$

We performed a calculation on the velocity field at the final time step and noted that $\langle |\mathbf{u}|^2 \rangle \approx \langle |\phi|^2 \rangle$ in this region of wavenumber space, but as an additional test the correlation between the two fields was computed. The general correlation between two zero-mean fields, a and b, is defined by,

$$R(a, b; k) = \frac{\langle a_\alpha(\mathbf{k}) b_\alpha(-\mathbf{k}) \rangle}{\langle |\mathbf{a}(\mathbf{k})|^2 \rangle^{1/2} \langle |\mathbf{b}(\mathbf{k})|^2 \rangle^{1/2}} \tag{8.5}$$

and $R(u, \phi; k)$ is plotted in Figure 8.2 for six different time steps.

By the final time step, the level of correlation is excellent for $k > 5$ and good for $k > 1$. The increasing quality of correlation with increasing k is to be expected as a consequence of the idea that higher wavenumbers evolve faster than lower wavenumbers — something which is borne out by looking at the correlations

computed at earlier time steps. The deviation in the first shell is anticipated as this is where the forcing term has its effect and is outside the valid range of equation (8.4).

Finally, it is worth noting that in order to compute ϕ-fields for different cutoff wavenumbers, k_c, the entire DNS must be performed again from initial conditions up to the fully evolved state. This has limited the extent to which the ϕ-fields have been examined — only two different partitioning wavenumbers, k_c, have been considered, and the simulation runs have been restricted to a resolution of 64^3 grid points. Such limitations do *not* apply to the ψ-fields.

8.3 Results at low Reynolds number

The results in this section correspond to data taken from a 64^3 simulation with $R_\lambda \approx 70$. We begin by considering the *integrated* nonlinear term, ϕ. We compute the correlation, as given by equation (8.5), between ϕ and its partitions, and also a measure of their relative magnitudes, $r(k)$, given by,

$$r(a,b;k) = \frac{\langle |\mathbf{b}(\mathbf{k})|^2 \rangle}{\langle |\mathbf{a}(\mathbf{k})|^2 \rangle}. \tag{8.6}$$

Results are plotted in Figures 8.3 and 8.4 for $k_c = 16$ and 24, with both functions plotted against k/k_c and we first note that, once scaled in this way, the precise choice of k_c appears to have little effect on the shape of the graphs.

The general trends are easy to spot — both $R(k)$ and $r(k)$ show that, prior to the cutoff, ϕ_{--} makes the most significant contribution to the total while this drops off after the cutoff and ϕ_{-+} takes its place. The ϕ_{++} partition is both small and poorly correlated with ϕ over the entire range of wavenumber space considered.

In the first few shells ($k < 0.5k_c$) of $R(k)$, plotted in Figure 8.3, we observe some erratic behaviour associated with ϕ_{-+} and ϕ_{++}. It is believed that this may be due to the proximity of the forcing — in any case, the small magnitude

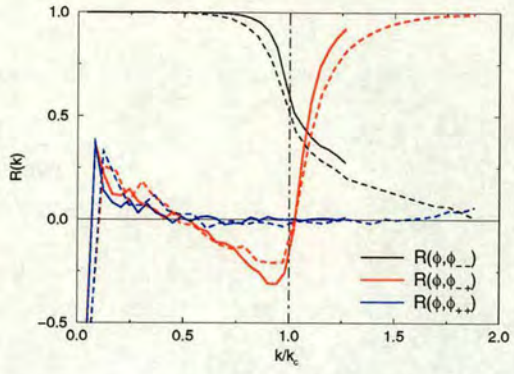

Figure 8.3: Correlation between ϕ and its partitions, solid line: $k_c = 24$; dashed line: $k_c = 16$. The vertical dot-dashed line indicates $k = k_c$.

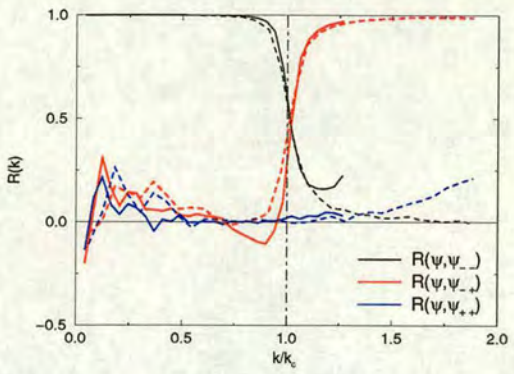

Figure 8.5: Correlation between ψ and its partitions, solid line: $k_c = 24$; dashed line: $k_c = 16$. The vertical dot-dashed line indicates $k = k_c$.

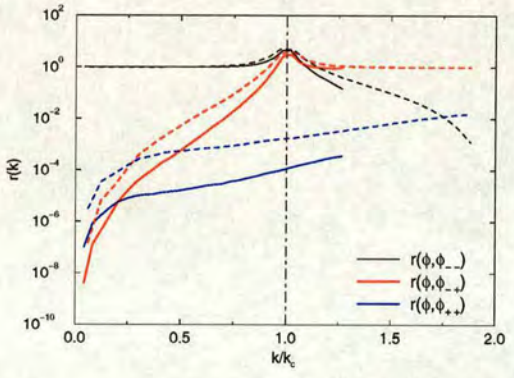

Figure 8.4: Magnitude comparison between ϕ and its partitions, solid line: $k_c = 24$; dashed line: $k_c = 16$. The vertical dot-dashed line indicates $k = k_c$.

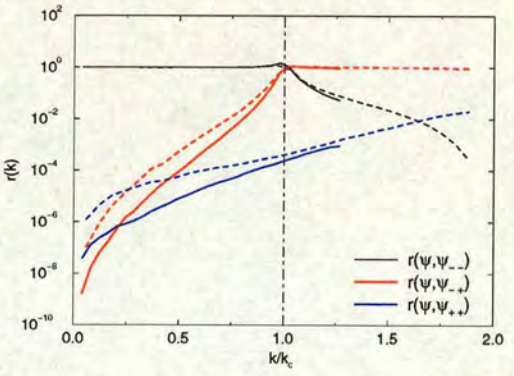

Figure 8.6: Magnitude comparison between ψ and its partitions, solid line: $k_c = 24$; dashed line: $k_c = 16$. The vertical dot-dashed line indicates $k = k_c$.

of these partitions in this region of k-space means that the erratic nature of the correlations should not affect the significance of these terms.

We shall not concern ourselves any further with the integrated nonlinear term, ϕ. As noted earlier, the computational effort involved in the computation of its partitions is enormous. By moving on now to consider the *instantaneous* nonlinear term, ψ, we gain instantly the flexibility to consider not only a wider range of wavenumbers but also, and more importantly, to examine higher Reynolds number data.

In Figures 8.5 and 8.6, we have plotted the correlation and relative magnitude functions for the ψ-fields, using the same two cutoff wavenumbers as considered earlier. Comparison with the data for ϕ and its partitions (Figures 8.3 and 8.4) immediately shows that the results are strikingly similar.

Taking advantage of the reduction in computational effort we can now recompute the correlations for a wider range of cutoff wavenumbers and the results, for ψ_{--}, ψ_{-+} and ψ_{++} respectively, are given in Figures 8.7, 8.8 and 8.9. We consider the results for each partition in turn.

For ψ_{--}, Figure 8.7, we see an excellent collapse of the data for the range of cutoff wavenumbers considered. The line showing the greatest deviation corresponds to the smallest cutoff wavenumber, $k_c = 4$. Again we see that for $k < k_c$, ψ_{--} correlates well with the total nonlinear term, while this correlation drops rapidly to zero for $k > k_c$. We also note that, mathematically, $\psi_{\alpha--}(\mathbf{k}, t) = 0$ for $|\mathbf{k}| > 2k_c$ and so the small non-zero values observed in this region can be attributed to aliasing effects and other small numerical errors.

For ψ_{-+}, Figure 8.8, the collapse of data is less complete for $k < k_c$ where we once again witness erratic behaviour. In spite of this, however, the correlation is low in this region but rises rapidly to become approximately unity for $k > k_c$, where the data collapse also becomes more complete. For large k, the correlation starts to die away.

Finally, for ψ_{++}, Figure 8.9, we have relatively poor data collapse — except around the cutoff where all but the correlations corresponding to the two lowest cutoff wavenumbers coincide. For these two lowest values of k_c, ψ_{++} appears to be considerably more significant than in the other cases. The erratic behaviour for low-k is still present, and we observe a rise in the correlation as we move towards high-k, corresponding to the decrease seen in the ψ_{-+} correlations.

Each of these graphs show cusp-like behaviour at high-k and we believe this to be

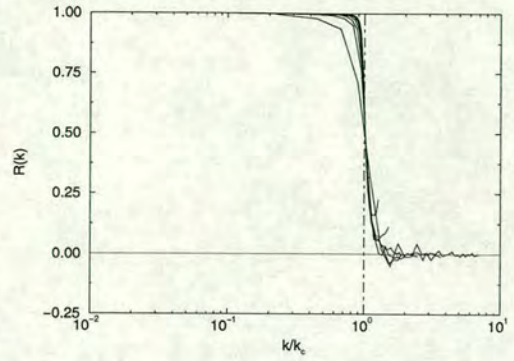

Figure 8.7: Low-Re. Correlation between ψ and ψ_{--} for cutoff wavenumbers $k_c = 4, 8, 12, 16, 20, 24, 28$. The vertical dot-dashed line indicates $k = k_c$.

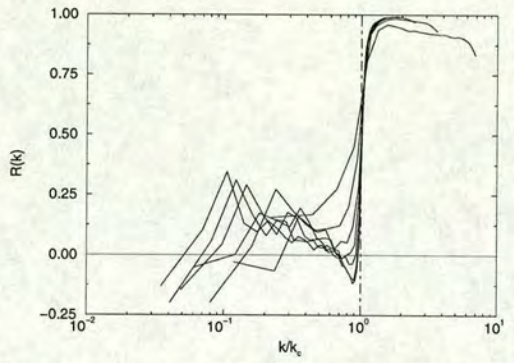

Figure 8.8: Low-Re. Correlation between ψ and ψ_{-+} for cutoff wavenumbers $k_c = 4, 8, 12, 16, 20, 24, 28$. The vertical dot-dashed line indicates $k = k_c$.

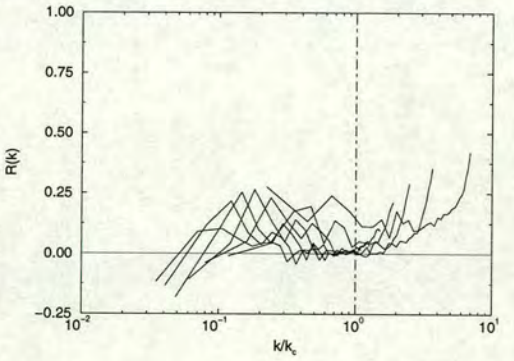

Figure 8.9: Low-Re. Correlation between ψ and ψ_{++} for cutoff wavenumbers $k_c = 4, 8, 12, 16, 20, 24, 28$. The vertical dot-dashed line indicates $k = k_c$.

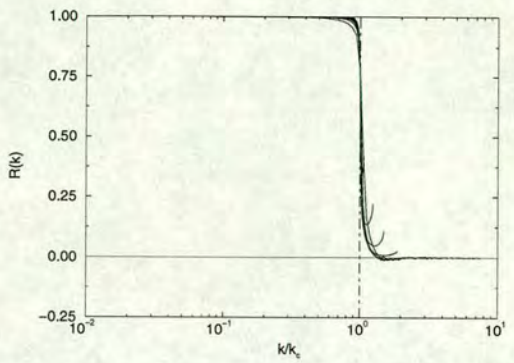

Figure 8.10: High-Re. Correlation between ψ and ψ_{--} for cutoff wavenumbers $k_c = 16, 32, 48, 64, 80, 96, 112$. The vertical dot-dashed line indicates $k = k_c$.

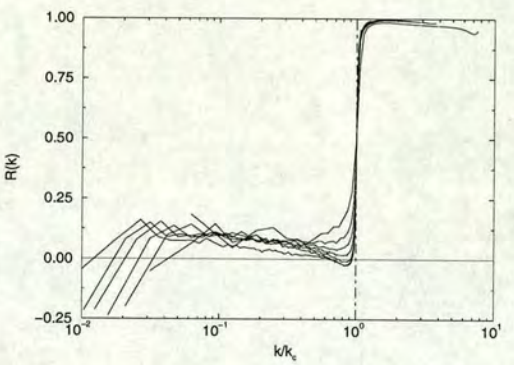

Figure 8.11: High-Re. Correlation between ψ and ψ_{-+} for cutoff wavenumbers $k_c = 16, 32, 48, 64, 80, 96, 112$. The vertical dot-dashed line indicates $k = k_c$.

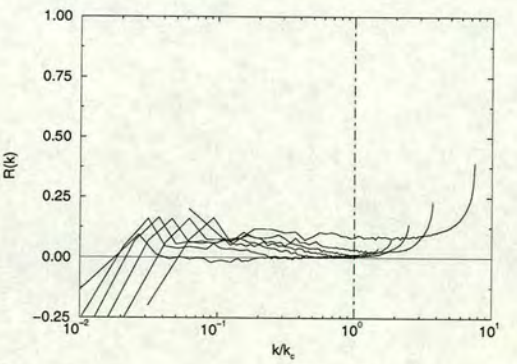

Figure 8.12: High-Re. Correlation between ψ and ψ_{++} for cutoff wavenumbers $k_c = 16, 32, 48, 64, 80, 96, 112$. The vertical dot-dashed line indicates $k = k_c$.

an artefact of the truncation at $k = k_{max}$, rather than being a genuine property of the fields under consideration.

8.4 Results at high Reynolds number

As noted earlier, the ψ-fields are relatively easy to compute, and it was possible to repeat the correlation computations described above at a higher-resolution (256^3) and, hence, at a higher Reynolds number ($R_\lambda \approx 190$). For much of the rest of this Chapter we shall consider the data from this simulation.

Firstly, in Figures 8.10–8.12, we have replotted our correlations. These results were obtained by averaging over the data of five independent velocity fields, taken from our 256^3 simulation and each separated by approximately 1.25 eddy turnover times. Comparing the results of the low and high resolution simulations side by side, it is clear that, qualitatively at least, the results are unchanged. The only significant effect of the move to a higher resolution seems to have been to refine the results — particularly in the low-k regions of the ψ_{-+} and ψ_{++} correlations. This effect was noticeable in the results obtained from each of the five velocity fields individually, as well as in the averaged results presented here.

The relative importance of the two subgrid scale terms, ψ_{-+} and ψ_{++}, noted here is reinforced by *a posteriori* tests carried out by Dubois, Jauberteau and Zhou [73]. They carried out numerical simulations in which first ψ_{-+} and then ψ_{++} was omitted from the Navier-Stokes equation. They found that while, over time, the absence of either term had detrimental effects, it was the omission of the ψ_{-+} term which caused more significant problems, in less time.

8.5 Partitioned transfer spectra

As noted earlier in equation (2.66), the energy balance equation may be written,

$$\left(\frac{\partial}{\partial t} + 2\nu k^2\right) E(k,t) = T(k,t) + \varepsilon_w(k,t), \tag{8.7}$$

where, in our current notation, the *energy transfer* term, $T(k,t)$, may be written,

$$T(k,t) = 4\pi k^2 \left\langle u_\alpha(-\mathbf{k},t)\psi_\alpha(\mathbf{k},t)\right\rangle. \tag{8.8}$$

With this in mind, it seems an obvious step to define the *partitioned transfer spectra* as,

$$T_{--}(k,t) = 4\pi k^2 \left\langle u_\alpha(-\mathbf{k},t)\psi_{\alpha--}(\mathbf{k},t)\right\rangle, \tag{8.9}$$

$$T_{-+}(k,t) = 4\pi k^2 \left\langle u_\alpha(-\mathbf{k},t)\psi_{\alpha-+}(\mathbf{k},t)\right\rangle, \tag{8.10}$$

$$T_{++}(k,t) = 4\pi k^2 \left\langle u_\alpha(-\mathbf{k},t)\psi_{\alpha++}(\mathbf{k},t)\right\rangle, \tag{8.11}$$

where it follows that,

$$T(k,t) = T_{--}(k,t) + T_{-+}(k,t) + T_{++}(k,t). \tag{8.12}$$

Partitioned transfer spectra of this type have been previously computed by Zhou and Vahala [74], although they restricted their attention to the low-k modes. We note, however, that in this region we appear to be in reasonable agreement with their results. Domaradzki [59] also considered what we would call T_{--} for decaying turbulence, comparing it with the total transfer term. Again there is qualitative agreement with our results.

For our data, the partitioned transfer spectra have been plotted in Figures 8.13–8.16 using four different choices of cutoff wavenumber, k_c. The y-axes of all four graphs have been truncated in order to emphasize the features of interest — in actuality the energy transfer out of the first shell due to T_{--} is approximately a factor of four larger.

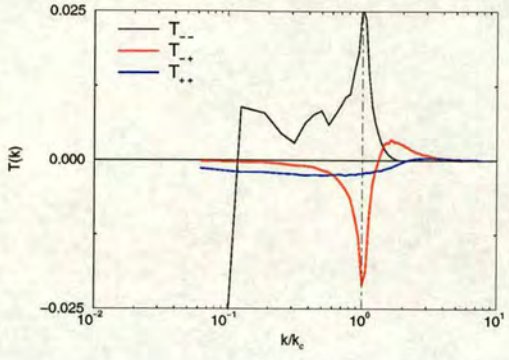

Figure 8.13: Partitioned transfer spectra for the case $k_c = 16$. The vertical dot-dashed line indicates $k = k_c$.

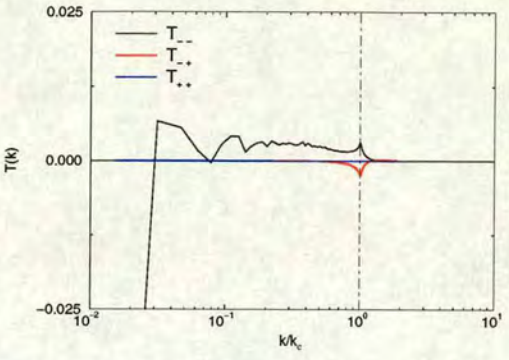

Figure 8.15: Partitioned transfer spectra for the case $k_c = 64$. The vertical dot-dashed line indicates $k = k_c$.

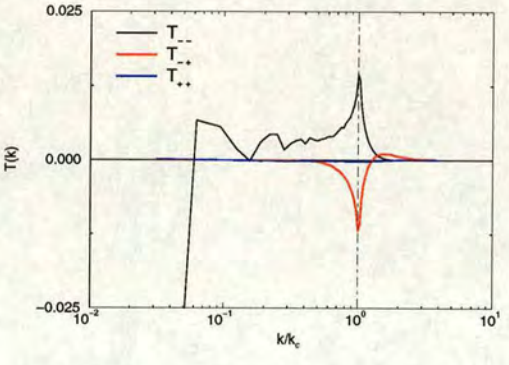

Figure 8.14: Partitioned transfer spectra for the case $k_c = 32$. The vertical dot-dashed line indicates $k = k_c$.

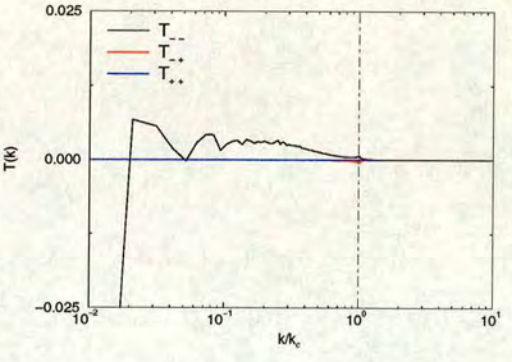

Figure 8.16: Partitioned transfer spectra for the case $k_c = 96$. The vertical dot-dashed line indicates $k = k_c$.

As k_c is increased, we see that energy transfer due to T_{-+} and T_{++} becomes progressively less significant — as we would expect. In fact, the effect of the T_{++} becomes negligible very rapidly (in agreement with the correlation results presented in the previous section) and we are left to consider T_{--} and T_{-+}. These terms appear to have a complementary effect with T_{--} piling energy up around the cutoff and with T_{-+} removing it.

Recalling both the definition of a spectral eddy-viscosity given in equation (6.35) and also the plateau/cusp shape seen in Figure 6.4 it becomes clear that T_{-+} is responsible for the cusp while, for small values of k_c, T_{++} appears to be largely responsible for the plateau. This also agrees with the conclusions of Zhou and

Vahala [74].

If we wish to consider the actual *transfer* of energy — rather than just the additive or subtractive effects of the partitioned spectra, we must be very careful. An important property of the full transfer term, $T(k)$, is that it can neither create nor destroy energy, but only move it from one wavenumber mode to another. This is reflected in the fact that its integral over all wavenumber space must be zero,

$$\int_0^\infty T(k)\ \mathrm{d}k = 0. \tag{8.13}$$

If we consider similar integrals for our partitioned spectra, we find that, individually, they do *not* conserve energy.

8.5.1 Partitioned transfer spectra and conservation of energy

When considering the transfer of energy between modes, we need to think about *triads* — that is, triples of interacting modes. The three modes in question ($\mathbf{k}$, $\mathbf{j}$ and $\mathbf{k}-\mathbf{j}$) can be seen clearly when we expand out the transfer term, $T(k)$, as given most recently in equation (8.8),

$$T(k) = 4\pi k^2 \left\langle u_\alpha(-\mathbf{k}) M_{\alpha\beta\gamma}(\mathbf{k}) \int \mathrm{d}^3 j\ u_\beta(\mathbf{j}) u_\gamma(\mathbf{k}-\mathbf{j}) \right\rangle. \tag{8.14}$$

Now consider, for example, the T_{-+} transfer term in the low-k region, denoted by T^-_{-+}. In full, this term looks like,

$$T^-_{-+}(k) = 4\pi k^2 \left\langle u^-_\alpha(-\mathbf{k}) 2M^-_{\alpha\beta\gamma}(\mathbf{k}) \int \mathrm{d}^3 j u^-_\beta(\mathbf{j}) u^+_\gamma(\mathbf{k}-\mathbf{j}) \right\rangle. \tag{8.15}$$

It is clear that this represents energy transfer to a particular low-k mode as a result of its interactions with all pairs of one low- and one high-k mode. We shall refer to triads, such as this, involving two low- and one high-k mode (*in any configuration*), as $\{-,-,+\}$ interactions. Taken as a whole, i.e. for all $k < k_c$, T^-_{-+} gives the effect of all such interactions on low-k modes — but we are missing

part of the picture. What is the result of these interactions in high-k region? The high-k part of T_{-+} is given by,

$$T^{+}_{-+}(k) = 4\pi k^2 \left\langle u^{+}_{\alpha}(-\mathbf{k}) 2M^{+}_{\alpha\beta\gamma}(\mathbf{k}) \int \mathrm{d}^3 j u^{-}_{\beta}(\mathbf{j}) u^{+}_{\gamma}(\mathbf{k}-\mathbf{j}) \right\rangle . \tag{8.16}$$

While this does, indeed, represent energy transfer to the high-k modes, it is apparent that it is a $\{-,+,+\}$ interaction and so does *not* form the complementary part of the energy transfer described by T^{-}_{-+}. This is precisely the reason why, on its own, T_{-+} does not conserve energy — it is representing the partial effects of two separate types of interaction.

Using these ideas, however, we can recombine the transfer spectra as defined in equations (8.9)–(8.11) to give transfer spectra which *do* conserve energy. One must ensure that each particular type of interaction is considered in full. The *energy conserving* transfer spectra are defined as follows,

$$T_{\{-,-,-\}} = T^{-}_{--}, \tag{8.17}$$

$$T_{\{+,+,+\}} = T^{+}_{++}, \tag{8.18}$$

$$T_{\{-,+,+\}} = T^{-}_{++} + T^{+}_{-+}, \tag{8.19}$$

$$T_{\{-,-,+\}} = T^{-}_{-+} + T^{+}_{--}. \tag{8.20}$$

Note that $T_{\{-,-,-\}}$ is only defined in the low-k region, and $T_{\{+,+,+\}}$ is only defined in the high-k region. This is because they are obviously incapable of transferring energy across the cutoff.

These energy conserving transfer spectra are plotted in Figures 8.17–8.20 for a selection of choices of k_c, with the $\{-,-,-\}$- and $\{+,+,+\}$ interactions combined. At first glance, these graphs may appear identical to those presented in Figures 8.13–8.16 and, indeed, the only real difference is one of relabelling. However, by representing the data in this way we can get a better feel for the energy transfer that takes place due to the interactions between low- and high-k modes.

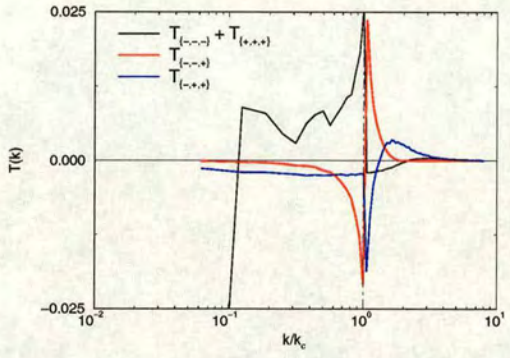

Figure 8.17: Energy conserving transfer spectra for the case $k_c = 16$. The vertical dot-dashed line indicates $k = k_c$.

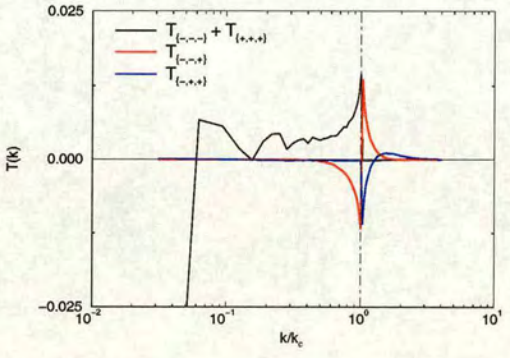

Figure 8.18: Energy conserving transfer spectra for the case $k_c = 32$. The vertical dot-dashed line indicates $k = k_c$.

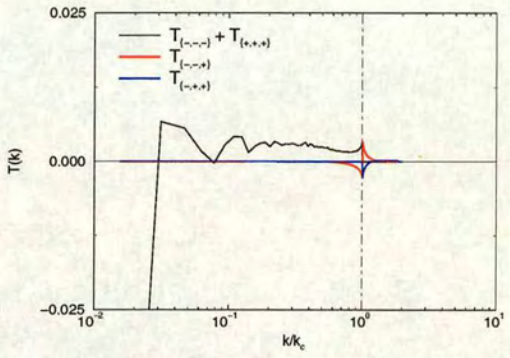

Figure 8.19: Energy conserving transfer spectra for the case $k_c = 64$. The vertical dot-dashed line indicates $k = k_c$.

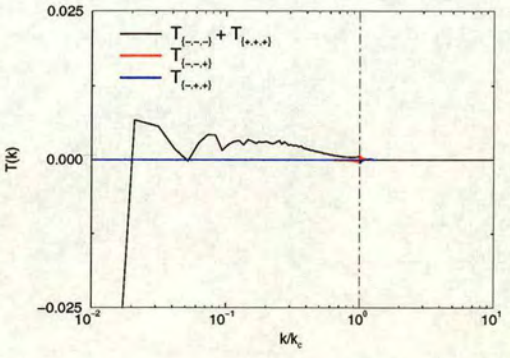

Figure 8.20: Energy conserving transfer spectra for the case $k_c = 96$. The vertical dot-dashed line indicates $k = k_c$.

8.5.2 Partitioned transport power spectra

One reason for our careful pursuit of *energy conserving* transfer spectra has been to allow us now to define appropriate transport powers. Recalling the definition of the transport power in equation (2.77) as an integral over the transfer spectrum:

$$\Pi(k,t) = \int_k^\infty T(k',t)\mathrm{d}k', \tag{8.21}$$

it might have seemed like a good idea to define partitioned transport powers in terms of the basic partitioned transfer spectra. However, we have seen that these do not conserve energy and so a quantity such as,

$$\Pi_{--}(k,t) = \int_k^\infty T_{--}(k',t)\mathrm{d}k', \tag{8.22}$$

could *not* be regarded as a measure of energy flux.

Instead, we use our energy conserving transfer spectra to define,

$$\Pi_{\{-,-,-\}}(k,t) = \int_k^\infty T_{\{-,-,-\}}(k',t)\mathrm{d}k', \tag{8.23}$$

$$\Pi_{\{-,-,+\}}(k,t) = \int_k^\infty T_{\{-,-,+\}}(k',t)\mathrm{d}k', \tag{8.24}$$

$$\Pi_{\{-,+,+\}}(k,t) = \int_k^\infty T_{\{-,+,+\}}(k',t)\mathrm{d}k', \tag{8.25}$$

$$\Pi_{\{+,+,+\}}(k,t) = \int_k^\infty T_{\{+,+,+\}}(k',t)\mathrm{d}k'. \tag{8.26}$$

These are plotted in Figures 8.21–8.24 where we have again combined the $\{-,-,-\}$ and $\{+,+,+\}$ terms into a single line.

Our basic conclusions are unchanged, but considering the data in this way will allow us, in the next section, to illuminate some additional points.

8.5.3 Interscale energy transfer

A number of studies have investigated the mechanisms by which energy flows between different scales. This includes the work of Ohkitani and Kida [75] who carried out a DNS of isotropic turbulence at a Reynolds number of $R_\lambda \approx 180$,

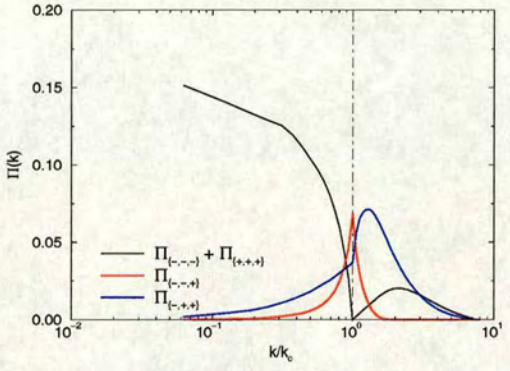

Figure 8.21: Energy conserving transport power for the case $k_c = 16$. The vertical dot-dashed line indicates $k = k_c$.

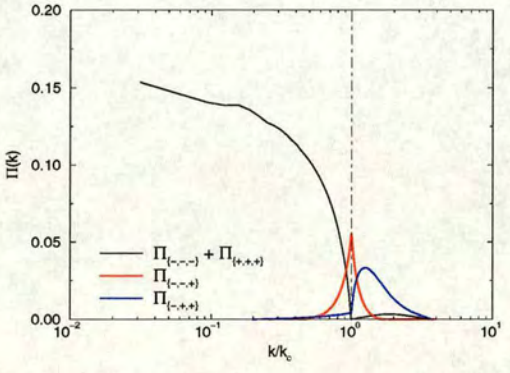

Figure 8.22: Energy conserving transport power for the case $k_c = 32$. The vertical dot-dashed line indicates $k = k_c$.

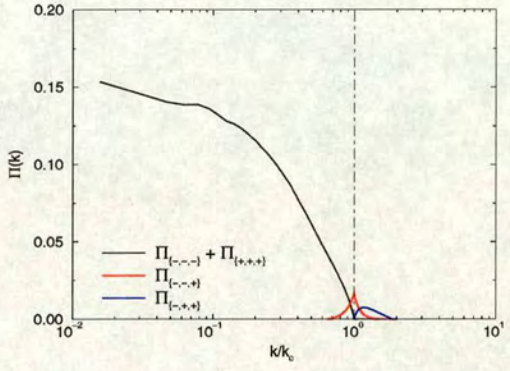

Figure 8.23: Energy conserving transport power for the case $k_c = 64$. The vertical dot-dashed line indicates $k = k_c$.

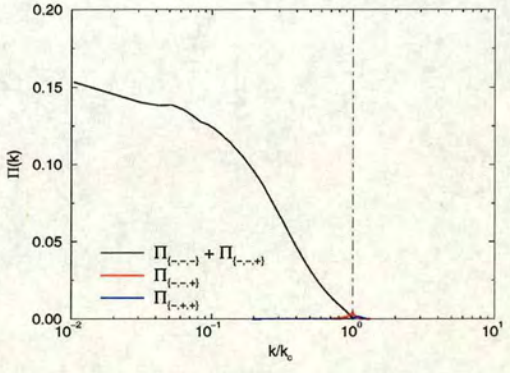

Figure 8.24: Energy conserving transport power for the case $k_c = 96$. The vertical dot-dashed line indicates $k = k_c$.

using a highly symmetric flow to reduce the computational effort [76] and that of Brasseur and Wei [77] who studied chains of interlinked triads.

In both cases, triad interactions were classified by the way in which each wavevector in the triad compared with the other two. For example, if the three wavevectors were of approximately the same magnitude, then the interaction would be deemed *local*. Our classification system — defined in terms of the number of low- and high-k modes present — was chosen to best explore the partitions of the nonlinear term but it has also allowed us to make a brief examination of the way in which energy is transferred across the cutoff wavenumber. We note, however, that it is clear that each of our classifications will include the effects of all of those given by Brasseur and Wei. Nevertheless, in the following discussion we shall tie some of the results together. Using the results we have seen for the (energy conserving) transfer and transport spectra, we can make some general comments on the observed effects of each type of interaction.

The $\{-,-,-\}$ interactions transfer energy from the forced modes up to the cutoff. It is obvious that these interactions cannot transfer energy beyond the cutoff, and this is illustrated graphically in the transport power plots as the flux drops to zero at this point.

For low values of k_c, the $\{+,+,+\}$ interactions assist in the transfer of energy from modes just beyond the cutoff to higher k. Otherwise they seem to have a minimal effect.

The dominant effect of the $\{-,-,+\}$ interactions is to transfer energy across the cutoff, at which point the peak energy flux occurs. From the transport power plots, this appears to be a fairly local effect, with the phenomenon restricted to wavenumbers close to the cutoff.

For the behaviour of our $\{-,+,+\}$ interactions, we can turn to Ohkitani and Kida [75] who found that energy exchanges occurred predominantly between two

comparable scales. They noted, therefore, that in an interaction involving two "long" wavevectors and one "short" wavevector, energy was transferred between the two long wavevectors with the short wavevector acting almost like a catalyst. This type of interaction probably accounts for the dominant effect of our $\{-,+,+\}$ interactions. Its primary role appears to be the transfer of energy from the modes just above the cutoff to higher-k — i.e. energy transfer between high-k modes, with the low-k mode acting as a catalyst. The peak energy flux appears to take place at $k \sim 1.25k_c$.

For small values of k_c, these interactions also become significant in the low-k region. In this situation, there is less scale separation between the three modes and we move closer to local interactions, for which energy transfer between the modes contained in the triad is expected to be more evenly spread.

8.6 Eddy-viscosities with sharp cutoffs

In Chapter 6 we discussed the fact that, in the case of an actual LES, subgrid scale modelling requires the use of theoretical assumptions of one form or another. However, we noted that with the data from a fully-resolved DNS to hand, we can take a pragmatic approach and calculate "exact" eddy-viscosities, corresponding to the sort of cutoff wavenumbers, k_c, seen in the the previous sections. That is, by virtue of knowing both u^- and u^+ we can compute the net effect of the u^+ modes on the u^- modes.

As well as using our "complete" knowledge of the system to compare eddy-viscosities, it is also possible to make a direct comparison between the subgrid contributions to the nonlinear term and the model. Such '*a priori*' tests were first carried out by Clark, Ferziger and Reynolds [78] who performed a numerical simulation at a resolution of 64^3 and tested the performance of a number of real-space eddy-viscosity models including that due to Smagorinsky [54]. They found

that there was relatively poor agreement between the model and exact subgrid stress and that the exact choice of model made little difference to the result.

More recently, Borue and Orszag [79] carried out hyperviscous simulations [80] in which the normal Newtonian dissipation — the last term in equation (3.1) — is replaced by a higher power of the Laplacian. This is a computational expedient which has been shown to extend the inertial range present in a simulation. They performed tests on a variety of eddy-viscosity types and also included results for a variety of different filter functions, including the sharp cutoff filter used in spectral LES. They again found that simple eddy-viscosity models showed poor correlation with the exact subgrid terms and further demonstrated a dependency on the type of filter, with the sharp cutoff filter performing least well.

Given all of this negativity, it is worth bearing in mind throughout the rest of this chapter that *a priori* tests are now regarded cautiously in the field. Smagorinsky's model, for example, while performing badly in *a priori* tests has been shown to give good results when used as the basis for a LES. On the other hand, although the similarity model due to Bardina [81] has performed well in *a priori* tests, it has been found that, in practice, it requires an additional eddy-viscosity term in order for sufficient energy dissipation to take place [82].

Using our own data, we shall now look, in the context of a *spectral* LES, at how well an eddy-viscosity model captures the effects of the exact subgrid terms. We begin by rewriting the Navier-Stokes equation, for the low-k modes only:

$$\left[\frac{\partial}{\partial t} + \nu k^2\right] u^-(\mathbf{k},t) = \psi^-_{\alpha--}(\mathbf{k},t) + \psi^-_{\alpha(--)}(\mathbf{k},t) + f^-(\mathbf{k},t), \tag{8.27}$$

recalling that $\psi_{(--)}$ represents the subgrid effects and is given by,

$$\psi^-_{\alpha(--)}(\mathbf{k},t) = \psi^-_{\alpha-+}(\mathbf{k},t) + \psi^-_{\alpha++}(\mathbf{k},t). \tag{8.28}$$

These two terms are grouped together as they represent the missing terms in a large eddy simulation, where a model, $Y^-_{(--)}$, has to be introduced. Employing a

standard eddy-viscosity model, this may be written as,

$$Y^-_{\alpha(--)}(\mathbf{k},t) = -\delta\nu(k)k^2 u^-_\alpha(\mathbf{k},t), \tag{8.29}$$

where $\delta\nu(k)$ is the viscosity increment.

Without having to specify a form for $\delta\nu(k)$, we can test its general properties by considering the correlation $R(\psi^-_{(--)}, Y^-_{(--)}; k)$. Expanding out this correlation, but omitting many of the wavenumber, time and index arguments for clarity, this gives,

$$\begin{aligned}
R(\psi^-_{(--)}, Y^-_{(--)}; k) &= \frac{\langle \psi^-_{(--)} \cdot Y^-_{(--)} \rangle}{\langle \psi^-_{(--)} \cdot \psi^-_{(--)} \rangle^{1/2} \langle Y^-_{(--)} \cdot Y^-_{(--)} \rangle^{1/2}} \\
&= \frac{\langle \psi^-_{(--)} \cdot (-\delta\nu(k)k^2 u^-) \rangle}{\langle \psi^-_{(--)} \cdot \psi^-_{(--)} \rangle^{1/2} \langle \delta\nu(k)^2 k^4 u^- \cdot u^- \rangle^{1/2}} \\
&= -\frac{\delta\nu(k)k^2 \langle \psi^-_{(--)} \cdot u^- \rangle}{|\delta\nu(k)|k^2 \langle \psi^-_{(--)} \cdot \psi^-_{(--)} \rangle^{1/2} \langle u^- \cdot u^- \rangle^{1/2}} \\
&= -\mathrm{sgn}[\delta\nu(k)] \frac{\langle \psi^-_{(--)} \cdot u^- \rangle}{\langle \psi^-_{(--)} \cdot \psi^-_{(--)} \rangle^{1/2} \langle u^- \cdot u^- \rangle^{1/2}}.
\end{aligned} \tag{8.30}$$

This may be re-expressed simply as,

$$R(\psi^-_{(--)}, Y^-_{(--)}; k) = -\mathrm{sgn}[\delta\nu(k)] R(\psi^-_{(--)}, u^-; k), \tag{8.31}$$

which, aside from the choice of sign, is *totally independent* of the exact nature of the eddy-viscosity and is very straightforward to calculate from a DNS velocity field.

From the investigations of Chapter 6, it would seem that for large Reynolds numbers, the eddy-viscosity will be positive for all values of k. However, at the Reynolds number corresponding to our 256^3 simulation, we have seen that the eddy-viscosity does, in fact, have negative values at low-k. Nonetheless, for the purpose of obtaining results, we shall assume that $\mathrm{sgn}[\delta\nu(k)] = 1$ since negative values would simply flip the sign of the correlation.

Results of the correlation calculation are shown in Figure 8.25. Taking the results as a whole, we see that $|R| < 0.5$ for the major part of k-space. The implication

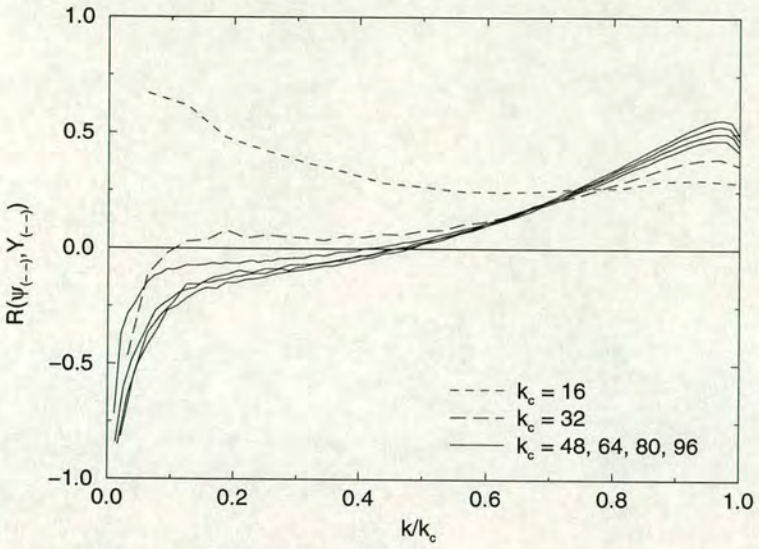

Figure 8.25: The correlation between the exact subgrid terms, $\psi^{-}_{(--)}$ and the "grid scale" velocity field, u^{-} for a number of cutoff wavenumbers.

of this is that an eddy-viscosity model (independent of the exact choice of $\delta\nu(k)$) is, in general terms, a poor substitute for the effects of the missing modes.

Also worth noting is the change in behaviour as k_c is reduced. For $k_c > 48$, the correlation results are comparable. For the two lowest values of k_c, however, something different happens, and we see that the level of correlation starts to increase. The underlying cause of this is unclear, but it may be due, in some way, to the very large number of "eliminated" modes, or it might be attributable to the increasing proximity of k_c to the inertial range. This is an important point and it will be considered further in Section 8.9. This behaviour mimics that seen when eddy-viscosities were computed (see Figure 6.4) and we also note that the regions of apparently negative correlation correspond to regions of negative eddy-viscosity. This is contrary to the assumption of positive eddy-viscosity made earlier ($\text{sgn}\,[\delta\nu(k)] = 1$) and so we conclude that, for actual eddy-viscosities, the correlation will most likely be positive.

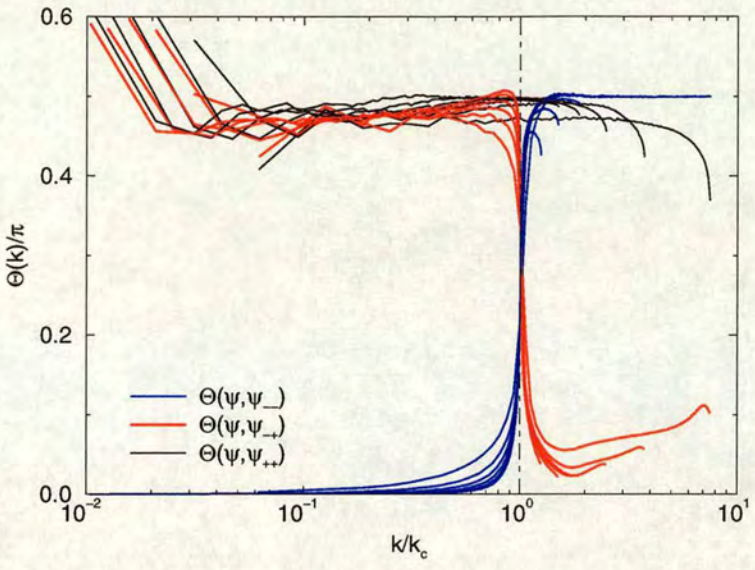

Figure 8.26: The average phase difference between the nonlinear term and each of its partitions.

8.7 Phase issues

The poor correlation between the various quantities we have studied must be due to the fields being out of phase, in some sense. To begin this section, we must first make some sort of sensible definition of what we mean by the *phase difference* between two complex vectors, $\mathbf{a}$ and $\mathbf{b}$ say. For a pair of real vectors, the scalar product provides a means of making such a definition and we might write,

$$\Theta(\mathbf{a},\mathbf{b}) = \cos^{-1}\left(\frac{\mathbf{a}\cdot\mathbf{b}}{|\mathbf{a}||\mathbf{b}|}\right). \tag{8.32}$$

However, for complex vectors, $\mathbf{a}\cdot\mathbf{b}$ will not generally be real. To avoid this problem, we will therefore associate each three-dimensional complex vector with a six-dimensional real vector, i.e.,

$$\mathbf{a} = \begin{pmatrix} a+bi \\ c+di \\ e+fi \end{pmatrix} \equiv \begin{pmatrix} a \\ b \\ c \\ d \\ e \\ f \end{pmatrix} = \mathbf{a}_R. \tag{8.33}$$

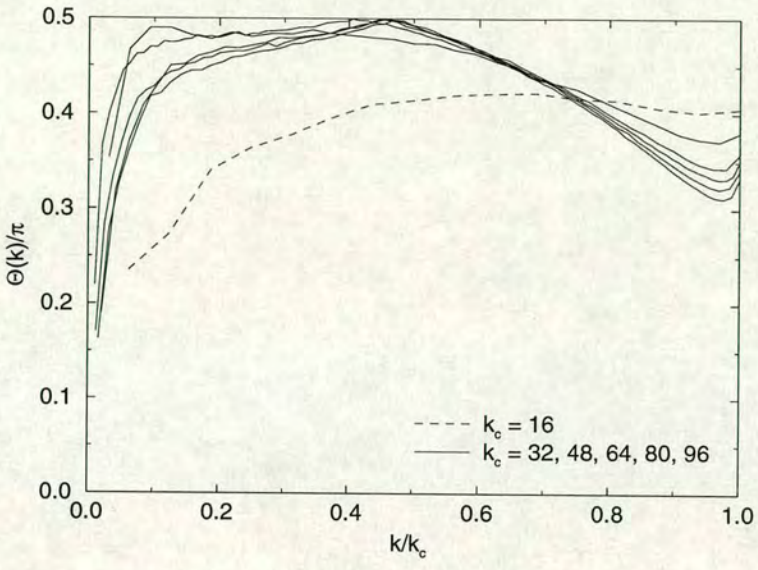

Figure 8.27: The average phase difference between the subgrid contribution to the nonlinear term and an eddy-viscosity model.

We then define,

$$\Theta\left(\mathbf{a},\mathbf{b}\right)=\cos^{-1}\left(\frac{\mathbf{a}_R\cdot\mathbf{b}_R}{|\mathbf{a}_R||\mathbf{b}_R|}\right). \tag{8.34}$$

This will be our definition of the phase difference between $\mathbf{a}$ and $\mathbf{b}$[1].

We have computed shell-averaged values of this phase difference,

$$\Theta\left(\mathbf{a},\mathbf{b};k\right)=\left\langle\Theta\left[\mathbf{a}(\mathbf{k}),\mathbf{b}(\mathbf{k})\right]\right\rangle, \tag{8.35}$$

for a number of different pairs of vector fields.

We begin by comparing the nonlinear term, ψ, with each of its partitions. The results are shown in Figure 8.26. As may be seen, these results are very similar to those seen earlier in Figures 8.10–8.12. This is as we would expect, with a correlation of $R=1$ corresponding to an average phase difference of $\Theta=0$, and a correlation of $R=0$ corresponding to an average phase difference of $\Theta=\pi/2$.

We end this section by looking at $\Theta\left(\psi^-_{(--)},-\mathrm{sgn}[\delta\nu(k)]\mathbf{u}^-\right)$, which has been plotted in Figure 8.27. Again, the results reflect those obtained by the correlation

[1]We note in passing that $\mathbf{a}_R\cdot\mathbf{b}_R/|\mathbf{a}_R||\mathbf{b}_R|$ is essentially a component-level correlation of $\mathbf{a}$ and $\mathbf{b}$.

method. For the majority of choices of k_c we see that, on average, the model field and the exact subgrid field is out of phase by $\pi/3 \leq \Theta \leq \pi/2$. Once more we see that for $k_c = 16$, the smallest value considered here, the results suggest a better match between the modelled and exact fields.

8.8 Results at very high Reynolds number

By performing tests on DNS data we are limiting ourselves to relatively low Reynolds numbers and, ideally, we would like to see if there is any behavioural change as the Reynolds number is increased.

In Section 6.3.1 it was explained how some authors have used LES velocity fields to compute eddy-viscosities by introducing a second cutoff wavenumber $k_c' < k_c$. In this section, we have taken velocity fields from a number of fixed-spectrum LES runs (see Section 6.3.2) and reperformed our analyses. Referring back to Table 6.1, the velocity fields used have been obtained from runs IV, V and VI — corresponding to Reynolds numbers of $R_\lambda \approx 680$, 1773 and 4871 respectively.

We must be very careful in our interpretations of any results obtained in this manner. We note firstly that while we have complete $\mathbf{u}^-$ fields (with respect to k_c') the $\mathbf{u}$ and $\mathbf{u}^+$ fields are limited by $k < k_c$. Secondly, while the fixed-spectrum LES fields have sensible energy spectra, they have been evolved in the absence of small-scale modes and hence we cannot guarantee the accuracy of the phase information they contain.

Nevertheless, we have recomputed the correlations between the nonlinear term and its partitions, for $k_c' = \frac{1}{2}k_c = 16$. As Figure 8.28 clearly demonstrates, we find ourselves with a picture in good agreement with that obtained previously for small k_c (in Figures 8.10–8.12 for example).

Next we compute the correlation between the subgrid contributions to the nonlinear term, $\psi^-_{(--)}$, and the basis of an eddy-viscosity model, $-u^-$, which is given

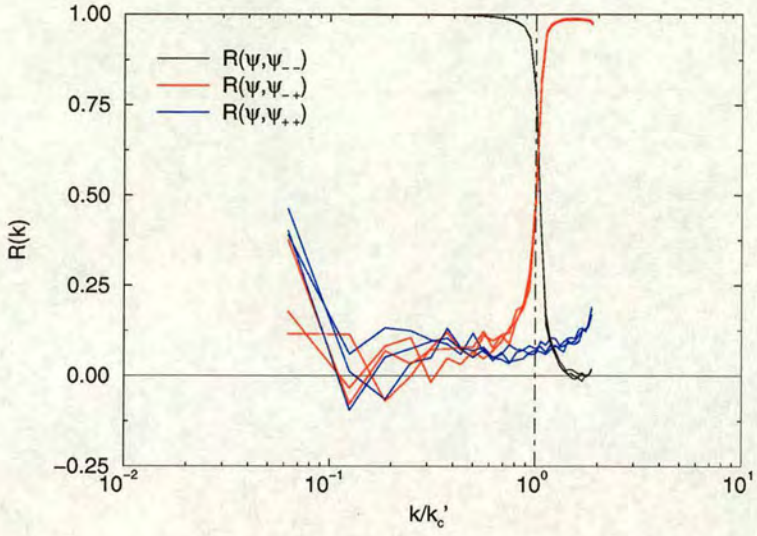

Figure 8.28: The correlation between the nonlinear term and each of its partitions for data taken from three fixed-spectrum LES runs with $k_c' = \frac{1}{2}k_c = 16$.

in equation (8.29). The results are shown in Figure 8.29 and again there is good agreement with the results from the DNS data for low cutoff wavenumbers (Figure 8.25).

These results suggest that the behaviour seen in the DNS data is representative of the behaviour present over a wide range of Reynolds numbers.

8.9 Implications for eddy-viscosity models

The results discussed in this chapter would appear to have severe implications for eddy-viscosity models. By comparing a general model with the term it is intended to replace, we have seen that the two correspond very poorly. However, we know that eddy-viscosities are widely used, and to good effect (see, for example, [12, 83]). How can we address this apparent contradiction?

Firstly, we may refer back to the results of previous sections. Figures 8.10–8.12 showed how each of the partitions of the nonlinear term correlate with the full nonlinear term. We have noted that, in the region $k < k_c$, it is the ψ_{--} term

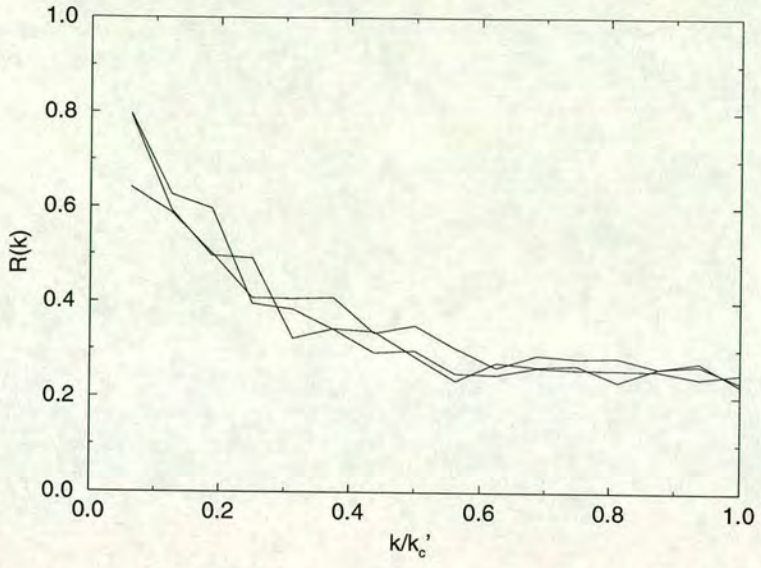

Figure 8.29: The correlation between the subgrid contributions to the nonlinear term and an eddy-viscosity model for data taken from three fixed-spectrum LES runs with $k_c' = \frac{1}{2}k_c = 16$.

which dominates. In the context of a LES, this corresponds to the *explicit* part of the nonlinear term. The eddy-viscosity must then deal with the less important *subgrid* terms, which only become significant around the cutoff.

Secondly, we recall the definition of an eddy-viscosity given by equation (6.35) which relates it unambiguously to the energy and subgrid scale energy transfer spectra. We may therefore conclude that, *assuming the resolved energy spectrum is correct*, an eddy-viscosity can correctly model inter-shell energy transfers — and this, of course, ties in with the idea of *a posteriori* testing giving better results than *a priori* tests of the type discussed here. However, the poor correlation between $\psi^-_{(--)}$ and $-u^-$ is indicative of the two fields being out of phase, a point which we have probed directly, and since energy transfer is given by a term like $u^-_\alpha \psi^-_{\alpha(--)}$ we may conclude that an eddy-viscosity model cannot give the correct energy transfer to a particular mode *within* a shell. This is in addition to an eddy-viscosity's lack of phase information and it is apparent, therefore, that over time the retained velocity field, u^-, will degrade — a point noted by Herring [84].

Finally, we have seen that, for low values of k_c, the eddy-viscosity model appears to perform slightly better. From our results it is not entirely clear whether this is simply because k_c is so small, or whether it has to do with a change in behaviour as k_c approaches an inertial range. We note that, for a fixed low value of k_c, the correlation did not increase with Reynolds number (fixed-spectrum LES results) and showed no decrease when we considered the data from our 64^3 simulation in which no inertial range exists. This would seem to lend some support to the former explanation.

Additionally, we recall the work of Ohkitani and Kida [75] and their suggestion that, in an interaction involving two "long" and one "short" wavevectors, energy transfer will take place between the two similar scales. For large values of k_c, and with $k \ll k_c$, the ψ^-_{++} term must fall into this category which suggests that, irrespective of the existence of an inertial range, the *energy transferring* effects of this term will be small[2].

[2]The transfer of structure, or phase, is a different matter, but as eddy-viscosity models cannot reproduce this anyway, we need not concern ourselves with it here.

Chapter 9

The Partial Time Average

9.1 Defining the full ensemble and the biased subensemble

A conditional average of some description is needed for any renormalization group treatment of turbulence [7, 66, 85]. Such an average is defined in terms of a subensemble of velocity field realizations, selected from the full ensemble.

In principle, the full ensemble might be generated as follows. Consider a velocity field, evolving in time according to the Navier-Stokes equations, and suppose that we have knowledge of this field for a very long period of time. We now select times, sufficiently far apart so that the velocity fields at each instant have no dynamical connection[1]. This process might then be repeated for many other solutions of the Navier-Stokes equations until a very large sample has been collected. This is our ensemble, which we shall denote as $\left\{\mathcal{W}_\alpha^{(i)}(\mathbf{k})\right\}$.

Now, following the work of McComb *et al*, outlined in Chapter 7, we define the *biased* subensemble which contains those members of the full ensemble satisfying,

$$\left|\theta^-(k)\mathcal{W}_\alpha^{(i)}(\mathbf{k}) - v_\alpha^-(\mathbf{k})\right| \leq \xi, \tag{9.1}$$

[1]This is best measured by way of two-time correlations. For our 256^3 simulation, for example, it was found that such correlations became negligible once a time difference of the order of half an eddy turnover time was reached, indicating that the fields are statistically independent.

where $\mathbf{v}(\mathbf{k})$ is a preferred realization. This selection process is illustrated in Figure 9.1[2].

9.2 Velocity correlations between members of the biased subensemble

Let us now relate each of the fields in our subensemble to the preferred realization by writing,

$$\mathcal{W}_\alpha^{(i)}(\mathbf{k}) = v_\alpha(\mathbf{k}) + \Phi_\alpha^{(i)}(\mathbf{k}), \tag{9.2}$$

where $\Phi_\alpha^{(i)}(\mathbf{k})$ is simply the difference between them. In addition to the relationship given in equation (9.2) we will specify one further constraint — namely that each member of the subensemble should have the same shell-averaged energy spectra, implying that,

$$\left\langle \mathcal{W}_\alpha^{(i)}(\mathbf{k})\mathcal{W}_\alpha^{(i)}(-\mathbf{k}) \right\rangle_s = \langle v_\alpha(\mathbf{k})v_\alpha(-\mathbf{k})\rangle_s \,, \tag{9.3}$$

where $\langle\cdots\rangle_s$ denotes shell averaging. We may use equation (9.2) to give another expression for the energy spectrum of the $\mathcal{W}_\alpha^{(i)}(\mathbf{k})$ field thus,

$$\begin{aligned} &\left\langle \mathcal{W}_\alpha^{(i)}(\mathbf{k})\mathcal{W}_\alpha^{(i)}(-\mathbf{k}) \right\rangle_s \\ &= \langle v_\alpha(\mathbf{k})v_\alpha(-\mathbf{k})\rangle_s + 2\left\langle v_\alpha(\mathbf{k})\Phi_\alpha^{(i)}(-\mathbf{k}) \right\rangle_s + \left\langle \Phi_\alpha^{(i)}(\mathbf{k})\Phi_\alpha^{(i)}(-\mathbf{k}) \right\rangle_s , \end{aligned} \tag{9.4}$$

which can be combined with equation (9.3) to give,

$$\left\langle \Phi_\alpha^{(i)}(\mathbf{k})\Phi_\alpha^{(i)}(-\mathbf{k}) \right\rangle_s = -2\left\langle v_\alpha(\mathbf{k})\Phi_\alpha^{(i)}(-\mathbf{k}) \right\rangle_s . \tag{9.5}$$

We will now use these equations to obtain an expression for the correlation between the two fields,

$$R(v, \mathcal{W}^{(i)}; k) = \frac{\left\langle v_\alpha(\mathbf{k})\mathcal{W}_\alpha^{(i)}(-\mathbf{k}) \right\rangle_s}{\langle v_\alpha(\mathbf{k})v_\alpha(-\mathbf{k})\rangle_s^{1/2} \left\langle \mathcal{W}_\alpha^{(i)}(\mathbf{k})\mathcal{W}_\alpha^{(i)}(-\mathbf{k}) \right\rangle_s^{1/2}}. \tag{9.6}$$

[2]This figure kindly provided by Craig Johnston.

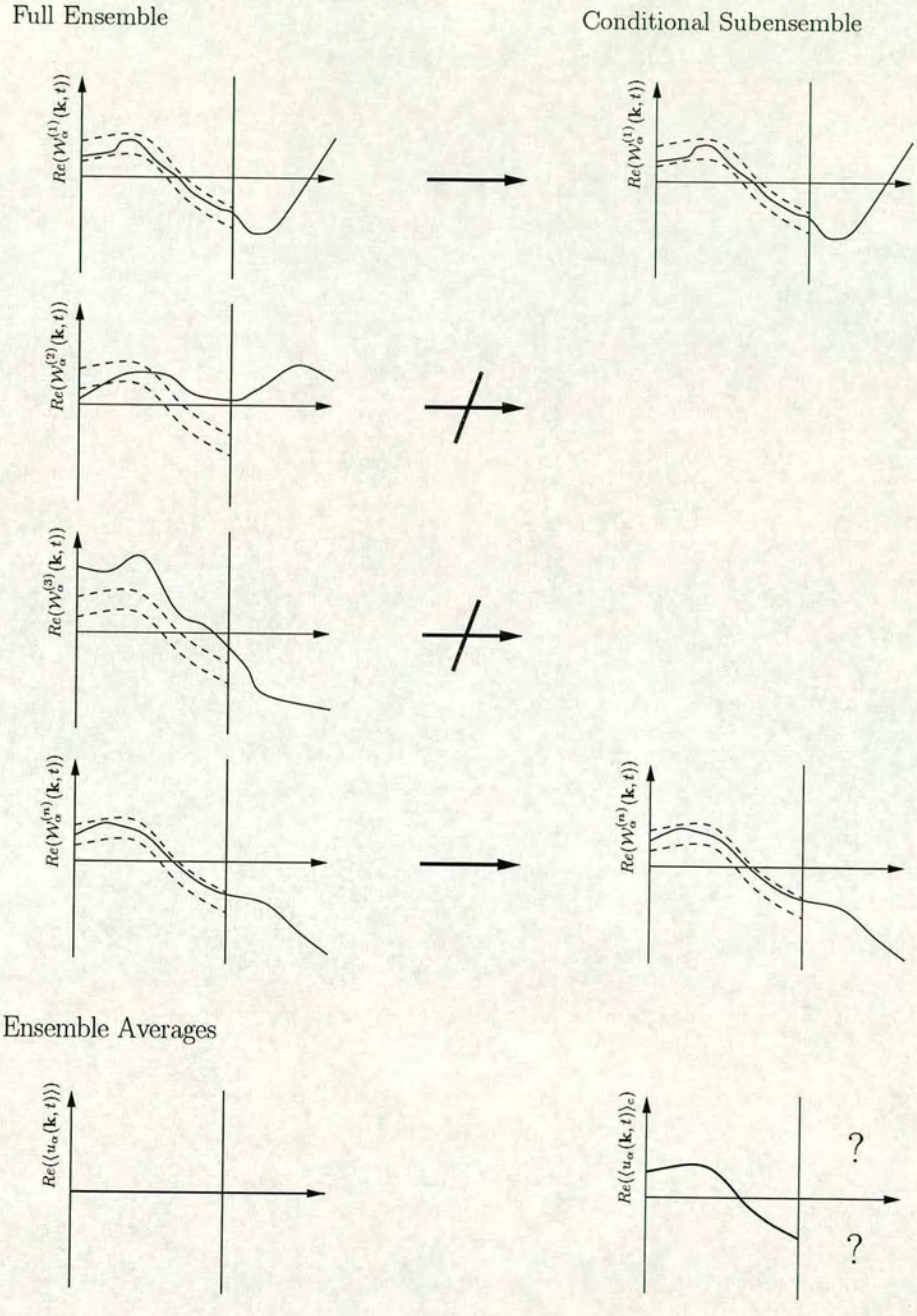

Figure 9.1: A schematic illustration showing how members of the full ensemble (LHS) are chosen to form the biased subensemble (RHS), and anticipated results of the two averaging operations. The dashed lines indicate the constraint on the low-wavenumber modes.

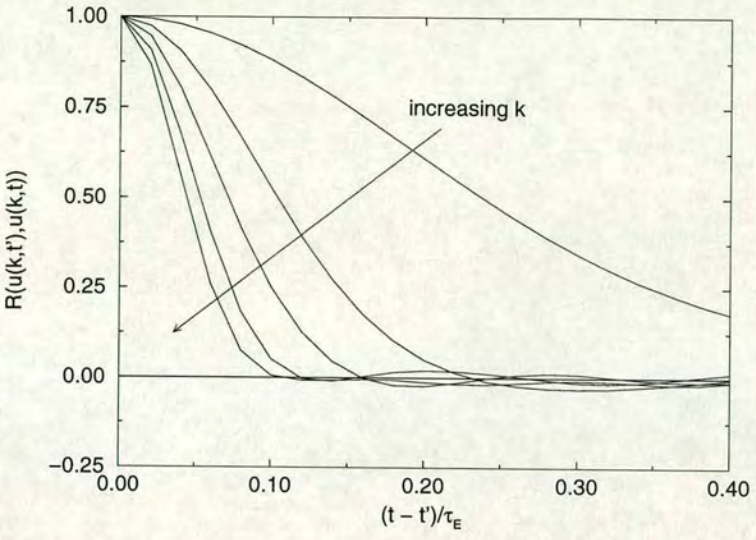

Figure 9.2: Two-time correlations in a forced 64^3 simulation. The reference time is given by t'. The correlation is shown as a function of the time difference, $t - t'$, scaled on the eddy turnover time, τ_E, for $k = 5{,}10{,}15{,}20{,}25$.

Equation (9.2) is used to expand the numerator and equation (9.3) to rewrite the denominator, giving

$$\begin{aligned} R(v, \mathcal{W}^{(i)}; k) &= \frac{\langle v_\alpha(\mathbf{k}) v_\alpha(-\mathbf{k}) \rangle_s + \left\langle v_\alpha(\mathbf{k}) \Phi_\alpha^{(i)}(-\mathbf{k}) \right\rangle_s}{\langle v_\alpha(\mathbf{k}) v_\alpha(-\mathbf{k}) \rangle_s} \\ &= 1 + \frac{\left\langle v_\alpha(\mathbf{k}) \Phi_\alpha^{(i)}(-\mathbf{k}) \right\rangle_s}{\langle v_\alpha(\mathbf{k}) v_\alpha(-\mathbf{k}) \rangle_s}. \end{aligned} \tag{9.7}$$

At this point, equation (9.5) can be invoked to give,

$$R(v, \mathcal{W}^{(i)}; k) = 1 - \tfrac{1}{2} \frac{\left\langle \Phi_\alpha^{(i)}(\mathbf{k}) \Phi_\alpha^{(i)}(-\mathbf{k}) \right\rangle_s}{\langle v_\alpha(\mathbf{k}) v_\alpha(-\mathbf{k}) \rangle_s}. \tag{9.8}$$

This result clearly demonstrates that if $\mathcal{W}_\alpha^{(i)}$ and v_α are close for low-k, then they must also have a non-zero correlation in this region.

9.3 Testing the conditional average numerically

Using a 64^3 simulation ($R_\lambda \approx 70$) we have plotted, in Figure 9.2, the two-time autocorrelation of the velocity field, as a function of the time difference, $t - t'$.

This shows a familiar picture which has the correlation falling away to zero as the time difference is increased.

For a computational run of any practical length, we would not expect to see the correlation rise significantly once zero correlation has been reached. Taking $\mathbf{v}(\mathbf{k}) \equiv \mathbf{u}(\mathbf{k}, t')$, we would therefore not expect to find any velocity field which was close to our reference field, during the lifetime of the simulation, without also being close in time. However, what happens over extremely long times is another matter. Landau and Lifshitz [86] express the velocity field as a series of time-periodic functions and hence show that, "in the course of a sufficiently long time the fluid passes through states arbitrarily close to any given state"[3]. This sufficiently long time is essentially $t \to \infty$ which certainly puts it beyond computational reach, and we must conclude, therefore, that it is not possible to directly probe the conditional average numerically.

In the work of Machiels (detailed in [44, 34]), an expedient was introduced as follows. Firstly, a set of 200 statistically independent velocity fields were generated from a 256^3 DNS. Then, by carrying out a Fourier transform along a single coordinate axis, an ensemble of 2533 one-dimensional *strip-realizations* were obtained. From this ensemble, a number of pairs of strip-realizations were selected so that they were close over some region of low-k. It was found that in order for there to be a reasonable number of these pairs the applied constraint had to be quite weak, both in terms of the degree of "closeness" and the size of the range over which the constraint was applied. An analysis of these pairs showed that beyond the "close" region of wavenumber space, the members of each pair diverged rapidly.

A second strand of Machiels' work involved the study of probability density functions (PDFs) of the velocity increment, $\delta\mathbf{u}(\mathbf{x}, \mathbf{h}) = \mathbf{u}(\mathbf{x}+\mathbf{h}) - \mathbf{u}(\mathbf{x})$, projected out along the $\mathbf{h}$ vector. Data subsets were chosen by restricting the allowable range

[3]Although this will necessarily give rise to a significant correlation, we note that this is coincidental and not indicative of a dynamical connection.

of velocity increments at a large scale (corresponding to a low wavenumber) and looking at the PDFs of the increment at a small scale (corresponding to a high wavenumber) for both the restricted and complete data sets. It was found that, as the constraint was tightened, the PDF taken from the restricted data set diverged from that taken from the complete set. However, it was noted that in all the cases explored, then central part of the PDFs showed a good match.

Both of these results are predictability studies which lend support to the idea of a conditional average without actually attempting to compute one. In this thesis we shall pursue an alternative approach to the problem of numerically investigating the conditional average, and turn our attention to *partial time averages.*

9.4 Definition and computation of the partial time average

We shall define the partial time average to be given by,

$$\langle X(\mathbf{k},t)\rangle_\tau \equiv \frac{1}{2\tau}\int_{t-\tau}^{t+\tau} X(\mathbf{k},s)\,ds. \tag{9.9}$$

The idea is that by choosing τ to be sufficiently small, we will ensure that all of the velocity fields considered in the average are close over some range of low wavenumbers.

Computationally, this is performed as a rolling time average and, as an expedient, rather than holding the central time constant, we hold the lower time constant. That is to say, for fixed values t and τ, we compute,

$$\langle X(\mathbf{k},t+\tau)\rangle_\tau \equiv \frac{1}{2\tau}\int_{t}^{t+2\tau} X(\mathbf{k},s)\,ds \approx \frac{1}{3}\sum_{n=0}^{2} X(\mathbf{k},t_n), \tag{9.10}$$

$$\langle X(\mathbf{k},t+2\tau)\rangle_{2\tau} \equiv \frac{1}{4\tau}\int_{t}^{t+4\tau} X(\mathbf{k},s)\,ds \approx \frac{1}{5}\sum_{n=0}^{4} X(\mathbf{k},t_n), \tag{9.11}$$

$$\langle X(\mathbf{k},t+3\tau)\rangle_{3\tau} \equiv \frac{1}{6\tau}\int_{t}^{t+6\tau} X(\mathbf{k},s)\,ds \approx \frac{1}{7}\sum_{n=0}^{6} X(\mathbf{k},t_n), \tag{9.12}$$

and so on.

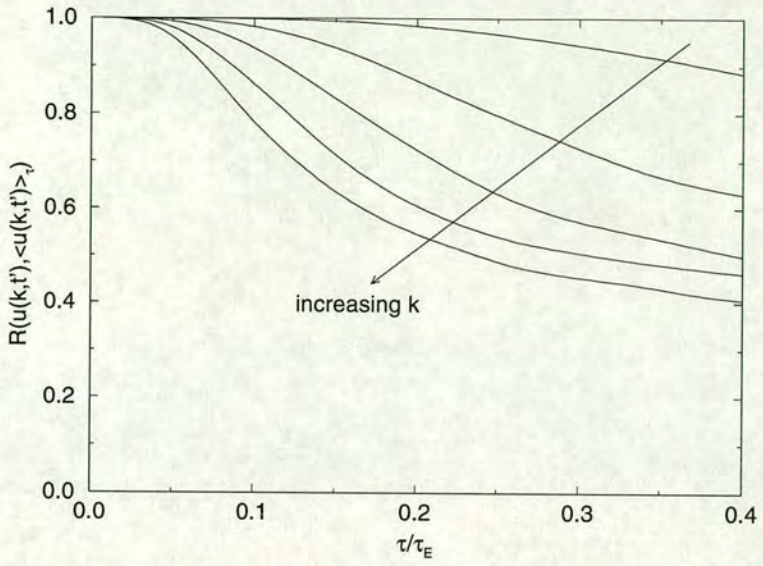

Figure 9.3: The correlation between the instantaneous value, $u_\alpha(\mathbf{k},t)$, and the partially time averaged value, $\langle u_\alpha(\mathbf{k},t)\rangle_\tau$, computed from a 64^3 simulation. The correlation is shown as a function of the averaging time, τ, scaled on the eddy turnover time, τ_E, for $k = 5,10,15,20,25$.

Runs have been performed on a 64^3 grid, with a Reynolds number of $R_\lambda \approx 70$. The velocity field was first evolved until a statistically stationary state was achieved and then averages of the sort defined in equations (9.10)–(9.12) were computed for a range of averaging times.

We have investigated the relationship between an instantaneous velocity field, $u_\alpha(\mathbf{k},t)$, and its partially time averaged value, $\langle u_\alpha(\mathbf{k},t)\rangle_\tau$.

9.5 Results

Here, we consider the correlation between an instantaneous velocity field, $u_\alpha(\mathbf{k},t)$, and its partially time averaged value, $\langle u_\alpha(\mathbf{k},t)\rangle_\tau$. As usual, this is given by,

$$R(u,\langle u\rangle_\tau;k) = \frac{\langle u_\alpha(\mathbf{k},t)\,\langle u_\alpha(-\mathbf{k},t)\rangle_\tau\rangle_s}{\langle u_\alpha(\mathbf{k},t)u_\alpha(-\mathbf{k},t)\rangle_s^{1/2}\,\langle\langle u_\alpha(\mathbf{k},t)\rangle_\tau\,\langle u_\alpha(-\mathbf{k},t)\rangle_\tau\rangle_s^{1/2}}. \qquad (9.13)$$

Results are plotted in Figure 9.3. As we would expect, the level of the correlation falls as the averaging time, τ, is increased. We note, however, that over the range

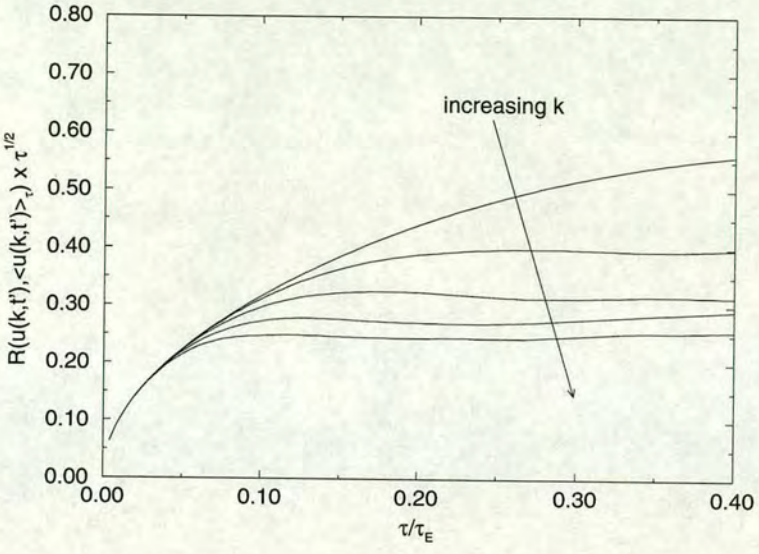

Figure 9.4: The correlation between the instantaneous value, $u_\alpha(\mathbf{k},t)$, and the partially time averaged value, $\langle u_\alpha(\mathbf{k},t)\rangle_\tau$, scaled on $\tau^{-1/2}$ to demonstrate the behaviour as τ increases. The correlation is shown as a function of the averaging time, τ, scaled on the eddy turnover time, τ_E, for $k = 5,10,15,20,25$.

of averaging times considered here, the correlation has not yet reached zero.

Suppose that we define $t_c(k)$ to be the approximate time difference after which two velocity fields are uncorrelated. That is,

$$\langle u_\alpha(\mathbf{k},t)\, u_\alpha(-\mathbf{k},t+t_c(k))\rangle_s \approx 0. \tag{9.14}$$

For example, with reference to Figure 9.2, we would say that $t_c(k=15) \approx 0.17\tau_E$. With this definition, it may be shown (see Appendix A) that

$$R(u,\langle u\rangle_\tau;k) \sim \tau^{-1/2} \quad \text{for} \quad \tau \gg t_c(k), \tag{9.15}$$

assuming that the averaging time does not include later coincidental recorrelations of the sort discussed by Landau and Lifshitz [86]. The validity of this relationship is supported by Figure 9.4. Here we have plotted the correlation again, but this time we have scaled it on $\tau^{-1/2}$. As predicted, we see the appearance of plateaus in the data corresponding to our largest choices of k.

It may also be shown (Appendix A) that an r.m.s. value of the partially time

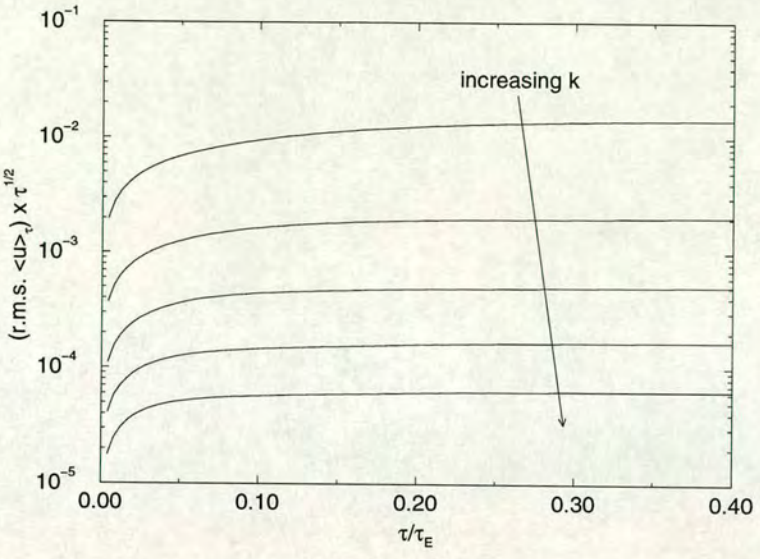

Figure 9.5: r.m.s. values of the partially time averaged field, $\langle u_\alpha(\mathbf{k},t)\rangle_\tau$, scaled on $\tau^{-1/2}$ to demonstrate the behaviour as τ increases. The r.m.s. value is shown as a function of the averaging time, τ, scaled on the eddy turnover time, τ_E, for $k = 5,10,15,20,25$.

averaged field exhibits similar behaviour, i.e.,

$$\langle \langle u_\alpha(\mathbf{k},t)\rangle_\tau \langle u_\alpha(-\mathbf{k},t)\rangle_\tau \rangle_s^{1/2} \sim \tau^{-1/2}. \tag{9.16}$$

Again, this result is supported by our data, as demonstrated in Figure 9.5.

An implication of this last result, since the ensemble average of u must be zero, is that the way in which the partial time average collapses to the full ensemble average will also be governed by $\tau^{-1/2}$. This suggests that we require infinite time for the time average to be the same as the ensemble average (as once would expect), but that we might obtain an arbitrarily close approximation to the ensemble average over a suitably chosen finite time.

A discussion of how the results of this chapter may be applied to the conditional average will be deferred until Chapter 12.

Chapter 10

The Model Field of Yang

The model field of Yang [9] was described in in Section 7.2.1. In this chapter we have attempted to compute the model field numerically, and have proceeded to carry out direct tests of its properties which we may compare with those that the theory proposes.

10.1 Recap of governing equations

Recall that the $\mathbf{v}^-$ field is simply the low-k modes of a member of the full ensemble, and hence its evolution will be governed by the Navier-Stokes equation,

$$\left(\frac{\partial}{\partial t} + \nu k^2\right) V_\alpha(\mathbf{k}, t) = M_{\alpha\beta\gamma}(\mathbf{k}) \sum_{\mathbf{j}} V_\beta(\mathbf{j}, t) V_\gamma(\mathbf{k} - \mathbf{j}, t), \tag{10.1}$$

where we will make the definition $\mathbf{v}^- \equiv \mathbf{V}^-$.

The $\mathbf{v}^+$ field is defined in terms of its evolution equation, given previously in equation (7.36) and repeated here:

$$\begin{aligned} &\left[\frac{\partial}{\partial t} + \nu_0 k^2\right] v_\alpha^+(\mathbf{k}, t) \\ &= M^+_{\alpha\beta\gamma}(\mathbf{k}) \int \mathrm{d}^3 j \; v_\beta^-(\mathbf{j}, t) v_\gamma^-(\mathbf{k} - \mathbf{j}, t) + v_\beta^+(\mathbf{j}, t) v_\gamma^+(\mathbf{k} - \mathbf{j}, t). \end{aligned} \tag{10.2}$$

We may refer to this field as being *parasitic*, which is to say that it "feeds" off the $\mathbf{v}^-$ field, while the $\mathbf{v}^-$ field is itself unaffected.

Our aim is to simulate equation (10.2), and to make some deductions about the properties of the $\mathbf{v}^+$ field.

10.2 Computational details

The basic DNS code is obviously sufficient for the calculation of the $\mathbf{V}$ field — it is simply the Navier-Stokes equation again. The $\mathbf{v}^+$ field is calculated alongside the $\mathbf{V}$ field using a Runge-Kutta method analogous to that explained in Section 3.8.

The simulation has been performed in the following manner:

1. From random initial conditions, integrate the $\mathbf{V}$ field forward through time until it is fully evolved. This is simply a standard DNS.

2. Generate an initial $\mathbf{v}^+$ field.

3. Simultaneously evolve $\mathbf{V}$ and $\mathbf{v}^+$ forward through time.

We have carried out this simulation on a 64^3 grid with a kinematic viscosity of $\nu = 0.01189$ and an energy input rate of $\varepsilon_w = 1$. This gave a microscale Reynolds number of $R_\lambda \approx 70$. The $\mathbf{V}$ field was considered to have evolved (the dissipation rate had begun varying around the energy input rate) after approximately 8 evolved eddy turnover times and so it was at this point that the $\mathbf{v}^+$ field was generated by setting,

$$\mathbf{v}^+(\mathbf{k}, t = t_s) = \mathbf{V}^+(\mathbf{k}, t = t_s), \tag{10.3}$$

where t_s is the time at which the $\mathbf{v}^+$ field was generated. We have considered two choices of cutoff wavenumber, $k_c = 16$ and $k_c = 24$.

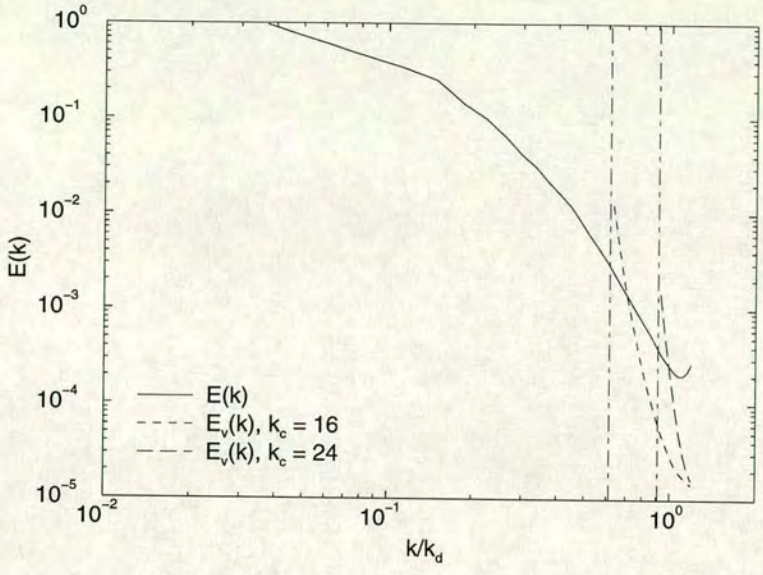

Figure 10.1: The energy spectra obtained from Yang's model field for two choices of cutoff wavenumber, $k_c = 16$ and $k_c = 24$, compared with the usual energy spectrum.

10.3 Results

10.3.1 Model field spectra

In defining the model field, Yang states that it is hoped that the term which has been omitted from the $\mathbf{v}^+$ equation does not play "the dominant role in energy transfer between scales" [9]. Our analysis of the partitioned nonlinear term in Chapter 8 suggests that, in fact, quite the contrary appears to be true and this is borne out when we look at the energy spectra of the model field. The energy spectrum of the $\mathbf{V}$ field, $E(k)$, is defined in the usual way, with the spectrum of the $\mathbf{v}^+$ field defined analogously as,

$$E_v(k) = 2\pi k^2 \left\langle v_\alpha^+(\mathbf{k},t) v_\alpha^+(-\mathbf{k},t) \right\rangle, \tag{10.4}$$

on the interval $k_c \leq k \leq k_{max}$.

These energy spectra are plotted in Figure 10.1 for both our cutoff wavenumbers. We see that the energy spectra of the $\mathbf{v}^+$ fields are an order of magnitude larger than the standard energy spectrum at $k = k_c$ and an order of magnitude smaller

at $k = k_{max}$. Referring back to the partitioned transfer spectra given in Figures 8.13–8.16 the reason for this shape is clear. The retained $v^- v^-$ term transfers energy to just beyond the cutoff at which point, the $v^- v^+$ term would usually transfer the energy to higher wavenumbers. However, in its absence, energy builds up around k_c and is not properly transferred to higher-k, giving rise to the observed deficit.

10.3.2 Field comparisons at high wavenumber

A further comparison between the $\mathbf{V}^+$ and $\mathbf{v}^+$ fields has been made by computing correlations, defined in the usual way,

$$R(V^+, v^+; k) = \frac{\langle V_\alpha^+(\mathbf{k}) v_\alpha^+(-\mathbf{k}) \rangle}{\langle |\mathbf{V}^+(\mathbf{k})|^2 \rangle^{1/2} \langle |\mathbf{v}^+(\mathbf{k})|^2 \rangle^{1/2}}. \tag{10.5}$$

Correlation results for cutoff wavenumbers of $k_c = 16$ and $k_c = 24$ are given in Figures 10.2 and 10.3 respectively. From these results it would appear that the $\mathbf{v}^+$ field takes up an approximately fixed relationship with $\mathbf{V}^+$, which is reached within approximately half an eddy turnover time. This relationship implies some sort of continuing dependency on $\mathbf{V}^- \equiv \mathbf{v}^-$ which would seem to contradict the idea that "there is no phase relationship ... between $\mathbf{v}^-$ and $\mathbf{v}^+$" [9]. We note that the correlation seems to drop away to zero for $k \gg k_c$ which implies that the two fields become out of phase in this limit. However, as the results in the next section will demonstrate, the strong deterministic connection between the two fields appears to remain.

10.3.3 Alternative initial model fields

To test that the apparent dependency of the $\mathbf{v}^+$ field on the $\mathbf{v}^-$ field was not simply a result of initial conditions, the $k_c = 24$ run was performed again, this time setting $\mathbf{v}^+(\mathbf{k}, t = t_s) = 0$.

If was found that after only approximately 0.2 of an eddy turnover time, the new

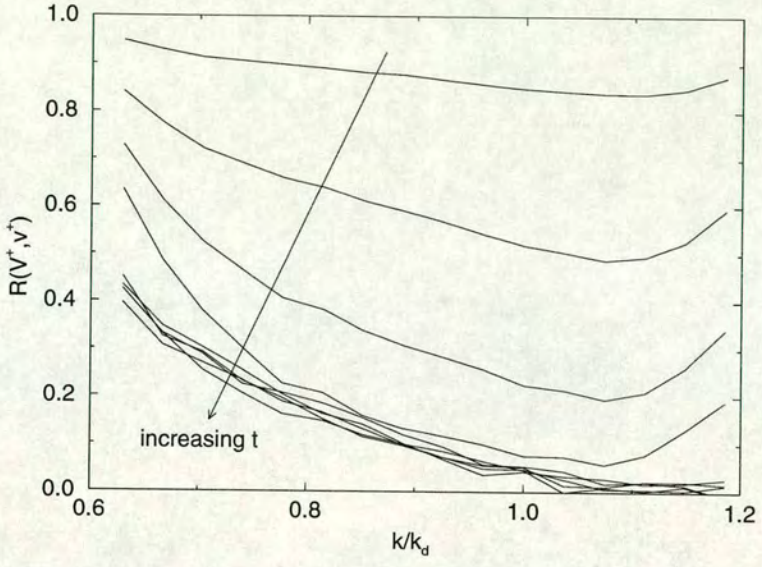

Figure 10.2: The correlation between Yang's model field and the usual field in the high-wavenumber region, for $k_c = 16$.

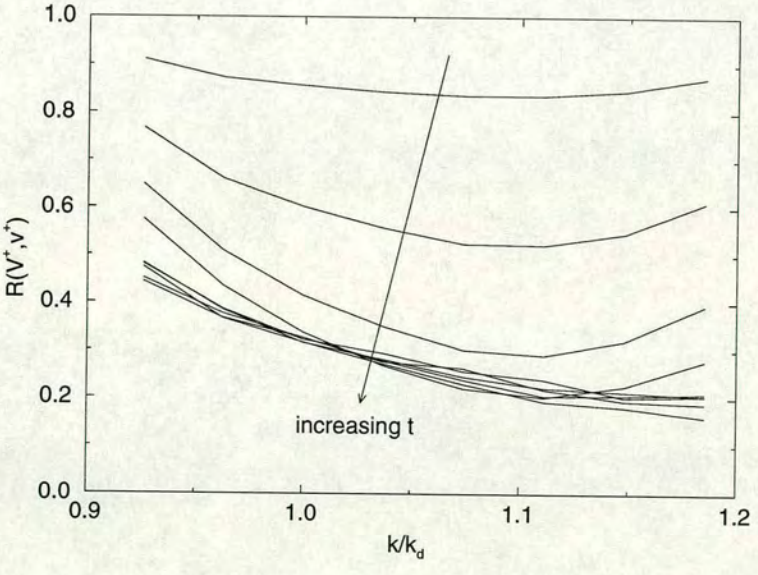

Figure 10.3: The correlation between Yang's model field and the usual field in the high-wavenumber region, for $k_c = 24$.

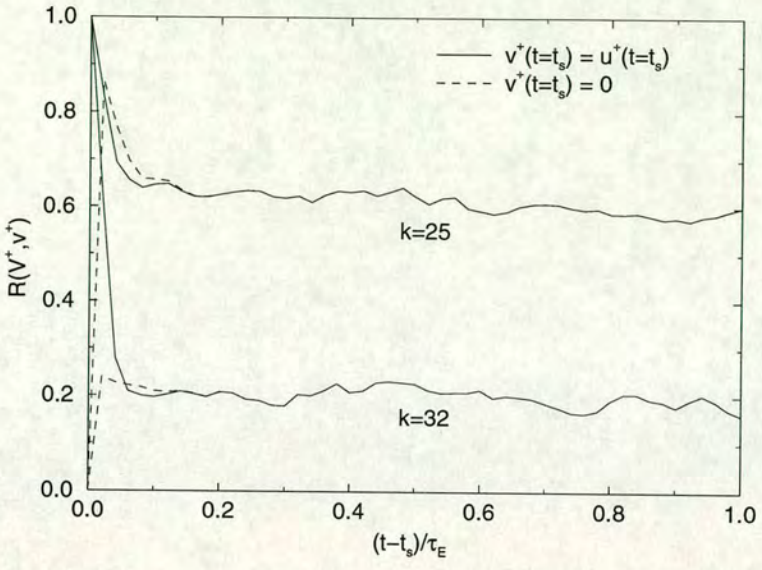

Figure 10.4: The correlation between Yang's model field and the usual field in the high-wavenumber region plotted against time for different field initialisations and for $k_c = 24$.

$\mathbf{v}^+$ field had developed an *identical* energy spectrum and an *identical* correlation with the $\mathbf{V}^+$ field. This latter point is illustrated in Figure 10.4 where the correlation values for the two initial conditions have been plotted against time for $k = 25$ and $k = 32$.

The implication is that the two $\mathbf{v}^+$ fields are themselves identical and this raises a serious problem when we consider the theoretical properties of the $\mathbf{v}^+$ field. Recall (Section 7.2.1) that while $\mathbf{v}^-$ is fixed, it is hoped that $\mathbf{v}^+$ is unconstrained so that,

$$\left\langle \mathbf{v}^+ \right\rangle_c = \left\langle \mathbf{v}^+ \right\rangle = 0. \tag{10.6}$$

In fact, it would appear that to fix $\mathbf{v}^-$ is to fix $\mathbf{v}^+$ (which is perhaps unsurprising considering the deterministic nature of the governing equation) so that,

$$\left\langle \mathbf{v}^+ \right\rangle_c = \mathbf{v}^+, \tag{10.7}$$

an undesirable result.

10.4 Conclusions

The numerical tests which have been performed suggest that the model field proposed by Yang [9] does not have the desired properties.

In particular, the assumption that the omitted term in the governing equation for $\mathbf{v}^+$ would not contribute greatly to the transfer of energy seems flawed. This conclusion is based both upon the *a priori* study of partitioned transfer spectra (as given in Chapter 8) and on the *a posteriori* examination of a field evolved according to the proposed equation.

Secondly, the connection between the $\mathbf{v}^-$ and $\mathbf{v}^+$ fields is retained, meaning that fixing $\mathbf{v}^-$ also fixes $\mathbf{v}^+$. This would seem to rule out one of the desired properties of the $\mathbf{v}^+$ field — i.e. that its conditional average should reduce to an ensemble average.

Our usual caveat, that we are working at relatively low Reynolds numbers, must of course apply. This is exacerbated in this case in that the simulation itself has only been performed on a 64^3 grid — although we note that the transfer spectra results were obtained on a 256^3 grid. Additionally, the determinism of the model field equation (apparently leading to the permanent connection between the $\mathbf{v}^-$ and $\mathbf{v}^+$ fields) will remain true irrespective of the Reynolds number considered.

Chapter 11

An Operational Procedure for Large Eddy Simulation

In this chapter we introduce an *ad hoc* operational large eddy simulation (OpLES) procedure where we take a pragmatic approach to the problem of the missing scales of motion. Although the technique itself is somewhat different from a standard eddy-viscosity model, we shall see that it may be interpreted in terms of such a quantity.

11.1 The effect of mode removal

We begin by asking the question: what happens to a numerical simulation if we simply drop wavenumbers beyond some cutoff, k_c? Experience shows us that the answer is that we see a build-up of energy appearing in the energy spectrum at the cutoff. We shall refer to this feature as an *upturn*. Indeed, this effect is clearly present in our DNS results (see Figure 5.13, for example). However, in this case, $k_c > k_d$ and hence the overall effect is small and localized.

In the case of a truncation with $k_c \ll k_d$, the effects are more severe. To illustrate this point, we have performed a simulation with the same input parameters as our 256^3 simulation, so that $k_d \approx 110$, but have set $k_c = 30$. There is no form of

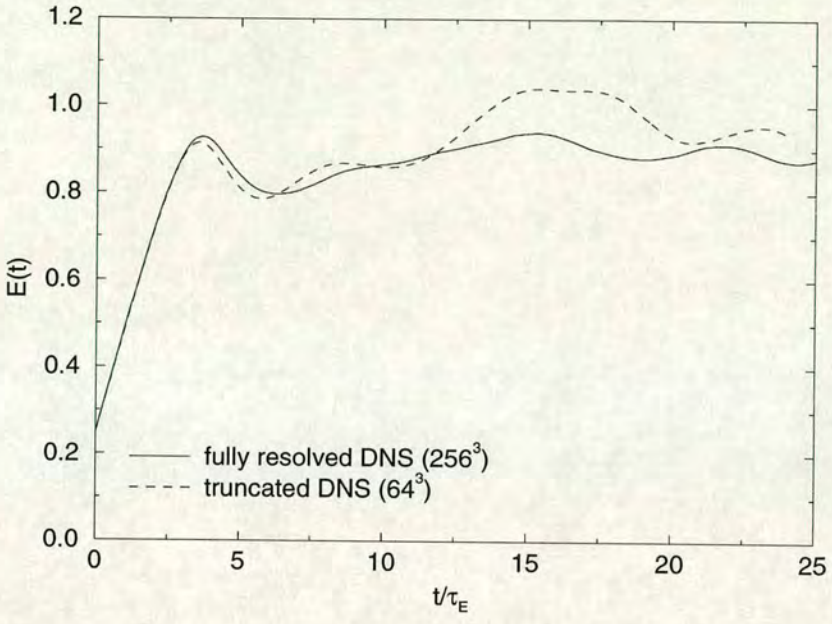

Figure 11.1: The evolution of total energy of a truncated (64^3) DNS, compared to that from a fully resolved (256^3) simulation. For the most part there appears to be reasonable agreement.

subgrid modelling to compensate for the missing modes.

Figure 11.1 shows the evolution of total energy resulting from such a simulation. At this level of comparison, there do not appear to be many problems. However, a comparison of evolved energy spectra, plotted in Figure 11.2, shows that the distribution of energy within the retained modes is clearly wrong. In this figure we can see both the small upturn at the end of the fully-resolved DNS spectrum, and the very large upturn in the truncated DNS spectrum.

Additionally, an examination of the velocity derivative skewness enables us to get some feel for the structural aspects of turbulence. For a 256^3 DNS, we have already seen that we obtain a skewness of approximately -0.5. However, in the case of a truncated DNS or LES we have thrown away the small scales which give rise to a large proportion of that skewness [73] and so would expect a lower value. In order to provide a value for comparison, therefore, we have taken six 256^3 velocity fields, truncated them down to 64^3 and then measured the skewness.

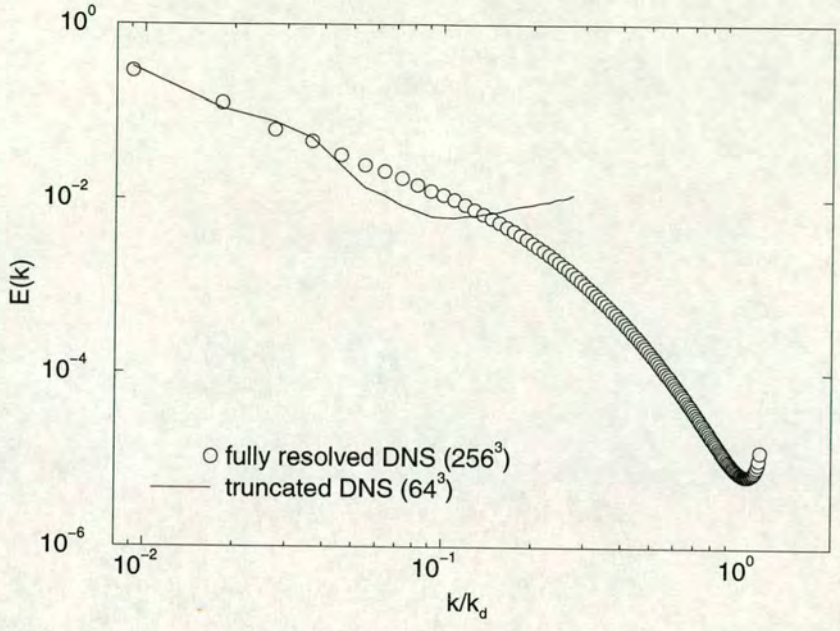

Figure 11.2: The energy spectrum of a truncated (64^3) DNS, compared to that from a fully resolved (256^3) simulation. An upturn is seen to dominate the truncated spectrum.

The value was found to be -0.33 ± 0.04. In contrast, the *unresolved* 64^3 simulation gives a velocity derivative skewness of -0.12 ± 0.04, which is well below this value and indicative of structural problems.

The operational procedure which will be proposed in this Chapter has been designed in an attempt to eliminate the upturn in the energy spectrum.

11.2 A proposed operational procedure

The upturn seen in Figure 11.2 is an extreme example — the result of the long time integration of a truncated system, with no model for the absent modes. In practice, we would like to apply our operational procedure at each step and prevent the development of a large upturn.

Figure 11.3 shows an example of how an upturn might look at an earlier stage of development. Because we will be working extensively with logarithmic quantities, we will use the shorthand notation, $\mathcal{E} = \ln E$ and $\mathcal{K} = \ln k$.

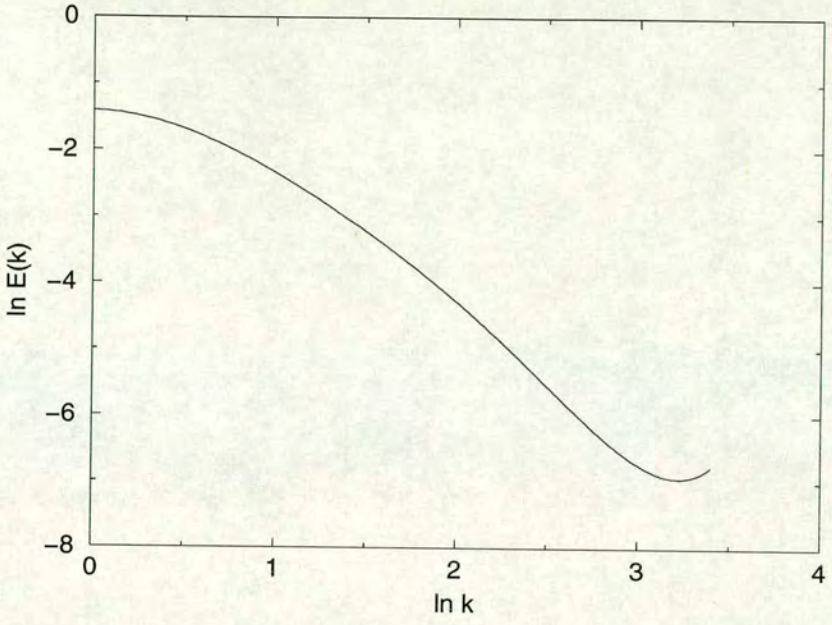

Figure 11.3: A developing upturn in the energy spectrum of a truncated (64^3) DNS.

We now introduce the ansatz that will form the basis of our operational LES procedure:

> *$\mathcal{E}(\mathcal{K})$ should decrease with increasing $\mathcal{K}$. Furthermore, the rate of that decrease should itself be non-increasing.*

To put this in more mathematical terms, we require that,

$$\frac{\mathrm{d}\mathcal{E}}{\mathrm{d}\mathcal{K}} < 0, \tag{11.1}$$

$$\frac{\mathrm{d}^2\mathcal{E}}{\mathrm{d}\mathcal{K}^2} \leq 0. \tag{11.2}$$

With this in mind, we will define the onset of the upturn, $\mathcal{K}_{upturn}$, to be at the minimum of $\mathrm{d}\mathcal{E}/\mathrm{d}\mathcal{K}$. Furthermore, we will denote the minimum value of the derivative to be,

$$\Gamma = \left.\frac{\mathrm{d}\mathcal{E}}{\mathrm{d}\mathcal{K}}\right|_{\mathcal{K}_{upturn}}. \tag{11.3}$$

The proposed OpLES procedure is then,

1. Carry out time-integration in the usual way.

2. Compute the shell-averaged energy spectrum, $\mathcal{E}_S(\mathcal{K})$.

3. Identify $\mathcal{K}_{upturn}$, the onset of the upturn.

4. Generate a corrected spectrum, $\mathcal{E}_C(\mathcal{K})$, by extrapolating $\mathcal{E}_S(\mathcal{K})$ forward from $\mathcal{K}_{upturn}$ with a constant gradient of Γ.

5. Apply the corrected spectrum to the velocity field.

We note that there is an implicit locality assumption made here. We suppose that there is some wavenumber, k_{upturn}, prior to which the system is unaffected by the truncation at k_c. It is then further assumed that the information in modes $k \leq k_{upturn}$ will allow us to infer the rest of the spectrum, up to k_c.

Steps 1, 2, 4 and 5 of the proposed algorithm are computationally straightforward — indeed, steps 1 and 2 are already present in a standard DNS. However, step 3 has proven somewhat trickier to turn into a computational algorithm. The development of a means of carrying out this step is detailed over the next few sections.

11.3 Identifying the upturn — the problem

Having computed the shell-averaged energy spectrum, $\mathcal{E}_S(\mathcal{K})$, we wish to then generate its derivative and an obvious means of doing this would be to use the centred difference method, that is,

$$\left.\frac{\mathrm{d}\mathcal{E}_S}{\mathrm{d}\mathcal{K}}\right|_{\mathcal{K}'} \approx \frac{\mathcal{E}_S(\mathcal{K}'+\Delta\mathcal{K}) - \mathcal{E}_S(\mathcal{K}'-\Delta\mathcal{K})}{2\Delta\mathcal{K}}. \tag{11.4}$$

In practice, however, the shell-averaged energy spectrum is insufficiently smooth for this to be effective and this is illustrated in Figure 11.4.

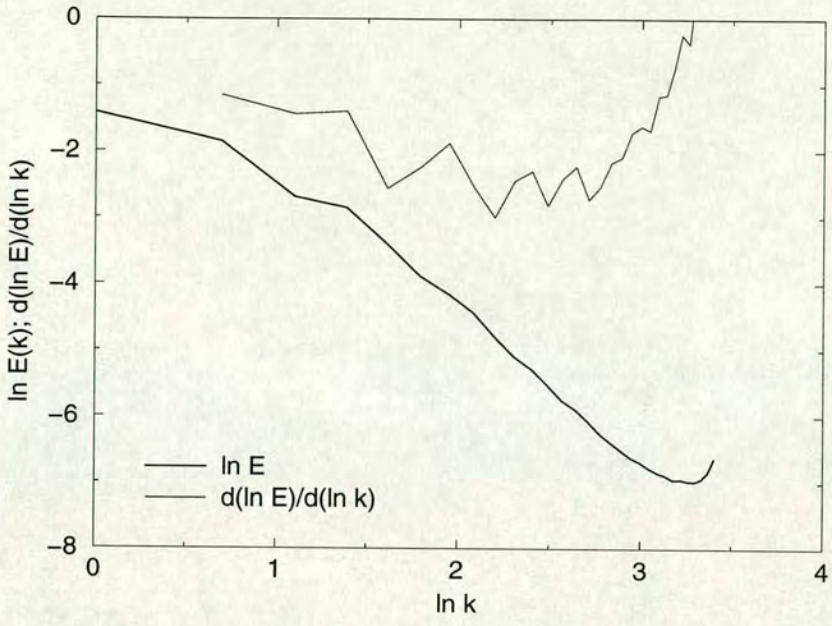

Figure 11.4: An actual shell-averaged energy spectrum with its derivative, computed using the centred difference method.

It seems obvious, therefore, that we need to apply some sort of smoothing to the shell-averaged energy spectrum before determining its derivative. Two possible methods of achieving this were explored.

11.4 Identifying the upturn — Method I

11.4.1 Proposed algorithm

Initially, we investigated what would happen if the shell-averaged energy spectrum, $E_S(k)$, were smoothed simply by averaging over neighbouring points to give $E_A(k)$. If we have shells for $k_n = 1, 2, \ldots, k_N$ then this operation may be expressed as:

$$E_A(k_1) = [E_S(k_1) + E_S(k_2)]/2 \tag{11.5}$$

$$E_A(k_n) = [E_S(k_{n-1}) + E_S(k_n) + E(k_{n+1})]/3 \text{ for } 1 < n < N \tag{11.6}$$

$$E_A(k_N) = [E_S(k_{N-1}) + E_S(k_N)]/2. \tag{11.7}$$

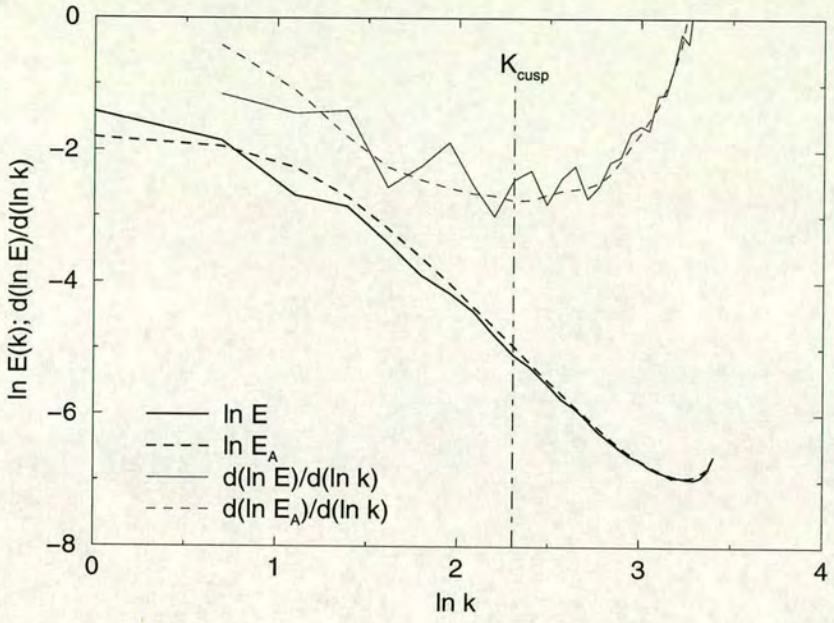

Figure 11.5: The smoothed and unsmoothed energy spectra, with their derivatives.

This procedure can be repeated as many times as required — although there is always a trade-off between the smoothness of the spectrum obtained and how well it matches the original.

Figure 11.5 shows the result of applying three such smoothing steps to our example spectrum with the clear result of a better behaved derivative. We note also that the averaged spectrum is a relatively poor match to the original at low-k, but that it provides a better match at higher-k — most importantly, at $\mathcal{K} = \mathcal{K}_{upturn}$.

The upturn identification step then became,

3a. Smooth the energy spectrum using equations (11.5)–(11.7).

3b. Compute $\mathrm{d}\mathcal{E}_{\mathcal{A}}/\mathrm{d}\mathcal{K}$ and use it to find $\mathcal{K}_{upturn}$ (the location of the minimum) and Γ (the minimum value).

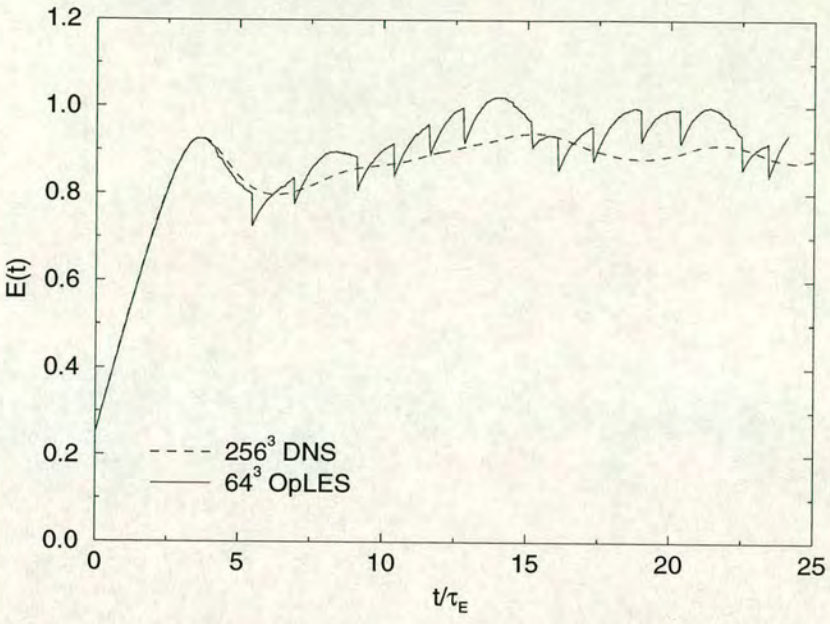

Figure 11.6: The evolution of total energy for a 64^3 OpLES using method I, compared to that for a 256^3 DNS with the same input parameters.

11.4.2 Results

We carried out an OpLES, using the above algorithm, on a 64^3 grid, with input parameters set up to match those of our 256^3 DNS ($\varepsilon_w = 0.149$ and $\nu = 0.001$). This allows us to compare our results directly.

Figure 11.6 shows how the total energy in the system evolves with time. From this result alone, it might appear that the OpLES procedure is outperformed by the truncated DNS described earlier in the chapter (see Figure 11.1). However, if we look at the time-averaged energy spectrum, plotted in Figure 11.7 then we see a great improvement. It should also be noted that this spectrum exhibits very large error bounds, particularly at high-k. This reflects the fact that the instantaneous energy spectra vary greatly and corresponds to the sharp energy losses seen in Figure 11.6.

The cause of these energy losses can be clearly seen in Figure 11.8. The problem arises when the (log of the) shell-averaged energy spectrum, $\mathcal{E}(\mathcal{K})$ has a fairly con-

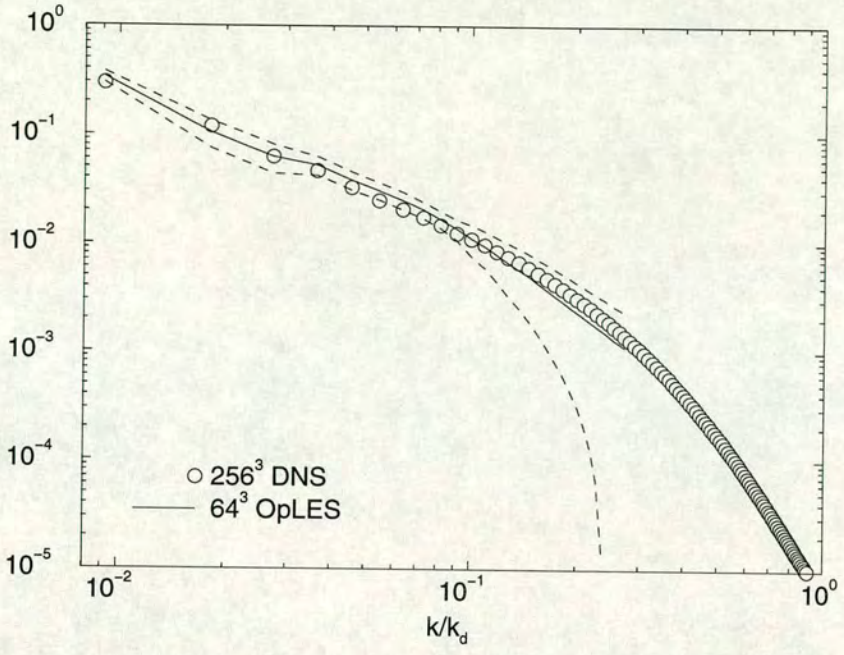

Figure 11.7: Time-averaged energy spectrum for a 64^3 OpLES using method I, compared to that for a 256^3 DNS with the same input parameters. The dashed lines, here and in subsequent energy spectra plots, indicate the error bounds on the OpLES spectrum, defined as twice the standard deviation.

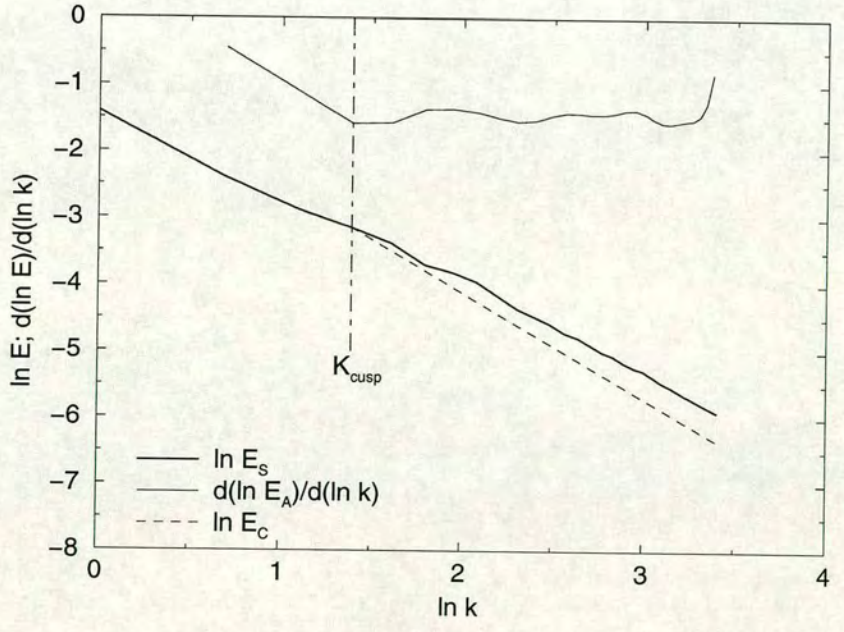

Figure 11.8: Energy spectra before ($\mathcal{E}_S$) and after ($\mathcal{E}_C$) the application of OpLES method I, showing the cause of the sharp energy losses.

stant gradient. In this circumstance it is entirely possible to misidentify $\mathcal{K}_{upturn}$ with the result that the OpLES procedure removes far too much energy.

This figure (with data taken from the actual OpLES run) also demonstrates how an upturn actually looks in practice. With the OpLES procedure not allowing the upturn to develop it is practically invisible when one examines $\mathcal{E}(\mathcal{K})$, but is obvious when one looks at the derivative.

In an attempt to prevent this from happening, a slightly modified method was developed.

11.5 Identifying the upturn — Method Ia

11.5.1 Proposed algorithm

Here, the smoothing algorithm is unchanged, but we modify our definition of $\mathcal{K}_{upturn}$:

> $\mathcal{K}_{upturn}$ is the point at which the derivative, $\mathrm{d}\mathcal{E}/\mathrm{d}\mathcal{K}$, starts increasing monotonically.

In other words we seek out the final local minimum. For the case shown in Figure 11.8, this would make $\mathcal{K}_{upturn} \approx 3.25$ and should result in a more suitable corrected spectrum.

11.5.2 Results

We performed another OpLES with the same input parameters as previously, but this time using the modified upturn identification scheme.

Figures 11.9 and 11.10 give the total energy and time-averaged energy spectrum respectively. It is immediately obvious that we are seeing a great improvement.

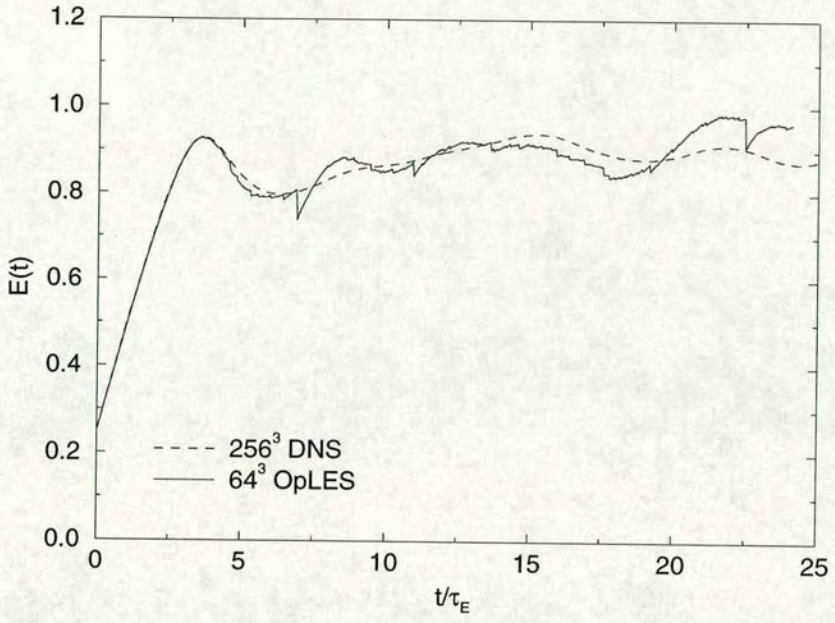

Figure 11.9: The evolution of total energy for a 64^3 OpLES using method Ia, compared to that for a 256^3 DNS with the same input parameters.

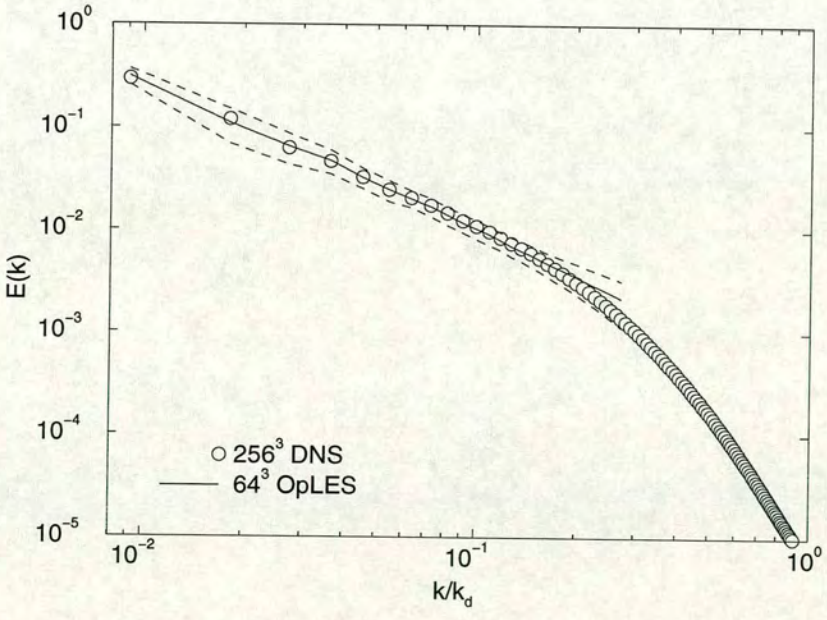

Figure 11.10: Time-averaged energy spectrum for a 64^3 OpLES using method Ia, compared to that for a 256^3 DNS with the same input parameters.

While the total energy is still a little spiky, the number of large energy losses has been reduced dramatically. This also has the effect of significantly reducing the error bounds on the time-averaged energy spectrum whilst still keeping the mean value in good agreement with the DNS spectrum.

11.6 Identifying the upturn — Method II

In this section we outline the technique that was finally settled upon for the upturn identification step, and which will be used for the results given in the rest of this chapter. The aim here was to devise a means of smoothing the shell-averaged energy spectrum in a way which was mathematically more rigourous than that which was given in Section 11.4. In essence, rather than carrying out local averaging on the spectrum, we fit a curve to it[1].

Given the simple shape of an energy spectrum, we have chosen to use a fourth-order polynomial as our fitting function. We found that lower order fits did not reproduce the cusp, while significantly higher orders followed the spectrum too closely, and hence did not give the required degree of smoothing. The use of a fourth-order polynomial also simplifies later calculations. Our smoothed/fitted energy spectrum, $\mathcal{E}_F(\mathcal{K})$, is thus defined by,

$$\mathcal{E}_S(\mathcal{K}) \approx \mathcal{E}_F(\mathcal{K}) = a_0 + a_1\mathcal{K} + a_2\mathcal{K}^2 + a_3\mathcal{K}^3 + a_4\mathcal{K}^4. \tag{11.8}$$

Numerically, we have used a singular value decomposition (SVD) method to generate the fitting coefficients, $a_0, \ldots, a_4$ [87].

One of the advantages of such a polynomial fit is that the upturn identification process can now be performed mathematically. Recall, that we are looking for

[1] A curve fitting technique was also used in the work of Lamballais *et al* [65]. Here the gradient of the energy spectrum at the cutoff was determined and used to modify the magnitude of an EDQNM-based eddy-viscosity. This, however, is quite distinct from the *ad hoc* method discussed here.

the minimum of the derivative, $\mathcal{E}'_F \equiv \mathrm{d}\mathcal{E}_F/\mathrm{d}\mathcal{K}$ which is now simply given by,

$$\mathcal{E}'_F(\mathcal{K}) = a_1 + 2a_2\mathcal{K} + 3a_3\mathcal{K}^2 + 4a_4\mathcal{K}^3. \tag{11.9}$$

To find the two turning points of such a third order polynomial it is just a case of solving the quadratic equation,

$$\mathcal{E}''_F(\mathcal{K}) = 2a_2 + 6a_3\mathcal{K} + 12a_4\mathcal{K}^2 = 0, \tag{11.10}$$

giving us,

$$\mathcal{K}_{upturn} = \frac{-3a_3 \pm \sqrt{9a_3^2 - 24a_2a_4}}{12a_4}. \tag{11.11}$$

The minimum may then be identified by seeing which of the two solutions has $\mathcal{E}'''_F(\mathcal{K}) > 0$, i.e. we must have,

$$4a_4\mathcal{K}_{upturn} > -a_3. \tag{11.12}$$

In the event that this method fails to locate a suitable $\mathcal{K}_{upturn}$ (if, for example, the discriminant in equation (11.11) is negative, or if the computed $\mathcal{K}_{upturn} < 0$) then no corrections are made to the spectrum.

As will be seen, this method provides both a smoother total energy curve and tighter error bounds on the time-averaged energy spectrum than either of the previous two methods. Full results will be given in Section 11.8 after a complete statement of the OpLES algorithm.

11.7 The complete OpLES algorithm

1. Carry out time-integration in the usual way.

2. Compute the shell-averaged energy spectrum, $\mathcal{E}_S(\mathcal{K})$.

3. Generate $\mathcal{E}_F(\mathcal{K})$, a fourth-order polynomial fit to $\mathcal{E}_S(\mathcal{K})$.

4. Identify $\mathcal{K}_{upturn}$ and Γ by finding the minimum of $\mathcal{E}'_F(\mathcal{K})$.

5. Generate a corrected spectrum, $\mathcal{E}_C(\mathcal{K})$, by extrapolating $\mathcal{E}_S(\mathcal{K})$ forward from $\mathcal{K}_{upturn}$ with a constant gradient of Γ:

$$\mathcal{E}_C(\mathcal{K}) = \begin{cases} \mathcal{E}_S(\mathcal{K}) & \text{for } \mathcal{K} \leq \mathcal{K}_{upturn} \\ \mathcal{E}_S(\mathcal{K}_{upturn}) + \Gamma(\mathcal{K} - \mathcal{K}_{upturn}) & \text{for } \mathcal{K} \geq \mathcal{K}_{upturn} \end{cases}, \tag{11.13}$$

or, equivalently,

$$E_C(k) = \begin{cases} E_S(k) & \text{for } k \leq k_{upturn} \\ E_S(k_{upturn})(k/k_{upturn})^{\Gamma} & \text{for } k \geq k_{upturn} \end{cases}. \tag{11.14}$$

6. Rescale the velocity field using,

$$\mathbf{u}_C(\mathbf{k}) = \mathbf{u}(\mathbf{k})\sqrt{E_C(k)/E_S(k)}, \tag{11.15}$$

in order to give corrected spectrum when shell-averaged.

11.8 Results

11.8.1 Equivalent eddy-viscosities

In addition to the sort of comparisons that we have been making so far, it is also possible to make a direct comparison between the OpLES and a traditional spectral LES by generating an equivalent eddy-viscosity, $\delta\nu(k, t_n)$, at each time step.

This is introduced in exactly the same way as was done for a fixed-spectrum LES in Section 6.3.2. We begin by noting that, for a single computational time step, the evolution of the energy spectrum is a two stage process:

$$E(k, t_n) \overset{\text{integration}}{\longrightarrow} E_S(k, t_{n+1}) \overset{\text{OpLES}}{\longrightarrow} E_C(k, t_{n+1}) \equiv E(k, t_{n+1}),$$

From this, we may state that the rate of energy removal due to the OpLES procedure is given approximately by,

$$\left.\frac{\mathrm{d}E(k,t)}{\mathrm{d}t}\right|_{t=t_n}^{\text{(due to OpLES)}} \approx \frac{E(k, t_{n+1}) - E_S(k, t_{n+1})}{\delta t}. \tag{11.16}$$

Run	N	ν	ε_w	k_c/k_d	k_c	k_d	R_λ
I	64	1×10^{-3}	0.149	0.27	30	110	190
II	64	4×10^{-4}	0.150	0.14	30	220	280
III	128	2×10^{-4}	0.274	0.14	60	430	430
IV	64	6×10^{-5}	0.150	0.033	30	913	680

Table 11.1: Details of runs performed.

Following the method given in the discussion of fixed-spectrum LES, this leads us to a definition of the OpLES eddy-viscosity of,

$$\delta\nu(k, t_n) \equiv \frac{E_S(k, t_{n+1}) - E(k, t_{n+1})}{2k^2 \delta t E(k, t_n)}. \tag{11.17}$$

Equivalent eddy-viscosities of this type will be presented for each of the runs that have been performed.

11.8.2 Details of runs performed and comparisons made

Table 11.1 gives details of the four OpLES runs which have been performed. Run I corresponds to the input parameters for our 256^3 simulation and results for OpLES runs using methods I and Ia have been presented in earlier sections. All of the results presented in this section were produced using OpLES method II.

For run I, we are able to make direct comparisons with the results taken from our 256^3 simulation. For the other runs, we will make comparisons with the model energy spectrum given by Qian [63] and taking the form,

$$E(k) = 1.19\varepsilon_w^{2/3} k^{-5/3} \left(1 + 5.3\,(k/k_d)^{2/3}\right) \exp\left(-5.4\,(k/k_d)^{4/3}\right). \tag{11.18}$$

This model was discussed in Section 6.3.2. We have also used Qian's model spectrum to obtain estimates of the total energy, the eddy turnover time, τ_E (which has been used to scale time), and the Taylor Reynolds number.

For run I, we may also use our 256^3 DNS data to provide an eddy-viscosity (see Section 6.3.1) for comparison with that obtained from the OpLES. For the other runs we have computed eddy-viscosities using the fixed-spectrum LES technique

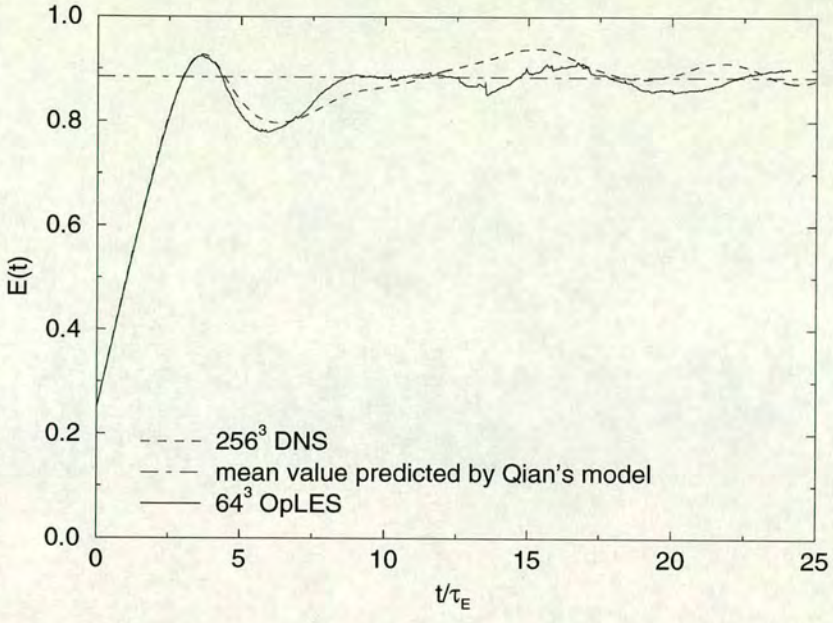

Figure 11.11: Run I: The evolution of total energy for a 64^3 OpLES, compared to that for a 256^3 DNS with the same input parameters. Also plotted is the mean energy value predicted by Qian's model.

given in Section 6.3.2. We will also make comparisons with the eddy-viscosity obtained using the Eddy Damped Quasinormal Markovian (EDQNM) closure approximation,

$$\delta\nu(k) = \left(0.267 + 9.21e^{-3.03(k_c/k)}\right)\left[\frac{E(k_c,t)}{k_c}\right]^{1/2}, \tag{11.19}$$

discussed extensively in Section 6.3.2.

11.8.3 Run I

Figure 11.11 shows how the total energy evolved for run I. This graph may be compared with Figures 11.6 and 11.9 to see that OpLES method II provides a significant improvement. There is still the occasional sharp energy loss but these occurrences are both less frequent and less severe.

The OpLES total energy is in good agreement with that of the DNS and with the value obtained by integrating Qian's model spectrum.

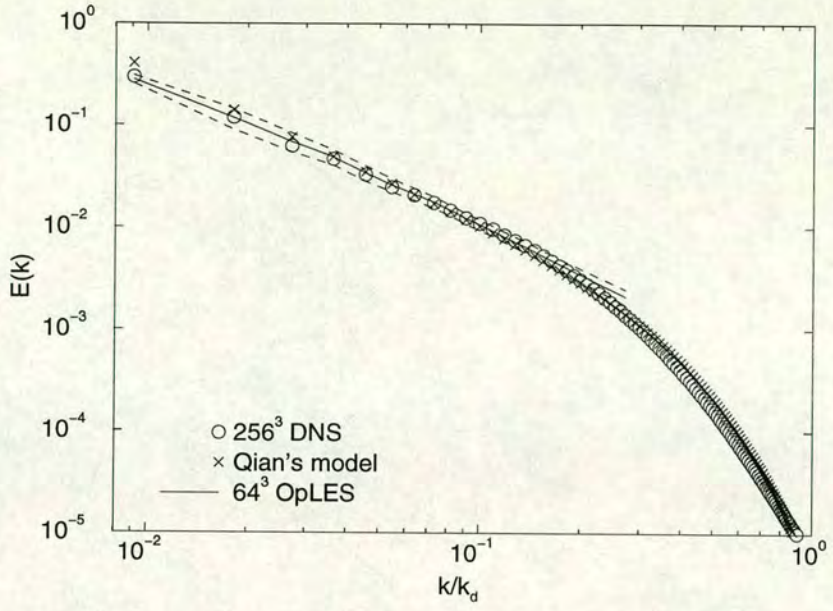

Figure 11.12: Run I: Time-averaged energy spectrum for a 64^3 OpLES, compared to that for a 256^3 DNS with the same input parameters. Also plotted is Qian's model spectrum.

The OpLES energy spectrum (time-averaged over the final 15 eddy turnover times of the simulation) is plotted in Figure 11.12. Again, it is worth comparing this graph with the results given by OpLES methods I and Ia (Figures 11.7 and 11.10) to note that while the mean value is approximately unchanged, the error bounds have been reduced considerably.

The OpLES spectrum compares well with the DNS spectrum, except for a slight overshoot at high-k. This is attributable to the way that OpLES works — once it has located the upturn it extrapolates forward with a constant gradient and hence is unable to reproduce a spectrum, such as this, which continues to grow steeper.

Figure 11.13 shows two instantaneous OpLES eddy-viscosities, computed in the manner described in Section 11.8.1. One corresponds to a "well-behaved" point in the evolution of the total energy, while the other demonstrates what happens when a sharp energy loss occurs.

In computing an average OpLES eddy-viscosity, we do not wish to include the

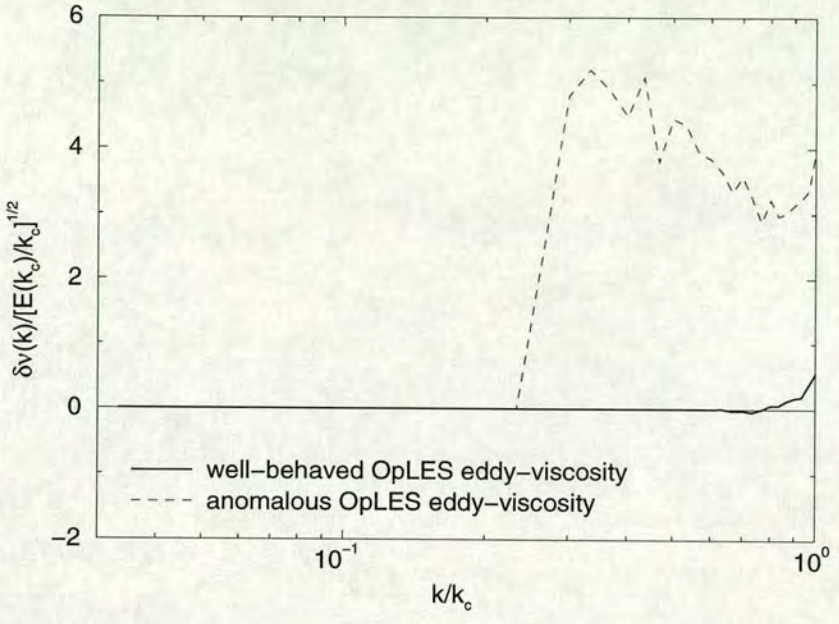

Figure 11.13: Two instantaneous OpLES eddy-viscosities — one taken from a "well-behaved" point in the evolution, the other corresponding to the sharp energy loss at $t/\tau_E \approx 13.5$.

data from such anomalous time steps. To this end, once the mean and standard deviation have been computed, averaging is reperformed, but this time neglecting data which lies outside the bounds given by the mean value plus or minus one standard deviation. This process is then iterated until the mean value converges (defined, in this case, as a change of less that 1% from one step of the iteration to the next).

This is demonstrated in Figure 11.14 where it may be seen that the mean value at low-k is reduced, as hoped, whilst being relatively unchanged elsewhere.

In Figure 11.15, then, we have plotted this averaged eddy-viscosity alongside the predictions from DNS data and from the fixed-spectrum LES run. We have also given the EDQNM eddy-viscosity. We see that there is reasonable agreement between the OpLES eddy-viscosity and the DNS/fixed-spectrum LES predictions although the former is, in general, too low. This corresponds to the energy overshoot seen when we consider the steepening of the energy spectrum at high-

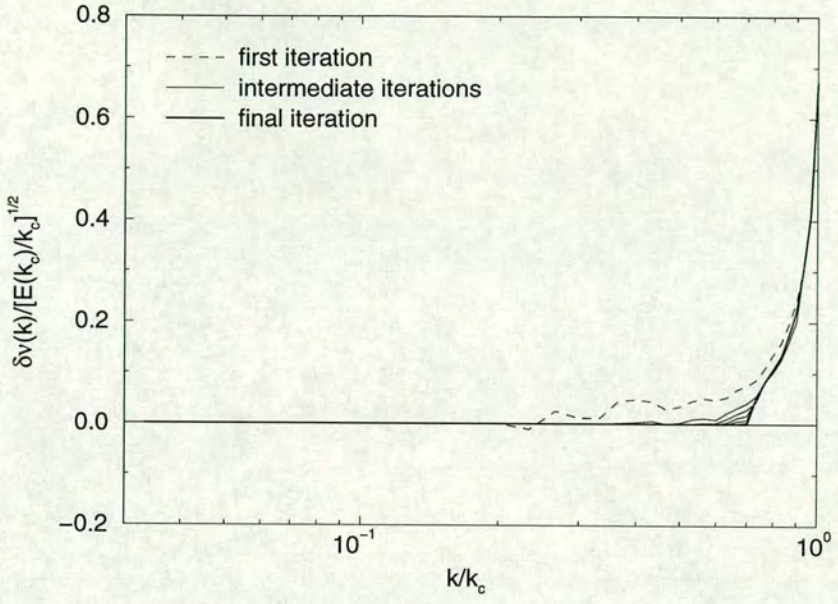

Figure 11.14: Demonstration of the iterative process by which the value of the mean eddy-viscosity is improved upon by repeatedly removing anomalous data.

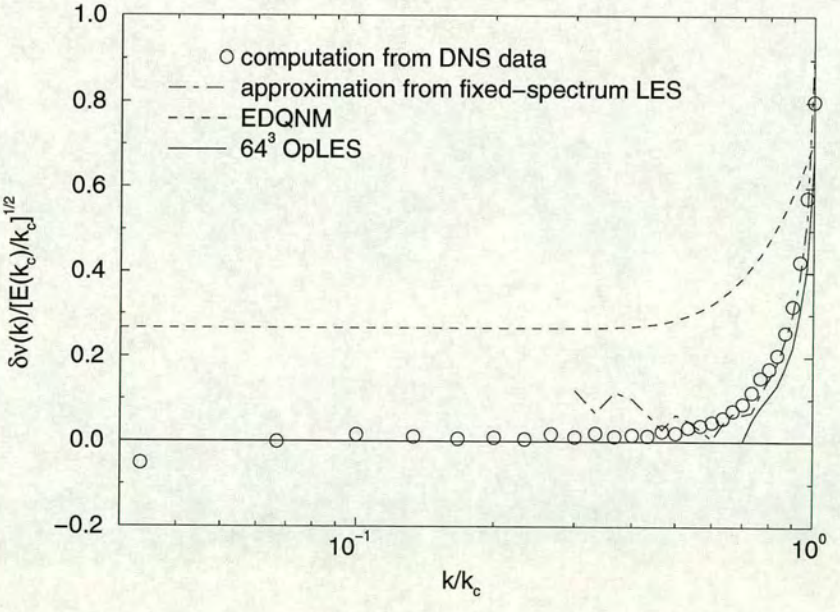

Figure 11.15: Run I: Averaged equivalent eddy-viscosity for a 64^3 OpLES, compared to that obtained from a 256^3 DNS velocity field and that given by a fixed-spectrum LES. Also plotted is the EDQNM eddy-viscosity.

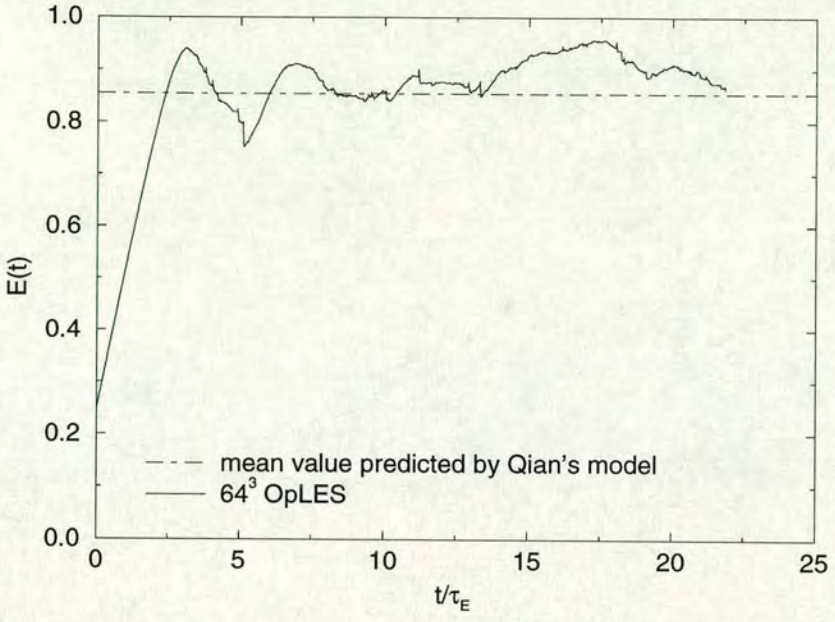

Figure 11.16: Run II: The evolution of total energy for a 64^3 OpLES, compared with the mean energy value predicted by Qian's model.

k. We have already seen (Section 6.3.2) that the EDQNM calculation does not appear to give results comparable to those obtained via the fixed-spectrum LES method at the sort of Reynolds numbers we are considering here.

11.8.4 Run II

For the second run ($R_\lambda \approx 280$), the total energy (Figure 11.16) shows reasonable agreement with the prediction based on Qian's model albeit with a tendency to be slightly too high. The evolution of the total energy appears to be fairly well behaved, although the frequency of the sharp energy losses has increased.

The OpLES energy spectrum (Figure 11.17) matches Qian's model well, although there is, once more, a slight overshoot at high-k. The error bounds have also widened, reflecting the greater variation in the shape of the spectrum over the averaging period.

There is good agreement between the OpLES eddy-viscosity and that predicted

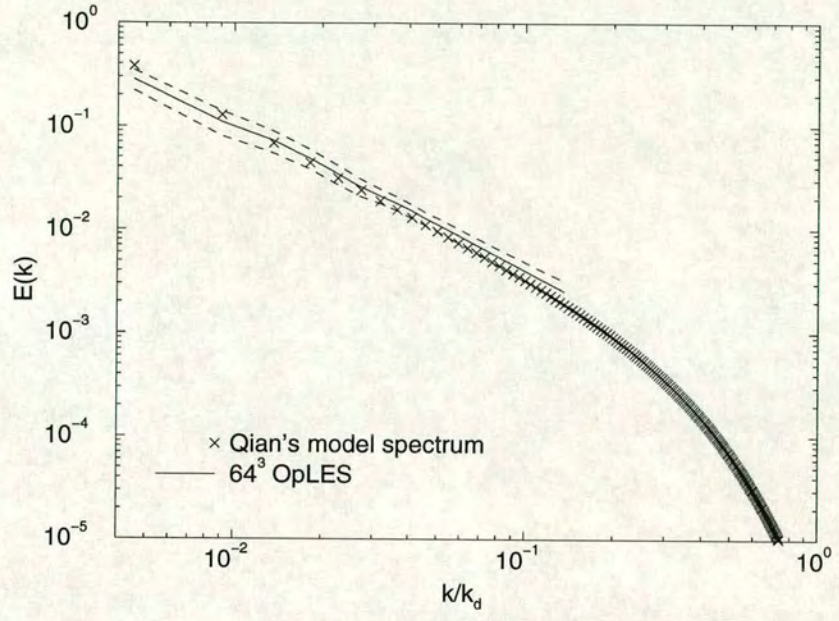

Figure 11.17: Run II: Time-averaged energy spectrum for a 64^3 OpLES, compared to Qian's model spectrum.

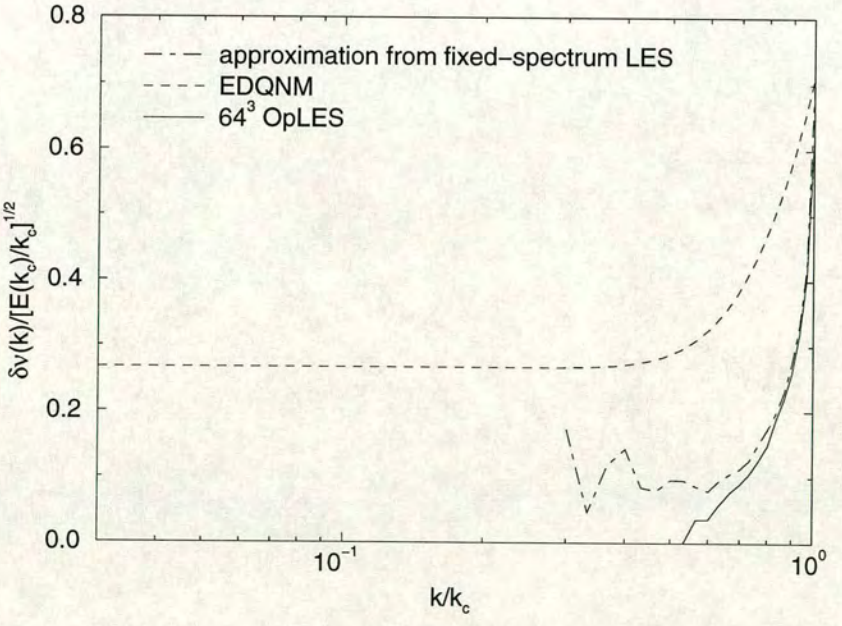

Figure 11.18: Run II: Averaged equivalent eddy-viscosity for a 64^3 OpLES, compared with the fixed-spectrum LES and EDQNM results.

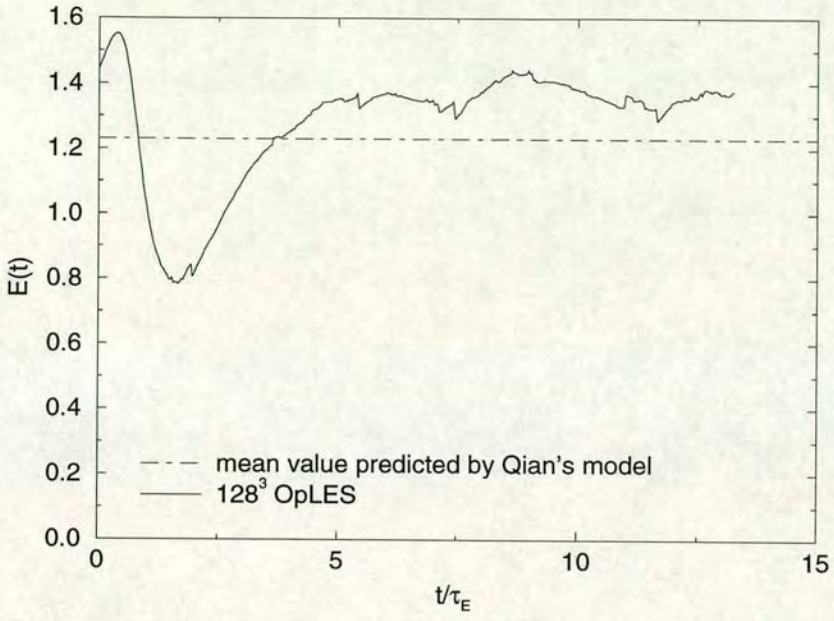

Figure 11.19: Run III: The evolution of total energy for a 128^3 OpLES, compared with the mean energy value predicted by Qian's model.

by the fixed-spectrum LES (Figure 11.18) at high-k — indeed the deficit seen for run I has gone, due to the fact the energy spectrum now has an approximately constant (logarithmic) gradient for $k \leq k_c$. The non-zero plateau at low-k, which one can visualize by imagining an extension of the fixed-spectrum LES plot to low-k, is, however, not present. Indeed, the OpLES algorithm is such that it can *never* give rise to such plateau and this point will be returned to later.

11.8.5 Run III

The third run represents a higher Reynolds number still ($R_\lambda \approx 430$) although by increasing the resolution of the OpLES run from 64^3 to 128^3, we have maintained approximately the same ratio of k_c/k_d.

The total energy (Figure 11.19) is in reasonable agreement with the prediction from Qian's model, but again appears to be a little too high.

The averaged energy spectrum (Figure 11.20) agrees well with Qian's model al-

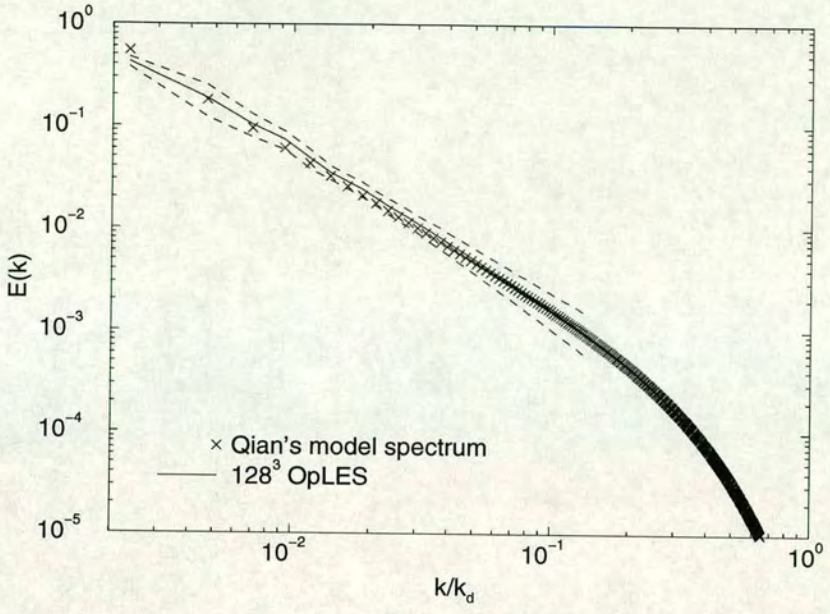

Figure 11.20: Run III: Time-averaged energy spectrum for a 128^3 OpLES, compared to Qian's model spectrum.

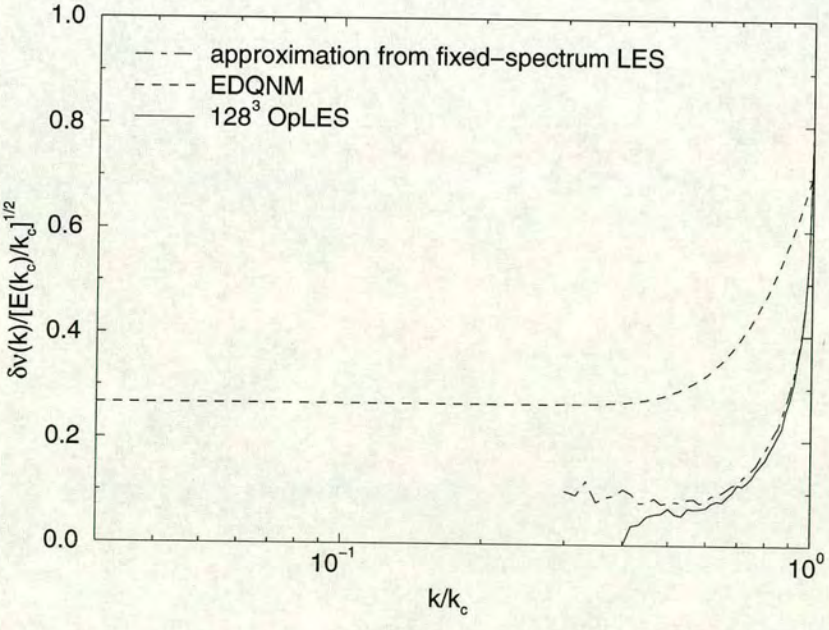

Figure 11.21: Run III: Averaged equivalent eddy-viscosity for a 64^3 OpLES, compared with the fixed-spectrum LES and EDQNM results.

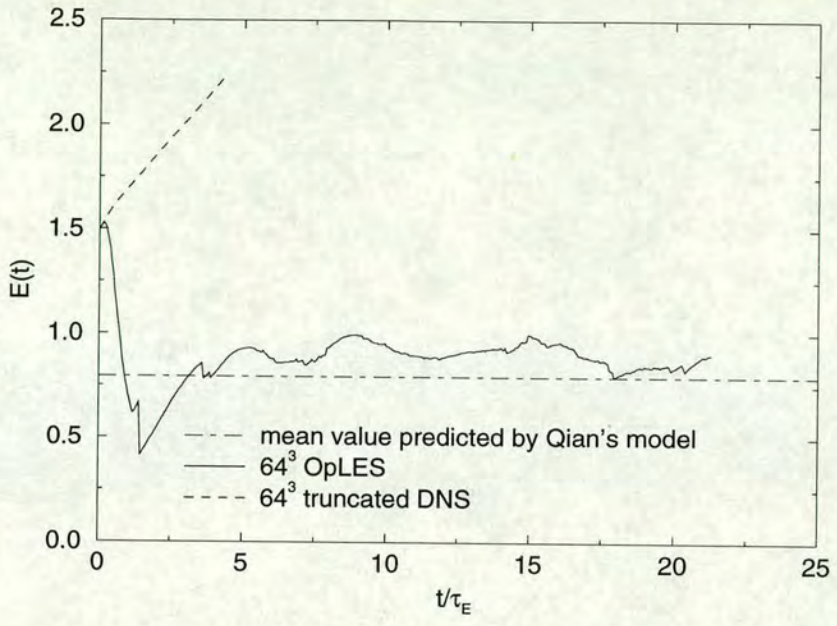

Figure 11.22: Run IV: The evolution of total energy for a 64^3 OpLES, compared with the mean energy value predicted by Qian's model. Also plotted is the total energy for a 64^3 truncated DNS run.

though we again note that the error bounds have grown slightly.

The OpLES eddy-viscosity (Figure 11.21) shows good agreement with that predicted by the fixed-spectrum LES at high-k. Moving towards low-k, we see what appears to be the beginnings of a plateau region but, as noted earlier, this cannot continue and it does, indeed, soon drop to zero.

11.8.6 Run IV

For this final run, we return to a 64^3 OpLES, but further increase the Reynolds number ($R_\lambda \approx 680$). For this run, less than 5% of the "significant" wavenumber modes (i.e. $k < k_d$) are retained and hence this is a severe test of the method.

Figure 11.22 shows that the total energy is once again kept under control and in reasonable agreement with the prediction from Qian's model. The number of sharp energy losses has, again, seen a slight increase. For comparison purposes, (the first few thousand time steps of) a 64^3 truncated DNS run with the

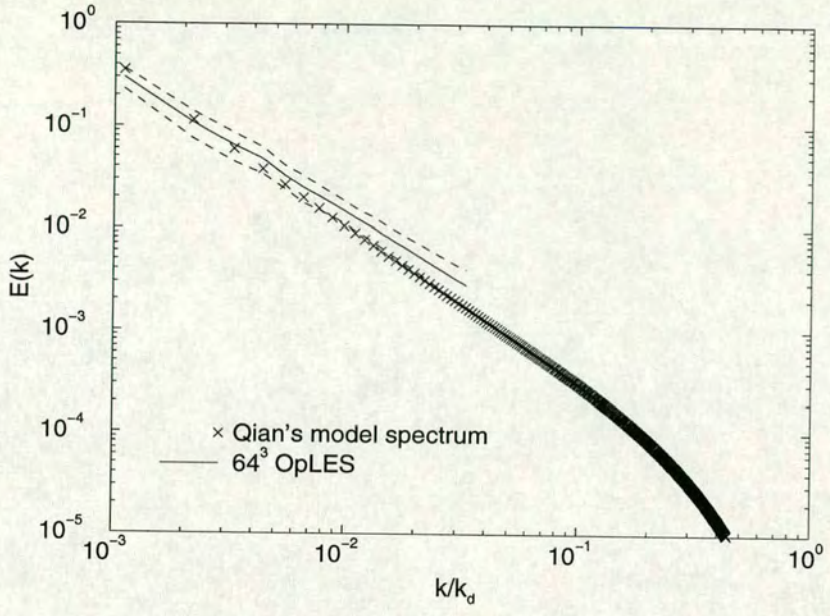

Figure 11.23: Run IV: Time-averaged energy spectrum for a 64^3 OpLES, compared to Qian's model spectrum.

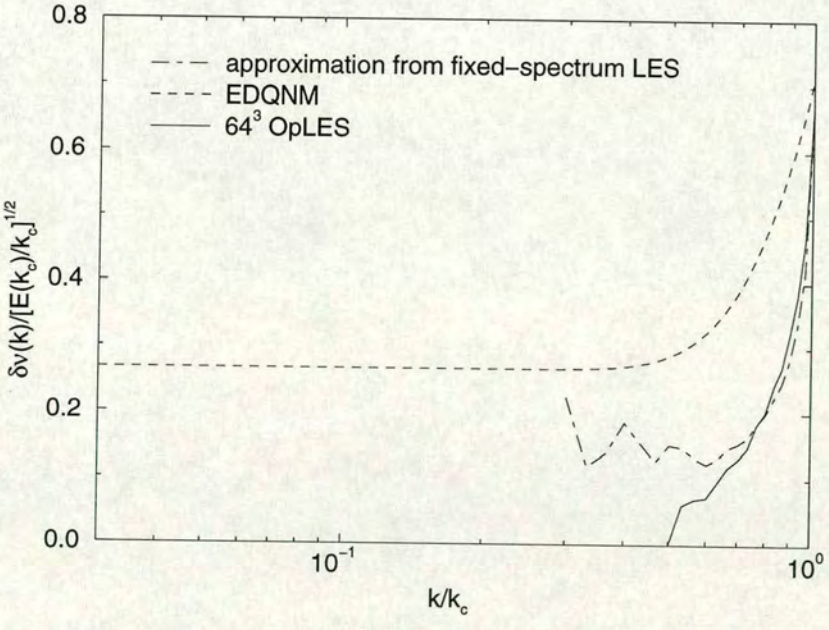

Figure 11.24: Run IV: Averaged equivalent eddy-viscosity for a 64^3 OpLES, compared with the fixed-spectrum LES and EDQNM results.

Run	S
DNS	-0.33 ± 0.04
I	-0.30 ± 0.06
II	-0.29 ± 0.06
III	-0.34 ± 0.05
IV	-0.27 ± 0.05
IV (truncated DNS)	0.00 ± 0.01

Table 11.2: Velocity derivative skewness values obtained from the OpLES runs.

same input parameters has also been plotted. This illustrates far more clearly than Figure 11.1 how badly wrong things can go in the absence of any form of compensation for the missing modes.

The energy spectrum (Figure 11.23) shows some qualitative agreement with Qian's model but has a significant overshoot for high-k. Qian's model spectrum does, however, lie at the lower edge of the error bounds.

As with previous runs, there is reasonable agreement at high-k between the OpLES eddy-viscosity (Figure 11.24) and that predicted by the fixed-spectrum LES, but the plateau at low-k is again missing.

11.9 Skewness comparisons

Table 11.2 shows the skewness values obtained from each of the OpLES runs. In all cases, there is reasonable agreement with the predicted result obtained from our DNS velocity fields although, in general, the mean values obtained from the OpLES simulations are little too low. Run III corresponds to our 128^3 OpLES simulation and the presence of additional scales seems to have increased the magnitude of the skewness in this case.

For comparison, we have also included the value obtained from the truncated DNS which was performed with the parameters of run IV. Here we see that the skewness is approximately zero, markedly different from the expected result.

11.10 Conclusions

It has been demonstrated that the OpLES method of simulating turbulence is able to eliminate the build up of energy at the cutoff wavenumber for a wide range Reynolds numbers.

It is also able to give energy spectra which are in reasonable agreement with those given by Qian's model spectrum although the general trend seems to be for the quality of the agreement to fall off with increasing Reynolds number.

Increasing Reynolds number also brings with it an increase in the frequency of sharp energy losses which may be attributed to the OpLES algorithm misidentifying the upturn. The frequency of this problem was significantly reduced by altering the way the upturn is located from a simple smoothing method to a line-fitting method and it may be possible to improve matters further by devising yet more sophisticated schemes.

We have generated eddy-viscosities, equivalent to the OpLES procedure, which we have seen to be in very good agreement at high-k with those predicted by a fixed-spectrum LES. For lower Reynolds numbers, however, there is an underestimation at high-k which may be attributed to the fact that the correct $\mathcal{E}(\mathcal{K})$ in this region continues to grow steeper. We also see a problem at low-k for all Reynolds numbers examined, in that the OpLES procedure cannot give the required eddy-viscosity plateau — although in the case of our 128^3 simulation (run III) it did appear as though the OpLES was showing the beginnings of a plateau.

In addition, we have also seen that the OpLES eddy-viscosities have, at all Reynolds numbers considered, agreed far better with the results obtained by the fixed-spectrum LES method than those given by the EDQNM calculation. This, we believe, lends mutual support to the validity of both techniques.

Chapter 12

Discussion

12.1 Eddy-viscosities

In Chapter 6 the idea of spectral large eddy simulations was introduced. Then, in Chapter 8 we explored the partitions of the nonlinear term. In this section we shall provide a summary of the ways in which the results presented within these two chapters may be interpreted in the context of eddy-viscosity modelling.

12.1.1 Conclusions

Using DNS data we were able to generate eddy-viscosities empirically, and saw qualitative agreement with the numerical results of other authors [59, 60, 61, 74] as well as with analytical results obtained from the EDQNM closure theory [57]. The form of such eddy-viscosities, with strong cusp-like behaviour exhibited at the cutoff, suggests that the immediate effects of mode truncation on energy transfer are localised [59]. That is to say, it is those modes closest to the cutoff which need the greater compensation for the absent scales.

Further support for this idea of localness may be provided by the correlations we computed between the nonlinear term and each of its partitions. We saw that the '$--$' term, representing coupling within the retained modes, correlates very

strongly with the complete nonlinear term until just before the cutoff. Because these results are a comparison between *instantaneous* quantities, they suggest that the effect of truncation on *phase* transfer is also local.

By correlating the velocity field with the subgrid scale part of the nonlinear term we have directly tested the eddy-viscosity assumption that the latter quantity may be expressed as wavenumber dependent scalar multiple of the former. In agreement with earlier results [78, 79] it was seen that the two fields correlated very poorly. The saving graces for LES are twofold: firstly, the localness ideas we have just discussed mean that the exact properties of the eddy-viscosity only become very significant near the cutoff. Secondly, we know — virtually by definition — that eddy-viscosities are capable of representing the effects of the missing modes when one considers the energy balance equation. However, we have noted that while energy transfer may be correct on a shell-to-shell basis (i.e. on average), it is almost certainly not so when one considers unaveraged point-to-point interactions.

Our results agree with the idea that it is the '$-+$' term which gives rise to the cusp in an eddy-viscosity, while the '$++$' term is responsible for the plateau [74]. We have also seen that while the cusp is present under all of the situations considered, the plateau is often absent. The presence of a plateau seems to indicate either that the cutoff wavenumber, k_c is small, or that the Reynolds number is high meaning that k_c lies in or near an inertial range. From the results available to us it seems likely that either situation may be sufficient. For example, eddy-viscosities computed from 64^3 simulation data (not presented) show plateau behaviour for $k_c = 8$ in the absence of an inertial range. On the other hand, our fixed-spectrum LES results suggest that as Reynolds number is increased, so too is the level of the plateau. These results also gave support to the idea that larger values of k_c could still give rise to plateaus, providing that the Reynolds number was sufficiently high, and further hinted at a connection between the size of the

eddy-viscosity and the value of k_c/k_d.

12.1.2 Suggestions for future work

The idea that the eddy-viscosity might have a direct connection with the value of k_c/k_d is an interesting one. Miyauchi *et al* [61] suggested an eddy-viscosity scaling which included a factor of $(k_c/k_d)^{1/2}$ which did not apply to our data, but it might be worth pursuing the matter further.

Such an investigation might begin with a series of additional fixed-spectrum LES runs, carefully chosen to have identical values for k_c/k_d. However, it is clear that such results would need to be separated from any question of the validity of the fixed-spectrum LES technique and one would therefore require access to a data set representing a velocity field which would allow a suitably large value of k_c to be chosen, and from which one could compute eddy viscosities. Ideally, this data would contain information about all scales — i.e. it would result from a DNS — although it seems likely that such a computational exercise, for large values of k_d, will be beyond the available resources for the foreseeable future. Instead, then, one would have to turn either to a high-resolution LES, or to an idea such as hyperviscosity.

12.2 Renormalization group theories

Here, we take some of the results of the preceding chapters and discuss how they may be cautiously applied to the renormalization group theories of McComb *et al.*

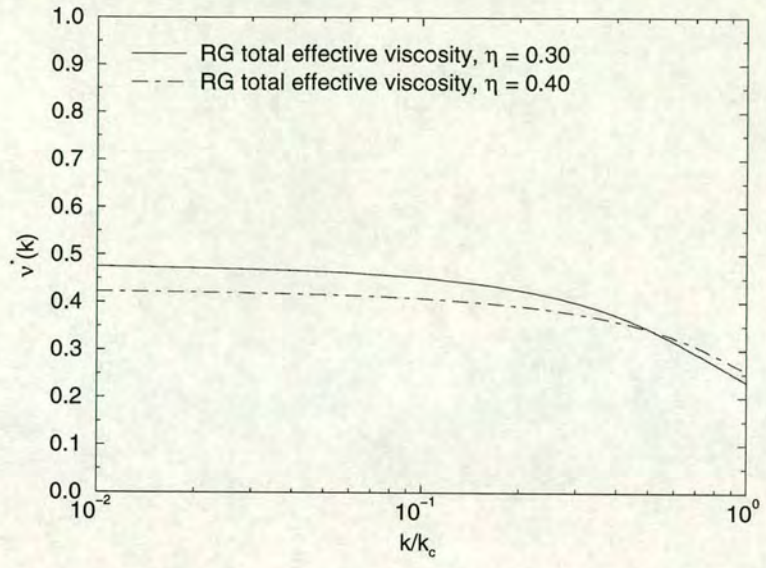

Figure 12.1: The scaled effective viscosity obtained from RG calculations for bandwidths, $\eta = 0.30$ and $\eta = 0.40$.

12.2.1 The effective viscosity

Figure 12.1 shows the total scaled effective viscosity obtained from the RG theory for $\eta = 0.30$ and $\eta = 0.40$ (within the valid range discussed in Section 7.3). The RG eddy-viscosities were computed using a code written by Craig Johnston [11].

A comparison with the empirical eddy-viscosities discussed in Section 6.3.1 immediately indicates a significant qualitative difference in the behaviour as $k \to k_c$. Indeed, the work presented within this thesis has helped to bring about a realisation that the downturn seen in the RG viscosity is almost certainly non-physical.

Furthermore, recent theoretical developments [88] suggest that the eddy-viscosity may only be valid in a heuristic sense — that is to say, while it does not give the correct behaviour when one considers the evolution of a single velocity field it may perform better when ensemble-averaged quantities are considered.

12.2.2 Partitions of the nonlinear term

Part way through the derivation of the two-field theory, equation (7.18) is given for the low-k modes. Employing our current notation, this may be rewritten as,

$$\left[\frac{\partial}{\partial t} + \nu k^2\right] u_\alpha^-(\mathbf{k},t) = \psi_{\alpha--}^-(\mathbf{k},t) + \left\langle \psi_{\alpha++}^-(\mathbf{k},t)\right\rangle_c + \mathrm{O}(\eta^2). \tag{12.1}$$

Using the results obtained throughout this chapter, we can make some attempt to comment on the validity of this equation.

Firstly, we see that the cross term, ψ_{-+}, is not *directly* retained — the subgrid effects are represented solely by the *conditional average* of the ψ_{++} term. This is not the same as the unaveraged value and hence will have different properties including, possibly, some of the effects ordinarily attributed to the cross term, However, we have seen that the cross term plays a vital role in the transfer of energy across the cutoff and that it is responsible for the cusp-like behaviour seen in an eddy-viscosity as $k = k_c$. As such a cusp is not present in the two-field theory's eddy-viscosity, it seems likely that the absence of the cross term is causing problems near $k = k_c$, either directly or indirectly.

We must stress that our DNS results correspond to a system with a relatively low Reynolds number, exhibiting only the very beginnings of an inertial range. It can be argued that the two-field theory requires extended inertial range behaviour and, consequently, we should be cautious about the degree to which our results may be applied to it. In order to address this point, we have attempted to obtain results for a range of Reynolds numbers. By using LES rather than DNS fields we have extended our analysis to Reynolds numbers approaching $R_\lambda = 5000$ and found results very similar to those seen in our DNS at $R_\lambda \approx 190$. We note, however, that the analysis of incomplete LES fields represents a different situation to that of fully-resolved DNS data.

12.2.3 Partial time averaging

We have seen that the true conditional average is beyond the reach of our computational resources, both now and for the foreseeable future. Instead we looked at partial time averages and we now ask how these compare with the conditional average.

The strongest similarity is in the "closeness" of the low-k modes. For a sufficiently short time-difference, the low-k modes will still be significantly correlated with one another. Hence a partial time average taken over such a period will approximately satisfy at least one of the defining properties of the conditional average, namely $\langle u^- \rangle_c = u^-$ or, in our case, $\langle u^- \rangle_\tau \approx u^-$.

There is, however, one very important difference in that all of the velocity fields considered within the partial time average have a strong dynamical connection. We would expect the members of a biased subensemble, used to define the conditional average, to be very widely separated in time and hence truly independent of one another. Consequently we must be cautious in how we apply the results of our investigation to the conditional average.

The increasingly rapid decorrelation as wavenumber is increased does lend some support to the idea of a conditional average. In the derivation of the two-field theory, it is assumed that,

$$\lim_{k \to k_{max}} \left\langle u^+ \right\rangle_c \to \left\langle u^+ \right\rangle, \tag{12.2}$$

and this is central to recent work on *asymptotic freedom* [88]. In our experiments we have not seen such a collapse to the full ensemble average, but we would anticipate the limiting case,

$$\lim_{k_{max}/k_c \to \infty} \left\{ \lim_{k \to k_{max}} \left\langle u^+ \right\rangle_\tau \right\} \to \left\langle u^+ \right\rangle, \tag{12.3}$$

so that we again have an approximation to a desired property of the conditional average.

Of course, we have also seen that the partial time average will collapse to the full ensemble average in a manner governed by $\tau^{-1/2}$. For an average over statistically independent fields we might reasonably expect a more rapid collapse for high-k, and this brings us back to the central difference between the partial time average and the conditional average — namely the strong dynamical connection between the velocity fields considered in the former case.

In conclusion, we may state that the partial time average gives, as approximations, some of the properties attributed to the conditional average. However, the strong dynamical connection present in the low-k modes carries through to the high-k modes, albeit in an increasingly weakened form as k is increased. This is a significant deviation from the anticipated properties of the members of a biased subensemble, and hence limits the extent to which our conclusions may be applied to the conditional average.

12.2.4 Suggestions for future work

In practice, the results of two-field theory are obtained iteratively, a fact that we have been unable to reflect in the results presented here. Instead, we have concentrated either on the final results (Section 12.2.1) or on the elimination of the first band (Section 12.2.2).

An interesting exercise might be to perform a computation in which the iterative procedure was modelled in some way. For example, rather than using DNS data to obtain an eddy-viscosity by way of a single cutoff, it might be possible to build the eddy-viscosity up over a number of steps and to compare its development with that given by the two-field theory.

Further attention might also be concentrated on the problem of testing the conditional average, and addressing some of the drawbacks of previous attempts. The work of Machiels [44, 34], for example, was necessarily restricted to very

weak constraints and no actual averaging was performed. The work presented in Chapter 9 included the averaging of full three-dimensional velocity fields, but relied on a strong dynamical connection to maintain the necessary properties in the low-k region.

One possible investigative route would be to begin with a known low-k velocity field, u^-, and then to modify it slightly in order to generate u'^-, say. A suitable u'^+ field (or possibly a series of them) might then be generated by carrying out a simulation in which the high-k modes are allowed to evolve, while u'^- is kept fixed. It would then be possible to compare the properties of u'^+ with the u^+ field attached to the unperturbed u^- field. The obvious problem with such a study is that the physical validity of a velocity field generated in this way is uncertain. However, it might allow for a greater understanding of the connection between the low- and high-k modes.

12.3 The operational LES procedure

12.3.1 Conclusions

In Chapter 11, we introduced an *ad hoc* method to compensate for the absent turbulence modes in a truncated simulation. By considering a wide range of Reynolds numbers, we demonstrated that this technique was able to eliminate the build up of energy at the cutoff associated with the truncation and that it gave energy spectra which were in reasonable agreement with Qian's model.

Underlying the OpLES technique is an assumption of localness in that we assume that, over a single time integration step, there will be some wavenumber, k_{upturn}, prior to which the missing modes will not have an effect. This point was discussed earlier in this Chapter (Section 12.1.1) and the results of the OpLES seem to lend further support.

Additionally, it was noted that the OpLES technique is simply unable to mimic the behaviour of an eddy-viscosity plateau. In spite of this, and in spite of our belief that such a plateau *should* have been present for the majority of the runs performed, there certainly appeared to be a range of Reynolds numbers for which its absence did not seem to be having a detrimental effect. This again supports ideas of localness, in that, for an eddy-viscosity, the cusp-like behaviour near the cutoff is more important than the plateau at low-k.

Of course, for our highest Reynolds number simulation, we saw that the OpLES energy spectrum showed significant deviation from that predicted by Qian's model. This is perhaps an indication of the point at which the idea of localness is starting to break down and, as a consequence, an eddy-viscosity plateau starts to play an important role.

12.3.2 Suggestions for future work

Any future development of the OpLES method should probably concentrate on two areas — namely the further reduction of sharp energy losses and the improvement of the energy spectra.

The first of these will be related to the method used to locate the upturn and it might be worth exploring changes in both the high-level definition of the upturn (currently "the minimum of $\mathrm{d}\left[\ln E\right]/\mathrm{d}\left[\ln k\right]$") and the lower-level computational algorithm actually used (currently the polynomial fitting method).

For the second, changes would need to be made to what happens once the upturn has been found. Some sort of higher-order extrapolation may give a better match in cases where the correct energy spectrum continues to grow significantly steeper beyond k_{upturn} — although this is only likely to be the case for relatively low-Reynolds number runs and so is possibly not worth the effort. Improvements may also be obtained by directly addressing the lack of a non-zero plateau in the

OpLES eddy-viscosity, perhaps by introducing the plateau value from some other eddy-viscosity model.

Appendix A

Long time behaviour of the partial time average

We want to explore the long time behaviour of the correlation function,

$$R(u,\langle u\rangle_\tau;k)=\frac{\overbrace{\langle u_\alpha(\mathbf{k},t)\,\langle u_\alpha(-\mathbf{k},t)\rangle_\tau\rangle_s}^{(A)}}{\underbrace{\langle u_\alpha(\mathbf{k},t)u_\alpha(-\mathbf{k},t)\rangle_s^{1/2}}_{(B)}\underbrace{\langle\langle u_\alpha(\mathbf{k},t)\rangle_\tau\,\langle u_\alpha(-\mathbf{k},t)\rangle_\tau\rangle_s^{1/2}}_{(C)}}, \tag{A.1}$$

We first introduce,

$$\langle u_\alpha(\mathbf{k},s)u_\alpha(-\mathbf{k},r)\rangle_s=Q(k,|s-r|), \tag{A.2}$$

where we assume that,

$$Q(k,|\delta s|)\geq 0, \tag{A.3}$$

and that,

$$Q(k,|\delta s|)\approx 0 \text{ for } \delta s\geq t_c(k), \tag{A.4}$$

for some $t_c(k)$, subject also to the condition that δs is not so large as to include the theoretical very long time coincidental recorrelations [86]. We further assume that the partial averaging time satisfies,

$$\tau\geq t_c(k). \tag{A.5}$$

Using the definition of the short-time average given in equation (9.9) we may write (A) as

$$\begin{aligned}\langle u_\alpha(\mathbf{k},t)\,\langle u_\alpha(-\mathbf{k},t)\rangle_\tau\rangle_s &= \left\langle u_\alpha(\mathbf{k},t)\frac{1}{2\tau}\int_{t-\tau}^{t+\tau} u_\alpha(-\mathbf{k},s)\,\mathrm{d}s\right\rangle_s \\ &= \frac{1}{2\tau}\int_{t-\tau}^{t+\tau}\langle u_\alpha(\mathbf{k},t)u_\alpha(-\mathbf{k},s)\,\mathrm{d}s\rangle_s\,. \qquad \text{(A.6)}\end{aligned}$$

Substituting in from equation (A.2) for Q and applying a change of variable, $s' = s - t$, gives

$$\begin{aligned}\langle u_\alpha(\mathbf{k},t)\,\langle u_\alpha(-\mathbf{k},t)\rangle_\tau\rangle_s &= \frac{1}{2\tau}\int_{-\tau}^{\tau} Q(k,|s'|)\,\mathrm{d}s' \\ &= \frac{1}{2\tau}c(k), \qquad \text{(A.7)}\end{aligned}$$

where the last step follows from (A.4) and (A.5) and where,

$$c(k) = \int_{-t_c(k)}^{t_c(k)} Q(k,|s'|)\,\mathrm{d}s'. \qquad \text{(A.8)}$$

Next we consider (C),

$$\begin{aligned}&\langle\langle u_\alpha(\mathbf{k},t)\rangle_\tau\,\langle u_\alpha(-\mathbf{k},t)\rangle_\tau\rangle_s \\ &= \left\langle\left(\frac{1}{2\tau}\int_{t-\delta t}^{t+\delta t} u_\alpha(\mathbf{k},s)\,ds\right)\left(\frac{1}{2\tau}\int_{t-\tau}^{t+\tau} u_\alpha(-\mathbf{k},s)\,ds\right)\right\rangle_s \qquad \text{(A.9)} \\ &= \frac{1}{4\tau^2}\int_{t-\tau}^{t+\tau}\int_{t-\tau}^{t+\tau}\langle u_\alpha(\mathbf{k},s)u_\alpha(-\mathbf{k},r)\rangle_s\,\mathrm{d}r\mathrm{d}s. \qquad \text{(A.10)}\end{aligned}$$

Substituting for Q and applying the changes of variable, $s' = s + \tau - t$ and $r' = r + \tau - t$ gives,

$$\langle\langle u_\alpha(\mathbf{k},t)\rangle_\tau\,\langle u_\alpha(-\mathbf{k},t)\rangle_\tau\rangle_s = \frac{1}{4\tau^2}\int_0^{2\tau}\int_0^{2\tau} Q(k,|s'-r'|)\,\mathrm{d}r'\mathrm{d}s'. \qquad \text{(A.11)}$$

Next, we split the integral into three parts to give,

$$\begin{aligned}\langle\langle u_\alpha(\mathbf{k},t)\rangle_\tau\,\langle u_\alpha(-\mathbf{k},t)\rangle_\tau\rangle_s &= \frac{1}{4\tau^2}\int_{t_c(k)}^{2\tau-t_c(k)}\int_0^{2\tau} Q(k,|s'-r'|)\,\mathrm{d}r'\mathrm{d}s' \\ &+ \frac{1}{4\tau^2}\int_0^{t_c(k)}\int_0^{2\tau} Q(k,|s'-r'|)\,\mathrm{d}r'\mathrm{d}s' \\ &+ \frac{1}{4\tau^2}\int_{2\tau-t_c(k)}^{2\tau}\int_0^{2\tau} Q(k,|s'-r'|)\,\mathrm{d}r'\mathrm{d}s'. \qquad \text{(A.12)}\end{aligned}$$

The range of the inner integral in the first term of equation (A.12) always includes $[s - t_c(k), s + t_c(k)]$ and so we may write,

$$\begin{aligned}\int_{t_c(k)}^{2\tau - t_c(k)} \int_0^{2\tau} Q(k, |s' - r'|)\, \mathrm{d}r'\mathrm{d}s' &= \int_{t_c(k)}^{2\tau - t_c(k)} c(k)\mathrm{d}s' \\ &= 2c(k)\left(\tau - t_c(k)\right). \end{aligned} \tag{A.13}$$

Applying the change of variables, $s'' = 2\tau - s'$ and $r'' = 2\tau - r'$ to integrals in the third term of equation (A.12) gives,

$$\begin{aligned}\int_{2\tau - t_c(k)}^{2\tau} \int_0^{2\tau} Q(k, |s'' - r''|)\, \mathrm{d}r''\mathrm{d}s'' &= \int_{t_c(k)}^{0} \int_{2\tau}^{0} Q(k, |s'' - r''|)\, \mathrm{d}r''\mathrm{d}s'' \\ &= \int_0^{t_c(k)} \int_0^{2\tau} Q(k, |s'' - r''|)\, \mathrm{d}r''\mathrm{d}s'', \end{aligned} \tag{A.14}$$

where the last step results from reversing the direction of integration and we note that this is the same as the integral in the second term of equation (A.12). The inner integral always contains the range $[0, s'' + t_c(k)]$ and so we can write,

$$\int_0^{t_c(k)} \int_0^{2\tau} Q(k, |s'' - r''|)\, \mathrm{d}r''\mathrm{d}s'' = d(k), \tag{A.15}$$

where

$$\begin{aligned} d(k) &= \int_0^{t_c(k)} \int_0^{2t_c(k)} Q(k, |s'' - r''|)\, \mathrm{d}r''\mathrm{d}s'' \\ &< \int_0^{t_c(k)} \int_{-t_c(k)}^{2t_c(k)} Q(k, |s'' - r''|)\, \mathrm{d}r''\mathrm{d}s'' \\ &= \int_0^{t_c(k)} c(k)\mathrm{d}s'' \\ &= c(k)t_c(k). \end{aligned} \tag{A.16}$$

Putting all of this back into equation (A.12) gives,

$$\left\langle \left\langle u_\alpha(\mathbf{k}, t)\right\rangle_\tau \left\langle u_\alpha(-\mathbf{k}, t)\right\rangle_\tau \right\rangle_s = \frac{c(k)}{2\tau} + \frac{d(k) - c(k)t_c(k)}{2\tau^2}. \tag{A.17}$$

Finally we note that term (B) in equation (A.1) is a constant (with respect to τ),

$$\left\langle u_\alpha(\mathbf{k}, t) u_\alpha(-\mathbf{k}, t)\right\rangle_s = b(k), \text{ say.} \tag{A.18}$$

We now combine equations (A.7), (A.17) and (A.18) with equation (A.1) to give,

$$R(k) = \frac{a(k)}{\sqrt{\tau - t_c(k) + \frac{d(k)}{c(k)}}}, \tag{A.19}$$

where

$$a(k) = \sqrt{\frac{c(k)}{2b(k)}} \tag{A.20}$$

and where, from equation (A.16),

$$\frac{d(k)}{c(k)} < t_c(k). \tag{A.21}$$

So, for $\tau \gg t_c(k)$ we can write that,

$$R(k) \sim \tau^{-1/2}. \tag{A.22}$$

Additionally, if we again assume that $\tau \gg t_c(k)$, we may rewrite equation (A.17) to give,

$$\left\langle \langle u_\alpha(\mathbf{k}, t) \rangle_\tau \langle u_\alpha(-\mathbf{k}, t) \rangle_\tau \right\rangle_s \sim \tau^{-1}. \tag{A.23}$$

Taking the square root then gives us an expression in terms of an r.m.s. value of the partially time averaged quantity and we see that this behaves in a similar fashion to the correlation function,

$$\left\langle \langle u_\alpha(\mathbf{k}, t) \rangle_\tau \langle u_\alpha(-\mathbf{k}, t) \rangle_\tau \right\rangle_s^{1/2} \sim \tau^{-1/2}. \tag{A.24}$$

Appendix B

The DNS Code — A Users' Guide

B.1 Running the DNS code

This appendix is intended to give simple instructions in the use of the DNS code for simulations of both decaying and stationary turbulence. The code also allows conventional, operational and static large eddy simulations to be performed.

In order to carry out a simulation, you need to have a directory which contains at least the following three things:

- the `dns` executable
- an `input.dns` file which defines the simulation
- a `data/` directory, where the various outputs will be written

A sample `input.dns` file is given in Figure B.1. It is intended to be self-explanatory, but the various options are covered in greater detail in the following sections. It is important to note that you should not change the number of "comment" lines, although you are free to change their content.

```
**** The title for this run
"256f - 256^3 simulation, forced turbulence"
**** The length of the side of the box, L, divided by 2*pi
1.0
**** The viscosity, nu
0.001
**** The time step, deltat
0.001
**** 0 :  decaying turbulence
**** <>0 :  forcing with desired dissipation rate set to this value
0.149
**** Initial spectrum
**** 0 :  use c1,...,c4 (defined below) to give E(k) = c1*(k^c2)*exp[-c3*(k^c4)]
**** 1 :  Taylor-Green vortex
0
**** The parameters which define the initial energy spectrum, c1,...,c4
0.063830764
4.0
0.5
2.0
**** k_0, the ultraviolet cutoff wavenumber shell (0 :  no cutoff)
120
**** 0 :  no anti-aliasing
**** 1 :  partial anti-aliasing (random shifting method)
1
**** 0 :  no OpLES procedure; 1 :  activate OpLES procedure
**** 2 :  fix to Qian; 3 :  fix to Kolmogorov
0
**** "" :  no eddy viscosity; "visc" read in named file; "EDQNM" - edqnm visc.
""
**** time step to use as base for two-time correlations (-1 :  no correlations)
-1
**** How often the energy spectrum etc.  should be computed (must be >= 2)
25
**** How often a realization should be dumped (0 :  never)
500
**** Realization directory (must be in quotes, include trailing /, max 80 chars)
"/work6/ed/ajy/"
**** Random number seed
1000
**** inital time step - 0 :  fresh run; n :  resume from realization file n
0
**** The final time step (must be > than initial time step)
1000
```

Figure B.1: A sample `input.dns` file — line numbers have been added to enhance readability.

B.1.1 Setting a simulation title

You may place an arbitrary simulation title (containing no more than 80 characters) in line 2. This title will appear near the top of the `run.dat` output file.

B.1.2 System size

Line 4 allows you to set the size of the box, L_{box}. This value is assumed to be in units of 2π, so that a value of '1.0' actually corresponds to the conventional choice of $L_{box} = 2\pi$.

B.1.3 Kinematic viscosity

The kinematic viscosity of the system is set on line 6. Inviscid runs are possible, simply by setting this value to '0'.

B.1.4 Time step

The size of the computational time step is set on line 8.

B.1.5 Decaying/stationary turbulence

Line 11 of the `input.dns` file determines whether the turbulence will undergo free decay, or whether it be maintained via a forcing term. A value of '0' will give free decay, while any other value will be used to set the energy input rate, ε_w.

B.1.6 Initial conditions

The type of initial velocity field is set in line 15. A value of '1' here will set up a Taylor-Green vortex, as defined in Section 5.1. If a '0' is entered here, then a random velocity field is set up to give a required initial energy spectrum,

$E(k,0) = c_1 k^{c_2} \exp(-c_3 k^{c_4})$, where the parameters $c_1, \ldots, c_4$ are specified in lines 17–20. Details of random field generation may be found in Section 3.3.

B.1.7 Truncation

The value set on line 22 corresponds to the maximum shell of wavenumbers which will be included in the simulation. If a value of '0' is set here, every point on the N^3 grid will be set to contain energy.

B.1.8 Anti-aliasing

Putting a '1' in line 25 will activate partial dealiasing by the random shifting method outlined in Section 3.7.2. A '0' indicates that no anti-aliasing should take place.

Anti-aliasing by truncation (see Section 3.7.1) is possible by setting an appropriate value on line 22.

B.1.9 Large eddy simulations

The operational LES procedure can be activated by placing a '1' on line 28. Values of '2' and '3' here will cause static LES runs to be performed using Qian's model spectrum and a Kolmogorov spectrum respectively.

It is also possible to read in a conventional eddy-viscosity by placing its filename on line 30. The eddy-viscosity file should contain 101 points, giving $\delta\nu(k)$ for $k = 0$ to $k = k_0$, where k_0 refers to the *outer edge* of the maximum shell. For example, if the maximum shell (set on line 22) is 30, and the shell width (equal to $2\pi/L_{box}$, set on line 4) is 1, then $k_0 = 30.5$. The format of an eddy viscosity file is shown in Figure B.1.9.

Finally, a run may be performed using the EDQNM viscosity by putting '`"EDQNM"`'

1	0.0,	$\delta\nu(0)$
	⋮	⋮
n	k,	$\delta\nu(k)$
	⋮	⋮
101	k_0,	$\delta\nu(k_0)$

Figure B.2: A sample eddy-viscosity file — line numbers have been added to enhance readability.

on line 30.

B.1.10 Two-time correlations

The DNS code is capable of computing two-time correlations, relative to a single, user defined time. If the value '-1' is placed in line 32, then no correlations will be performed, otherwise correlations will be performed with the time step set on this line.

Note: If velocity field output is active (see Section B.1.12), then a realization file must exist for the time step with which the correlations are being performed.

B.1.11 Controlling the output

Line 34 controls how often the DNS code will compute things like the energy spectrum and dissipation rate. A value of '25', for example, would generate output every 25 time steps. This value must be set to at least 2.

B.1.12 Velocity field output

The ability to write entire velocity fields to files is provided for two reasons: firstly so that it is possible to split a long simulation into many smaller runs, and secondly so that a velocity field may later be read back in for further analysis.

The frequency with which these velocity field dumps take place is set on line 36.

A value of '500' here will ensure that the velocity field is written out at time steps 500, 1000, 1500 etc. The directory given on line 38 identifies the location to which these realization files will be written.

Note: Dummy realization files must exist *prior* to a velocity field dump being performed. They should have names of the type `realization.nnnnnnnn.dat` where `nnnnnnnn` is the zero-padded time step. If you are performing two-time correlations, then the base field will also be dumped, and a `vfield-real.nnnnnnnn.dat` file must also exist. The program `generate` will create these files for you.

B.1.13 Random number seed

If two simulations are performed, one after the other, without the contents of the `input.dns` file being altered, they will both produce identical results. Altering the value of the random number seed, set on line 40, allows you to perform simulations with, for example, identical initial spectra, but completely uncorrelated phase information.

B.1.14 Initial and final time steps

The initial and final time steps for a particular simulation run are set on lines 42 and 44 respectively. If the initial time step is set to '0', an initial velocity field will be generated, and the run will progress from there. If any other value is entered, the simulation will attempt to read in the velocity field corresponding to that time step from disk and will then continue from that point. The location of velocity field file is set on line 38.

`direct_flatness.dat`	velocity derivative flatness — computed in x-space
`direct_skewness.dat`	velocity derivative skewness — computed in x-space
`diss_rate.dat`	dissipation rate
`et.dat`	eddy turnover time
`int_reyn.dat`	integral Reynolds number
`int_scale.dat`	integral length scale
`isotropy.dat`	measure of system isotropy
`kdiss.dat`	Kolmogorov dissipation wavenumber
`mic_reyn.dat`	Taylor microscale Reynolds number
`microscale.dat`	Taylor microscale
`rms_vel.dat`	r.m.s. velocity
`skewness.dat`	velocity derivative skewness — computed in k-space
`total_energy.dat`	total energy
`trans_max.dat`	maximum transport power
`k_turn.dat`	*OpLES only* — the point of activation
`gamma.dat`	*OpLES only* — the gradient at the point of activation
`run.dat`	file containing information about the simulation
`Espec.nnnnnnnn`	energy spectra
`Tspec.nnnnnnnn`	transfer spectra
`isotropy.nnnnnnnn`	shell-by-shell isotropy measure
`trans.nnnnnnnn`	transport power spectra
`uv-corr.nnnnnnnn`	two-time correlation
`cusp.nnnnnnnn`	*OpLES only* — spectra with cusps
`dnu.nnnnnnnn`	*OpLES only* — equivalent eddy-viscosities
`smooth.nnnnnnnn`	*OpLES only* — smoothed spectra

Table B.1: A description of each file output by the DNS code.

B.2 Description of output files

The output files produced by the DNS code, and deposited in the `data/` directory beneath the executable, come in two types. Those with a `.dat` extension contain data corresponding to the time evolution of a particular quantity — each line of such a file represents a value at a particular time step. Files with numeric extensions (`.nnnnnnnn`) each correspond to a particular time step and will contain spectral information — one line for each k-shell.

Details of all DNS output files are presented in Table B.1.

Bibliography

[1] K.R. Sreenivasan. Fluid turbulence. *Rev. Mod. Phys.*, 71(2 (Centenary)):S383–S395, 1999.

[2] W.D. McComb. *The Physics of Fluid Turbulence.* Oxford University Press, 1 edition, 1990.

[3] S. Goldstein. Fluid mechanics in the first half of this century. *Ann. Rev. Fluid Mech.*, 1:1–28, 1969.

[4] O. Reynolds. An experimental determination of the circumstances which determine whether the motion of water shall be direct or sinuous, and of the law of resistance in parallel channels. *Phil. Trans. R. Soc. A*, 174:935–982, 1883.

[5] G.I. Taylor. Statistical theory of turbulence. *Proc. R. Soc. Lond. A*, 151:421–454, 1935.

[6] W.D. McComb and A.G. Watt. Conditional averaging procedure for the elimination of the small-scale modes from incompressible fluid turbulence at high Reynolds numbers. *Phys. Rev. Lett.*, 65(26):3281–3284, 1990.

[7] W.D. McComb, W. Roberts, and A.G. Watt. Conditional-averaging procedure for problems with mode-mode coupling. *Phys. Rev. A*, 45(6):3507–3515, 1992.

[8] W.D. McComb and A.G. Watt. Two-field theory of incompressible-fluid turbulence. *Phys. Rev. A*, 46(8):4797–4812, 1992.

[9] T.-J. Yang. *A Study of Renormalization Group Methods Applied to Fluid Turbulence.* PhD thesis, University of Edinburgh, 1998.

[10] A. Hunter. PhD thesis, University of Edinburgh, 1999.

[11] C. Johnston. PhD thesis, University of Edinburgh, 1999.

[12] M. Lesieur and R. Rogallo. Large-eddy simulation of passive scalar diffusion in isotropic turbulence. *Phys. Fluids A*, 1(4):718–722, 1989.

[13] H. P. Robertson. The invariant theory of isotropic turbulence. *Proc. Cam. Phil. Soc.*, 36:209–223, 1940.

[14] G.K. Batchelor. *The theory of homogeneous turbulence.* Cambridge University Press, 1953.

[15] A.N. Kolmogorov. The local structure of turbulence in incompressible viscous fluid for very large Reynolds' numbers. *C.R.Acad.Sci.URSS*, 30(4):301–305, 1941.

[16] A.N. Kolmogorov. Dissipation of energy in the locally isotropic turbulence. *C.R.Acad.Sci.URSS*, 32(1):16–18, 1941.

[17] G.I. Taylor. The spectrum of turbulence. *Proc. R. Soc. Lond.*, A164:476–490, 1938.

[18] R.H. Kraichnan. The structure of isotropic turbulence at very high reynolds numbers. *J. Fluid Mech.*, 5:497, 1959.

[19] D.C. Leslie. *Developments in the theory of modern turbulence.* Clarendon Press, Oxford, 1973.

[20] U. Frisch. *Turbulence: The Legacy of A.N. Kolmogorov.* Cambridge University Press, 1995.

[21] S. Orszag. Numerical methods for the simulation of turbulence. *Phys. Fluids (suppl. 2)*, 12:250–257, 1969.

[22] H.F. Davis and A.D. Snider. *Introduction to Vector Analysis.* Wm. C. Brown, sixth edition, 1991.

[23] P.K. Yeung, J.G. Brasseur, and Q. Wang. Dynamics of direct large-small scale couplings in coherently forced turbulence: concurrent physical- and fourier-space views. *J. Fluid Mech*, 283:43–95, 1995.

[24] P. Moin and K. Mahesh. Direct numerical simulation: a tool in turbulence research. *Ann. Rev. Fluid Mech.*, 30:539–578, 1998.

[25] R.D. Moser and P. Moin. The effects of curvature in wall-bounded turbulent flows. *J. Fluid Mech.*, 175:479–510, 1987.

[26] V. Eswaran and S.B. Pope. An examination of forcing in direct numerical simulations of turbulence. *Computers & Fluids*, 16(3):257–278, 1988.

[27] L.-P. Wang, S. Chen, J.G. Brasseur, and J.C. Wyngaard. Examination of hypotheses in the kolmogorov refined turbulence theory through high-resolution simulations. part 1. velocity field. *J. Fluid Mech.*, 309:113–156, 1996.

[28] J. Jiménez and A.A. Wray. On the characteristics of vortex filaments in isotropic turbulence. *J. Fluid Mech.*, 373:255–285, 1998.

[29] M.R. Spiegel. *Theory and Problems of Vector Analysis.* McGraw-Hill, SI (metric) edition, 1974.

[30] S. Orszag. Numerical simulation of incompressible flows within simple boundaries. I. Galerkin (spectral) representations. *Stud. Appl. Maths.*, 50(4):293–327, 1971.

[31] G.S. Patterson Jr. and S. Orszag. Spectral calculations of isotropic turbulence: Efficient removal of aliasing interactions. *Phys. Fluids*, 14:2538–2541, 1971.

[32] R.S. Rogallo. Numerical experiments in homogeneous turbulence. *NASA TM-81315*, 1981.

[33] H.R. Schwarz. *Numerical Analysis — A Comprehensive Introduction.* John Wiley & Sons, 1989.

[34] L. Machiels. Predictability of small-scale motion in isotropic fluid turbulence. *Phys. Rev. Lett.*, 79(18):3411–3414, 1997.

[35] G.I. Taylor and A.E. Green. Mechanism of the production of small eddies from large ones. *Proc. R. Soc. Lond.*, 158:499–521, 1937.

[36] M.E. Brachet, D.I. Meiron, S.A. Orszag, B.G. Nickel, R.H. Morf, and U. Frisch. Small-scale struction of the Taylor-Green vortex. *J. Fluid Mech.*, 130:411–452, 1983.

[37] J. Jeong and F. Hussain. On the identification of a vortex. *J. Fluid Mech.*, 285:69–94, 1995.

[38] A. Vincent and M. Meneguzzi. The spatial structure and statistical properties of homogeneous turbulence. *J. Fluid Mech.*, 225:1–20, 1991.

[39] M. Briscolini and P. Santangelo. The non-Gaussian statistics of the velocity field in low-resolution large-eddy simulations of homogeneous turbulence. *J. Fluid Mech.*, 270:199–217, 1994.

[40] I. Hosokawa, S.-I. Oide, and K. Yamamoto. Existence and significance of 'soft worms' in isotropic turbulence. *J. Phys. Soc. Japan*, 66(10):2961–2964, 1997.

[41] P.K. Yeung and Y. Zhou. Universality of the Kolmogorov constant in numerical simulations of turbulence. *Phys. Rev. E*, 56:1746–1752, 1997.

[42] K.R. Sreenivasan. An update on the energy dissipation rate in isotropic turbulence. *Phys. Fluids*, 10(2):528–529, 1998.

[43] Z.-S. She, S. Chen, G. Doolen, R.H. Kraichnan, and S.A. Orszag. Reynolds number dependence of isotropic Navier-Stokes turbulence. *Phys. Rev. Lett.*, 70(21):3251–3254, 1993.

[44] W.D. McComb, T.-J. Yang, A. Young, and L. Machiels. Investigation of renormalization group methods for the numerical simulation of isotropic turbulence. In *Proc. Eleventh Symposium on Turbulent Shear Flows*, 1997.

[45] J. Jiménez, A.A. Wray, P.G. Saffman, and R.S. Rogallo. The structure of intense vorticity in isotropic turbulence. *J. Fluid Mech.*, 255:65–90, 1993.

[46] G. Stolovitzky, K.R. Sreenivasan, and A. Juneja. Scaling functions and scaling exponents in turbulence. *Phys. Rev. E*, 48(5):R3216–R3220, 1993.

[47] J.H. Curry, J.R. Herring, J. Loncaric, and S.A. Orszag. Order and disorder in two- and three-dimensional Bénard convection. *J. Fluid Mech.*, 147:1–38, 1984.

[48] G.H. Fullerton. PhD thesis, University of Edinburgh, 1999.

[49] M. Lesieur and O. Métais. New trends in large-eddy simulations of turbulence. *Ann. Rev. Fluid Mech.*, 28:45–82, 1996.

[50] A. Leonard. Energy cascade in large-eddy simulations of turbulent fluid flows. *Adv. Geophys.*, 18a:237–248, 1974.

[51] J.H. Ferziger. Subgrid-scale modelling. In B. Galperin and S.A. Orszag, editors, *Large Eddy Simulation of Complex Engineering and Geophysical Flows*, pages 37–54. Cambridge University Press, 1993.

[52] J. Boussinesq. Essai sur la théorie des eaux courantes. *Mém. prés. par div. savants à l'Acad. Sci*, 23:1–680, 1877.

[53] J.O. Hinze. *Turbulence — An Introduction to Its Mechanism and Theory.* McGraw-Hill Book Company, 1959.

[54] J. Smagorinsky. General circulation experiments with the primitive equations. *Mon. Weather Rev.*, 91(3):99–164, 1963.

[55] D.K. Lilly. In J.R. Herring and J.C. McWilliams, editors, *Lecture Notes on Turbulence*, pages 117–218. Singapore: World Scientific, 1987.

[56] R.H. Kraichnan. Eddy viscosity in two and three dimensions. *J. Atmos. Sci.*, 33:1521–1536, 1976.

[57] J.-P. Chollet and M. Lesieur. Parameterization of small scales of three-dimensional isotropic turbulence utilizing spectral closures. *J. Atmos. Sci.*, 38(12):2747–2757, 1981.

[58] J.-P. Chollet. Two-point closure used for a sub-grid scale model in large-eddy simulation. In L.J.S. Galperin *et al*, editor, *Turbulent Shear Flows IV*, pages 62–72. Springer, 1985.

[59] J.A. Domaradzki, R.W. Metcalfe, R.S. Rogallo, and J.J. Riley. Analysis of subgrid-scale eddy viscosity with use of results from direct numerical simulations. *Phys. Rev. Lett.*, 58(6):547–550, 1987.

[60] O. Métais and M. Lesieur. Spectral large-eddy simulation of isotropic and stably stratified turbulence. *J. Fluid Mech.*, 239:157–194, 1992.

[61] T. Miyauchi, M. Tanahashi, and T. Kakuwa. Evaluation of energy transfer between grid scale and subgrid scale by use of direct numerical simulation database. *JSME Int. J. B*, 40(3):343–350, 1997.

[62] Y.-H. Pao. Structure of turbulent velocity and scalar fields at large wavenumbers. *Phys. Fluids*, 8:1063–1075, 1965.

[63] J. Qian. Universal equilibrium range of turbulence. *Phys. Fluids*, 27(9):2229–2233, 1984.

[64] M. Lesieur, O. Métais, and R. Rogallo. Étude de la diffusion turbulente par simulation des grandes échelles. *C. R. Acad. Sci. Paris Serie II*, 308:1395–1400, 1989.

[65] E. Lamballais, O. Métais, and M. Lesieur. Influence of a spanwise rotation upon the coherent-structure dynamics in a turbulence channel flow. In J.-P. Chollet, P.R. Voke, and L. Kleiser, editors, *Direct and Large-Eddy Simulation II*, pages 225–236. Kluwer Academic Publishers, 1997.

[66] K.G. Wilson. Renormalization Group Methods. *Adv. Math.*, 16:170–186, 1975.

[67] H.A. Rose. Eddy diffusivity, eddy noise and subgrid-scale modelling. *J. Fluid Mech.*, 81(4):719–734, 1977.

[68] D. Forster, D. R. Nelson, and M. J. Stephen. Long-time tails and the large-eddy behaviour of a randomly stirred fluid. *Phys. Rev. Lett.*, 36(15):867–869, 1976.

[69] D. Forster, D. R. Nelson, and M. J. Stephen. Large-distance and long-time properties of a randomly stirred fluid. *Phys. Rev. A*, 16(2):732–749, 1977.

[70] V. Yakhot and S. A. Orszag. Renormalization Group analysis of turbulence. I. Basic theory. *J. Sci. Comp.*, 1(1):3–51, 1986.

[71] V. Yakhot and S. Orszag. Renormalization-Group analysis of turbulence. *Phys. Rev. Lett.*, 57(14):1722–1724, 1986.

[72] A.G. Watt. *A study of isotropic turbulence.* PhD thesis, University of Edinburgh, 1991.

[73] T. Dubois, F. Jauberteau, and Y. Zhou. Influences of subgrid scale dynamics on resolvable scale statistics in large-eddy simulations. *Physica D*, 100:390–406, 1997.

[74] Y. Zhou and G. Vahala. Reformulation of recursive-renormalization-group-based subgrid modelling of turbulence. *Phys. Rev. E*, 47(4):2503–2519, 1993.

[75] K. Ohkitani and S. Kida. Triad interactions in a forced turbulence. *Phys. Fluyids A*, 4(4):794–802, 1992.

[76] S. Kida. Three-dimensional periodic flows with high-symmetry. *J. Phys. Soc. Japan*, 54(6):2132–2136, 1985.

[77] J.G. Brasseur and C.-H. Wei. Interscale dynamics and local isotropy in high reynolds number turbulence within triadic interactions. *Phys. Fluids*, 6:842–870, 1994.

[78] R.A. Clark, J.H. Ferziger, and W.C. Reynolds. Evaluation of subgrid-scale models using an accurately simulated turbulent flow. *J. Fluid Mech.*, 91(1):1–16, 1979.

[79] V. Borue and S.A. Orszag. Local energy flux and subgrid-scale statistics in three-dimensional turbulence. *J. Fluid Mech.*, 366:1–31, 1998.

[80] V. Borue and S.A. Orszag. Forced three-dimensional homogeneous turbulence with hyperviscosity. *Europhys. Lett.*, 29:687–692, 1995.

[81] J. Borue, J.H. Ferziger, and W.C. Reynolds. Improved subgrid scale models for large eddy simulation. *AIAA Paper 80-1357*, 1980.

[82] S. Liu, C. Meneveau, and J. Katz. On the properties of similarity subgrid-scale models as deduced from measurements in a turbulent jet. *J. Fluid Mech.*, 275:83–119, 1994.

[83] M. Lesieur, P. Compte, E. Lamballais, O. Métais, and G. Silvestrini. Large-eddy simulations of shear flows. *J. Eng. Maths.*, 32:195–215, 1997.

[84] J.R. Herring. Subgrid scale modelling — an introduction and overview. In F. Durst, B.E. Launder, and F.W. Schmidt, editors, *Turbulent Shear Flows I*, pages 347–352. Springer-Verlag, 1979.

[85] G.L. Eyink. The renormalization group method in statistical hydrodynamics. *Phys. Fluids*, 6(9):3063–3078, 1994.

[86] L.D. Landau and E.M. Lifshitz. *Fluid Mechanics.* Pergamon Press, 1959.

[87] W.H. Press, S.A. Teukolsky, W.T. Vetterling, and B.P. Flannery. *Numerical Recipes in Fortran 77. The Art of Scientific Computing.* Cambridge University Press, second edition, 1997.

[88] W. D. McComb and C. Johnston. Elimination of turbulent modes using a conditional average with asymptotic freedom. Preprint NI99005-TR, Isaac Newton Institute for Mathematical Science, 1999.